

DOCTORAL THESIS

Production and Properties of Additively Manufactured Electrical Machine Cores

Hans Tiismus

TALLINN UNIVERSITY OF TECHNOLOGY
DOCTORAL THESIS
49/2022

Production and Properties of Additively Manufactured Electrical Machine Cores

HANS TIISMUS



TALLINN UNIVERSITY OF TECHNOLOGY

School of Engineering

Department of Electrical Power Engineering and Mechatronics

This dissertation was accepted for the defence of the degree 20/06/2022

Supervisor:

Prof. Ants Kallaste
School of Engineering
Tallinn University of Technology
Tallinn, Estonia

Co-supervisor:

Dr. Toomas Vaimann
School of Engineering
Tallinn University of Technology
Tallinn, Estonia

Opponents:

Prof. Ahmed Jawad Qureshi
Faculty of Engineering
Mechanical Engineering Department
University of Alberta
Edmonton, Canada

Dr. Jenni Pippuri-Mäkeläinen
VTT Technical Research Center of Finland
Espoo, Finland

Defence of the thesis: 02/09/2022, Tallinn

Declaration:

Hereby I declare that this doctoral thesis, my original investigation and achievement, submitted for the doctoral degree at Tallinn University of Technology has not been submitted for doctoral or equivalent academic degree.

Hans Tiismus

signature



European Union
European Regional
Development Fund



Investing
in your future

Copyright: Hans Tiismus, 2022

ISSN 2585-6898 (publication)

ISBN 978-9949-83-879-0 (publication)

ISSN 2585-6901 (PDF)

ISBN 978-9949-83-880-6 (PDF)

TALLINNA TEHNIKAÜLICOOL
DOKTORITÖÖ
49/2022

**Kihtlisandus meetodil valmistatud
elektrimasinate magnetsüdamikud ja
nende omadused**

HANS TIISMUS



Contents

List of Publications	6
Author's Contribution to the Publications	8
Introduction	9
1.1 Electrical Machines	9
1.2 Additive Manufacturing of Electrical Machines	9
1.3 Hypotheses of the Thesis	12
1.4 Objectives of the Thesis	12
1.5 Scientific Contributions	13
1.6 Outline of the Thesis	13
2 State of the Art.....	15
2.1 Metal Additive Manufacturing.....	15
2.2 State-of-the-art of AM Electromagnetic materials and EM components	18
3 Additive Manufacturing of Electrical Steel.....	25
3.1 Soft Magnetic Materials.....	25
3.2 Sample Preparation and Characterization Methods.....	29
3.3 Printed Material Process Optimization and Properties Results	32
3.3.1 Powder Characterization.....	32
3.3.2 Density Optimization.....	32
3.3.3 DC Magnetic Properties	35
3.3.4 AC Magnetic Properties	37
3.3.5 Material Properties Library, Results Summary	39
4 Prototyping of AM Electrical Machines.....	42
4.1 Transformer Prototyping	42
4.2 Induction Motor Prototyping	45
5 Conclusions and Future Work	50
References	53
Acknowledgements.....	65
Abstract.....	66
Lühikokkuvõte.....	67
Appendix	69
Curriculum vitae.....	161
Elulookirjeldus.....	162

List of Publications

The list of author's publications, on the basis of which the thesis has been prepared:

- I H. Tiismus, A. Kallaste, T. Vaimann, and A. Rassõlkin, "State of the Art of Additively Manufactured Electromagnetic Materials for Topology Optimized Electrical Machines," *Addit. Manuf.*, vol. 55, no. July 2022, doi: 10.1016/j.addma.2022.102778.
- II H. Tiismus, A. Kallaste, T. Vaimann, L. Lind, I. Virro, A. Rassõlkin, and T. Dedova, "Laser Additively Manufactured Magnetic Core Design and Process for Electrical Machine Applications," *Energies*, vol. 15, no. 10, 2022, doi: <https://doi.org/10.3390/en15103665>.
- III H. Tiismus, A. Kallaste, M. U. Naseer, T. Vaimann, and A. Rassolkin, "Design and Performance of Laser Additively Manufactured Core Induction Motor," *IEEE Access*, pp. 50137–50152, 2022, doi: 10.1109/ACCESS.2022.3173317.
- IV H. Tiismus, A. Kallaste, A. Belahcen, A. Rassolkin, T. Vaimann, and P. Shams Ghahfarokhi, "Additive Manufacturing and Performance of E-Type Transformer Core," *Energies*, vol. 14, no. 11, p. 3278, Jun. 2021, doi: 10.3390/en14113278.
- V M. Sarap, S. Member, A. Kallaste, S. Member, P. S. Ghahfarokhi, H. Tiismus, S. Member, T. Vaimann, and S. Member, "The effect of build direction on the thermal conductivity of additively manufactured AlSi 10 Mg and silicon-steel samples," in *Proceedings - 2022 International Conference on Electrical Machines, ICEM 2022, Sept 2022*. (accepted, under publication).

Other Publications:

- VI H. Tiismus *et al.*, "AC Magnetic Loss Reduction of SLM Processed Fe-Si for Additive Manufacturing of Electrical Machines," *Energies*, vol. 14, no. 5, p. 1241, 2021, doi: 10.3390/en14051241.
- VII H. Tiismus, A. Kallaste, A. Belahcen, T. Vaimann, A. Rassõlkin, and D. Lukichev, "Hysteresis Measurements and Numerical Losses Segregation of Additively Manufactured Silicon Steel for 3D Printing Electrical Machines," *Appl. Sci.*, vol. 10, no. 18, p. 6515, 2020, doi: 10.3390/app10186515.
- VIII H. Tiismus, A. Kallaste, A. Belahcen, A. Rassolkin, and T. Vaimann, "Challenges of Additive Manufacturing of Electrical Machines," in *Proceedings of the 2019 IEEE 12th International Symposium on Diagnostics for Electrical Machines, Power Electronics and Drives, SDEMPED 2019*, 2019, pp. 44–48. doi: 10.1109/DEMPED.2019.8864850.
- IX H. Tiismus, A. Kallaste, A. Belahcen, A. Rassolkin, and T. Vaimann, "Hysteresis loss evaluation of additively manufactured soft magnetic core," in *Proceedings - 2020 International Conference on Electrical Machines, ICEM 2020*, Aug. 2020, pp. 1657–1661, doi: 10.1109/ICEM49940.2020.9270836.
- X H. Tiismus, A. Kallaste, T. Vaimann, and A. Rassõlkin, "Eddy Current Loss Reduction Prospects in Laser Additively Manufactured Soft Magnetic Cores," in *Proceedings - 2022 International Conference on Electrical Machines, ICEM 2022*, Sept. 2022. (accepted, under publication).
- XI H. Tiismus, A. Kallaste, A. Rassõlkin, and T. Vaimann, "Preliminary analysis of soft magnetic material properties for additive manufacturing of electrical machines," *Key Eng. Mater.*, vol. 799 KEM, pp. 270–275, 2019, doi: 10.4028/www.scientific.net/KEM.799.270.

- XII H. Tiismus, A. Kallaste, T. Vaimann, A. Rassolkin, and A. Belahcen, "Technologies for Additive Manufacturing of Electrical Machines," *Int. Conf. Young Spec. Micro/Nanotechnologies Electron Devices, EDM*, vol. 2019-June, pp. 651–655, 2019, doi: 10.1109/EDM.2019.8823462.
- XIII H. Tiismus, A. Kallaste, T. Vaimann, A. Rassolkin, and A. Belahcen, "Electrical resistivity of additively manufactured silicon steel for electrical machine fabrication," *2019 Electr. Power Qual. Supply Reliab. Conf. 2019 Symp. Electr. Eng. Mechatronics, PQ SEEM 2019*, pp. 8–11, 2019, doi: 10.1109/PQ.2019.8818252.
- XIV H. Tiismus, A. Kallaste, T. Vaimann, A. Rassolkin, and A. Belahcen, "Axial Synchronous Magnetic Coupling Modeling and Printing with Selective Laser Melting," *2019 IEEE 60th Annu. Int. Sci. Conf. Power Electr. Eng. Riga Tech. Univ. RTUCON 2019 - Proc.*, 2019, doi: 10.1109/RTUCON48111.2019.8982344.
- XV H. Tiismus, A. Kallaste, T. Vaimann, A. Rassolkin, and A. Belahcen, "Additive Manufacturing of Prototype Axial Flux Switched Reluctance Electrical Machine," *2021 28th Int. Work. Electr. Drives Improv. Reliab. Electr. Drives, IWED 2021 - Proc.*, pp. 11–14, 2021, doi: 10.1109/IWED52055.2021.9376337.
- XVI A. Rassolkin, A. Kallaste, T. Vaimann, and H. Tiismus, "Control Challenges of 3D Printed Switched Reluctance Motor," *2019 26th Int. Work. Electr. Drives Improv. Effic. Electr. Drives, IWED 2019 - Proc.*, 2019, doi: 10.1109/IWED.2019.8664282.
- XVII M. Sarap, A. Kallaste, P. Shams Ghahfarokhi, H. Tiismus, and T. Vaimann, "Utilization of Additive Manufacturing in the Thermal Design of Electrical Machines: A Review," *Machines*, vol. 10, no. 4, p. 251, Mar. 2022, doi: 10.3390/machines10040251.
- XVIII M. Sarap, A. Kallaste, P. S. Ghahfarokhi, H. Tiismus, and T. Vaimann, "Determining the Thermal Conductivity of Additively Manufactured Metal Specimens," in *2022 29th International Workshop on Electric Drives: Advances in Power Electronics for Electric Drives (IWED)*, Jan. 2022, pp. 1–4. doi: 10.1109/IWED54598.2022.9722591.
- XIX M. Shafiq, P. Taklaja, I. Kiitam, H. Tiismus, I. Palu, and L. Kutt, "Performance Evaluation of Additive Manufacturing Based Test Samples for Studies of Defects in Electrical Insulation," no. December, pp. 1–6, 2022, doi: 10.1109/icecet52533.2021.9698476.
- XX P. S. Ghahfarokhi, A. Podgornovs, A. Kallaste, A. J. M. Cardoso, A. Belahcen, T. Vaimann, H. Tiismus, and B. Asad, "Opportunities and Challenges of Utilizing Additive Manufacturing Approaches in Thermal Management of Electrical Machines," *IEEE Access*, vol. 9, pp. 36368–36381, 2021, doi: 10.1109/ACCESS.2021.3062618.
- XXI E. Andriushchenko, A. Kallaste, A. Belahcen, T. Vaimann, A. Rassolkin, H. Heidari, and H. Tiismus, "Optimization of a 3d-printed permanent magnet coupling using genetic algorithm and taguchi method," *Electron.*, vol. 10, no. 4, pp. 1–16, 2021, doi: 10.3390/electronics10040494.
- XXII B. Asad, H. Tiismus, T. Vaimann, A. Belahcen, A. Kallaste, A. Rassolkin, and P. S. Ghahfarokhi, "Sliding mean value subtraction-based dc drift correction of b-h curve for 3d-printed magnetic materials," *Energies*, vol. 14, no. 2, pp. 1–10, 2021, doi: 10.3390/en14020284.

Author's Contribution to the Publications

Contributions to the papers in this thesis are:

- I Hans Tiismus is the primary author of this article. He conducted the full literature survey and wrote the initial draft of the paper.
- II Hans Tiismus is the primary author of this article. He planned the experiments, printed the samples, measured their properties, and wrote the initial draft of the paper.
- III Hans Tiismus is the primary author of this article. He modeled and printed the motor components, supervised its machining and assembly, conducted the measurements, and wrote the initial draft of the paper.
- IV Hans Tiismus is the primary author of this article. He designed and printed and assembled the 3D printed transformer core, conducted the measurements, and wrote the initial draft of the paper.
- V Hans Tiismus is the secondary author of this article. He printed the samples for the thermal characterization of the material.

Introduction

Additive manufacturing (AM) methods have been suggested as a technological enabler for producing next-generation electrical machines (EM)s. AMs principal advantage: unprecedented three-dimensional fabrication freedom can be employed to a great effect when optimizing the topology of the machines for enhancing the electromagnetic, structural, and thermal capabilities of EMs.

1.1 Electrical Machines

Electrical machines are the workhorses of the modern world. They are produced on almost every scale, from the small (mW or W) or medium-sized devices (kW) that we use every day domestically to the large machines (MW) designed for more specific industrial, propulsion, or energy applications. Electromechanical conversion facilitates the production of nearly all the electrical energy on Earth. In 2019, solar energy accounted for only 4.4% of all electricity produced in the EU, with all other sources involving rotating electrical machines (nuclear, wind, hydro, geothermal, and thermal power plants) [1]. In parallel, the motors employed in the industry consume over 40% of all the electrical energy produced [2].

Electrical machine designs are constantly developed by the sizable EM research community: driven by specific application requirements or political directives, and always pushed forward by technological advancements. Requirements for EMs are ever-increasing: higher efficiencies, more accurate control, vibration/noise reduction, simpler integration into assemblies /goods, and size reduction are only a few of the targeted optimization goals. It is challenging to construct electric motors that satisfy these growing requirements. For example, only a 2% additional gain in machine energy efficiency, from 92 to 94 %, requires a full 25% additional reduction in machine losses [3]. This has led to the need to look for a new alternative, cost-effective production options for constructing novel electrical machines. Additive manufacturing has been suggested as a potential alternative method for producing full electrical machines or their subcomponents. Although the method is still relatively immature, the first experimental results in the printed material properties and prototyping possibilities show great promise.

1.2 Additive Manufacturing of Electrical Machines

Metal additive manufacturing technologies have emerged as a strong competition to traditional subtractive methods. The four advantages of AM over conventional methods, which we consider the most prominent, are illustrated in Fig. 1.1. These include its production capacity for novel topologies and rapid prototyping, alongside its streamlined and simplified production cycles. AM benefits are often summarized in two terms: “complexity for free” and “individualization for free” [4]. Namely, with AM, the costs involved are largely invariant from part complexity and part lot size, meaning that cost-effective small volume production of parts with complex topologies is achievable. First, in the production of simple parts in large volumes, AM is uncompetitive. With sufficient part complexity, it will become cost-effective – as the subtractive alternatives become much too resource extensive (i.e., long 5-axis milling jobs, small volume casting, or welding/soldering of complex assemblies from smaller machined parts). For example,

3D printing has been utilized for the cost-effective production of inductor coils (previously assembled from 12 parts) [8] and aircraft fuel nozzles (previously assembled from 20 parts) [9].

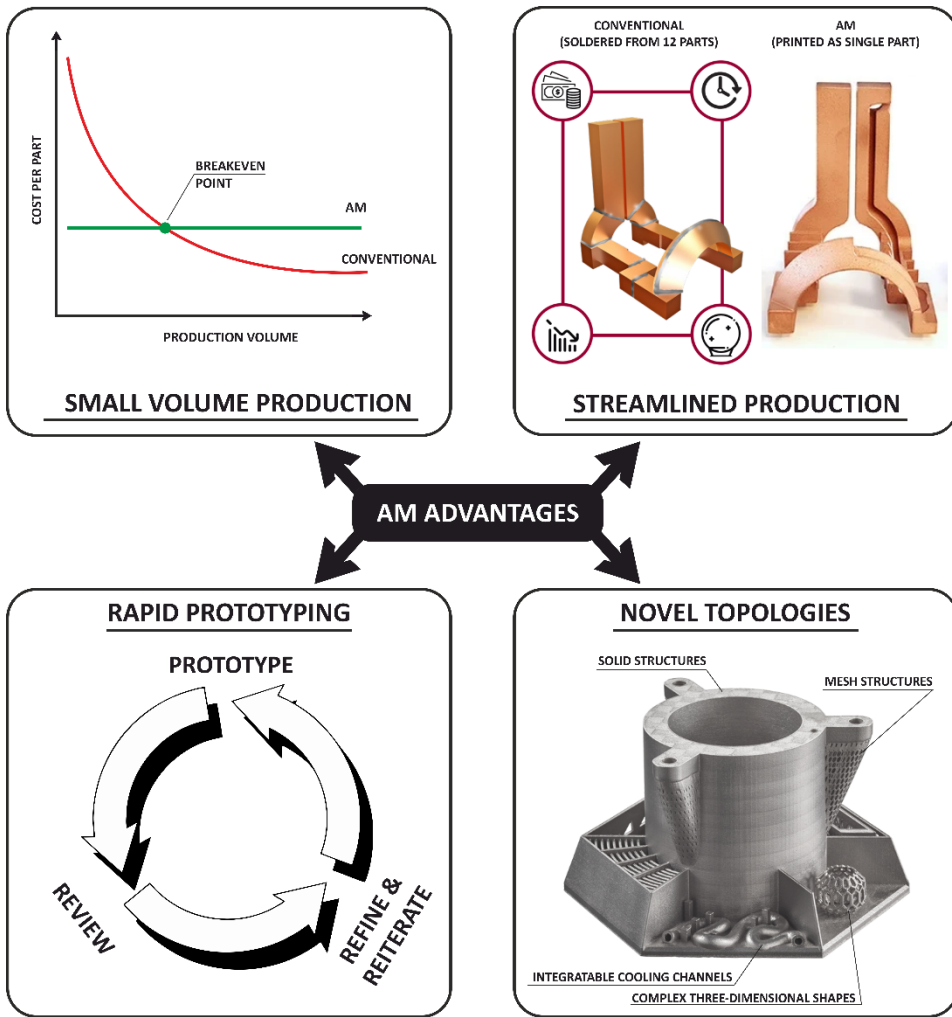


Figure 1.1. Advantages of Additive Manufacturing. [5-7]

Finally, at a certain part complexity level, novel features, some of which are completely unobtainable with traditional production methods, can be integrated into the parts. This is the largest draw of AM, as the almost freeform method is well suited for the realization of highly intricate, topology-optimized parts [4]. For EMs, the freeform design would present new opportunities for electromagnetic and thermal optimization of the machines: as flux paths and electrical/thermal conductors could be shaped in three dimensions. In parallel, the AM streamlined production possibilities would enable the research groups to prototype these novel topology optimized designs in-house, considerably simplifying the verification process and the overall design cycle.

The emerging field of additive manufacturing of electrical machines has its roots in 2013–2015, with the first experimentations and discussions in 3D printing of electro-mechanical systems [10-11]. The first metal additively manufactured motor components (synchronous rotors) were presented in 2016 [12-13]. Overviews on the feasibility of AM electrical machines started appearing a few years later (2018–2019) [14-16]. Up to date, the additive manufacturing of complete electrical machines is yet to be accomplished. Considerable progress, however, has been made in material sciences and individual machine component prototyping. By now, several reviews have been published on the topic. Some of the reviews focus more on novel motor design options: [17-20]; some on AM magnetic materials: [21-24]; and some on AM copper: [25-27]. Based on the literature, the overall perspective of the EM research community on integrating AM methods in the EM production cycle is twofold. First, the objective is to currently work on prototyping novel components and developing new optimization methods. And secondly, with future breakthroughs in AM fabrication speed and multi-material capacity, build upon the previous work to establish AM electrical machines on a larger scale. [7]

The main current challenges in the additive manufacturing EMs are related to the practical limits of the available printing systems and the technically demanding nature of electrical machine production. High spatial accuracy must be met for the moving machine parts, which are produced from at least three different materials. The materials involved are a soft ferromagnetic for the core, an excellent electrical conductor for the windings, and a dielectric for the insulation layers within both the core and the winding. Presently, the parallel printing of these materials is complicated, as the vast majority of metal printing systems are only effective in producing parts from a single material at a time. Though some multi-material options are emerging, the technology is largely untested. Therefore, full machine assemblies have not been produced additively, and AM of electrical machines has been limited to the printing of individual single-material components, which have been integrated into an assembly post-printing.

Obtaining high-performance materials with additive means can be a complicated procedure, as the method is well known for its capriciousness. In order to produce parts with both the desired dimensions and performance, the printing should be controlled through finely tuned processing parameters. For laser-based printing systems, the optimal input energy window is relatively narrow. Excessive energy input has been linked to part deformation and cracking during printing and insufficient energy – high part porosity due to poor consolidation of the raw powder. A similar optimal balance must be determined for a multitude of other parameters, including raw material shape/composition, raw material supply rate, printing layer thickness, pre-heating temperature, printing patterns, support patterns, etc. It is also important to note that depending on the printing method involved, the printed parts require different pre- and post-processing steps for the printed parts to exhibit useful properties. These operations can range from thermal, chemical, or mechanical treatments encompassing the whole part or a specific part surface. In addition to the potential advantages of additive manufacturing, it offers numerous new challenges to the research community, which require solutions for the technology to mature.

1.3 Hypotheses of the Thesis

The research field of additive manufacturing of electrical machines is still at an early stage. Strong advantages have been linked to the process, yet several critical challenges are as of yet unsolved. Most prominently, 3D printing processes require further optimization to ensure high material quality and build job accuracy/reliability. Based on the current state-of-the-art and our expertise in the field, we propose the following hypotheses:

- With optimized processing, printed soft magnetic cores can reach similar or superior values of magnetic properties compared to common commercial materials: with medium-grade lamination materials and soft magnetic composites (SMCs). The performance of top-grade materials is likely out of reach with the current technology.
- Non-magnetic material properties, such as mechanical yield strength, electrical resistivity, and thermal conductivity of the printed silicon steel, are likely similar to the typical values of its conventional counterparts.
- Insulation layers cannot be effectively printed with laser powder bed fusion (L-PBF) within soft magnetic cores. Bulk (non-laminated) soft magnetic cores exhibit high eddy current losses. By introducing voids (air-gaps) within printed single-material components, these losses can be reduced substantially.
- Laser powder bed fusion printing method (L-PBF) is capable of fusing full-sized electrical machine components with comparable, though likely with slightly reduced performance.

1.4 Objectives of the Thesis

The main objective of the thesis is to provide a firm foundation that the future work on additive manufacturing of topology-optimized electrical machines and their components can be built upon. The work is focused on L-PBF prepared soft magnetic core materials: the material we consider the most influential for motor shape optimization. The goals of this work are:

- Conduct a literature survey on the current state-of-the-art, perspectives, and challenges of additively manufactured EM active part materials: soft magnetic, hard magnetic, and conductive materials.
- Fine-tune the printing setup to achieve the printing of soft magnetic parts from silicon steel powder with high relative density (above 99.5%).
- Develop and implement the process workflow to obtain printed silicon steel soft magnetic cores with useful magnetic properties.
- Characterize the non-magnetic properties of the printed silicon steel for future topology optimization purposes. These properties include electrical conductivity, thermal conductivity, and mechanical yield strength.
- Demonstrate the practical capability of L-PBF for printing functional electromagnetic devices, including the performance evaluation for comparison with conventional counterparts.

1.5 Scientific Contributions

Scientific Novelty

The scientific novelty of the doctoral thesis consists of the following:

- Development and implementation of process flow-charts for both printed material properties optimization and prototype electrical motor production.
- Modelling, fabrication, and verification of novel structures within printed soft magnetic parts for AC magnetic loss reduction, including the interlocking core design and the bi-directionally gapped core.
- L-PBF printing of the world's first prototype EMs with fully 3D printed metal cores (power transformer and induction motor) characterized in terms of performance.

Practical Novelties

- Development and tuning of the L-PBF printing setup for 3.7% silicon content steel printing.
- Tuning of post-printing annealing parameters for effective heat-treating of the printed soft magnetic cores
- Development of hysteresis curve analysis software for the core loss calculation based on spline fitting.
- Improvement of the utilized SLM-280 printers' custom recoating mechanism: increasing the efficient printable part height tenfold.
- Creation of properties library for the printed 3.7% silicon content steel for future machine design optimization efforts.

1.6 Outline of the Thesis

The thesis is divided into four larger subsections, which provide a comprehensive overview on the topic. First, the state of the art of 3D printing materials and components for electric motors is discussed. Secondly, the work process of obtaining high-quality soft magnetic cores by L-PBF is presented. Thirdly, prototyping of full magnetic circuits for functional EMs is demonstrated. And in the final chapter, conclusions on the conducted work are drawn, and future work is suggested. A brief description of the main chapters are as follows:

Chapter 2 focuses on the state of the art of additively manufactured electromagnetic materials and their implementation for prototyping electrical machines. The paragraph is divided into three larger parts. In the first half of this chapter, a short overview is given regarding the history and most common methods of metal additive manufacturing. The second part describes the current state-of-the-art of AM electromagnetic materials: soft magnetic, hard magnetic, and electrically conductive materials. In the final part of the chapter, the recent advances and trends in the prototyping of 3D-printed electrical machines are presented.

Chapter 3 describes the in-house L-PBF prepared soft magnetic material preparation process. Workflow for obtaining suitable material properties is proposed and verified empirically. Material characterization results of L-PBF fused 3.7% silicon content

electrical steel samples include DC and AC magnetic properties, electrical resistivity, thermal conductivity, and mechanical yield strength.

Chapter 4 presents the additional considerations and important steps when utilizing the characterized printed material for producing full prototype magnetic cores for functional devices. Two prototype cores are prepared. A passive EM: a 20 VA power transformer, and an active rotating EM: a 68 W three-phase induction motor. The assembled machines are characterized in terms of performance and compared with typical commercial machines of the same size to demonstrate the current state-of-the-art of printed EMs. The prototyping process and challenges encountered are mapped to provide a reference point for future work.

Chapter 5 presents the conclusions of this work and the discussion on future work related to the additive manufacturing of electrical machines.

2 State of the Art

The state-of-the-art of AM electromagnetic materials is researched to provide the answers to two questions. First, what can we expect from 3D printed materials – how wide of a gap can we expect between commercial and printed materials? And secondly, can 3D printing be used for producing functional electrical machine components? The paragraph is divided into three larger parts: metal additive manufacturing, printing of electromagnetic materials, and the prototyping of AM electrical machines. The chapter follows closely the results presented in published work I: “State of the Art of Additively Manufactured Electromagnetic Materials for Topology Optimized Electrical Machines.”

2.1 Metal Additive Manufacturing

Incrementally adding material during a production process is an ancient technique. It can be encountered in traditional crafting methods, such as smithing, weaving, or pottery. The modern process of AM is different from these time-worn techniques mainly by the process increment and its resolution (accuracy), which for modern systems can be up to ~25 micrometers. Without fully automated production systems, this level of repeatable accuracy is out of reach for additive methods, which is why AM has come into prominence relatively lately. The very first metal AM system was launched in 1998 – a directed energy deposition printer (by Optomec), which was followed one year later by a laser power bed fusion system (by SLM Solutions) [28]. This was followed by a period of rapid improvement of the technology, and in roughly the mid-2010s, metal 3D printing systems started entering the mainstream. Previously, the poor price-quality relationship made the printers unaffordable for scientific work and small-scale niche production.

Four types of printing systems have been used to the greatest extent in the literature for the printing of electromagnetic materials. These include different powder bed-based setups: electron beam powder bed fusion (EB-PBF), laser powder bed fusion (L-PBF), and binder jetting (BJ); and other setups with a print head, including directed energy deposition (DED), and various extrusion-based methods (FFF-fused filament fabrication, FDM – fuse deposition modeling). The main differences between the methods are outlined in Figure 2.1. In powder bed-based technologies, the printed parts are submerged into the raw powder pool one layer at a time. For both laser and electron beam powder bed fusion, the part is consolidated through an energy beam, in binding jetting – with a binding agent. In contrast to the powder bed-based systems, in DED and FDM, the part is typically stationary while the print head is in a three-dimensional motion. In these methods, the raw material is supplied by the system print head. In the case of DED, the process is supplied with a mixture of powder and inert gas or through a wire feeder, for FDM by a filament of mixed metal particles within a thermoplastic binder agent. For the methods without directed energy for the melting and fusion of powder, such as FDM and BJ, additional post-printing steps are necessary. More specifically, in these methods, the binding agent needs to be removed through chemical and thermal treatments in order to promote metallic phase densification. The advantages and disadvantages of each of the four methods are discussed in Table 2.1.

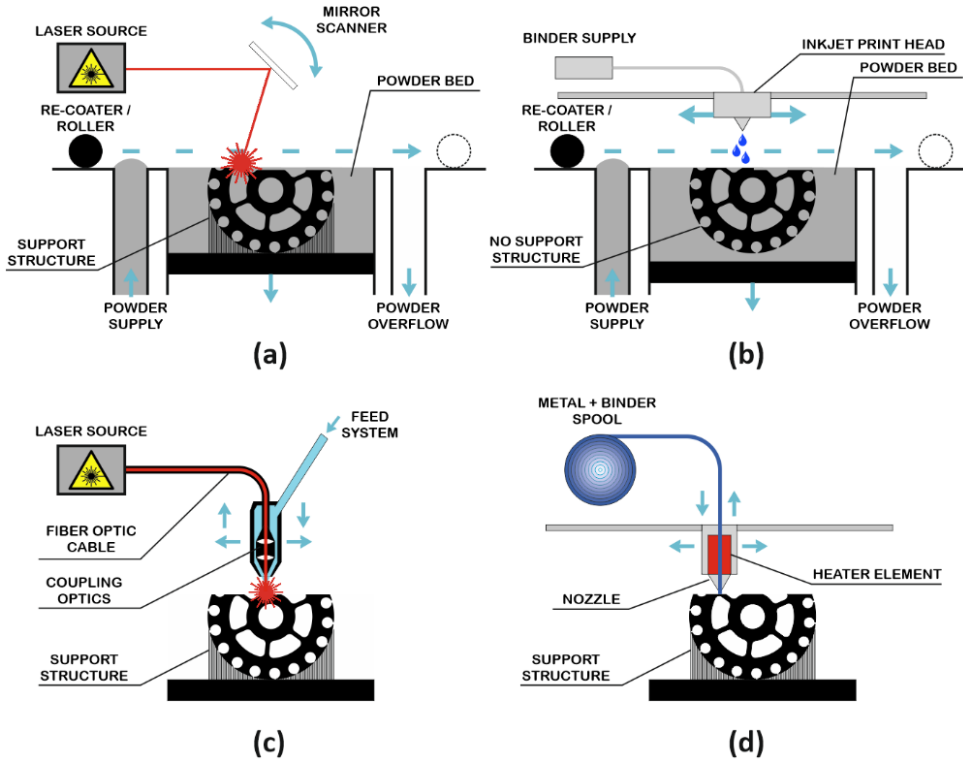


Figure 2.1. Established metal printing methods: (a) laser powder bed fusion (L-PBF), (b) binder jetting (BJ), (c) directed energy deposition (DED), (d) fuse deposition modelling (FDM). [7]

Table 2.1 Comparison of common metal printing methods. [7]

AM Method	Advantages	Disadvantages
L-PBF	<ul style="list-style-type: none"> • High printed material density – typically >99% for iron alloys [29] • High spatial accuracy – printing resolution up to 15 μm (dependent on the powder and laser spot size) [30]. • Promising future multi-material printing possibilities [31]. 	<ul style="list-style-type: none"> • Low build rate: L-PBF processes are well known for their low build rate. The reported rates are anywhere between 5 (single laser 200 W) [32] to ~90 cm^3/h (manufacturer declaration – dual 1kW lasers [33]). Most of the reported rates in the literature fall somewhere in between. • Printing systems are typically more expensive. • Requires extensive supporting during printing; support removal can be time-consuming and complicated.

Table 2.1 Comparison of common metal printing methods (continued). [7]

AM Method	Advantages	Disadvantages
DED	<ul style="list-style-type: none"> • Excellent for repair or feature addition – can print directly on parts. [34] • Fast build rate: depending on the feed mechanism: 70 (powder) – 700 (wire) cm³/h [35]. • High printed material density – typically >99% for iron alloys. [36] • Simple integration with subtractive manufacturing 	<ul style="list-style-type: none"> • Low accuracy and surface finish – limited complexity of printed parts. [34] • Very limited maximum overhang angle. [37] • Increased waste material – parts are typically printed larger and machined to net-shape.
BJ	<ul style="list-style-type: none"> • No printing supports – less post-processing, more design options [38] • Fast build rate – some authors claim practical speeds up to 200 cm³/min [39] are achievable. • Best for indirect production – preparation of sand-casting cores and molds. 	<ul style="list-style-type: none"> • Shrinkage – typically 15 – 20 % [39], [40] depending on the density of the green part, alloy type, and sintering temperature. Unpredictable shrinkage can result in non-desired part dimensions. • Low density – obtaining 50 – 90% relative density is common for BJ sintered iron alloy samples [40-41] in the literature; some studies describe obtaining densities above 99% [42] – but with unspecified ratio of metallic to binder phase
FDM	<ul style="list-style-type: none"> • Most simplistic and least expensive approach to metal 3D printing [34]. • Largest extrusion-based printers (BAAM) are well known for their impressive size (in multiple meters) and build rate (50 kg/h) [43]. • Currently the most capable multi-metal printing options [44]. • Machinery can be considered the easiest and safest to operate [45]. 	<ul style="list-style-type: none"> • Shrinkage – similar to BJ process, FDM metal parts undergo debinding and sintering post-printing. FDM parts have shown similar shrinkage: in the range of 15 – 20 % [46-48]. • Low relative density – results range from 93 – 95% dense steel samples [49-50] to insignificant metallic phase content samples [51-52].

The best balance between functionality and system limitations is currently found in L-PPF printing systems. The method enables the fusion of high-purity parts with excellent spatial accuracy, albeit at a relatively low fabrication speed. High spatial accuracy is critical for the preparation of electrical machines due to the high tolerance requirements of their components. FDM, BJ, and DED printers all exhibit faster build rates but require significant post-processing after printing and are more limited in possible printed shapes. Even though PBF printing systems offer no multi-material functionality currently, first steps have been made in the direction with hopes of PBF printing systems exhibiting the best multi-material capacity in the near future [31].

2.2 State-of-the-art of AM Electromagnetic materials and EM components

Comparative analysis of printed electromagnetic material properties was performed to evaluate their current level of maturity for adoption into electrical machine construction. Three types of materials were evaluated: soft magnetic materials, hard magnetic materials, and electrically conductive materials. The chapter follows closely the results disclosed in publication I: “State of the Art of Additively Manufactured Electromagnetic Materials for Topology Optimized Electrical Machines.” The main evaluation criteria were specific for each material type, based on their most relevant characteristics:

- Soft magnetic – core losses (W/kg) and polarization (T) at specific field strength
- Hard magnetic – coercivity (kA/m) and remanence (T) magnetization
- Electrically conductive – relative electrical conductivity (% IACS)

The secondary goal of the survey was to compare the available electromagnetic material data within the same framework – as there is little standardization in the field (irregular test conditions and different units are common – CGS, metric, imperial). A total of 63 academic references were identified from the literature, which included all the data that was necessary to compose the comparative analysis. Nearly half (47 %) of all the studies involved the application of L-PBF systems. The summary of the references, both in terms of publication date and studied alloy, is presented in Figure 2.2, with the quantity of identified references for each grouping denoted in the parenthesis. References of less studied compounds were compacted to larger nominators, including polymer-bound, amorphous, and Cu alloys.

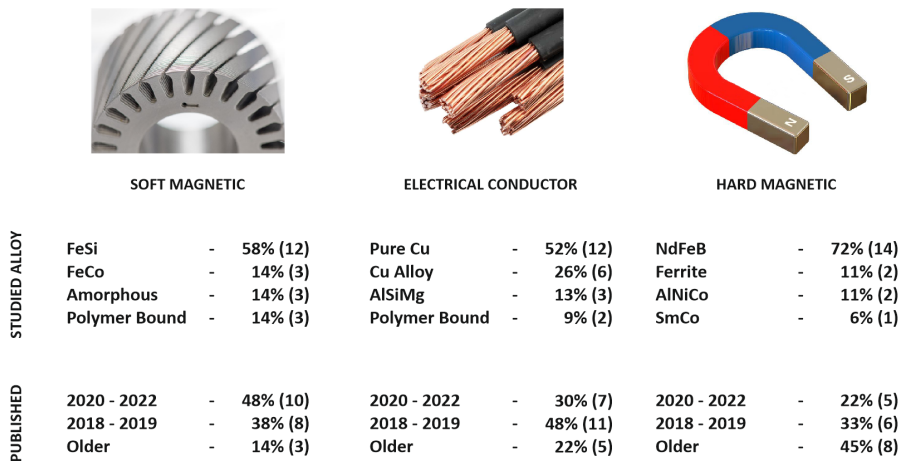


Figure 2.2. Reference sources distribution matrix based on alloy type and publication date. [7]

Based on the publication date, the references were divided into three time periods: 2021–2020, 2019–2019, and older articles. It can be concluded that research into printing electromagnetic material properties is a novel field, as 75% of the reviewed articles have been published between 2018 and 2021. The oldest research data of the survey was published in 2014. The survey indicates that research interest in permanent magnet

materials has not increased over the recent years, whereas the interest in electrically conductive and especially soft magnetic materials has been increasing. Material properties study results are presented in Figures 2.3–2.4. Detailed findings and methods of the study, plus the subsequent discussion regarding the challenges of each of the investigated materials types, are presented in the full-length article [7].

Figure 2.3 (a) outlines the polarization achieved in printed soft magnetic materials, specified in terms of printing method and alloy composition. Two distinct groups of measurements can be identified: results obtained at low (10^3 – 10^4 A/m) and high field strength ($\sim 10^6$ A/m) values. The most widely represented material was L-PBF processed silicon steel, which exhibited similar values of magnetic polarization when compared to commercial non-oriented $\sim 6.5\%$ and $\sim 3\%$ silicon steel sheets [53]. These properties were obtained with near fully dense samples (prepared from high purity powder), which were annealed at high (~ 1200 °C) temperature. Figure 2.3 (b) presents the comparison of iron losses in printed and commercial materials. The losses are compared at $W_{10,50-60}$. This means iron losses at magnetization of 15 kGauss (1.5 T), and at 50-60 Hz field frequency. In fully dense printed material, the core losses are significant, reaching up to approximately 10 W/kg ($W_{10,50}$). By introducing air-gaps inside the single-material printed cores, the losses were reduced significantly. Core losses as low as 1.2–1.7 W/kg ($W_{10,50}$) have been achieved, depending on the individual sample silicon content, size, and the quality of the insulating layers.

Figure 2.4 (a) compares the properties of printed and commercial hard magnetic materials, focusing on material coercivity and remanence. Printed NdFeB rare earth permanent magnets (PMs) have received the highest research interest. Despite the high performance of their commercial counterparts, the maximum energy density of printed magnets is relatively low, currently not exceeding 58 kJm⁻³. This is slightly below 63 kJm⁻³ – the typical value for commercial isotropic neodymium bonded magnets and considerably below the typical value for sintered NdFeB magnets: 400 kJm⁻³ for grade N52 [24]. Despite the low remanence of the printed magnets, their coercivity was relatively high: reaching 700–800 kJm⁻¹ for the majority of the investigated samples in the literature. The 3D printing of permanent magnets has not evolved past early-stage attempts and will likely remain unsuitable for electric motor prototyping purposes in the near future. The main drawbacks of printed PMs are related to their low power density and limited feasible shapes (methods to imprint 3D patterns are under development) – commercial hard magnetic materials are currently superior in every way.

The current level of AM conductive materials is illustrated in Figure 2.4 (b), focusing on the electrical conductivity achieved in the printed material. For comparison, the conductivity values from the IACS standard were used. The international annealed copper standard (IACS) was created in 1913 and defined the 100% IACS as the conductivity of pure copper at normal conditions: 5.8×10^7 S/m at 20 °C. AM of pure copper was by far the most investigated material in this section, reaching electrical conductivity values equivalent to top-grade commercial materials with optimized processing methods. The quality of printed material was identified to be highly sensitive to material density: reaching ~ 96 – 102% IACS at near full density, but exhibiting ~ 50 – 60% IACS conductivity at lower $\sim 85\%$ relative density. Additively manufactured high-purity copper showed properties suitable for commercial applications. The highest density printed materials were obtained with beam powder bed methods: with electron beam melting and green laser PBF. Common infrared PBF was largely ineffective in fusing pure copper due to the high reflectivity of the material in the infrared diapason.

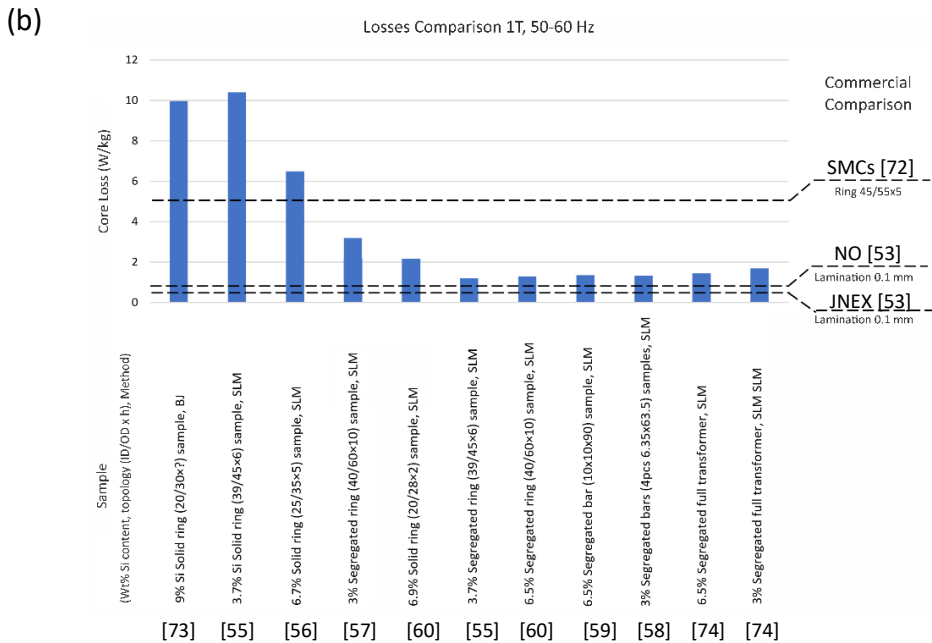
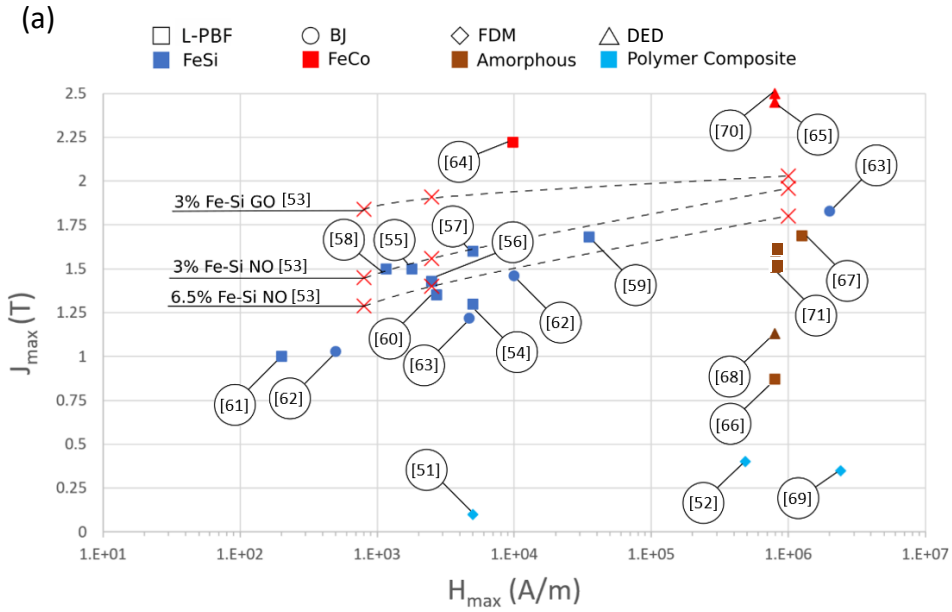


Figure 2.3. Maturity of AM soft magnetic materials: (a) Comparison of magnetic polarization of printed soft magnet with common commercial electrical steels, (b) comparison of iron losses in printed Fe-Si cores and typical commercial materials. (ID/OD x h) denotes the topology of the sample – inner diameter/outer diameter x h. [7]

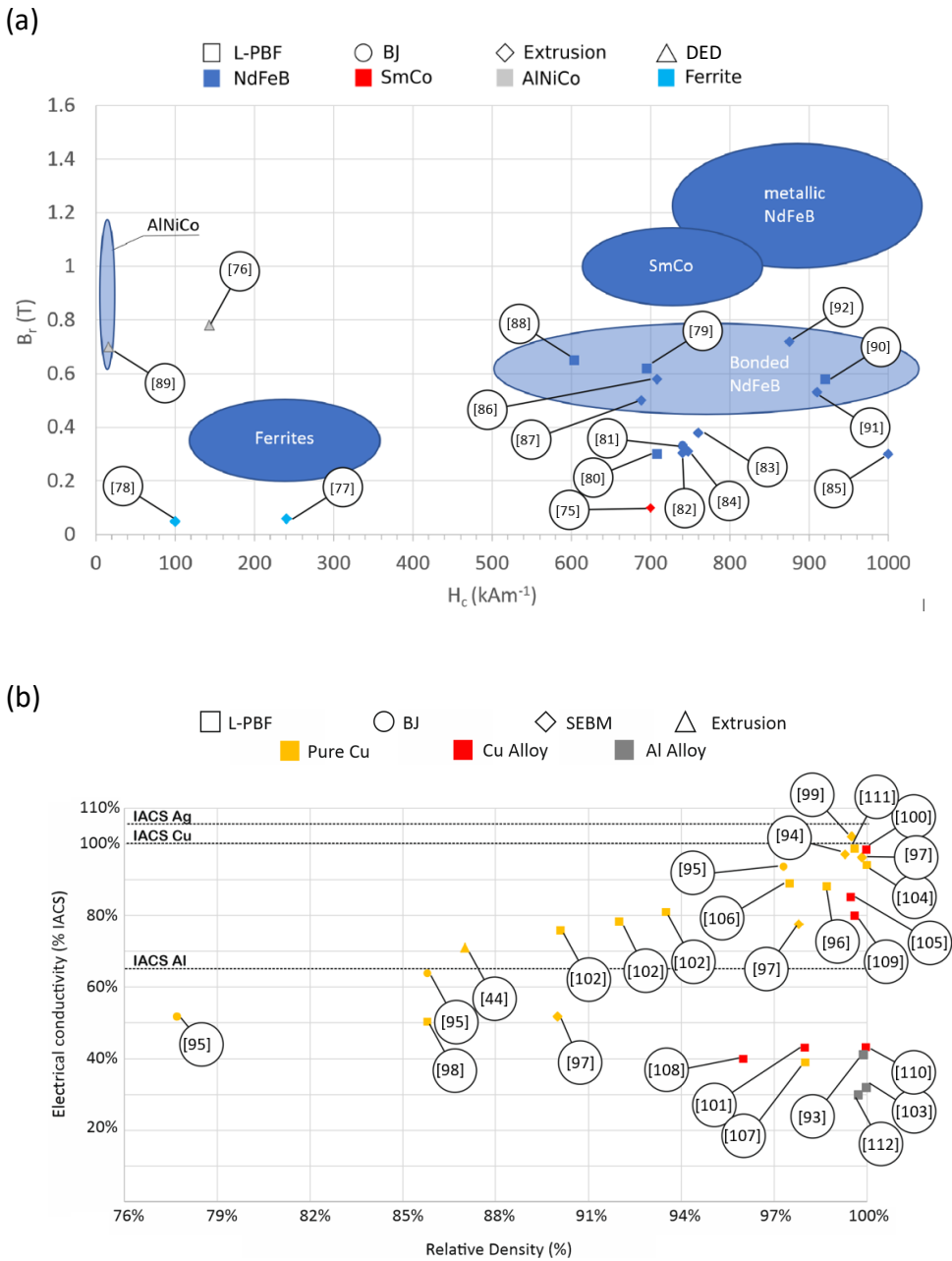


Figure 2.4. Comparison of printed hard magnetic and electrically conductive materials with commercial counterparts: (a) comparison of printed hard magnetic materials with common commercial materials [113-115] in terms of remanence and coercivity, (b) comparison of printed conductive materials in terms of relative DC conductivity (%IACS) and relative density. For comparison with traditional materials, %IACS limits are given for pure Ag, Cu, and Al. [7]

Fully printed EMs were not found in the literature, only individual single-material components. Printed EM prototype components could mainly be divided into three larger directions: synchronous rotors, windings, and heat exchangers. For all instances, the main prototype advantages were related to more intricate and complex shapes of the parts, which resulted in useful performance enhancements. Some of the main advantages included: weight/inertia reduction, increased efficiency, and enhanced cooling. Examples of EM prototype components are presented in Figure 2.5.

Prototype cores for time-varying field applications, such as motor stators, were virtually nonexistent in the literature. As discussed previously, this is likely due to significant challenges in suppressing eddy currents within single-material structures, translating to low component efficiency. As in synchronous rotors, the magnetic field is less dynamic, obtaining useful prototype performance is considerably less complicated. Ideally, the field would be quasi-static, but some fluctuations and consequently eddy currents are induced due to supply and design harmonics and the dynamic behavior of the machine. Permanent magnets have been utilized little in the prototypes, likely due to their low power density. In [86], a printed NdFeB permanent magnet was inserted into a commercial electrical motor, substituting one of its commercial PMs. The performance of the motor was largely unchanged. The same authors measured 110 °C for the maximum operating temperature of the printed magnet. This is similar to commercial M or H temperature class neodymium magnets but would require further enhancement for electrical machine applications, where temperatures can exceed 150 °C [116].

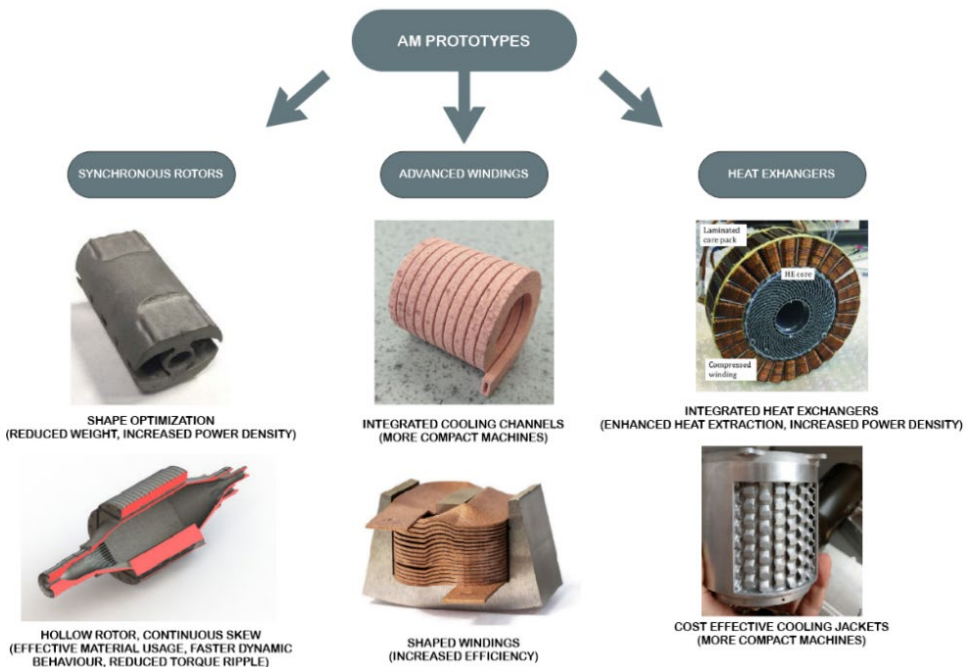


Figure 2.5. Main electrical machine component AM prototyping directions: synchronous rotors ([7-8]), advanced windings ([9,12]), and heat exchangers ([10-11]). [7]

Additive manufacturing of pure copper on green laser and electron beam powder bed fusion systems was identified as suitable for niche commercial applications. These systems are well suited for the fusion of high-purity powder with high relative density. The production freedom and associated streamlined assembly of AM are well suited for small-scale production of nonconventional windings – which are notoriously complex to produce due to the numerous assembly operations required. Undoubtedly, challenges still remain due to the single-material limitation. These are mainly related to the reliability of the insulation layers between the individual winding turns. Some additional benefits for printed coils have been shown in [117-118] and [119], including the preparation of conductors with variable cross-sections and braided conductors (Roebel principle).

The impact of AM systems on thermal management of electrical machines is twofold: first, the reduction of machine losses themselves through the optimized electromagnetic design of the machine; and second, more effective heat extraction from the machine. Prototype heat exchangers have successfully been printed and tested, including insertable heat pipes in-between EM coils [120], heat exchangers involving complex shapes [121], and directly liquid-cooled hollow coils [122].

The summary of the material properties study is presented in Figure 2.6: appraising the maturity of each of the studied material types for EM component production.

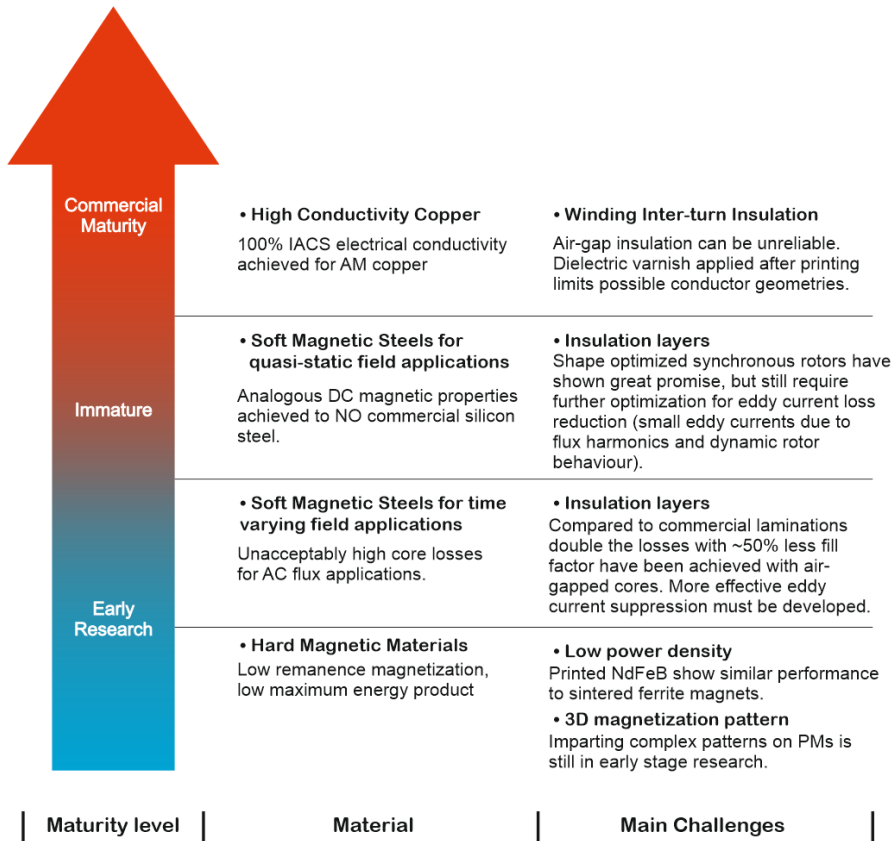


Figure 2.6. Maturity of AM materials for prototyping electrical machine components. [7]

With suitable printing systems and optimized methods, intrinsic material properties comparable to conventional materials for both magnetically and electrically conductive materials are achievable. In parallel, lowering eddy current losses in printed materials is a significant challenge. The integration of air-gaps into the material has been moderately successful. In order to obtain superior properties to conventional materials, multi-material printing methods are required. For AM hard magnetic materials, breakthroughs in the printing methods are necessary, as the achievable power densities are relatively low, and only simplistic patterns can be imprinted on the parts. For printed PMs to be truly innovative and superior to commercial materials, *in situ* magnetization of the material needs to be developed.

Considerable progress has been made over the past few years in metal additive manufacturing. Printing systems are developing rapidly, becoming more available economically, and facilitating the preparation of ever-improving material/part quality. In parallel, the methodological prowess of the research community is steadily increasing. Currently, PBF printing systems are best suited for rapid prototyping and small-volume production of electromagnetic materials and components. The systems enable high spatial accuracy of the printed parts, with near 100% density and high chemical purity. This enables the prototyping of novel electromagnetic components, with the focus likely on optimized electrical machine windings, heat exchangers, and synchronous rotors.

3 Additive Manufacturing of Electrical Steel

3D printing of high-performance soft magnetic materials is of critical importance in developing AM shape optimized electrical machines. In order to produce the material with useful magnetic properties, specific processing methods are required. This chapter describes the factors linked to desirable characteristics of crystalline silicon steel, its preparation process optimization, and material properties determination. Properties library for the printed 3.7% silicon content steel for future machine design optimization efforts is created, denoting the electrical and thermal conductivity, stress-strain characteristics, and magnetic behavior of the material. The chapter follows closely the results presented in published work II: “Laser Additively Manufactured Magnetic Core Design and Process for Electrical Machine Applications.”

3.1 Soft Magnetic Materials

In electrical motors, soft magnetic materials are used to improve their power density: these materials typically exhibit permeabilities 10^3 x higher than vacuum, so large electromagnetic forces and motor torque can be obtained. Additionally, soft magnetic materials are characterized by their low coercive field, which means minimal energy is absorbed in the cyclic material re-magnetization during machine operation. A wide variety of soft magnetic materials is available, with varying saturation and loss behavior at varying price points. For electrical machine purposes, the industrial standard is 3% silicon content steel, which offers the best balance for low-frequency applications where high power densities are not critical.

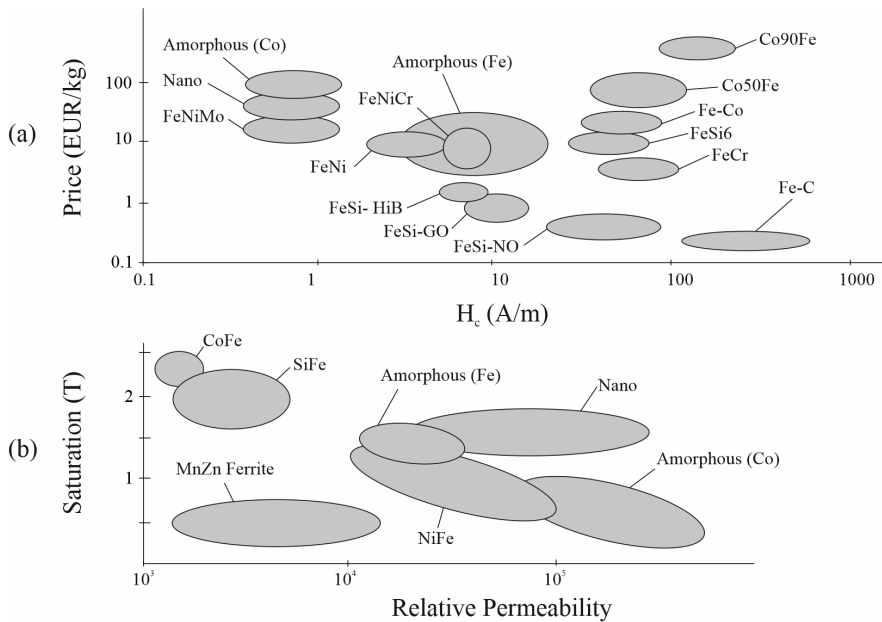


Figure 3.1. Common soft magnetic materials compared in terms of cost (a) and magnetic saturation (b) (adopted from [123]). [7]

Producing high-performance silicon steels is a technically challenging task with both conventional and additive methods. This is due to the high melting point and hardness of the iron-based alloys, complicating their casting/machining/printing. Secondly, their properties heavily depend on crystallographic texture. Based on previous studies, the five most impactful material characteristics determining the properties of electrical steel alloys are well known, including impurity content, granular size, internal residual stress, alloying silicon content, and lamination sheet thickness. The influence of these characteristics on crystalline steel properties is summarized in Figure 3.2.

Physical Characteristics	M_s	H_c	μ	P_{hyst}	P_{ce}	P_{an}	σ	λ	σ_y
↑ Impurities	↓	↑	↓	↑	↓	↓	↓	↓	↓
↑ Grain Size	-	↓	↑	↓	-	↑	-	-	↓
↑ Internal Stress	-	↑	↓	↑	-	-	-	-	↑
↑ Silicon Content	↓	↓	↑	↓	↓	↓	↓	↓	↓
↑ Sheet Thickness	↑	↓	↑	↓	↑	↑	↑	↑	↑

- Maximum magnetic saturation (at $\mu_r = 1$) is independent of grain size and proportional to the density of soft magnetic phase in material [124]. With lower sheet thickness and higher silicon content more nonmagnetic material is introduced to the core (varnish and silicon).
- Imperfections within the crystallographic structure (including lattice dislocations, grain deformation (internal stress), foreign substituting and interstitial atoms, grain boundaries, pores, cracks) act as pinning sites for the magnetic domains [125-126] – requiring more energy for orientation. Thinner lamination layers generally result in higher hysteresis losses due to restricted grain size [127].
- High silicon steel content (optimal 6.5%) reduces material magnetostriction (increased permeability) [128], requiring less energy for domain orientation within a magnetic field
- Chemical impurities and macroscopic material defects (cracks, pores, delaminations) reduce the overall electron mobility in the metals – reducing both the thermal and electrical conductivity, and by association Joule heating losses [129].
- Internal electrical resistance of electrical steel components is best increased through laminated structure – effectively suppressing induced eddy current losses [127].
- Anomalous losses account for the microscopic eddy currents arising from the domain wall motion – with smaller grains; reduced microscopic eddy currents are generated [130].
- With silicon content near 6.5 %, the brittleness of steels is increased substantially [131]. Ultimate yield strength of steel has been shown to be relatively insensitive to significant porosity content [132], but highly sensitive to any cracking/delamination [133].
- Material yield strength has been shown to be inversely proportional to the square root of its grain diameter [134]. The residual stresses from production processes or cold working (plastic deformation) increase a materials mechanical strength through dislocation accumulation [135].

Figure 3.2. Effect of physical characteristics on soft magnetic material properties. [136]

The analyzed properties include magnetic, thermal, and electric properties. Iron losses are divided into separate loss categories of hysteresis losses P_{hyst} , classical eddy current losses P_{ce} and excess eddy current losses P_{an} , based on the involved physical phenomena. Additionally, M_s denotes the saturation polarization, H_c – coercivity, σ_y – ultimate tensile strength, σ – material electrical conductivity, and λ - thermal conductivity.

It is well known that impurities (both crystallographic defects and chemical contaminants) are related to reduced magnetic properties. Both can be reduced during high-temperature annealing process. It promotes both metal grain structure recovery (internal stress relaxation) and their recrystallization (reduction of crystalline impurities). Additionally, in industrial annealing furnaces, steel sheets are decarburized (reduced contaminating elements) in specific process environments. While annealing can be used to a great effect to improve the material texture and intrinsic properties, it is largely ineffective or even detrimental from the perspective of AC losses. Excessive grain size is related to elevated anomalous iron losses, which can balance out any gains in hysteresis loss reduction of the annealed material. Classical eddy current losses can be reduced most effectively by increasing the internal resistance of the material. This can be done by increasing the resistivity of the magnetic material or by modifying the structure of the material to include insulating layers.

The emergence of additive manufacturing methods has considerably diversified the challenges encountered by the material and prototyping-focused research groups. This is because now the full production cycle of an electrical motor component can be completed in-house. Previously, commercial material was purchased, cut into the stampings of the desired geometry, and assembled into full electric motors. Based on our experience with L-PBF printing, the most impactful processing steps for producing high-performance soft magnetic materials are outlined in Figure 3.3.

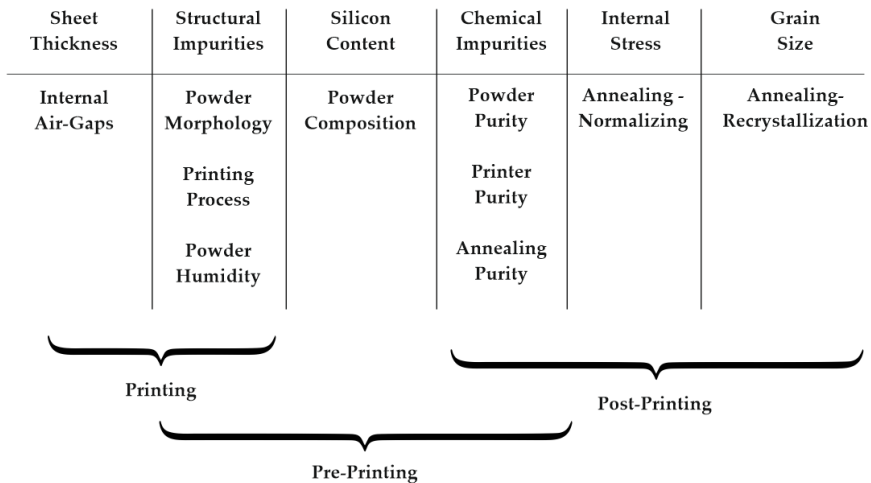


Figure 3.3. Main considerations for improving L-PBF printed Fe-Si characteristics. [136]

The considerations are divided according to their timing: whether they are applicable as part of the printing process, before or after it. A five-step workflow was developed to improve the process of preparing soft magnetic materials, with a focus on obtaining useful magnetic properties. The workflow is described in Figure 3.4.

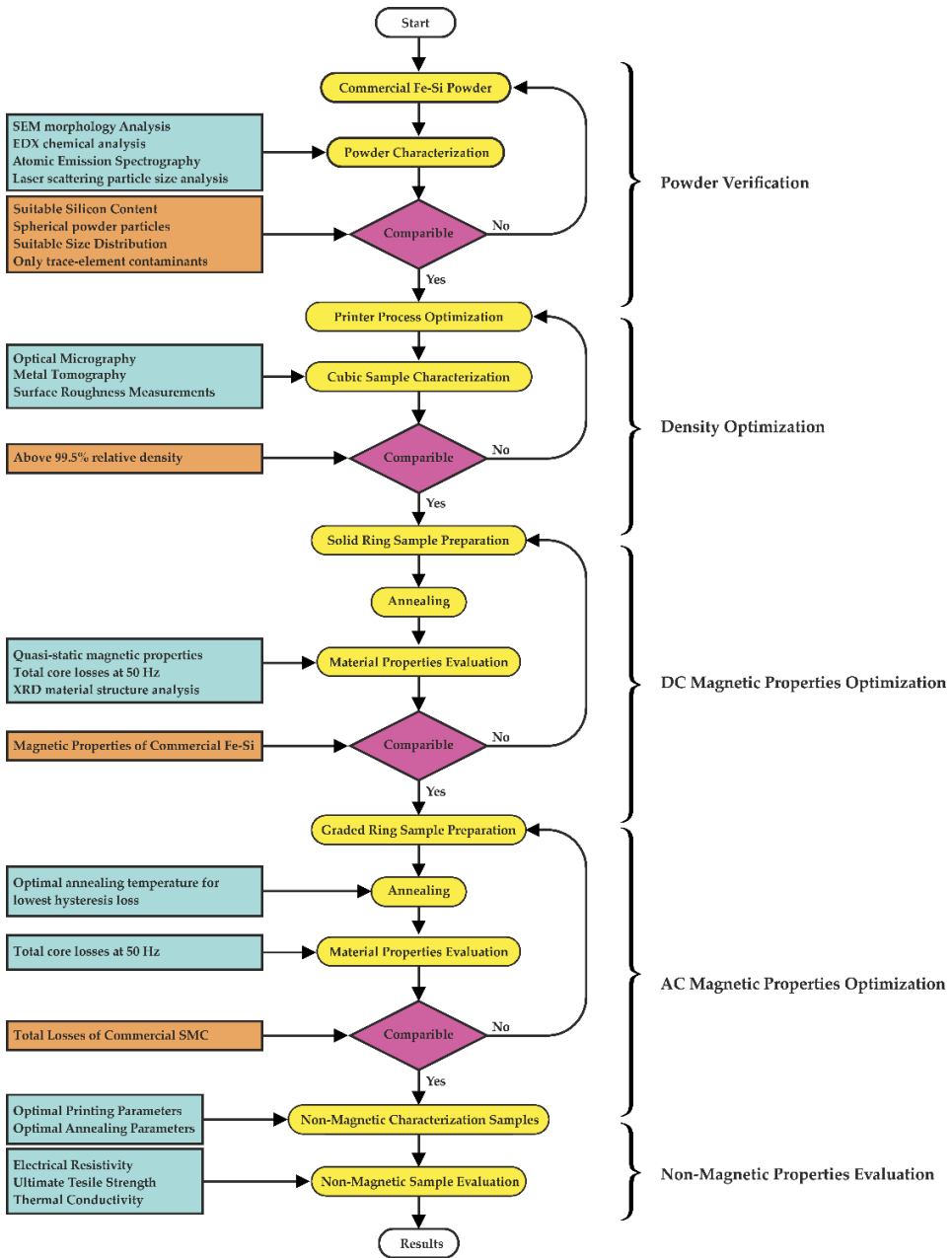


Figure 3.4. Five step flowchart for L-PBF preparation of Fe-Si magnetic core with useful magnetic properties. [136]

First, the quality of the raw powder is checked: that it has high chemical purity and recommended size and morphology for L-PBF processes. Secondly, the printing process parameters are optimized to achieve at least 99.5% relative density of the prepared samples with minimal surface roughness. Thirdly, the determined processing parameters

are applied for the fusion of magnetic measurement samples. These samples are heat-treated at different temperatures to determine the best annealing temperature, offering the highest soft magnetic material properties. The goal of the third step is to obtain quasi-static magnetic properties equivalent to conventional mid-range laminations. The fourth step in the workflow is obtaining eddy current loss reduction in printed cores. The objective is to achieve total core losses equivalent to or lower than SMCs by introducing air gaps within the printed core to act as insulation layers. In the fifth step of the process, secondary non-magnetic properties of the printed materials are mapped. These include electrical resistivity, thermal conductivity, and mechanical yield strength. The methods and facilities involved in material preparation and characterization are dissected in the next chapter.

3.2 Sample Preparation and Characterization Methods

The various material tests require the preparation of samples of varying sizes and shapes. Six types of samples were prepared for printing optimization and material properties measurements, as outlined in Figure 3.5. For the first process optimization step, no samples were printed; it included raw powder characterization. The raw powder was chosen with low silicon content (~3%) because it was commercially available, and its laser fusion was deemed less challenging than high silicon content steel in relation to its higher ductility. For the second step, 36 pcs 5 x 5 x 5 mm cubical samples were printed with varying printing parameters. The parametric sweep was performed for both laser power (250–400 W) and scanning velocity (0.25–2 m/s), with constant hatch distance (120 μm) and layer thickness (50 μm). These cubic samples were used to determine the optimal printing parameters yielding the best combination of relative density (at least above 99.5%) and surface roughness.

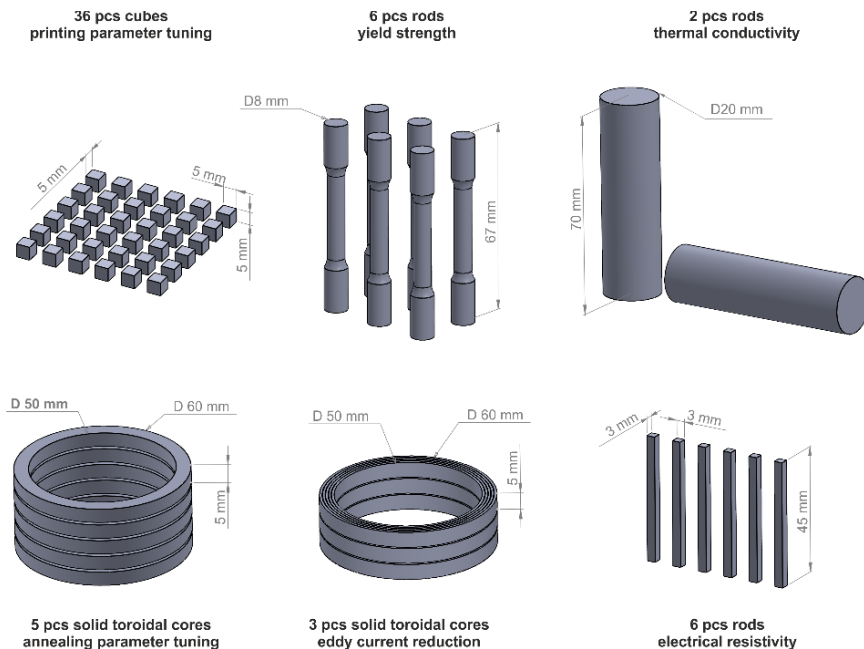


Figure 3.5. 3D printed samples characterized as part of the study.

Samples for the third step were five 5 x 5 x 60 mm bulk toroidal samples. The toroids were annealed in the temperature range 1200–1350 °C (50 °C increment) post-printing. The thermal treatment range was selected as the lower temperatures (up to 1200 °C) have already been relatively thoroughly investigated in the literature [57]. The most effective thermal treatment was chosen based on sample DC magnetic properties: obtaining the lowest hysteresis losses and highest maximum permeability. For dynamic magnetic loss reduction in step 4, the next set of toroids was prepared with integrated air-gaps. These included three samples with the same outer dimensions as the solid toroidal cores but with horizontal, vertical, and combined air-gaps printed in the core. In the process optimization final step, the non-magnetic properties of the printed material were mapped. For that, 6 pcs round tensile coupons for measuring the stress-strain characteristics, 6 pcs thin rods for measuring the electrical resistivity, and two thick rods for measuring the thermal conductivity of the material before and after annealing were printed.

Preparation of the samples was conducted on the SLM-280 L-PBF systems (SLM Solutions). The system is ideally sized for rapid prototyping and small-scale production. The build envelope of the printer is 280 x 280 x 350, and it exhibits a single 400W 1070 nm infrared yttrium scanning laser. As the powder swapping between projects is a large undertaking on the full-sized platform, a custom recoating system was added to the printer. It includes both a small circular reduced platform with a 100 mm diameter and a reworked feeding system. The add-ons and the printing system are shown in Figure 3.6.

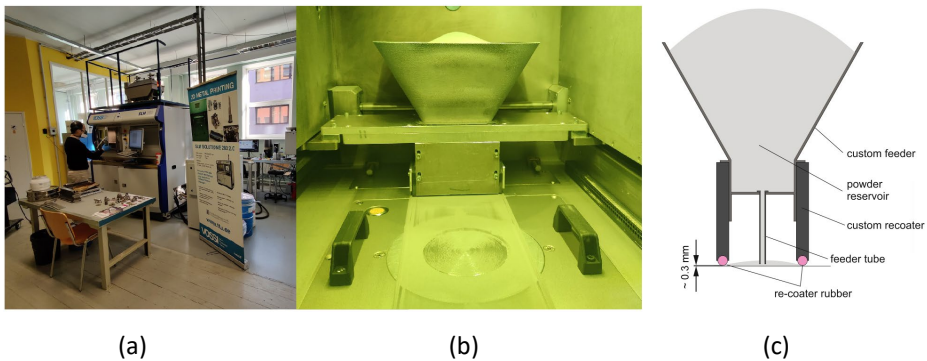


Figure 3.6. (a) SLM Solutions SLM 280 printing system in Taltech, (b) Printer build chamber with custom re-coater, powder reservoir, and reduced platform, (c) cross-section of the custom re-coater system. [136]

The thermal treatments after printing were applied in a small-scale D100 x 60 commercial vacuum furnace Webb-107 with a graphite-lined chamber. The annealing system is shown in Figure 3.7. For all treatments, the heating rate was 300 °C/h, and the chamber pressure was at ~0.1 mBar. After reaching the target temperature, the samples were slowly cooled inside the furnace until at room temperature.



Figure 3.7. (a) Printed soft magnetic core in the annealing furnace, (b) full annealing setup with Webb-107 vacuum furnace. [136]

The applied characterization methods, chosen by availability and relevancy of yielded information, are outlined in Figure 3.8. The facilities include both in-house setups for resistivity, heat flow, and magnetic properties measurements, alongside commercial facilities for more standardized tests. They are divided based on application into three larger arms: powder, printed structure, and material properties characterization. Detailed descriptions for the in-house setups can be found: magnetic measurements in [136], thermal conductivity in [137], and electrical resistivity in [55].

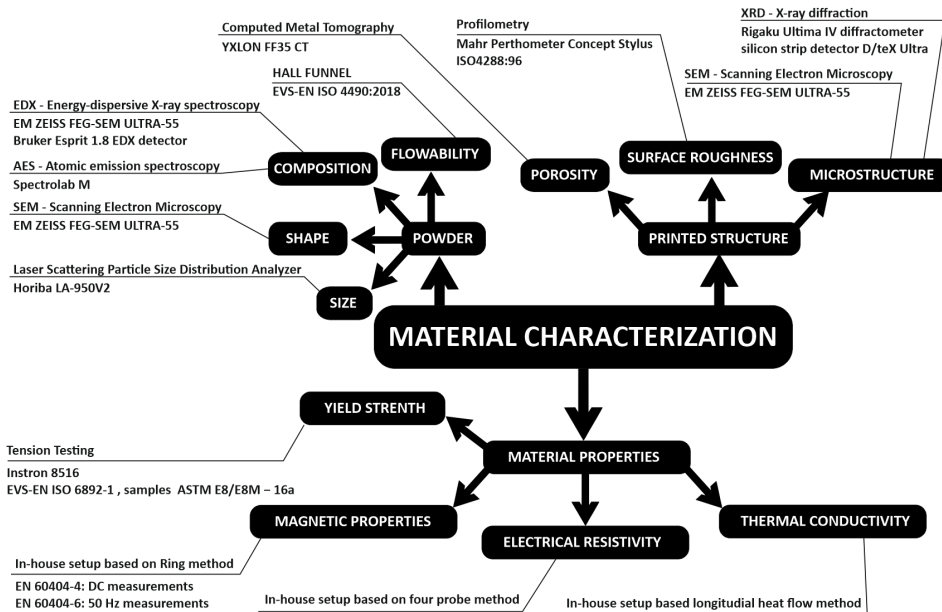


Figure 3.8. Facilities and methods for material characterization.

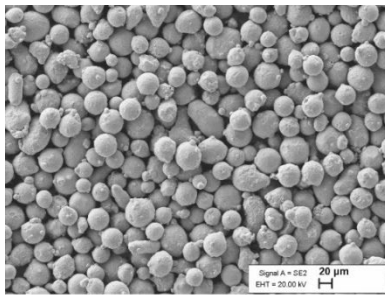
3.3 Printed Material Process Optimization and Properties Results

3.3.1 Powder Characterization

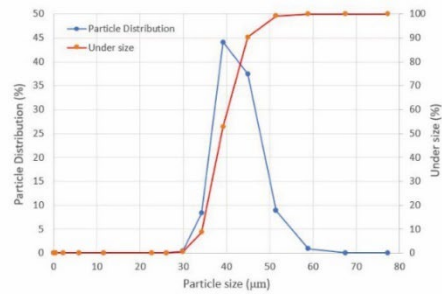
The characterization results of the commercial raw iron-silicon powder showed an accurate correlation with the manufacturer's declaration, with its chemical composition summarized in Table 3.1. The powder consists of nearly spherical particles ranging in size between 29–58 μm , with a median of 38 μm (d50), as shown in Fig 3.9 (a-b). The powder particle shape was not perfectly spherical; instead, a large particle fraction exhibited elongated shapes or minute satellites attached to them. The flow rate of the powder was measured as 19.7 ± 0.24 s/50g in the Hall funnel.

Table 3.1 Summary of powder chemical composition.

Elements	Fe	Si	Mn	Cr	Ni	C
Wt %	Balance	3.7	0.2	0.16	0.020	0.01



(a)



(b)

Figure 3.9. (a) SEM micrograph of the raw powder, (b) powder particle size analysis. [136]

3.3.2 Density Optimization

The summary of laser energy input's effect on the relative density and surface roughness of the printed cubic samples is outlined in Figure 3.10 (a-b). The window to produce parts with the desired properties was relatively narrow: it was evaluated to be in the range of 66–130 J/mm^3 . Below it, between 20–50 J/mm^3 , the energy input was insufficient to fully consolidate the powder into dense parts. At 166–233 J/mm^3 , the parts exhibited signs of over-melting, resulting in a deformed shape and reducing relative density. At 20.8 J/mm^3 , the highest defect content as part of the study was measured: the parts were only 47.91% dense. The highest density was measured at 100 J/mm^3 , reaching 99.87% relative density – considerably higher than the initially proposed value of 99.5%. At this setting and above, however, the surface roughness of the parts started slowly to increase. It was determined that the optimal scanning parameters of the study were 350 W laser power and 0.75 m/s laser scanning velocity, which resulted in the energy input density of 77 J/mm^3 . With these settings, an excellent relative density of 99.86% was obtained alongside low surface roughness ($R_a = 8 \mu\text{m}$, $R_z = 41 \mu\text{m}$).

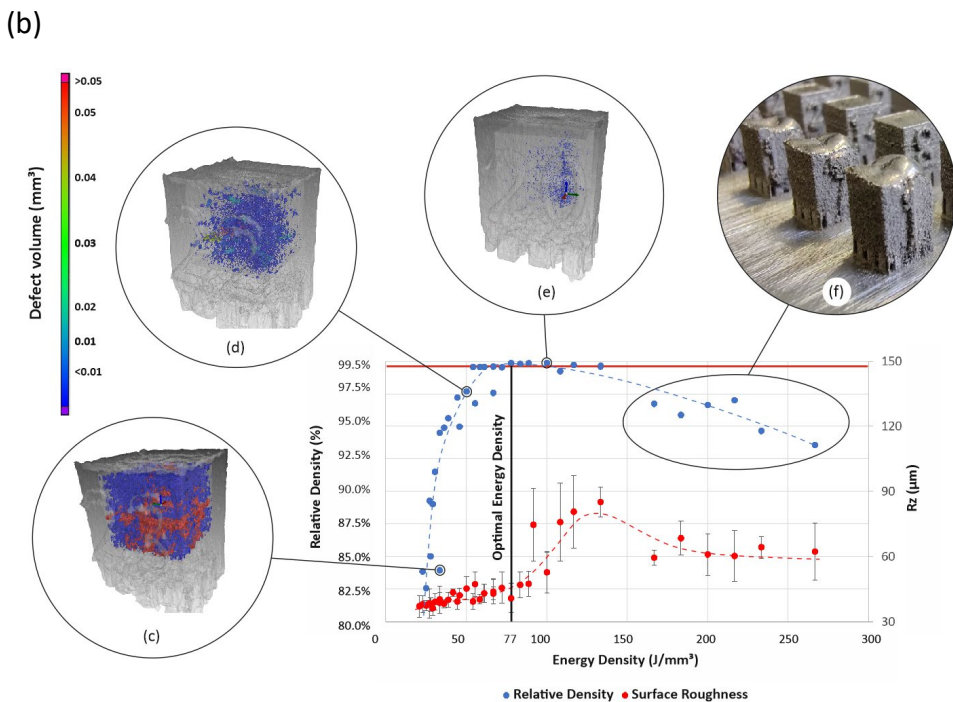
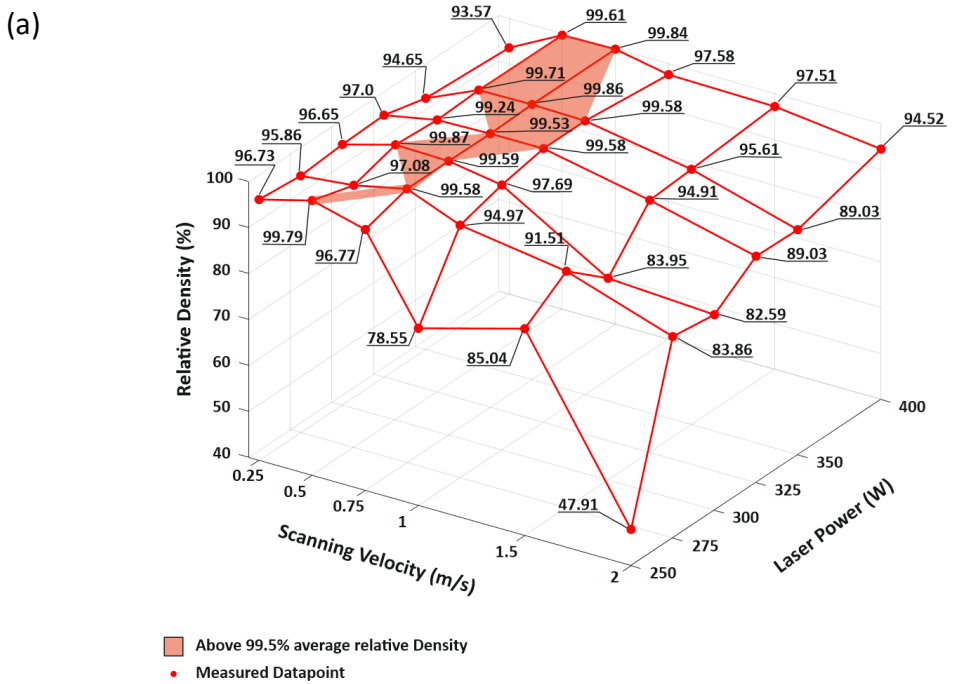


Figure 3.10. Printing process optimization: (a) relative density of the samples at different laser settings, (b) Correlation between the laser energy input, sample density and surface roughness, (c) sample fused with 300 W, 1.5 m/s, (d) sample fused with 22–300 W, 1 m/s, (e) sample fused with 20–300 W, 0.5 m/s, (f) deformed samples fused at 250–400 W, 0.25 m/s. [136]

The values for surface roughness ranged from 6.8–18.2 μm for R_a and 36.1–85.2 μm for R_z . Above 88 J/mm^3 laser input power, the surface roughness of the samples increased, reaching the maximum roughness at 133 J/mm^3 . The four of the most illustrative samples of the effect of laser parameters on the surface roughness of printed parts are presented in Figure 3.1. The summary of the fixed printing parameters and the optimal laser scanning parameters is outlined in Table 3.2.

Table 3.2 Most effective processing parameters identified within the study dataset, fusing 99.86% dense samples with mean surface roughness R_a of 8 μm .

Optimized Parameter	Unit	Value
Laser power	W	350
Scanning velocity	mm/s	750
Volumetric energy density	J/mm^3	77
Fixed Parameter	Unit	Value
Layer thickness	μm	50
Hatch distance	μm	120
Laser spot size	μm	~ 120
Scan strategy	-	Stripes
Print environment	-	Nitrogen
Preheating	-	No
Remelting	-	No
Print chamber oxygen content	%	~ 0.1

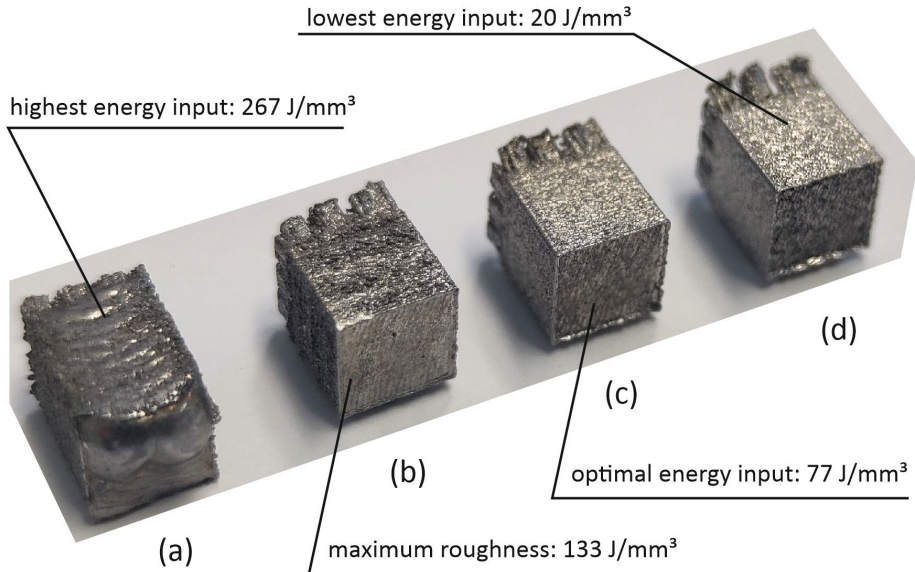


Figure 3.11. Effect of laser energy input on the printed part surface roughness: (a) highest energy input ($R_z = 62 \mu\text{m}$, $R_a = 12 \mu\text{m}$), (b) maximum surface roughness ($R_z = 85 \mu\text{m}$, $R_a = 18 \mu\text{m}$), (c) optimal energy density ($R_z = 41 \mu\text{m}$, $R_a = 8 \mu\text{m}$), (d) lowest energy input ($R_z = 37 \mu\text{m}$, $R_a = 7 \mu\text{m}$). [136]

3.3.3 DC Magnetic Properties

Quasi-static (DC) measurements, with an almost static applied magnetic field (25 mHz), indicated useful soft magnetic properties for the printed material. The properties were further enhanced after heat treatment. The printed cores: unannealed and annealed at 1200°, 1250°, 1300°, and 1350 °C, were subjected to rigorous testing with the ring measurement method. The effect of annealing on the magnetization curve and hysteresis losses of the material are detailed in Figure 3.12. The summary of the most effective identified heat-treatment parameters is presented in Table 3.3.

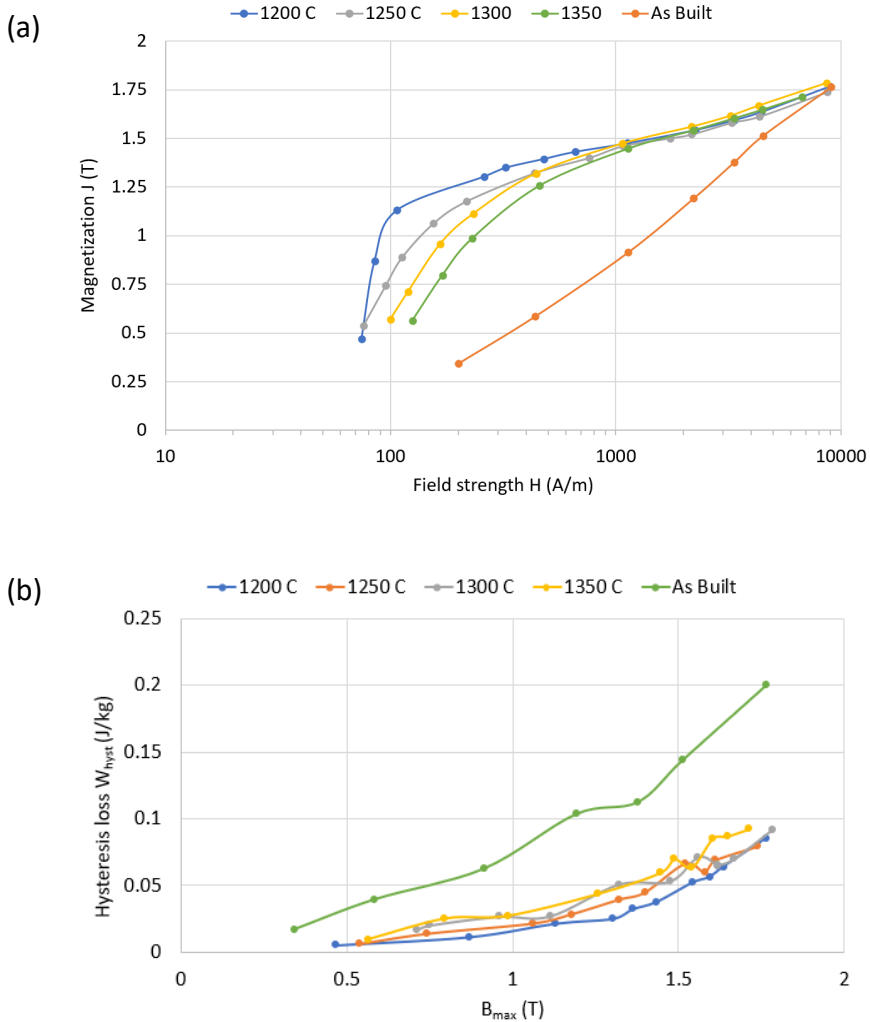


Figure 3.12. DC magnetic properties with different heat-treatments: (a) magnetization curves, (b) hysteresis losses. [136]

Post-heat-treatment, the magnetization of 1.5 T was achieved at approximately 1500 A/m on average. As-built sample reached the same level of magnetization at 4000 A/m. The coercivity of the samples varied from 52 A/m (1200 °C) up to 203 A/m (as-built). Hysteresis curves of the material annealed beyond 1200 °C showed a slight

deterioration of magnetic properties. This is apparent from the decreasing slope magnetization curves: annealing the samples over 1200 °C resulted in reduced permeability. Measurement noise of the method did not allow for the characterization of the annealed samples below ~0.5 T. Calculated maximum permeabilities decreased from 8846 (1200 °C) to 3700 (1350 °C) and reached as low as 1400 for the as-built sample.

The DC (hysteresis) losses of the samples were calculated from the areas of the measured quasi-static hysteresis loops. The results are detailed in Figure 3.12 (b). Due to the high grain boundary content (small grain size), the highest losses were identified for the as-build sample, which had not undergone any thermal treatment. The hysteresis loops of the annealed samples exhibited considerably higher inclines and narrower widths, translating to higher permeability and lower hysteresis loss. Amongst the annealed samples, 1200 °C exhibited the best soft magnetic properties, exhibiting losses as low as 0.043 J/kg at 1.5 T. At grid frequency (50 Hz), this corresponds to the hysteresis loss component of 0.8 W/kg at 1 T and 2.15 W/kg at 1.5 T.

Table 3.3 Most effective annealing parameters identified within the study dataset, applicable for 8846 maximum relative permeability and 0.8 W/kg hysteresis loss ($W_{10,50}$).

Optimized Parameter	Unit	Value
Annealing temperature	°C	1200
Fixed Parameter	Unit	Value
Annealing hold time	min	60
Annealing heating rate	°C/min	5

Quasi-static magnetic properties of the printed core samples were considered acceptable for AM electrical machine purposes. Printed core magnetization and its relative permeability were near equivalent to typical mid-range electrical steel laminations and superior to SMCs. A comparison of these properties for the in-house prepared material and typical commercial materials is presented in Figure 3.13.

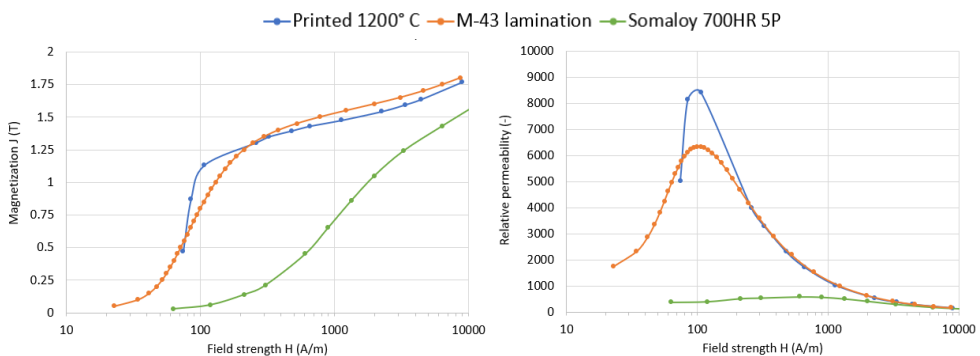


Figure 3.13. Comparison of commercial M-43 lamination material (equivalent to M400-50A [138], Somaloy soft magnetic composite [139], and the printed material annealed at 1200 °C. [136]

3.3.4 AC Magnetic Properties

At higher excitation frequencies (1 and 50 Hz), the iron losses increased substantially. The curve shearing and the thickening of the hysteresis curves with an increase in excitation frequency are illustrated in Figure 3.14. Indeed, eddy current losses are dominant (both classical and excess) in the fully-dense non-laminated 5 x 5 mm cores: constituting 95% of the losses at 1.5 T, 50 Hz. At lower, 1 Hz frequency, these additional losses comprise 66% of the total losses. Iron losses in all of the four annealed samples are similar: approximately 2 W/kg at 0.5 T, 11 W/kg at 1 T, 45 W/kg at 1.5 T, and 170 W/kg at 1.9 T.

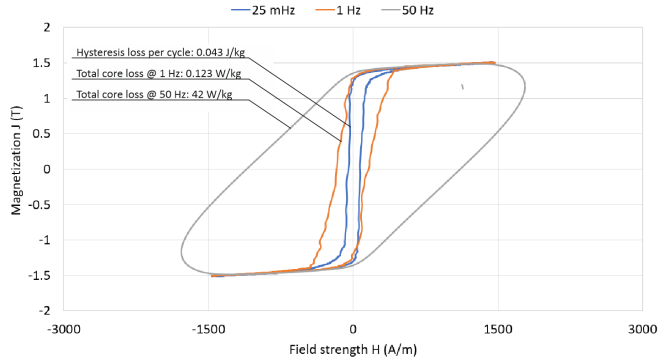


Figure 3.14. Eddy current loss-related curve shearing: measured loops at 1.5 T magnetization (~ 1500 A/m field strength), at 0.025, 1, and 50 Hz excitation. [136]

With graded core cross-sections, these iron losses were reduced substantially. The structure of the finalized prototype cores is presented in Figure 3.15, illustrating both the voids within the core and the supporting scaffolds.

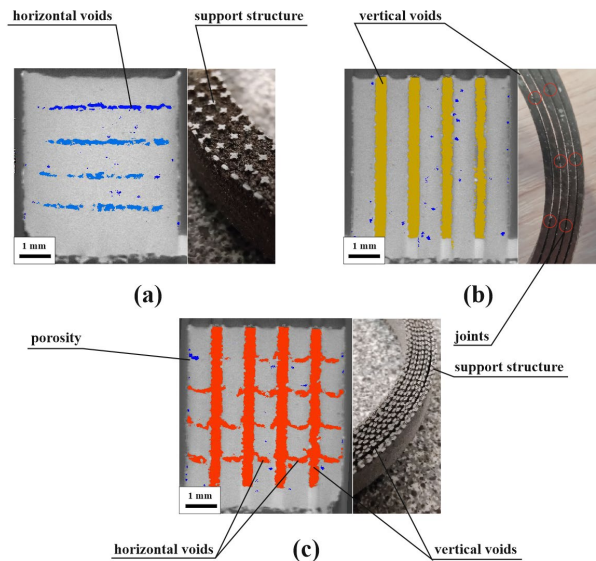


Figure 3.15. Topology of the segregated 3D printed magnetic cores: (a) horizontally graded, (b) vertically graded, (c) horizontally and vertically graded (hybrid). [136]

It is important to note that printed cores require some supporting structure between segregated topologies to ensure part integrity during printing and subsequent operation. Metal tomography results revealed the sample fill factors: 94.05% for the sample with horizontal air-gaps, 78.07% for the sample with vertical air-gaps, and 72.98% for the hybrid core with bi-directional air-gaps. The fill factor signifies the soft magnetic material content within the air-gapped cores. It was also included in the losses calculation in order to accurately calculate the iron losses within the cores per weight of the sample (specific loss). Slight dimensional deviations from the initial models were identified: the actual printed cores exhibited 0.32 mm vertical air-gaps separating 0.75 mm magnetic guides (instead of 0.19 mm gap, 0.85 mm core). The 0.32 mm vertical air gaps were sufficiently wide enough to eliminate any unintended short-circuiting over the gaps and to remove all of the un-melted powder from within the core. The horizontal air-gaps were printed with less success: the printed air-gap was narrow and uneven, resulting in significant electrical conductivity within the core. The effect of the air-gaps on the total core losses of the samples is presented in Figure 3.16.

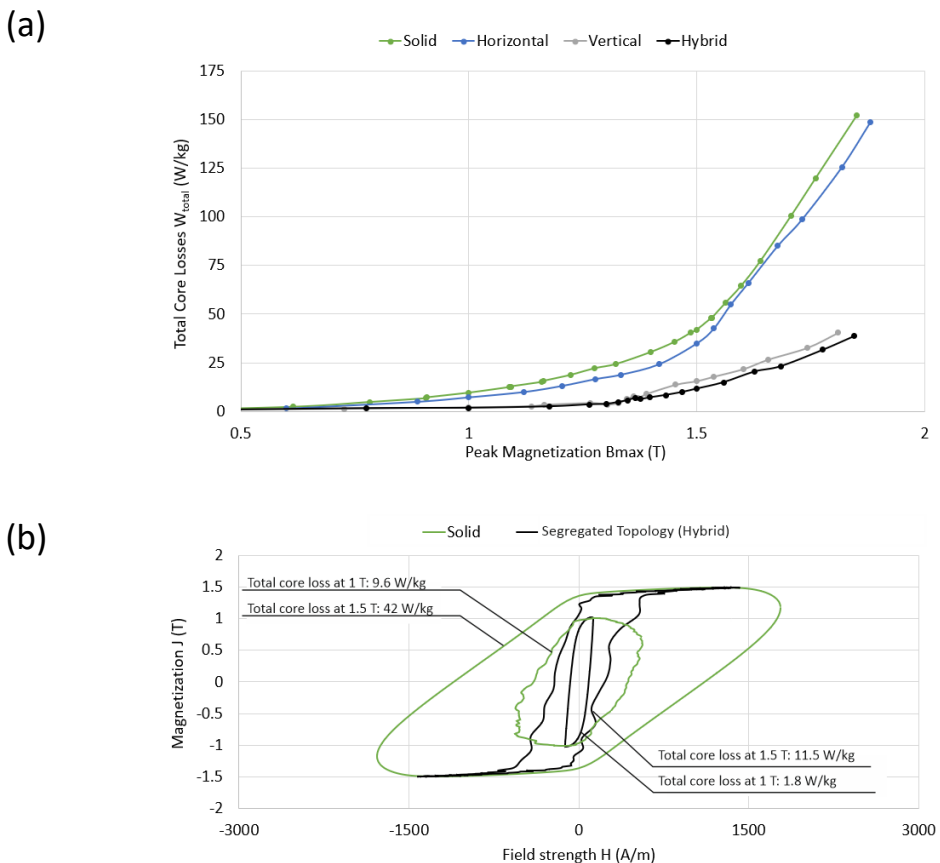


Figure 3.16. Total core loss reduction with segregated core topology: (a) core losses with different core topologies over the magnetization range of 0.5–1.9 T, (b) comparison of the hysteresis loops of the solid and “hybrid” topology results at 1 and 1.5 T magnetization. [136]

Compared to the non-segregated fully dense material, a significant reduction in losses was observed. Total iron losses decreased from 42 W/kg (solid) to 35 W/kg (horizontal gaps), 15.5 W/kg (vertical gaps), to as low as 11.7 W/kg (bi-directional gaps) at 1.5 T, 50 Hz. At lower 1 T flux density, adoption of the segregated topology resulted in an 81% reduction of the total core losses: from 9.6 W/kg for the solid sample to 1.8 W/kg for the bi-directionally segregated sample. At these conditions, the previously determined hysteresis losses of 0.8 W/kg constitute 44% of the 1.8 W/kg iron losses – a significant increase from the 17% of the fully dense sample. The comparison of the losses in printed cores with conventional materials is presented in Table 3.3. The comparative data is obtained from EN 10106: 2015 standard [140], which defines the specific total core losses requirements in the range of 0.9–5.8 W/kg ($W_{10,50}$) and 2.1 to 13 W/kg ($W_{15,50}$) for different grade steels.

Table 3.3 Specific core loss (W/kg) in printed cores and EN standard steels [140].

AM Steel	Specific loss at 1 T, 50 Hz	Specific loss at 1.5 T, 50 Hz
Bulk, unannealed	23	50
Bulk, 1200 °C	9.6	42
Graded “hybrid” gaps, 1200 °C	1.8	11.7
EN Standard Steel Grade	Specific loss at 1 T, 50 Hz	Specific loss at 1.5 T, 50 Hz
M210-35A	0.9	2.10
M300-35A	1.2	3.00
M400-50A	1.7	4.00
M700-50A	3.0	7.00
M1000-65A	4.4	10.00
M1300-100A	5.8	13.00

With the bi-directional air-gaps integrated into the core, the iron losses were reduced at low magnetization (1 T) to values similar to mid-grade laminations. At higher field strengths, the losses climbed rapidly from 1.8 ($W_{10,50}$) to 11.7 W/kg ($W_{15,50}$). This can be related to the suboptimal grain size of the prepared material for high field strength applications. The grains prepared as part of this study have ranged approximately between 500 μm [54] and 2500 μm [136]. Larger grain size has been shown to be more advantageous at low, but disadvantageous at higher field strengths. Shiozaki et al. demonstrated that in laminations under weak magnetic fields of $W_{14,50}$ or less, large grain diameter (220 to 230 μm) was optimal, offering minimum core loss and maximum permeability, whereas, in strong magnetic fields of $W_{15,50}$ or higher, better results were obtained with smaller grain diameters (190 to 110 μm) [141]. The prepared material is well suited for applications involving 1 T magnetic fields. For higher efficiency with stronger magnetic fields, further material microstructure optimization is required.

3.3.5 Material Properties Library, Results Summary

The summary of the material properties obtained through the process optimization workflow is presented in Figure 3.17 and Table 3.4. In parallel, the corresponding values for typical electrical steel are outlined in the table for comparison. The printed material data was drawn from the following publications: magnetic and mechanical properties from [136], thermal properties from [137], and electrical properties from

[142]. Both the obtained magnetic and non-magnetic properties are relatively close to typical medium-grade electrical steels, such as M400-50A (M-43).

Table 3.1. Material properties library for multi-physical modelling. Properties references: [136,137, 138,140,142,143].

Property	Unit	3D printed 3.7% FeSi	Typical Value
Relative permeability at 1 T	-	8846	6100
Relative permeability at 1.5 T	-	1056	1535
Hysteresis loss at 1.0 T, 50 Hz	W/kg	0.8	NA*
Hysteresis loss at 1.5 T, 50 Hz	W/kg	2.15	NA*
Total core loss at 1.0 T, 50 Hz	W/kg	1.8	1.7
Total core loss at 1.5 T, 50 Hz	W/kg	11.7	4.0
Electrical resistivity	$\mu\Omega\cdot\text{cm}$	56.9	45
Thermal conductivity	W/m·K	24.8	28
Yield strength	MPa	420	350

* hysteresis losses are typically not disclosed for commercial materials

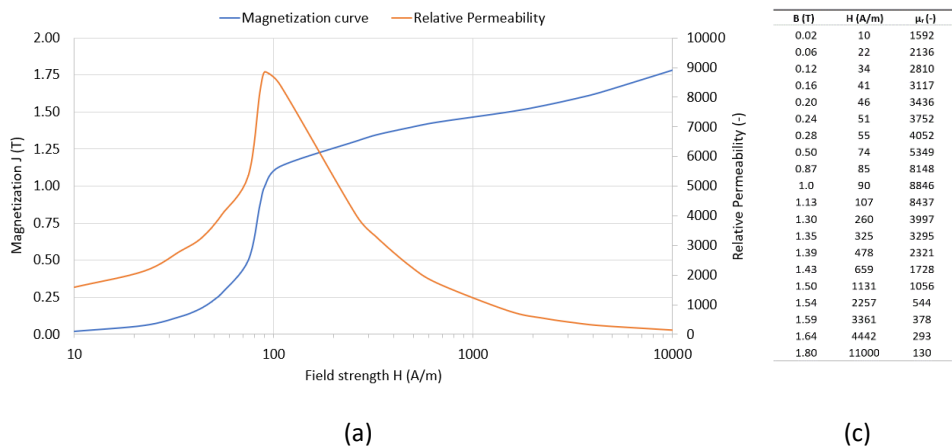


Figure 3.17. Printed material magnetization curve for multi-physical modeling: (a) normal magnetization curve and the corresponding relative permeabilities, (b) data for drawing the curves (initial values extrapolated).

High mechanical yield strength of the material gives reassurance that the printed components can handle the operation stresses in AM electrical motors. Excellent mechanical properties are critical for topology-optimized components as the refined geometries, and air-gapped structures would surely be subjected to higher stress concentrations than their conventional, more robust counterparts. On average, the printed material exhibited yield strength of 580 MPa before annealing and 420 MPa after it. As a comparison, in [144], the yield strength of Fe-Si laminations was shown to be highly silicon content-dependent: 365 MPa for 3% Si to Fe, 413 MPa for 3.7% Si to Fe, and 90 MPa for 6.5 % Si to Fe. Electron mobility within the printed samples was confirmed to be relatively unaffected by the additive production process. The obtained values were slightly lower than common values from the literature on low-silicon steels, likely due to

the slightly higher silicon content. Compared to the corresponding values provided for typical electrical steel laminations, the obtained thermal conductivity was 11% (24.8 W/m·K) lower and electrical resistivity 26 % higher (56.9 $\mu\Omega\cdot\text{cm}$). The expected values for electrical resistivity for 3% and 6% silicon steels are 47 [123] and 82 [145] $\mu\Omega\cdot\text{cm}$, respectively, showing a nearly linear relationship between resistivity and silicon content over the range of 3–8 wt% [112]. This relationship corresponds to 54 $\mu\Omega\cdot\text{cm}$ for 3.7% silicon content steel.

Regarding the magnetic properties of the cores, it can be summarized that L-PBF systems can be used to fabricate magnetic cores with useful properties. Magnetization of 1.5 T was roughly at 1500 A/m. Maximum relative permeability of 8846 was obtained at 90 A/m. In comparison, EU standards [140] require M400-50A electrical steel to reach 1.53 T at the maximum field strength of 2500 A/m. For higher grade steels, such as M210-35A, slightly lower saturation of 1.49 T is reached at the same field strength. Maximum relative permeabilities are not required to reach specific values by the standard but are typically slightly lower than the values obtained for the studied printed steel: somewhere between 5000–8000 [138]. As demonstrated in Table 3.3, the specific core losses of the printed steel are situated below the top- and high-grade silicon steels, in the range of medium-grade steels, such as M400-50A. Importantly, this comparison stands for the material losses at 1 T magnetization; at 1.5 T, the losses have climbed rapidly and are in the range of M1000-65A / M1300-100A laminations. For higher efficiency with stronger magnetic fields, further material microstructure optimization is required: the current granular structure seems to be best suited for low (1 T) field strength applications.

4 Prototyping of AM Electrical Machines

L-PBF systems can be used to prepare high-performance soft magnetic materials. This can be achieved through optimized printing, annealing, and topology of the printed cores. The challenges in prototyping full AM electrical machine cores are somewhat different from the printing of small-scale samples for material characterization. In particular, the printing of functional components typically involves more complex and larger topologies, which require additional process optimization. This chapter describes the manufacturing process flow and performance of functional EM magnetic cores. Two unique prototypes are printed and assembled as part of the work: the first transformer and induction motor in the scientific literature, which exhibit fully 3D printed magnetic parts and which are characterized in terms of performance. With this work, we aspire to demonstrate the current state of the art of AM magnetic cores for AC applications and map the main challenges involved. The chapter is based on the work presented in publications III and IV: “Design and Performance of Laser Additively Manufactured Core Induction Motor” [146] and “Additive Manufacturing and Performance of E-Type Transformer Core.” [147]

4.1 Transformer Prototyping

Prototypes of functional soft magnetic cores for time-varying magnetic fields are almost non-existent in the literature. This is likely due to two reasons. First, there are significant challenges involved in setting up an in-house production chain covering all the necessary steps from component design to its printing, post-processing, quality control, assembling, and component electrical performance measurements. Secondly, the achievable efficiencies for these printed cores would be lower than the conventional cores due to the difficulties in effectively suppressing eddy current losses within them. This makes the prototyping of AC cores somewhat unattractive compared to novel synchronous rotors, windings, or heat exchangers – prototypes that can demonstrate the advantages of the use of AM in electrical machine construction more clearly. A brief summary of the work in transformer core prototyping is presented in Figure 4.1.

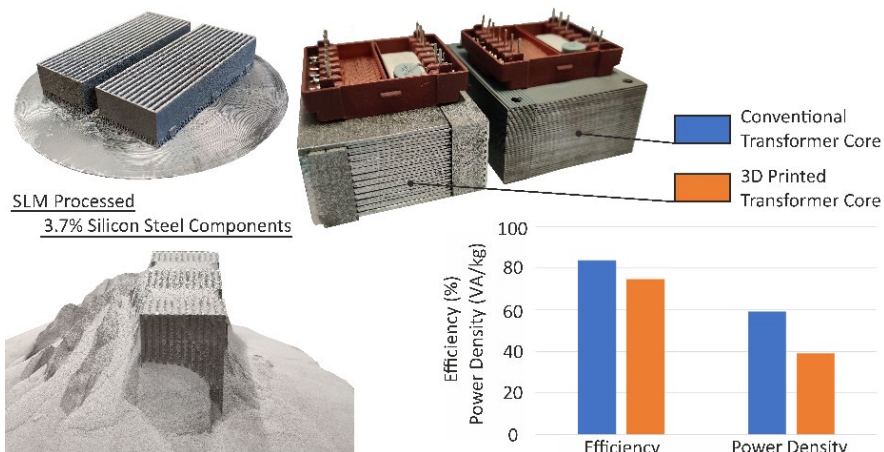


Figure 4.1. Summary of the prototyping study of 3D printing transformer cores. [147]

We selected a prototype E-type transformer as the next step in evaluating AM magnetic material capacity and performance for electrical machine applications. Its relatively simplistic design, involving no moving parts, makes it an ideal preliminary step before prototyping full electric motors. The full E-type transformer core was printed, characterized, and compared in terms of performance with a conventional Goss textured core. The 3D printed core was assembled from four novel interlocking components, which structurally imitated common E-type core laminations and facilitated the integration of a modular encased winding from the commercial counterpart. It was a small benchtop transformer with the overall core measurements of 58.5 x 49.5 x 26 mm. Similar to the samples investigated in the previous chapter, the prototype core was printed from 3.7% silicon steel with the SLM 280 L-PBF printer.

Lower power density of the printed core was confirmed after standard transformer no-load and full-load testing. This was related to grain-oriented structure of the Goss textured silicon steel M165-35S used within the conventional transformer core. The printed core exhibited non-oriented steel, perfect for electrical motors with a rotating magnetic field but less effective for electrical power transformers where the flux is unidirectional. The working point of the finished AM core was identified at 34% lower power density. This was at the same magnetizing current drawn from the supply – 40 mA, which could energize the conventional transformer core up to 230 V, and printed core up to 160 V. Energizing the printed core beyond this value resulted in a significant drop in its efficiency: due to ineffective usage of the core iron. The efficiency of the transformers was calculated from the load test measurements at both the ambient core temperature and the steady-state temperature at full load conditions. At full load, the measured efficiency of the transformers ranged from 83.8% (21 °C) to 80.4% (71 °C) for the conventional transformer and 74.7% (21 °C) to 70.1% (75 °C) for the prototype. The transformer efficiency-load characteristic is outlined in Figure 4.2. Highest efficiencies in the study were identified at ~40% load at 21 °C: for the conventional core 88.7% and for the prototype 80.5%. A difference of roughly 10 % in efficiency was identified for the cores over the full measurement range.

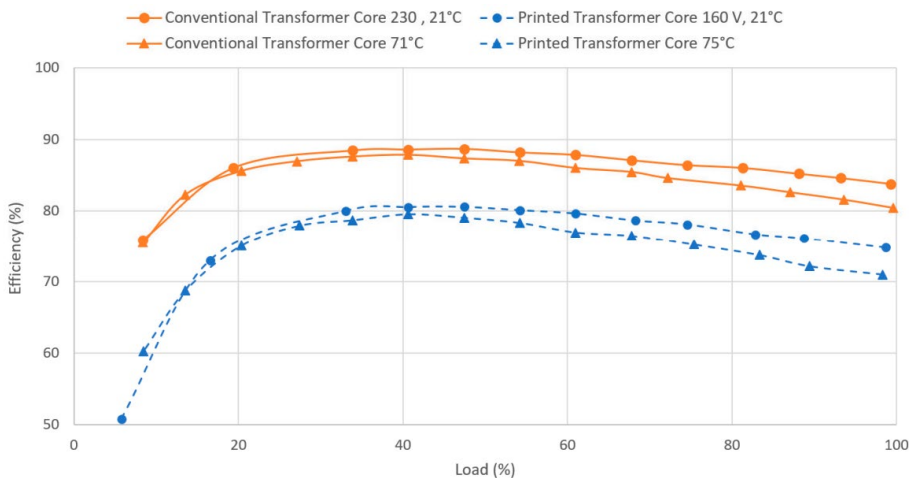


Figure 4.2. Efficiency-load characteristics of the conventional and prototype transformers. [147]

Results of performance characterization of both the printed and conventional transformer cores are summarized in Table 4.1. Both transformers show typical performance values for small single-phase 20–30 VA power rating devices. The typical efficiencies for 30 VA power transformers are in the range of 83% [148] – 81% [149], which decreases to 77% [148] at 22 VA and down to 65% [148] at 4.5 VA rated power. In parallel, the power densities are more dependent on the individual core designs, as some cores are with additional features or fully encased. From manufacturer datasheets, it can be found that for similar transformers as investigated as part of the study, the power densities are in the range of 56 [149] – 39 VA/kg [148].

Table 4.1. Comparison of the transformer cores performance. [147]

Parameter (full load, 21° C)	3D printed Core	Conventional Core
Nominal Voltage	160 V	230 V
Nominal Current	0.17 A	0.17 A
Power Factor	0.97	0.97
Input Power	27.2 VA	39.1 VA
Output power	19.8 VA	31.8 VA
Efficiency (ambient temperature)	74.7 %	83.8 %
Efficiency (operating temperature)	70.1%	80.5%
Power Density (Core)	47 VA/kg	72 VA/kg
Power Density (Full Transformer)	39 VA/kg	59 VA/kg

Several challenges were encountered when printing full-sized components. First, the initial tests of the transformer core printing resulted in failure: the topology of the core promoted uneven powder deposition on the substrate, resulting in a balling-related failure at some stage of the build job. The issue was solved by changing the orientation of the printed part to a 45-degree angle in relation to the re-coater. This resulted in a more even powder deposition on the substrate. Secondly, the transformer cores deformed significantly after removal from the base plate, due to the considerable internal stresses applied to them during the printing process and its thin-walled construction. This was resolved through cold working and bending of the part but could have been avoided entirely by low-temperature annealing (part normalization) before support removal. Thirdly, the power density of the transformer core was 1/3 less than the conventional counterpart. To increase the power density in AM power transformers, larger control should be obtained over the crystallographic texture of the cores. Grain-oriented steels reach significantly higher magnetization values than non-oriented steels under the same conditions but are only suitable for application with uni-directional magnetizing. Fourthly, utilizing a printed core in the transformer assembly resulting in a 10% efficiency drop. This can most prominently be attributed to the eddy currents generated in the 170% thicker laminations of the printed design.

The results are promising, AM full cores of electrical power devices show functional performance. Further prototyping efforts of AM transformer cores require the development of grain-oriented texture within the printed parts to match the power densities of conventional materials. In parallel, the non-oriented structure of the printed material is well suited for prototyping electric motors.

4.2 Induction Motor Prototyping

The printing of magnetic cores for electric motors is considerably more complicated than printing transformer components. This is mainly because of spatial accuracy requirements: the machines involve moving parts, and the thinner the gap between moving components, the higher the power density. In this work, an electrical motor with fully additively manufactured cores was produced and evaluated in terms of performance. The prototype incorporated a novel core internal structure in an attempt to limit eddy current losses. The main goal of this work was to establish a baseline for future design optimization purposes and to map the prototyping process for future reference.

The prototype was constrained by our production facilities and printed material properties, limiting the maximum diameter of the prototype to 90 mm and its nominal efficiency to a lower value than commercial motors of the same type and size. The type of motor was chosen as a squirrel-cage induction motor (IM) – as it is simple to operate from the grid. The initial design of the prototype was calculated through a procedure described by J. Pyrhönen *et. al.* in a design handbook titled: “*Design of Rotating Electrical Machines*” [150]. Two key challenges were identified for the prototype. First, minimizing eddy current losses within the printed cores and preparing them with sufficient accuracy to obtain a uniform air-gap. To reduce the losses, crack-like air-gaps were integrated into the core, running perpendicular to both the core axis and the printing direction. The chosen core segregation strategy is described in Figure 4.3.

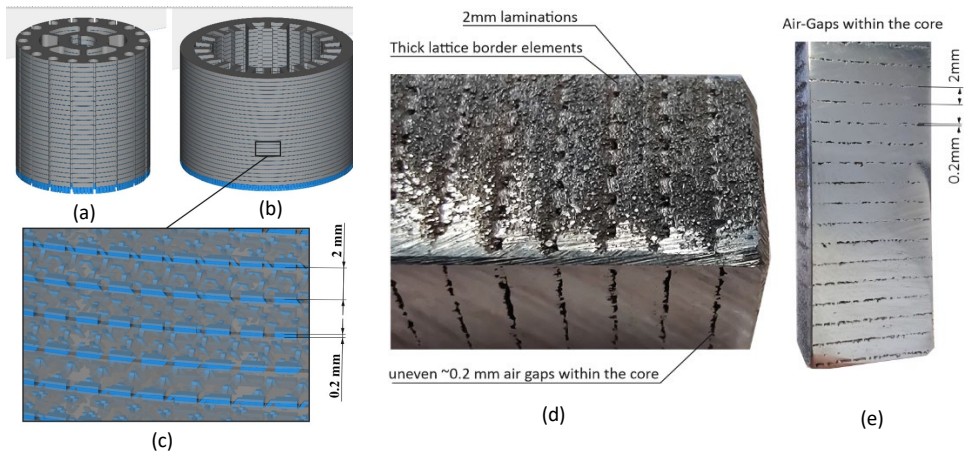


Figure 4.3. Eddy current loss strategy: (a) rotor core design, (b) stator core design, (c) insulating non-homogeneous layers, (d)-(e) Resultant printed motor core internal structure.

In the final design, 2 mm layers of magnetic material were separated with thin 0.2 mm air-gaps. To facilitate the printing, these gaps were filled with thin lattice-like structures. For obtaining a uniform motor air-gap, the parts were printed slightly larger than their final dimensions, and then machined to net shape after printing. The workflow for the prototype production is detailed in Figure 4.4, with illustrative images of the production in Figure 4.5.

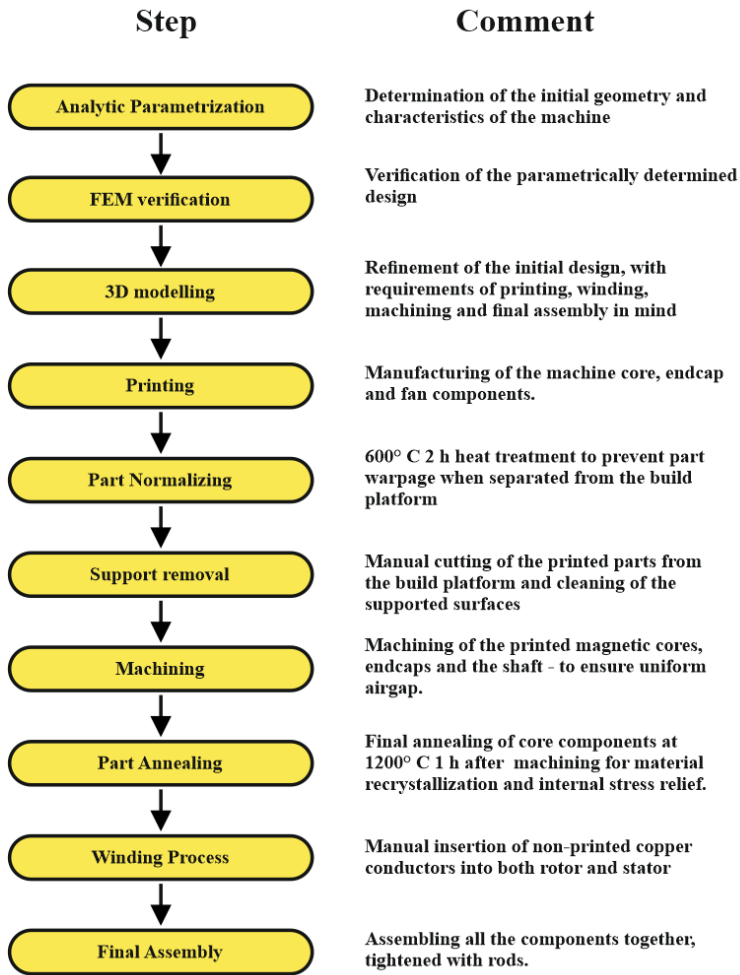


Figure 4.4. Workflow for producing the AM core prototype motor. [146]

After initial print testing, laser re-melting and “stripe” scan pattern settings were deemed unsuitable for the printing of larger parts (from material characterization samples), resulting in balling-related print failure. The survivability of the print job was increased substantially by adopting from double scan “stripe” to a single scan “chessboard” pattern. The printing duration of the cores was approximately 30 h. After printing and prior to cutting the cores off their build plates, the cores were normalized over a low-temperature annealing process. This managed to relax the internal stresses in the material, making it more malleable and less prone to deformations during the upcoming cold-working. After turning machining, a uniform air-gap of 0.35 mm was achieved for the prototype. With the necessary fitting and assembly preparations completed, the cores were subjected to high-temperature annealing, to promote grain growth of the material and remove any stresses introduced to the material with cold-working [155]. Next, the cores were wound: the stator with a distributed three-phase winding and the rotor with a squirrel cage. The prototype used commercial ball bearings on the shaft.

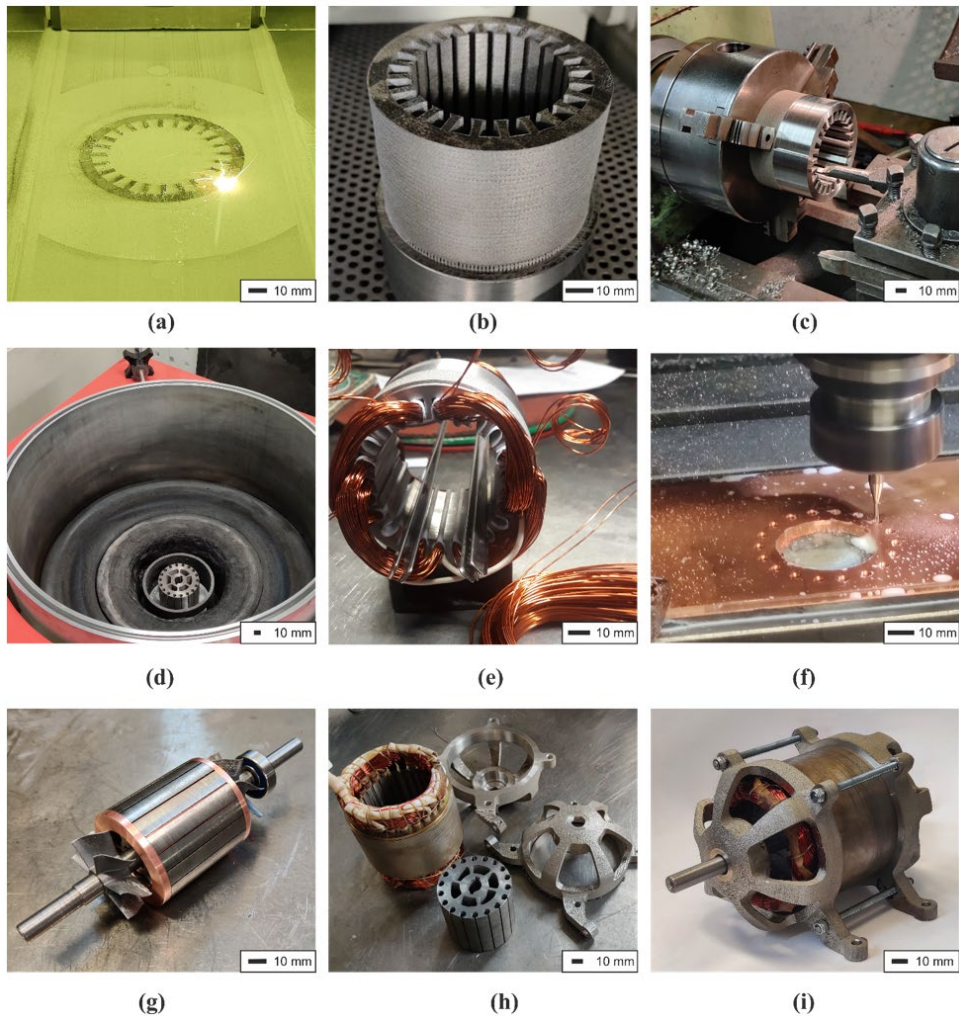


Figure 4.5. Production of the AM core motor: (a) L-PBF printing process of the stator core, (b) finished printed stator core supported on the build plate, (c) turning machining of the motor stator, (d) machine rotor in the annealing furnace, (e) stator winding process, (f) milling of the rotor end-rings, (g) assembled rotor with inserted cage, shaft, bearing and cooling fans, (h) motor stator, rotor core and endcaps, (i) fully assembled AM prototype. [146]

In order to evaluate the performance of the prototype, three standard tests were performed: the no-load, blocked rotor, and load test. For load testing, a benchmarking machine of the same type and similar size was obtained. Both the prototyping and the benchmarking machines were operated through the grid and controlled by autotransformers. The load test results of the benchmarking machine correlated well with its datasheet [151]. The nominal working point of the prototype was determined through an optimal balance (Figure 4.6) between its output power and efficiency, which was determined to be at 68 W, 34% efficiency. The results of the performance measurements are detailed in Table 4.3.

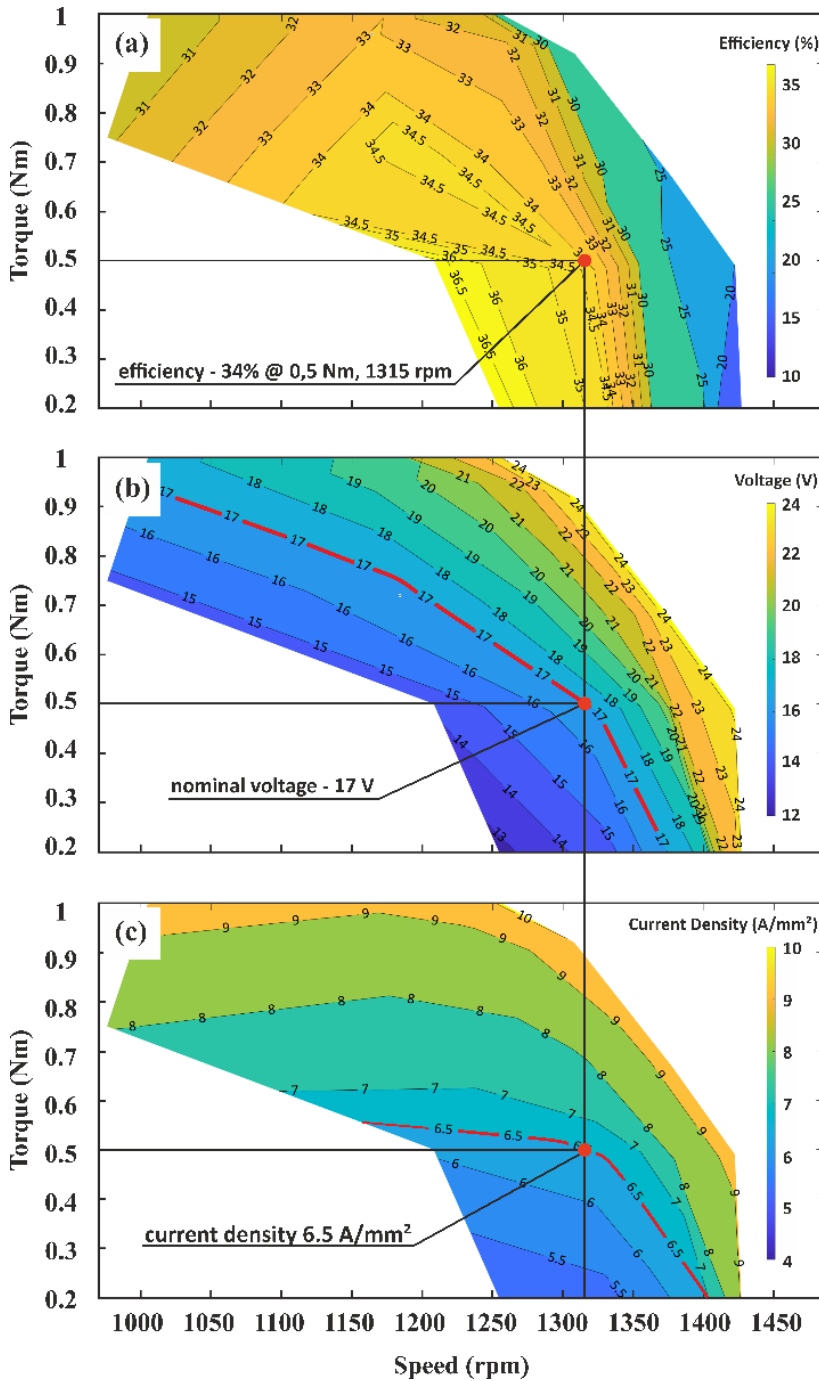


Figure 4.6. Determination of the prototype motor nominal parameters based on the full load test measurement results: (a) efficiency map, (b) speed-torque contour plot of terminal voltage, (c) speed-torque contour plot of winding current density. [146]

Table 4.3. Comparison of the commercial benchmarking machine and the designed / empirical values for the AM core prototype. [146]

Rated Values	Design	Experimental	Commercial
Power	80 W	68 W	60 W
Frequency	50 Hz	50 Hz	50 Hz
Rated Voltage	20 V	17 V	230 V
Rated Current	5.1 A	5.1 A	0.3 A
Rated Torque	0.55 Nm	0.5 Nm	0.4 Nm
Speed	1400 rpm	1315 rpm	1395 rpm
Efficiency	40 %	34 %	52 %
Power Factor	0.65	0.82	0.55

The efficiency of the commercial benchmarking motor was 52%, which was 3/2 of the efficiency of the prototype. For small-scale IMs, the efficiency in the range of 50% is typical [152]. There are no similar AM prototypes from the literature for comparison with current work. Some authors from both academic and non-academic sources have produced polymer core machines with neodymium permanent magnet arrays to compensate for the low magnetization of polymer cores [10], [153]. Perhaps the best comparative data can be obtained from [154], where a rotor of a commercial switched reluctance motor was substituted with a printed Fe-Si analog. The new assembly suffered from reduced efficiency – decreasing from 83% to 65% at 1500 rpm, ~1kw output power.

Laser additive manufacturing was used to successfully prepare both the rotor and stator of a prototype induction motor. The main challenges were related to core spatial accuracy and eddy current losses. Printing of the parts with the current setup resulted in slightly elliptical cores: approximately 0.2 mm, translating to a 0.1 mm distortion on the airgap. This is significant as air-gaps in an EM of this size are usually within the same range. After machining, the ellipticity was removed, and a uniform air-gap of 0.35 mm was obtained. The employed method for eddy current loss reduction was moderately successful. Approximately 29.5 W/kg of specific iron losses within the 2.4 kg motor cores at 50 Hz, 1.1 T magnetization ($W_{11,50}$) were identified. At the same conditions, the solid 5 x 5 mm cross-section core exhibited iron losses of 12.9 W/kg (Figure 3.16). The individual areas of the motor core were approximately 3 x 2 mm in the stator teeth and 7 x 2 mm in the stator yoke. This indicates that a significant electrical short circuit was present over the cracks printed into the material. The full core was massive in comparison with the sample toroid: 56 mm in height, 89 mm in outer diameter, and ~58 mm in inner diameter. The intra-core electrical conductivity could have also been enhanced by the sintering of the unmelted powder captured within the core during the annealing process. Nevertheless, despite these initial problems, 2/3 of the efficiency of the conventional benchmarking machine was obtained at similar power density. Output power of the machines was similar (60 W for commercial, 68 W for prototype) as well as their weight: 2.9 kg for full weight of the conventional motor, and 2.4 kg for the core weight of the prototype.

5 Conclusions and Future Work

3D printing of the prototype components indicated great potential for AM electrical motors. The obtained performance parameters were somewhat lower than their commercial counterparts, which is understandable, as these were the first generation of AM electric machine prototypes. Future designs can benefit from further optimized machine and magnetic core designs.

The core intrinsic material properties (Table 3.3) were similar to typical mid-range lamination sheets. Eddy current loss reduction still requires further work: it is possible to reduce them to an acceptable level, but currently only through air-gapped internal structure. This, however, lowers the fill factor of the cores, requiring a larger magnetic core volume (albeit at similar weight) to output the same power. In parallel, the core would likely suffer from reduced mechanical durability but would likely allow for greater possibilities in heat extraction. In the prototype induction motor, perpendicular air-gaps to the printing direction were integrated, with mixed success. The short circuit between the segregated areas of the core was still significant. Investigation of the magnetic cores showed higher efficiency of air-gaps (Figure 3.16) formed in parallel to the print direction to the perpendicular gaps. This orientation allowed to form wide uniform air-gaps, with minimalistic thin bridges connecting the individual laminations, both limiting inter-lamination electrical connection and enabling the removal of all the un-melted powder from within the core. This enabled to achieve iron losses as low as 1.8 W/kg ($W_{10,50}$), but at higher flux densities ($>W_{13,50}$), the losses increased substantially (Figure 3.16). This was determined to be related to excessive grain size, which has been shown to be beneficial at lower core flux densities and to be detrimental at higher flux densities. Further crystallographic texture optimization research is required. The nominal working points of the prototypes were also determined at moderate flux density values, for the E-type transformer: 1.16 T, exhibiting 3.05 W/kg losses, and for the induction motor 1.1 T, exhibiting 29.5 W/kg losses. The core design (interlocking cores) of the transformer proved considerably more effective in suppressing eddy currents than the prototype motor design, but would be considerably more difficult to implement in motors due to the rotating magnetic field, and possible assembling/machining challenges introduced to the process.

The main objectives of the work were achieved. By implementing methodological enhancements, useful material properties for the printed cores and functional performance full-sized prototype EMs were obtained. This provides a firm foundation the future work on additive manufacturing of topology-optimized electrical machines, and their components can be built upon. The main results for each thesis objective are the following:

- Literature survey on the current state-of-the-art, perspectives and challenges of additively manufactured EM active part materials was conducted.
 - The maturity of the AM prototyping and small volume production of electrical machines is currently highest with PBF printing systems, where high spatial accuracy, high purity, and near fully dense parts can be prepared.
 - Current PBF printing systems show great promise for small volume production or prototyping of unconventional topology optimized electrical machine windings, heat exchangers, and synchronous rotors.

- Fine-tuning of the printing setup was achieved, soft magnetic material parts from silicon steel powder with high relative density (above 99.5%) were prepared.
 - The optimal printing parameters for printing 3.7% silicon steel cores were: layer thickness 50 μm , hatch distance 120 μm , laser power 350 W, and scanning velocity 750 mm/s (laser energy density of 77 J/mm³).
 - These parameters were applied to print 99.86% dense test samples with 8 μm average surface roughness Ra.

- Full process workflow was developed and implemented to produce printed silicon steel soft magnetic cores with useful magnetic properties.
 - Annealing was determined as a critical additional step in preparing L-PBF fused soft magnetic cores.
 - The most useful magnetic properties were obtained with the annealing temperature 1200 °C, hold time 60 min, and heating rate 5 °C/min.
 - For higher field strength applications (~1.5 T), further process optimization is required to obtain the optimal crystallographic structure.
 - The magnetic cores processed through the developed workflow exhibited quasi-static hysteresis loss of 0.8 W/kg ($W_{10,50}$) and maximum relative permeability of 8800.
 - With integrated air-gaps, total iron losses in printed cores were shown to decrease 81%: from 9.6 to 1.8 W/kg ($W_{10,50}$). In parallel, the air-gaps resulted in material fill factor reduction to 73%.
 - The obtained losses are equivalent to mid-grade (M400-50A / M-43) soft magnetic laminations, which are required to exhibit iron losses no larger than 1.7 W/kg ($W_{10,50}$).

- Non-magnetic properties of the printed silicon steel were characterized for future topology optimization purposes.
 - The printed material exhibited yield strength of 420 MPa, thermal conductivity of 24.8 W/m·K and electrical resistivity of 56.9 $\mu\Omega\cdot\text{cm}$.
 - For a typical commercial lamination, the disclosed values in a datasheet are: yield strength of 350 MPa, thermal conductivity of 28 W/m·K and electrical resistivity of 45 $\mu\Omega\cdot\text{cm}$.

- Practical capacity of L-PBF printing systems was demonstrated for printing functional electromagnetic devices.
 - Magnetic cores for both an induction motor and a power transformer were printed successfully.
 - These first cores showed promising, though slightly lower performance than their commercial counterparts.
 - At nominal output, energy efficiency of 34% was obtained for the prototype induction motor and 70% for the prototype power transformer at nominal operating point. These are 2/3 and 7/8 respectively of equivalent commercial counterpart efficiencies.

A firm foundation for future work on additive manufacturing of topology-optimized electrical machines and their components has been established. Printed and annealed soft magnetic 3.7% silicon steel showed useful material properties and applicability for rapid prototyping of EMs. Future progress in the project will require efforts in both material science and topology optimization. The mapped magnetic, thermal, electrical, and mechanical properties will be used for the multi-physical modeling and three-dimensional shape optimization of novel electrical machines. To enable the printing of more complex designs, the printing of additional materials, both magnetic and non-magnetic, will be investigated. This will include materials for thermal and electrical conduction and more exotic soft magnetic materials, such as high-silicon steel and amorphous alloys, to achieve higher core efficiency. Undoubtedly, multi-material metal printing would radically change the perspective of AM electrical machines. It would enable both unparalleled control over part internal structure and the 3D printing of full electrical machines as a single process. These methods are likely to emerge soon and become available for research work.

References

- [1] “Electricity generation statistics – first results - Statistics Explained.” https://ec.europa.eu/eurostat/statistics-explained/index.php/Electricity_generation_statistics_-_first_results (accessed Apr. 14, 2021).
- [2] G. Bramerdorfer, J. A. Tapia, J. J. Pyrhonen, and A. Cavagnino, “Modern Electrical Machine Design Optimization: Techniques, Trends, and Best Practices,” *IEEE Trans. Ind. Electron.*, vol. 65, no. 10, pp. 7672–7684, 2018, doi: 10.1109/TIE.2018.2801805.
- [3] “Premium Efficiency Motor Selection and Application Guide.” Accessed: Jul. 15, 2021. [Online]. Available: https://www.energy.gov/sites/default/files/2014/04/f15/amo_motors_handbook_web.pdf
- [4] R. Poprawe, C. Hinke, W. Meiners, J. Schrage, S. Bremen, and S. Merkt, “SLM Production Systems: Recent Developments in Process Development, Machine Concepts and Component Design,” no. November, pp. 49–65, 2015, doi: 10.1007/978-3-319-12304-2_5.
- [5] “Reduce your costs by 50% with 3d printed copper induction coils.” <https://news.pminnovationblog.com/blog/how-reduce-cost-by-50-percent-with-3d-printed-copper-induction-hardening-coil> (accessed Apr. 18, 2022).
- [6] G. Additive, “REDUCE YOUR INDUCTION HARDENING COIL COSTS THROUGH 3D PRINTING.” <https://www.gknpm.com/globalassets/downloads/additive-manufacturing/brochures/e-brochure---inductors-and-3d-printing-a-perfect-production-fit.pdf/> (accessed Apr. 18, 2022).
- [7] H. Tiismus, A. Kallaste, T. Vaimann, and A. Rassõlkin, “State of the Art of Additively Manufactured Electromagnetic Materials for Topology Optimized Electrical Machines,” *Addit. Manuf.*, vol. 55, no. November 2021, p. 102778, 2022, doi: 10.1016/j.addma.2022.102778.
- [8] “How 3D printing is redefining inductor coil production | GKN Additive.” <https://www.gknpm.com/en/our-businesses/gkn-additive/how-3d-printing-is-redefining-inductor-coil-production/> (accessed Nov. 26, 2020).
- [9] “GE Aviation 3D Prints 30,000th Metal 3D Printed Fuel Nozzle at Auburn, Alabama Plant.” <https://3dprint.com/226703/ge-aviation-fuel-nozzle-3d-printed-30000/?fbclid=IwAR38NO-0dAf2BwlkXhVtIC18gAimKnQUSy5KRv-u08InfuK5Zl7Ql1P1HI> (accessed Nov. 26, 2020).
- [10] E. Aguilera, J. Ramos, D. Espalin, F. Cedillos, D. Muse, R. Wicker, and E. Macdonald, “3D Printing of Electro Mechanical Systems,” in *International Solid Freeform Fabrication Symposium*, 2013, pp. 950–961.
- [11] M. Garibaldi, C. Gerada, I. Ashcroft, R. Hague, H. Morvan, M. Garibaldi, C. Gerada, I. Ashcroft, R. Hague, and H. Morvan, “The Impact of Additive Manufacturing on the Development of Electrical Machines for MEA Applications : A Feasibility Study,” no. 1, pp. 2–5, 2015.
- [12] S. Metsä-Kortelainen, T. Lindroos, M. Savolainen, A. Jokinen, A. Revuelta, A. Pasanen, K. Ruusuvoori, and J. Pippuri, “Manufacturing of topology optimized soft magnetic core through 3D printing,” *NAFEMS Nord. Semin.*, 2016.

- [13] S. Lammers, G. Adam, H. J. Schmid, R. Mrozek, R. Oberacker, M. J. Hoffmann, F. Quattrone, and B. Ponick, "Additive Manufacturing of a lightweight rotor for a permanent magnet synchronous machine," in *2016 6th International Electric Drives Production Conference, EDPC 2016 - Proceedings*, 2016, vol. 13, pp. 41–45. doi: 10.1109/EDPC.2016.7851312.
- [14] R. H. Michele Garibaldi, Ian Ashcroft, Chris Gerada, "Laser Additive Manufacturing of Soft Magnetic Cores for Rotating Electrical Machinery: Materials Development and Part Design," 2018.
- [15] H. Tiismus, A. Kallaste, A. Belahcen, A. Rassolkin, and T. Vaimann, "Challenges of Additive Manufacturing of Electrical Machines," in *Proceedings of the 2019 IEEE 12th International Symposium on Diagnostics for Electrical Machines, Power Electronics and Drives, SDEMPED 2019*, 2019, pp. 44–48. doi: 10.1109/DEMPED.2019.8864850.
- [16] R. Wrobel and B. Mecrow, "A Comprehensive Review of Additive Manufacturing in Construction of Electrical Machines," in *Proceedings of the IEEE Workshop on Electrical Machines Design, Control and Diagnosis, WEMDCD, 2019*, 2019, pp. 15–22. doi: 10.1109/WEMDCD.2019.8887765.
- [17] R. Wrobel and B. Mecrow, "A Comprehensive Review of Additive Manufacturing in Construction of Electrical Machines," *IEEE Trans. Energy Convers.*, vol. 35, no. 2, pp. 1054–1064, 2020, doi: 10.1109/TEC.2020.2964942.
- [18] M. U. Naseer, A. Kallaste, B. Asad, T. Vaimann, and A. Rassolkin, "A Review on Additive Manufacturing Possibilities for Electrical Machines," *Energies*, vol. 14, no. 7, p. 1940, Mar. 2021, doi: 10.3390/en14071940.
- [19] P. S. Ghahfarokhi, A. Podgornovs, A. Kallaste, A. J. M. Cardoso, A. Belahcen, T. Vaimann, H. Tiismus, and B. Asad, "Opportunities and Challenges of Utilizing Additive Manufacturing Approaches in Thermal Management of Electrical Machines," *IEEE Access*, vol. 9, pp. 36368–36381, 2021, doi: 10.1109/ACCESS.2021.3062618.
- [20] A. Selema, M. N. Ibrahim, and P. Sergeant, "Metal Additive Manufacturing for Electrical Machines: Technology Review and Latest Advancements," *Energies*, vol. 15, no. 3, pp. 1076–1094, Jan. 2022, doi: 10.3390/en15031076.
- [21] T. Pham, P. Kwon, and S. Foster, "Additive Manufacturing and Topology Optimization of Magnetic Materials for Electrical Machines—A Review," *Energies*, vol. 14, no. 2, p. 283, 2021, doi: 10.3390/en14020283.
- [22] V. Chaudhary, S. A. Mantri, R. V. Ramanujan, and R. Banerjee, "Additive manufacturing of magnetic materials," *Prog. Mater. Sci.*, vol. 114, no. February 2019, p. 100688, 2020, doi: 10.1016/j.pmatsci.2020.100688.
- [23] V. Popov, A. Koptuyug, I. Radulov, F. Maccari, and G. Muller, "Prospects of additive manufacturing of rare-earth and non-rare-earth permanent magnets," *Procedia Manuf.*, vol. 21, no. 2017, pp. 100–108, 2018, doi: 10.1016/j.promfg.2018.02.199.
- [24] J. M. D. Coey, "Perspective and Prospects for Rare Earth Permanent Magnets," *Engineering*, vol. 6, no. 2, pp. 119–131, 2020, doi: 10.1016/j.eng.2018.11.034.
- [25] Q. Jiang, P. Zhang, Z. Yu, H. Shi, D. Wu, H. Yan, X. Ye, Q. Lu, and Y. Tian, "A review on additive manufacturing of pure copper," *Coatings*, vol. 11, no. 6, 2021, doi: 10.3390/coatings11060740.

- [26] T. Q. Tran, A. Chinnappan, J. K. Y. Lee, N. H. Loc, L. T. Tran, G. Wang, V. V. Kumar, W. A. D. M. Jayathilaka, D. Ji, M. Doddamani, and S. Ramakrishna, "3D printing of highly pure copper," *Metals (Basel)*, vol. 9, no. 7, pp. 12–20, 2019, doi: 10.3390/met9070756.
- [27] T. El-Wardany, Y. She, V. Jagdale, J. K. Garofano, J. Liou, and W. Schmidt, "Challenges in 3D printing of high conductivity copper," in *ASME 2017 International Technical Conference and Exhibition on Packaging and Integration of Electronic and Photonic Microsystems, InterPACK 2017, collocated with the ASME 2017 Conference on Information Storage and Processing Systems*, 2017, pp. 1–10. doi: 10.1115/IPACK2017-74306.
- [28] T. Gornet and T. Wohlers, "History of Additive Manufacturing," 2016. doi: 10.4018/978-1-5225-2289-8.ch001.
- [29] M. Yakout, M. A. Elbestawi, and S. C. Veldhuis, "Density and mechanical properties in selective laser melting of Invar 36 and stainless steel 316L," *J. Mater. Process. Technol.*, vol. 266, no. November 2018, pp. 397–420, 2019, doi: 10.1016/j.jmatprotec.2018.11.006.
- [30] X. Song, W. Zhai, R. Huang, J. Fu, M. Fu, and F. Li, "Metal-Based 3D-Printed Micro Parts & Structures," in *Reference Module in Materials Science and Materials Engineering*, Elsevier, 2020. doi: 10.1016/b978-0-12-819726-4.00009-0.
- [31] "Dual Metal LPBF - Aerosint." <https://aerosint.com/dual-metal-lpbf/> (accessed Nov. 27, 2020).
- [32] H. Wong, K. Dawson, G. A. Ravi, L. Howlett, R. O. Jones, and C. J. Sutcliffe, "Multi-Laser Powder Bed Fusion Benchmarking—Initial Trials with Inconel 625," *Int. J. Adv. Manuf. Technol.*, vol. 105, no. 7–8, pp. 2891–2906, 2019, doi: 10.1007/s00170-019-04417-3.
- [33] "LASERTEC 30 DUAL SLM - ADDITIVE MANUFACTURING Machines by DMG MORI." <https://en.dmgmori.com/products/machines/additive-manufacturing/powder-bed/lasertec-30-slm> (accessed Jan. 12, 2022).
- [34] T. D. Ngo, A. Kashani, G. Imbalzano, K. T. Q. Nguyen, and D. Hui, "Additive manufacturing (3D printing): A review of materials, methods, applications and challenges," *Compos. Part B Eng.*, vol. 143, no. December 2017, pp. 172–196, 2018, doi: 10.1016/j.compositesb.2018.02.012.
- [35] L. E. Murr and W. L. Johnson, "3D metal droplet printing development and advanced materials additive manufacturing," *J. Mater. Res. Technol.*, vol. 6, no. 1, pp. 77–89, 2017, doi: 10.1016/j.jmrt.2016.11.002.
- [36] M. S. I. . Kamariah, W. S. . Harun, F. Ahmad, and F. Tarlochan, "Mechanical Behaviours of Selective Laser Melting 316L Stainless Steel," *J. Addit. Manuf. Adv. Mater.*, vol. 1, no. 1, pp. 1–18, 2020.
- [37] E. Nassar, A and Reutzel, "Beyond layer-by-layer Additive Manufacturing – Voxel-wise Directed Energy Deposition A. R. Nassar* and E. W. Reutzel* * Applied Research Laboratory at the Pennsylvania State University, University Park, PA 16802," *Appl. reseach Lab. Penn State Univ.*, pp. 273–283, 2015, [Online]. Available: <https://pdfs.semanticscholar.org/26a2/215766598251218b8b7e8575e5481d873233.pdf>
- [38] S. A. M. Tofail, E. P. Koumoulos, A. Bandyopadhyay, S. Bose, L. O'Donoghue, and C. Charitidis, "Additive manufacturing: scientific and technological challenges, market uptake and opportunities," *Mater. Today*, vol. 21, no. 1, pp. 22–37, 2018, doi: 10.1016/j.mattod.2017.07.001.

- [39] M. Ziaee and N. B. Crane, "Binder jetting: A review of process, materials, and methods," *Addit. Manuf.*, vol. 28, no. December 2018, pp. 781–801, 2019, doi: 10.1016/j.addma.2019.05.031.
- [40] I. Rishmawi, M. Salarian, and M. Vlasea, "Tailoring green and sintered density of pure iron parts using binder jetting additive manufacturing," *Addit. Manuf.*, vol. 24, no. October, pp. 508–520, 2018, doi: 10.1016/j.addma.2018.10.015.
- [41] G. K. Meenashisundaram, Z. Xu, M. L. S. Nai, S. Lu, J. S. Ten, and J. Wei, "Binder jetting additive manufacturing of high porosity 316L stainless steel metal foams," *Materials (Basel)*, vol. 13, no. 17, pp. 1–23, 2020, doi: 10.3390/MA13173744.
- [42] T. Do, T. J. Bauder, H. Suen, K. Rego, J. Yeom, and P. Kwon, "Additively manufactured full-density stainless steel 316L with binder jet printing," *ASME 2018 13th Int. Manuf. Sci. Eng. Conf. MSEC 2018*, vol. 1, no. October, 2018, doi: 10.1115/MSEC2018-6681.
- [43] C. E. Duty, V. Kunc, B. Compton, B. Post, D. Erdman, R. Smith, R. Lind, P. Lloyd, and L. Love, "Structure and mechanical behavior of Big Area Additive Manufacturing (BAAM) materials," *Rapid Prototyp. J.*, vol. 23, no. 1, pp. 181–189, 2017, doi: 10.1108/RPJ-12-2015-0183.
- [44] F. Lorenz, J. Rudolph, and R. Wemer, "Design of 3D Printed High Performance Windings for Switched Reluctance Machines," *2018 XIII Int. Conf. Electr. Mach.*, pp. 2451–2457, 2018, doi: 10.1109/ICELMACH.2018.8506845.
- [45] T. N. Lamichhane, L. Sethuraman, A. Dalagan, H. Wang, J. Keller, and M. P. Paranthaman, "Additive manufacturing of soft magnets for electrical machines—a review," *Mater. Today Phys.*, vol. 15, p. 100255, 2020, doi: 10.1016/j.mtphys.2020.100255.
- [46] M. Quarto, M. Carminati, and G. D'Urso, "Density and shrinkage evaluation of AISI 316L parts printed via FDM process," *Mater. Manuf. Process.*, vol. 36, no. 13, pp. 1535–1543, 2021, doi: 10.1080/10426914.2021.1905830.
- [47] D. Syrlybayev, B. Zharylkassyn, A. Seisekulova, M. Akhmetov, A. Perveen, and D. Talamona, "Optimisation of strength properties of FDM printed parts—A critical review," *Polymers (Basel)*, vol. 13, no. 10, 2021, doi: 10.3390/polym13101587.
- [48] M. Quarto, M. Carminati, G. D'Urso, C. Giardini, and G. Maccarini, "Processability of metal-filament through polymer FDM machine," *ESAFORM 2021 - 24th Int. Conf. Mater. Form.*, vol. 13, pp. 1–11, 2021, doi: 10.25518/esaform21.2114.
- [49] Y. Thompson, J. Gonzalez-Gutierrez, C. Kukla, and P. Felfer, "Fused filament fabrication, debinding and sintering as a low cost additive manufacturing method of 316L stainless steel," *Addit. Manuf.*, vol. 30, no. May, p. 100861, 2019, doi: 10.1016/j.addma.2019.100861.
- [50] C. Tosto, J. Tirillò, F. Sarasini, and G. Cicala, "Hybrid metal/polymer filaments for fused filament fabrication (FFF) to print metal parts," *Appl. Sci.*, vol. 11, no. 4, p. 1, 2021, doi: 10.3390/app11041444.
- [51] M. Ralchev, V. Mateev, and I. Marinova, "3D Printing of Magnetic Materials by FFF Technology," *2020 12th Electr. Eng. Fac. Conf. Bulef 2020*, pp. 4–7, 2020, doi: 10.1109/Bulef51036.2020.9326060.
- [52] B. Khatri, K. Lappe, D. Noetzel, K. Pursche, and T. Hanemann, "A 3D-printable polymer-metal soft-magnetic functional composite-development and characterization," *Materials (Basel)*, vol. 11, no. 2, 2018, doi: 10.3390/ma11020189.

- [53] "Super Core TM Electrical steel sheets for high-frequency application." <https://www.jfe-steel.co.jp/en/products/electrical/catalog/f1e-002.pdf> (accessed May 13, 2021).
- [54] H. Tiismus, A. Kallaste, A. Belahcen, T. Vaimann, A. Rassõlkin, and D. Lukichev, "Hysteresis Measurements and Numerical Losses Segregation of Additively Manufactured Silicon Steel for 3D Printing Electrical Machines," *Appl. Sci.*, vol. 10, no. 18, p. 6515, 2020, doi: 10.3390/app10186515.
- [55] H. Tiismus, A. Kallaste, A. Belahcen, M. Tarraste, T. Vaimann, A. Rassõlkin, B. Asad, and P. Shams Ghahfarokhi, "AC Magnetic Loss Reduction of SLM Processed Fe-Si for Additive Manufacturing of Electrical Machines," *Energies*, vol. 14, no. 5, p. 1241, 2021, doi: 10.3390/en14051241.
- [56] D. Goll, D. Schuller, G. Martinek, T. Kunert, J. Schurr, C. Sinz, T. Schubert, T. Bernthaler, H. Riegel, and G. Schneider, "Additive manufacturing of soft magnetic materials and components," *Addit. Manuf.*, vol. 27, no. December 2018, pp. 428–439, 2019, doi: 10.1016/j.addma.2019.02.021.
- [57] M. Garibaldi, I. Ashcroft, J. N. Lemke, M. Simonelli, and R. Hague, "Effect of annealing on the microstructure and magnetic properties of soft magnetic Fe-Si produced via laser additive manufacturing," *Scr. Mater.*, vol. 142, pp. 121–125, 2018, doi: 10.1016/j.scriptamat.2017.08.042.
- [58] A. Plotkowski, J. Pries, F. List, P. Nandwana, B. Stump, K. Carver, and R. R. Dehoff, "Influence of scan pattern and geometry on the microstructure and soft-magnetic performance of additively manufactured Fe-Si," *Addit. Manuf.*, vol. 29, no. April, 2019, doi: 10.1016/j.addma.2019.100781.
- [59] B. Koo, M. S. Jang, Y. G. Nam, S. Yang, J. Yu, Y. H. Park, and J. W. Jeong, "Structurally-layered soft magnetic Fe-Si components with surface insulation prepared by shell-shaping selective laser melting," *Appl. Surf. Sci.*, vol. 553, no. February, pp. 1–5, 2021, doi: 10.1016/j.apsusc.2021.149510.
- [60] G. Stornelli, A. Faba, A. Di Schino, P. Folgarait, M. R. Ridolfi, E. Cardelli, and R. Montanari, "Properties of additively manufactured electric steel powder cores with increased si content," *Materials (Basel)*, vol. 14, no. 6, 2021, doi: 10.3390/ma14061489.
- [61] H. Tiismus, A. Kallaste, A. Belahcen, A. Rassolkin, and T. Vaimann, "Hysteresis loss evaluation of additively manufactured soft magnetic core," in *Proceedings - 2020 International Conference on Electrical Machines, ICEM 2020*, Aug. 2020, pp. 1657–1661. doi: 10.1109/ICEM49940.2020.9270836.
- [62] T. Q. Pham, S. Member, H. Suen, P. Kwon, S. N. Foster, and S. Member, "Reduction in Hysteresis Loss of Binder Jet Printed Iron Silicon," pp. 1669–1675, 2020.
- [63] C. L. Cramer, P. Nandwana, J. Yan, S. F. Evans, A. M. Elliott, C. Chinnasamy, and M. P. Paranthaman, "Binder jet additive manufacturing method to fabricate near net shape crack-free highly dense Fe-6.5 wt.% Si soft magnets," *Heliyon*, vol. 5, no. 11, p. e02804, 2019, doi: 10.1016/j.heliyon.2019.e02804.
- [64] T. Riipinen, S. Metsä-Kortelainen, T. Lindroos, J. S. Keränen, A. Manninen, and J. Pippuri-Mäkeläinen, "Properties of soft magnetic Fe-Co-V alloy produced by laser powder bed fusion," *Rapid Prototyp. J.*, 2019, doi: 10.1108/RPJ-06-2018-0136.
- [65] V. Chaudhary, N. M. Sai Kiran Kumar Yadav, S. A. Mantri, S. Dasari, A. Jagetia, R. V. Ramanujan, and R. Banerjee, "Additive manufacturing of functionally graded Co-Fe and Ni-Fe magnetic materials," *J. Alloys Compd.*, vol. 823, p. 153817, 2020, doi: 10.1016/j.jallcom.2020.153817.

- [66] H. Y. Jung, S. J. Choi, K. G. Prashanth, M. Stoica, S. Scudino, S. Yi, U. Kühn, D. H. Kim, K. B. Kim, and J. Eckert, "Fabrication of Fe-based bulk metallic glass by selective laser melting: A parameter study," *Mater. Des.*, vol. 86, pp. 703–708, 2015, doi: 10.1016/j.matdes.2015.07.145.
- [67] S. Alleg, R. Drablia, and N. Fenineche, "Effect of the Laser Scan Rate on the Microstructure, Magnetic Properties, and Microhardness of Selective Laser-Melted FeSiB," *J. Supercond. Nov. Magn.*, vol. 31, no. 11, pp. 3565–3577, 2018, doi: 10.1007/s10948-018-4621-z.
- [68] T. Borkar, R. Conteri, X. Chen, R. V. Ramanujan, and R. Banerjee, "Laser additive processing of functionally-graded Fe–Si–B–Cu–Nb soft magnetic materials," *Mater. Manuf. Process.*, vol. 32, no. 14, pp. 1581–1587, 2017, doi: 10.1080/10426914.2016.1244849.
- [69] E. Peng, X. Wei, T. S. Heng, U. Garbe, D. Yu, and J. Ding, "Ferrite-based soft and hard magnetic structures by extrusion free-forming," *RSC Adv.*, vol. 7, no. 43, pp. 27128–27138, 2017, doi: 10.1039/c7ra03251j.
- [70] M. S. K. K. Y. Nartu, S. Dasari, A. Sharma, V. Chaudhary, S. M. Varahabhatla, S. A. Mantri, E. Ivanov, R. V. Ramanujan, N. B. Dahotre, and R. Banerjee, "Reducing coercivity by chemical ordering in additively manufactured soft magnetic Fe–Co (Hiperco) alloys," *J. Alloys Compd.*, vol. 861, p. 157998, 2021, doi: 10.1016/j.jallcom.2020.157998.
- [71] S. Gao, X. Yan, C. Chang, E. Aubry, P. He, M. Liu, H. Liao, and N. Fenineche, "Microstructure and magnetic properties of FeSiBCrC soft magnetic alloy manufactured by selective laser melting," *Mater. Lett.*, vol. 290, p. 129469, 2021, doi: 10.1016/j.matlet.2021.129469.
- [72] "Sintex® Soft Magnetic Composites." <https://www.sintex.com/en/powder-metal/technical-data/category/smc> (accessed May 14, 2021).
- [73] T. Q. Pham, T. T. Do, P. Kwon, and S. N. Foster, "Additive Manufacturing of High Performance Ferromagnetic Materials," *2018 IEEE Energy Convers. Congr. Expo. ECCE 2018*, pp. 4303–4308, 2018, doi: 10.1109/ECCE.2018.8558245.
- [74] A. Plotkowski, K. Carver, F. List, J. Pries, Z. Li, A. M. Rossy, and D. Leonard, "Design and performance of an additively manufactured high-Si transformer core," *Mater. Des.*, vol. 194, 2020, doi: 10.1016/j.matdes.2020.108894.
- [75] H. A. Khazdozian, J. S. Manzano, K. Gandha, I. I. Slowing, and I. C. Nlebedim, "Recycled Sm-Co bonded magnet filaments for 3D printing of magnets," *AIP Adv.*, vol. 8, no. 5, 2018, doi: 10.1063/1.5007669.
- [76] E. M. H. White, A. G. Kassen, E. Simsek, W. Tang, R. T. Ott, and I. E. Anderson, "Net Shape Processing of Alnico Magnets by Additive Manufacturing," *IEEE Trans. Magn.*, vol. 53, no. 11, Nov. 2017, doi: 10.1109/TMAG.2017.2711965.
- [77] E. M. Palmero, D. Casaleiz, N. A. Jimenez, J. Rial, J. De Vicente, A. Nieto, R. Altimira, and A. Bollero, "Magnetic-polymer composites for bonding and 3d printing of permanent magnets," *IEEE Trans. Magn.*, vol. 55, no. 2, Feb. 2019, doi: 10.1109/TMAG.2018.2863560.
- [78] T. Hanemann, D. Syperek, and D. Nötzel, "3D printing of ABS barium ferrite composites," *Materials (Basel)*, vol. 13, no. 6, p. 1481, Mar. 2020, doi: 10.3390/ma13061481.
- [79] J. Jaćimović, F. Binda, L. G. Herrmann, F. Greuter, J. Genta, M. Calvo, T. Tomše, and R. A. Simon, "Net Shape 3D Printed NdFeB Permanent Magnet," *Adv. Eng. Mater.*, vol. 19, no. 8, pp. 1–7, 2017, doi: 10.1002/adem.201700098.

- [80] A. B. Baldissera, P. Pavez, P. A. P. Wendhausen, C. H. Ahrens, and J. M. Mascheroni, "Additive Manufacturing of Bonded Nd-Fe-B - Effect of Process Parameters on Magnetic Properties," *IEEE Trans. Magn.*, vol. 53, no. 11, Nov. 2017, doi: 10.1109/TMAG.2017.2715722.
- [81] M. P. Paranthaman, C. S. Shafer, A. M. Elliott, D. H. Siddel, M. A. McGuire, R. M. Springfield, J. Martin, R. Fredette, and J. Ormerod, "Binder Jetting: A Novel NdFeB Bonded Magnet Fabrication Process," *Jom*, vol. 68, no. 7, pp. 1978–1982, 2016, doi: 10.1007/s11837-016-1883-4.
- [82] C. Huber, C. Abert, F. Bruckner, M. Groenefeld, O. Muthsam, S. Schuschnigg, K. Sirak, R. Thanhoffer, I. Teliban, C. Vogler, R. Windl, and D. Suess, "3D print of polymer bonded rare-earth magnets, and 3D magnetic field scanning with an end-user 3D printer," *Appl. Phys. Lett.*, vol. 109, no. 16, 2016, doi: 10.1063/1.4964856.
- [83] A. Shen, C. P. Bailey, A. W. K. Ma, and S. Dardona, "UV-assisted direct write of polymer-bonded magnets," *J. Magn. Magn. Mater.*, vol. 462, pp. 220–225, 2018, doi: 10.1016/j.jmmm.2018.03.073.
- [84] C. Huber, C. Abert, F. Bruckner, M. Groenefeld, S. Schuschnigg, I. Teliban, C. Vogler, G. Wautischer, R. Windl, and Di. Suess, "3D Printing of Polymer-Bonded Rare-Earth Magnets with a Variable Magnetic Compound Fraction for a Predefined Stray Field," *Sci. Rep.*, vol. 7, no. 1, pp. 1–8, 2017, doi: 10.1038/s41598-017-09864-0.
- [85] B. G. Compton, J. W. Kemp, T. V. Novikov, R. C. Pack, C. I. Nlebedim, C. E. Duty, O. Rios, and M. P. Paranthaman, "Direct-write 3D printing of NdFeB bonded magnets," *Mater. Manuf. Process.*, vol. 33, no. 1, pp. 109–113, 2018, doi: 10.1080/10426914.2016.1221097.
- [86] L. Li, K. Jones, B. Sales, J. L. Pries, I. C. Nlebedim, K. Jin, H. Bei, B. K. Post, M. S. Kesler, O. Rios, V. Kunc, R. Fredette, J. Ormerod, A. Williams, T. A. Lograsso, and M. P. Paranthaman, "Fabrication of highly dense isotropic Nd-Fe-B nylon bonded magnets via extrusion-based additive manufacturing," *Addit. Manuf.*, vol. 21, no. July 2017, pp. 495–500, 2018, doi: 10.1016/j.addma.2018.04.001.
- [87] L. Li, A. Tirado, I. C. Nlebedim, O. Rios, B. Post, V. Kunc, R. R. Lowden, E. Lara-Curzio, R. Fredette, J. Ormerod, T. A. Lograsso, and M. P. Paranthaman, "Big Area Additive Manufacturing of High Performance Bonded NdFeB Magnets," *Sci. Rep.*, vol. 6, no. October, pp. 1–7, 2016, doi: 10.1038/srep36212.
- [88] J. Wu, N. T. Aboulkhair, M. Degano, I. Ashcroft, and R. J. M. Hague, "Process-structure-property relationships in laser powder bed fusion of permanent magnetic Nd-Fe-B," *Mater. Des.*, vol. 209, no. July, p. 109992, 2021, doi: 10.1016/j.matdes.2021.109992.
- [89] E. White, E. Rinko, T. Prost, T. Horn, C. Ledford, C. Rock, and I. Anderson, "Processing of Alnico Magnets by additive manufacturing," *Appl. Sci.*, vol. 9, no. 22, 2019, doi: 10.3390/app9224843.
- [90] D. Goll, F. Trauter, T. Bernthaler, J. Schanz, H. Riegel, and G. Schneider, "Additive manufacturing of bulk nanocrystalline fendb based permanent magnets," *Micromachines*, vol. 12, no. 5, 2021, doi: 10.3390/mi12050538.
- [91] J. Slapnik, I. Pulko, R. Rudolf, I. Anžel, and M. Brunčko, "Fused filament fabrication of Nd-Fe-B bonded magnets: Comparison of PA12 and TPU matrices," *Addit. Manuf.*, vol. 38, 2021, doi: 10.1016/j.addma.2020.101745.

- [92] K. Gandha, L. Li, I. C. Nlebedim, B. K. Post, V. Kunc, B. C. Sales, J. Bell, and M. P. Paranthaman, "Additive manufacturing of anisotropic hybrid NdFeB-SmFeN nylon composite bonded magnets," *J. Magn. Magn. Mater.*, vol. 467, no. June, pp. 8–13, 2018, doi: 10.1016/j.jmmm.2018.07.021.
- [93] T. Rautio, A. Hamada, J. Kumpula, A. Järvenpää, and T. Allam, "Enhancement of electrical conductivity and corrosion resistance by silver shell-copper core coating of additively manufactured AlSi10Mg alloy," *Surf. Coatings Technol.*, vol. 403, no. September, p. 126426, 2020, doi: 10.1016/j.surfcoat.2020.126426.
- [94] P. Frigola, O. Harrysson, T. Horn, H. West, R. Aman, J. Rigsbee, D. Ramirez, F. Medina, R. Wicker, and E. Rodriguez, "Fabricating Copper Components with Electron Beam Melting," *Adv. Mater. Process.*, p. 20, 2014.
- [95] A. Yegyan Kumar, J. Wang, Y. Bai, S. T. Huxtable, and C. B. Williams, "Impacts of process-induced porosity on material properties of copper made by binder jetting additive manufacturing," *Mater. Des.*, vol. 182, p. 108001, 2019, doi: 10.1016/j.matdes.2019.108001.
- [96] S. D. Jadhav, S. Dadbakhsh, L. Goossens, J. P. Kruth, J. Van Humbeeck, and K. Vanmeensel, "Influence of selective laser melting process parameters on texture evolution in pure copper," *J. Mater. Process. Technol.*, vol. 270, no. February, pp. 47–58, 2019, doi: 10.1016/j.jmatprotec.2019.02.022.
- [97] S. J. Raab, R. Guschlbauer, M. A. Lodes, and C. Körner, "Thermal and Electrical Conductivity of 99.9% Pure Copper Processed via Selective Electron Beam Melting," *Adv. Eng. Mater.*, vol. 18, no. 9, pp. 1661–1666, Sep. 2016, doi: 10.1002/adem.201600078.
- [98] C. Silbernagel, L. Gargalis, I. Ashcroft, R. Hague, M. Galea, and P. Dickens, "Electrical resistivity of pure copper processed by medium-powered laser powder bed fusion additive manufacturing for use in electromagnetic applications," *Addit. Manuf.*, vol. 29, no. July, p. 100831, 2019, doi: 10.1016/j.addma.2019.100831.
- [99] R. Guschlbauer, S. Momeni, F. Osmanlic, and C. Körner, "Process development of 99.95% pure copper processed via selective electron beam melting and its mechanical and physical properties," *Mater. Charact.*, vol. 143, no. March, pp. 163–170, 2018, doi: 10.1016/j.matchar.2018.04.009.
- [100] S. Zhang, H. Zhu, L. Zhang, W. Zhang, H. Yang, and X. Zeng, "Microstructure and properties of high strength and high conductivity Cu-Cr alloy components fabricated by high power selective laser melting," *Mater. Lett.*, vol. 237, pp. 306–309, 2019, doi: 10.1016/j.matlet.2018.11.118.
- [101] A. P. Ventura, C. J. Marvel, G. Pawlikowski, M. Bayes, M. Watanabe, R. P. Vinci, and W. Z. Misiolek, "The Effect of Aging on the Microstructure of Selective Laser Melted Cu-Ni-Si," *Metall. Mater. Trans. A Phys. Metall. Mater. Sci.*, vol. 48, no. 12, pp. 6070–6082, 2017, doi: 10.1007/s11661-017-4363-8.
- [102] M. Abdelhafiz, K. S. Al-Rubaie, A. Emadi, and M. A. Elbestawi, "Process–Structure–Property Relationships of Copper Parts Manufactured by Laser Powder Bed Fusion," *Materials (Basel)*, vol. 14, no. 11, p. 2945, May 2021, doi: 10.3390/ma14112945.
- [103] Y. Shi, P. Rometsch, K. Yang, F. Palm, and X. Wu, "Characterisation of a novel Sc and Zr modified Al–Mg alloy fabricated by selective laser melting," *Mater. Lett.*, vol. 196, pp. 347–350, 2017, doi: 10.1016/j.matlet.2017.03.089.

- [104] S. D. Jadhav, L. R. Goossens, Y. Kinds, B. Van Hooreweder, and K. Vanmeensel, "Laser-based powder bed fusion additive manufacturing of pure copper," *Addit. Manuf.*, vol. 42, no. February, 2021, doi: 10.1016/j.addma.2021.101990.
- [105] T. Wegener, J. Koopmann, J. Richter, P. Krooß, and T. Niendorf, "CuCrZr processed by laser powder bed fusion—Processability and influence of heat treatment on electrical conductivity, microstructure and mechanical properties," *Fatigue Fract. Eng. Mater. Struct.*, vol. 44, no. 9, pp. 2570–2590, 2021, doi: 10.1111/ffe.13527.
- [106] S. D. Jadhav, J. Vleugels, J. P. Kruth, J. Van Humbeeck, and K. Vanmeensel, "Mechanical and electrical properties of selective laser-melted parts produced from surface-oxidized copper powder," *Mater. Des. Process. Commun.*, vol. 2, no. 2, pp. 1–8, 2020, doi: 10.1002/mdp2.94.
- [107] S. D. Jadhav, S. Dadbakhsh, J. Vleugels, J. Hofkens, P. Van Puyvelde, S. Yang, J. P. Kruth, J. Van Humbeeck, and K. Vanmeensel, "Influence of carbon nanoparticle addition (and impurities) on selective laser melting of pure copper," *Materials (Basel)*, vol. 12, no. 15, 2019, doi: 10.3390/ma12152469.
- [108] D. Tiberto, U. E. Klotz, F. Held, and G. Wolf, "Additive manufacturing of copper alloys: influence of process parameters and alloying elements," *Mater. Sci. Technol. (United Kingdom)*, vol. 35, no. 8, pp. 969–977, 2019, doi: 10.1080/02670836.2019.1600840.
- [109] S. D. Jadhav, D. Fu, M. Deprez, K. Ramharter, D. Willems, B. Van Hooreweder, and K. Vanmeensel, "Highly conductive and strong CuSn0.3 alloy processed via laser powder bed fusion starting from a tin-coated copper powder," *Addit. Manuf.*, vol. 36, no. August, p. 101607, 2020, doi: 10.1016/j.addma.2020.101607.
- [110] S. Zhang, H. Zhu, Z. Hu, X. Zeng, and F. Zhong, "Selective Laser Melting of Cu–10Zn alloy powder using high laser power," *Powder Technol.*, vol. 342, pp. 613–620, 2019, doi: 10.1016/j.powtec.2018.10.002.
- [111] S. Gruber, L. Stepien, E. López, F. Brueckner, and C. Leyens, "Physical and geometrical properties of additively manufactured pure copper samples using a green laser source," *Materials (Basel)*, vol. 14, no. 13, 2021, doi: 10.3390/ma14133642.
- [112] C. Silbernagel, I. Ashcroft, P. Dickens, and M. Galea, "Electrical resistivity of additively manufactured AlSi10Mg for use in electric motors," *Addit. Manuf.*, vol. 21, pp. 395–403, May 2018, doi: 10.1016/J.ADDMA.2018.03.027.
- [113] O. Gutfleisch, M. A. Willard, E. Brück, C. H. Chen, S. G. Sankar, and J. P. Liu, "Magnetic materials and devices for the 21st century: Stronger, lighter, and more energy efficient," *Adv. Mater.*, vol. 23, no. 7, pp. 821–842, 2011, doi: 10.1002/adma.201002180.
- [114] B. M. Ma, J. W. Herchenroeder, B. Smith, M. Suda, D. Brown, and Z. Chen, "Recent development in bonded NdFeB magnets," *J. Magn. Magn. Mater.*, vol. 239, no. 1–3, pp. 418–423, 2002, doi: 10.1016/S0304-8853(01)00609-6.
- [115] A. Kallaste, T. Vaimann, and A. Belahcen, "Influence of magnet material selection on the design of slow-speed permanent magnet synchronous generators for wind applications," *Elektron. ir Elektrotehnika*, vol. 23, no. 1, pp. 31–38, 2017, doi: 10.5755/j01.eie.23.1.17581.
- [116] M. S. Kang, K. M. Kim, H. W. Kwon, D. H. Kim, J. G. Lee, and K. H. Shin, "Electrical resistivity and magnetic performance of ceramics-bonded nd-fe-b-type magnet consolidated using dielectric oxide binder," *IEEE Trans. Magn.*, vol. 55, no. 7, Jul. 2019, doi: 10.1109/TMAG.2019.2896889.

- [117] N. Simpson, D. J. North, S. M. Collins, and P. H. Mellor, "Additive Manufacturing of Shaped Profile Windings for Minimal AC Loss in Electrical Machines," *IEEE Trans. Ind. Appl.*, vol. 56, no. 3, pp. 2510–2519, May 2020, doi: 10.1109/TIA.2020.2975763.
- [118] N. Simpson and P. H. Mellor, "Additive manufacturing of shaped profile windings for minimal AC loss in gapped inductors," *2017 IEEE Int. Electr. Mach. Drives Conf. IEMDC 2017*, no. 1, pp. 1–7, 2017, doi: 10.1109/IEMDC.2017.8002337.
- [119] J. Jung, A. Helm, and J. Liebold, "Improved Efficiency of Electric Drives with Additively Manufactured Roebel Bar Windings," *MTZ Worldw.*, vol. 82, no. 4, pp. 54–58, 2021, doi: 10.1007/s38313-021-0634-2.
- [120] W. Sixel, M. Liu, G. Nellis, and B. Sarlioglu, "Ceramic 3-D Printed Direct Winding Heat Exchangers for Thermal Management of Concentrated Winding Electric Machines," *IEEE Trans. Ind. Appl.*, vol. 57, no. 6, pp. 5829–5840, 2021, doi: 10.1109/TIA.2021.3104273.
- [121] R. Wrobel, B. Scholes, A. Hussein, R. Law, A. Mustaffar, and D. Reay, "A metal additively manufactured (MAM) heat exchanger for electric motor thermal control on a high-altitude solar aircraft – Experimental characterisation," *Therm. Sci. Eng. Prog.*, vol. 19, no. July, p. 100629, 2020, doi: 10.1016/j.tsep.2020.100629.
- [122] C. Wohlers, P. Juris, S. Kabelac, and B. Ponick, "Design and direct liquid cooling of tooth-coil windings," *Electr. Eng.*, vol. 100, no. 4, pp. 2299–2308, 2018, doi: 10.1007/s00202-018-0704-x.
- [123] S. Tumanski, *Handbook of magnetic measurements*. Boca Raton, USA: CRC Press, 2011. doi: 10.1201/b10979.
- [124] H. IGARASHI and K. OKAZAKI, "Effects of Porosity and Grain Size on the Magnetic Properties of NiZn Ferrite," *J. Am. Ceram. Soc.*, vol. 60, no. 1–2, pp. 51–54, Jan. 1977, doi: 10.1111/J.1151-2916.1977.TB16092.X.
- [125] A. Goldman, *Handbook of Modern Ferromagnetic Materials*. Springer US, 1999. doi: 10.1007/978-1-4615-4917-8.
- [126] L. Li, "Stress effects on ferromagnetic materials: investigation of stainless steel and nickel," *Retrospect. Theses Diss.*, 2004, [Online]. Available: <https://lib.dr.iastate.edu/rtd/1179/>
- [127] A. Krings, M. Cossale, A. Tenconi, J. Soulard, A. Cavagnino, and A. Boglietti, "Magnetic materials used in electrical machines: A comparison and selection guide for early machine design," *IEEE Ind. Appl. Mag.*, vol. 23, no. 6, pp. 21–28, 2017, doi: 10.1109/MIAS.2016.2600721.
- [128] G. Ouyang, X. Chen, Y. Liang, C. Macziewski, and J. Cui, "Review of Fe-6.5 wt%Si high silicon steel—A promising soft magnetic material for sub-kHz application," *J. Magn. Magn. Mater.*, vol. 481, no. January, pp. 234–250, 2019, doi: 10.1016/j.jmmm.2019.02.089.
- [129] J. S. Galsin, "Physical Effects of Impurities in Metals," *Impurity Scatt. Met. Alloy.*, pp. 93–123, 2002, doi: 10.1007/978-1-4615-1241-7_5.
- [130] A. Belahcen, P. Rasilo, and A. Arkkio, "Segregation of iron losses from rotational field measurements and application to electrical machine," *IEEE Trans. Magn.*, vol. 50, no. 2, 2014, doi: 10.1109/TMAG.2013.2284606.
- [131] D. Hawezy, "The influence of silicon content on physical properties of non-oriented silicon steel," <https://doi.org/10.1080/02670836.2017.1295519>, vol. 33, no. 14, pp. 1560–1569, Sep. 2017, doi: 10.1080/02670836.2017.1295519.

- [132] A. E. Wilson-Heid, T. C. Novak, and A. M. Beese, "Characterization of the Effects of Internal Pores on Tensile Properties of Additively Manufactured Austenitic Stainless Steel 316L", doi: 10.1007/s11340-018-00465-0.
- [133] W. J. Sames, F. A. List, S. Pannala, R. R. Dehoff, and S. S. Babu, "The metallurgy and processing science of metal additive manufacturing FULL CRITICAL REVIEW The metallurgy and processing science of metal additive manufacturing," 2016, doi: 10.1080/09506608.2015.1116649.
- [134] N. Hansen, "Hall-petch relation and boundary strengthening," *Scr. Mater.*, vol. 51, no. 8 SPEC. ISS., pp. 801–806, 2004, doi: 10.1016/j.scriptamat.2004.06.002.
- [135] D. Raabe, "Recovery and Recrystallization: Phenomena, Physics, Models, Simulation," *Phys. Metall. Fifth Ed.*, vol. 1, pp. 2291–2397, Jan. 2014, doi: 10.1016/B978-0-444-53770-6.00023-X.
- [136] H. Tiismus, A. Kallaste, T. Vaimann, L. Lind, I. Virro, A. Rassõlkin, and T. Dedova, "Laser Additively Manufactured Magnetic Core Design and Process for Electrical Machine Applications," *Energies*, vol. 15, no. 10, 2022, doi: <https://doi.org/10.3390/en15103665>.
- [137] M. Sarap, S. Member, A. Kallaste, S. Member, P. S. Ghahfarokhi, H. Tiismus, S. Member, T. Vaimann, and S. Member, "The effect of build direction on the thermal conductivity of additively manufactured AlSi 10 Mg and silicon-steel samples," 2022.
- [138] "DC Magnetization Curves of Soft Magnetic Materials:Finite Element Method Magnetics." <https://www.femm.info/wiki/SoftMagneticMaterials> (accessed Mar. 28, 2022).
- [139] Hoganas, "Material data_Somaloy." www.hoganas.com/electromagnetic (accessed Jun. 09, 2020).
- [140] "EVS-EN 10106:2015 - Cold rolled non-oriented electrical steel strip and sheet delivered in the fully processed state." Accessed: Apr. 25, 2022. [Online]. Available: <https://www.evs.ee/et/evs-en-10106-2015>
- [141] M. Shiozaki and Y. Kurosaki, "The effects of grain size on the magnetic properties of nonoriented electrical steel sheets," *J. Mater. Eng.*, vol. 11, no. 1, pp. 37–43, 1989, doi: 10.1007/BF02833752.
- [142] H. Tiismus, A. Kallaste, A. Belahcen, M. Tarraste, T. Vaimann, A. Rassõlkin, B. Asad, and P. S. Ghahfarokhi, "AC Magnetic Loss Reduction of SLM Processed Fe-Si for Additive Manufacturing of Electrical Machines," pp. 1–14, 2021.
- [143] "Data sheet of isovac 400 - 50 A." Accessed: Mar. 14, 2021. [Online]. Available: https://www.voestalpine.com/stahl/content/download/4542/file/DB_isovac_400-50A_E_280715.pdf?inLanguage=eng-GB
- [144] R. M. Bozorth, *Ferromagnetism*. Wiley-IEEE Press, 1993.
- [145] G. Ouyang, X. Chen, Y. Liang, C. Macziewski, and J. Cui, "Review of Fe-6.5 wt%Si high silicon steel—A promising soft magnetic material for sub-kHz application," *J. Magn. Magn. Mater.*, vol. 481, no. October 2018, pp. 234–250, 2019, doi: 10.1016/j.jmmm.2019.02.089.
- [146] H. Tiismus, A. Kallaste, M. Usman Naseer, M. U. Naseer, T. Vaimann, and A. Rassolkin, "Design and Performance of Laser Additively Manufactured Core Induction Motor," *IEEE Access*, vol. XX, pp. 50137–50152, 2022, doi: 10.1109/ACCESS.2022.3173317.

- [147] H. Tiismus, A. Kallaste, A. Belahcen, A. Rassolkin, T. Vaimann, and P. Shams Ghahfarokhi, "Additive Manufacturing and Performance of E-Type Transformer Core," *Energies*, vol. 14, no. 11, p. 3278, Jun. 2021, doi: 10.3390/en14113278.
- [148] "Block - PCB Transformers." <http://www.farnell.com/datasheets/1897307.pdf> (accessed Mar. 01, 2021).
- [149] "Block - FL 30/12 Safety isolating transformer." https://www.block.eu/en_US/productversion/fl-3012/ (accessed Mar. 01, 2021).
- [150] J. Pyrhönen, T. Jokinen, and V. Hrabovcová, *Design of Rotating Electrical Machines*. Hoboken, USA: John Wiley & Sons, Ltd, 2008. doi: 10.1002/9780470740095.
- [151] Felandia, "Elektrimootor 0,06kW/1500 p/min MS 561-4 B34; IE1; IP55; 230/400V." https://www.felandia.eu/media/veelandia/product/eu.erply.com/1052-ms-561-4-0-06_tehnilised_andmed_v1.pdf (accessed May 09, 2022).
- [152] "Low voltage General performance IE2 high efficiency motors." <https://manualzz.com/doc/13816422/abb-all-ie2> (accessed Feb. 17, 2022).
- [153] "Building and Testing a 3D Printed Brushless Motor (until it explodes!)." <https://www.rs-online.com/designspark/building-and-testing-a-3d-printed-brushless-motor-until-it-explodes> (accessed Mar. 03, 2022).
- [154] L. Gargalis, V. Madonna, P. Giangrande, S. Member, R. Rocca, M. Hardy, I. A. N. Ashcroft, M. Galea, S. Member, and R. Hague, "Additive Manufacturing and Testing of a Soft Magnetic Rotor for a Switched Reluctance Motor," vol. 8, 2020, doi: 10.1109/ACCESS.2020.3037190.

Acknowledgements

I would like to thank my family, co-workers and supervisors for their support and advice on this journey. Without you this wouldn't have been possible, as I would have surely lost the motivation and the drive long long ago. In parallel, special thanks to my wife and newborn daughter, for reminding me (constantly) that there is more to life than research work. On more practical notes, this work was made possible by the Estonian government, through financial funding by start-up grant PSG-137.

Abstract

Production and Properties of Additively Manufactured Electrical Machine Cores

This work is focused on the methodological development of laser additive manufacturing of soft magnetic cores. The project was started at 2018, with little prior knowledge of the peculiarities of the L-PBF fusion mechanisms and metallurgical processes. The field itself was in its infancy at that time, with a few sparse initial attempts in fusing soft magnetic cores or electrical motor components. Thus, the main goal of this work was to provide a firm foundation of methodological understanding and printing expertise that the future work on additive manufacturing of topology-optimized electrical machines and their components can be built upon. This is the main future goal, to produce superior EMs to conventional machines in the future through the introduction of highly refined and intricate topologies. The thesis is supported by three major pillars of study. First, a literature survey was conducted to map the current material quality level for the 3D printed material involved in the active parts in electrical motors: the soft magnetic, hard magnetic, and electrically conductive. It was determined that the maturity level of AM electrical conductors is ready for commercial applications, albeit for niche applications at the moment, due to the difficulties in forming insulation layers during a print job. The same issue plagues printed soft magnetic cores, which significantly lose in their energy efficiency due to some siphoned into the eddy current generation. Secondly, a thorough analysis was conducted on the L-PBF printing process when fusing 3.7% silicon content steel. This work included the literature survey on the causalities behind poor material magnetic properties, based on which a workflow was proposed to address these concerns. The material preparation process was successful; properties not far from standard materials for magnetic flux guides were achieved. The last part of the thesis was to take the printing process to a larger level: to print full core components for actual electromagnetic devices. This was both to gather knowledge on what additional considerations should be taken into account when advancing from printing small material characterization samples into printing full cores; and to establish the current state of the art: what can we expect from functional printed EM cores performance-wise. The printed cores exhibited somewhat lower characteristics than their commercial counterparts, but that was unsurprising, as the built prototypes were the first of their kind. The future work on this project is the application of the acquired expertise and material mapping data to design novel machines with novel shaping of magnetic flux, thermal flux, or electric current conductors. Likely, AM electrical machines will remain a niche product until multi-material metal printing systems establish themselves on a larger scale. Considering the rate of the development of additive manufacturing systems, it is feasible that AM motors can reach mainstream in the next 50 years.

Lühikokkuvõte

Kihltisandus meetodil valmistatud elektrimasinate magnetsüdamikud ja nende omadused

Käesolev töö keskendub pehmete magnetiliste südamike laser kihltisandustootmise (AM) meetodilisele arendamisele. Projekti alustati 2018. aastal, mil oli vähe eelteadmisi L-PBF-sulatusmehhanismide ja metallurgiliste protsesside eripäradest. Valdkond oli sel ajal lapsekingades, oli mõni üksik katsetus magnetsüdamike või elektrimootorite komponentide sulatamisel. Seega oli selle töö peamine eesmärk luua kindel alus meetodilisele arusaamisele ja printimise alastele teadmiste, millele saab tulevikus rajada topoloogiliselt optimeeritud elektrimasinate ja nende komponentide kihtkisandustootmise alase töö. See on projekti peamine tulevikueesmärk, et tulevikus toota tavapärastest masinatest paremaid elektrimasinaid läbi keeruliste vormide ehk topoloogiate kasutuselevõtu. Doktoritöö toetub kolmele peamisele uurimissambale. Esiteks viidi läbi kirjandusuuring, et kaardistada elektrimootorite aktiivsetes osades kasutatavate prinditud materjalide praegune kvaliteeditase: nendeks materjalideks olid pehme magnetiline, kõva magnetiline ja elektrijuht materjalid. Tehti kindlaks, et AM-elektrijuhtide küpsusaste on valmis kaubanduslikuks kasutamiseks, kuigi praegu vaid niširakenduste jaoks, kuna isolatsioonikihtide moodustamine printimise käigus on keeruline. Sama probleem vaevab prinditud pehmeid magnetilisi südamikke, mis kaotavad oluliselt oma energiatõhususes pöörisvoolude tõttu. Teiseks analüüsiti põhjalikult L-PBF printimise protsessi 3,7% ränisisaldusega terase sulatamisel. See töö hõlmas kirjandusuuringut materjali kehvade magnetiliste omaduste taga olevate põhjuste kohta, mille põhjal pakuti välja tööprotsess nende probleemide lahendamiseks. Materjali ettevalmistusprotsess oli edukas, saavutati omadused, mis ei ole kaugel standardsetest magnetsüdamike materjalidest. Lõputöö viimane osa oli viia printimisprotsess suuremale tasandile: valmistada funktsionaalsed elektronmagnetilised seadmed täielikult prinditud magnetsüdamikega. Sellega sooviti koguda teadmisi lisakaalutluste mida arvesse võtta, kui liigutakse väikeste materjali iseloomustavate näidiste printimisest edasi täielike magnetsüdamikeni; ning paralleelselt kindlaks teha ka tehnoloogia hetkeseis: mida võime oodata prinditud südamikega funktsionaalsete seadmete jõudlusest. Mõõdeti mõnevõrra madalamaid näitajaid kui nende kaubanduslikel analoogidel, kuid see ei olnud üllatav, sest töös valmisid esimesed omalaadsed prototüübid. Selle projekti edasine töö on omandatud teadmiste ja kaardistatud materjalide andmete rakendamine edasisteks arvutusteks mootorite magnetvoo, soojusvoo või elektrivoolu juhtide kuju optimeerimiseks. Tõenäoliselt jäävad 3D prinditud elektrimasinad esialgu nišitooteks, kuni mitme materjali paralleelne kvaliteetne printimine saab kiireks ja kättesaadavaks. Võttes arvesse kihltisandus-tehnoloogial põhinevate tootmissüsteemide arengukiirust, on võimalik, et AM-mootorid jõuavad peavoolu järgmise 50 aasta jooksul

Appendix

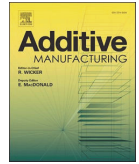
Publication I

H. Tiismus, A. Kallaste, T. Vaimann, and A. Rassõlkin, "State of the Art of Additively Manufactured Electromagnetic Materials for Topology Optimized Electrical Machines," *Addit. Manuf.*, vol. 55, no. July 2022, doi: 10.1016/j.addma.2022.102778.



Contents lists available at ScienceDirect

Additive Manufacturing

journal homepage: www.elsevier.com/locate/addma

Review

State of the art of additively manufactured electromagnetic materials for topology optimized electrical machines

Hans Tiismus^{*}, Ants Kallaste, Toomas Vaimann, Anton Rassõlkin

Tallinn University of Technology, Ehitajate tee 5, Tallinn 19086, Estonia

ARTICLE INFO

Keywords:

Additive manufacturing
Electrical machines
Soft magnetic materials
Hard magnetic materials
Conductors

ABSTRACT

Metal additive manufacturing (AM) technology is maturing. Although currently slower and less reliable than traditional production methods, AM systems shine when producing parts with unconventional topologies or in small quantities. Like countless other research communities, the electrical machine (EM) research community has shifted considerable efforts towards integrating AM systems into the EM production cycle to implement more powerful and efficient topology optimized (TO) next-generation EMs. In this paper, the state-of-the-art printing of soft magnetic, hard magnetic, and electrically conductive materials was investigated to evaluate the maturity of each material type for integration into EM construction. The highest maturity was identified for AM pure copper, showing characteristics equivalent to commercial high purity copper. In contrast, AM permanent magnets were the least mature: suffering from low power density and limited magnetization capacities. Printed soft magnetic steels were characterized as halfway in-between: on one side showing equivalent DC magnetic properties to conventional non-oriented steels, but on the other – suffering from high eddy current losses in AC applications. Based on the study's findings, it would appear that the emergence of additively manufactured EMs is only a matter of time. We predict a dramatic increase in the printing of prototype TO components within the next few years, focusing most likely on TO machine windings, heat exchangers, and synchronous rotors.

1. Introduction

1.1. Electrical machines

Electrical machines are the workhorses of modern society. They are built in virtually all scales: ranging from small (*mW* or *W* scale) or medium domestic machines (*kW* scale) we use daily, up to large machines (*MW* scale) for more specialized industrial, propulsion, or electrical power generation purposes. EMs, through electro-mechanical conversion, produce virtually all the electric power on Earth. In EU 2019, solar energy constituted only 4.4% of total electricity produced, with all the other sources involving electro-mechanical conversion (nuclear, wind, hydro, geothermal, and thermal powerplants) [1]. Electric motors for industrial applications use more than 40% of the total energy produced worldwide: a rough estimate of half a billion industrial electric motors are installed, and the amount is increasing by 15% annually [2]. As the EMs are so heavily utilized, the sizeable electrical machine research community is continuously developing the EM designs further: driven by specific application requirements, technological advancements, or

political directives. Presently signed EU directives obligate the efficiency class IE3 or better for all electric motors with nominal power of 0.75 up to 1000 kW starting from July 2021. These requirements are further raised to IE4 or better for motors between 75 and 200 kW after two years (April 2020 amendment to the EnEV). Constructing EMs satisfying these new standards is a challenging task, as only 2% additional gain in machine efficiency, from 92% to 94%, would mean a 25% further reduction in machine energy losses [3].

Arguably, the development of new materials and their industrial integration through next-generation production methods has had the most significant impact on electrical machine performance overall. Materials define the practical limits of the machines, whereas other research fields (control, design, optimization) – allow for the fine-tuning of the machine performance and their implementation for a specific application. Increasingly reliable insulation materials, more effective electrical and magnetic conductors, new permanent magnet alloys, and cost-effective manufacturing and processing methods allow realizing more powerful and complex machine designs available to the end consumer. Unfortunately, significant breakthroughs in EM materials have

^{*} Corresponding author.

E-mail address: hans.tiismus@taltech.ee (H. Tiismus).

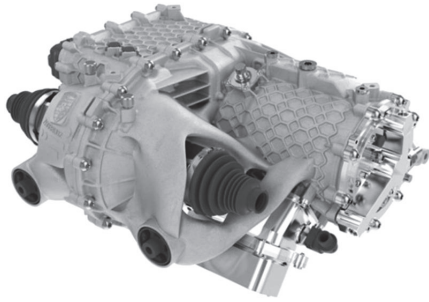


Fig. 1.1. 3D printed electrical drive housing by Porsche [4].

not been made in the recent past. The materials exhibit finite electromagnetic properties: both the magnetic material saturation flux density and the winding materials' electrical conductivity have remained unchanged for the past century and are likely to remain so. A possible solution to this stagnation in EM development has been proposed in novel additive manufacturing methods. AM enables approaching the EM design from a new angle, as previously unfeasible part topologies are finally obtainable.

1.2. Additive manufacturing of electrical machines

Metal additive manufacturing of structural components has matured and found widescale utilization for producing high-performance metallic parts. Currently, the cost per part of AM is still relatively high: it has been most applicable in high-tech industries to produce specialized TO parts. For example, Porsche [4] unveiled its first complete electrical drive housing, shown in Fig. 1.1. The new design boasts double the mechanical strength in heavily stressed areas with only 60% of the traditionally produced housing weight. The AM housing benefits also from a simplified production cycle - requiring less specialized machinery, production steps, and even reduced assembly time of the finished product. Similar successes for metal AM systems have also been reported for astronautic [5] and aerospace [6] sectors – applications where the reduction of every gram is relevant. Consequently, the sales of additive manufacturing systems are expected to triple within the next few years [7].

The unprecedented production freedom of AM systems can potentially also enable the further development of electrical machine designs. Finally, the EM research community has the opportunity to approach the machine design out-of-the-box and introduce previously unfeasible topologies. Conventionally, EMs are constructed from stacked thin layers of laminations: which, while providing effective means for eddy current loss reduction, limit practical machine topologies to relatively simplistic axially symmetric designs. This is primarily due to practical considerations in achieving cost-effective machine core assembly and mechanical integrity of the final stacking. AM would introduce completely new

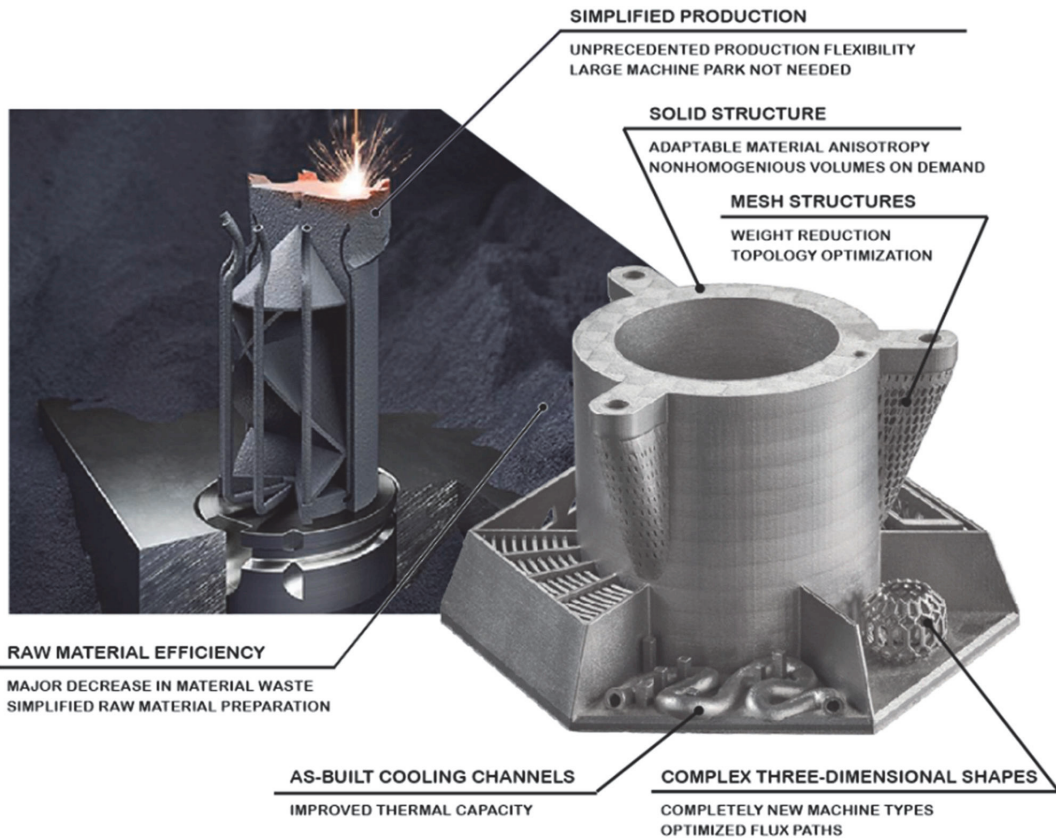


Fig. 1. Summary of AM Possibilities in part design and production (production artwork courtesy Additive Manufacturing Global [27]).

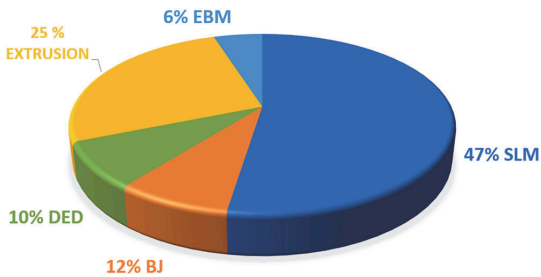


Fig. 1.3. Summary of the AM methods utilized in the reviewed articles describing the preparation and characterization of electromagnetic material properties.

design rules to the machine design, as it operates through a fundamentally different relation in cost, batch size, and product complexity [8]. Some of the well-known advantages of utilizing AM production facilities are illustrated in Fig. 1. While AM has been linked to more flexible and resource-effective small production business models [8], for EMs, the main advantage of AM would arise from its freeform fabrication capacity. Utilizing AM, complex three-dimensional shapes (which can include nonhomogeneous volumes) can be manufactured without significant extra costs involved over printing simple shapes. This means more opportunities for electromagnetic and thermal optimization of the machines: as flux paths and conductors can be shaped three-dimensionally according to the design requirements and more effective passive or active thermal exchangers integrated into the design.

The emerging field of additive manufacturing of electrical machines has its roots in 2013–2015 with the first experimentations and discussions in 3D printing of electro-mechanical systems [9], [10]. The first metal additively manufactured motor components (synchronous rotors) were presented in 2016 [11], [12]. Overviews on the feasibility of AM electrical machines started appearing a few years later (2018–2019) [13], [14], [15]. Up to date, the additive manufacturing of complete electrical machines is yet to be accomplished. Considerable progress, however, has been made in material sciences and individual machine component prototyping. By now, several reviews have been published on the topic. Some of the reviews focus more on novel motor design options: [16], [17], [18], [19]; some on AM magnetic materials: [20], [21], [22], [23]; and some on AM copper: [24], [25], [26].

The main challenges in 3D printing electrical machines can be related to both the printing systems' current limitations and the technically demanding nature of producing EMs in general. Tight tolerances must be met for moving machine parts while printing at least three dissimilar materials in parallel with high quality. Materials involved in EMs are an electrically conductive diamagnetic material for the windings, a soft ferromagnetic material with high electrical resistivity for the core, and a diamagnetic dielectric material for core/coil insulation layers. Although some success in the parallel printing of these materials has been met with extrusion-based methods [28], the extruded electromagnetic material characteristics are well below what can be expected of high-grade commercial materials. At the same time, considerably higher material characteristics are obtainable with dedicated metal printing systems, albeit without the multi-material option. A potential solution to this conundrum lies in the natural evolution of printing technology: dual-metal powder-bed printing systems with selective powder deposition capabilities are now becoming available [29]. The state-of-the-art research of AM electrical machines and electromagnetic materials involves process optimization to obtain the necessary methodical expertise to prepare high-performance AM materials and prototype parts. The optimization of AM processes is a lengthy and complicated procedure due to the inherent capriciousness of AM: they require finely tuned processing parameters to prepare a part with both

the desired dimensions and material characteristics. Excessive energy input, for example, can commonly be linked to part deformation during printing (warping, uneven growth due to balling, delaminations, thermal cracking). In contrast, insufficient energy input has been linked to poor fusion between printed layers/tracks and subsequent undesirable porosity. A similar balance must be determined between a myriad of other printing parameters, including raw material shape/composition, raw material supply rate, printing layer thickness, pre-heating temperature, printing patterns, support patterns, etc. Furthermore, in addition to optimizing printing parameters, the determination of optimal post-printing operations can be critical for the usefulness of the printing parts. These operations can range from thermal, chemical, or mechanical treatments encompassing the whole part or a specific part surface. Despite the highly complicated nature of the optimization of AM processes, considerable progress has been made over the last decade.

1.3. Review scope and overview

This paper presents a literature survey of material properties of additively manufactured electromagnetic materials. These materials, including soft magnetic materials (magnetic flux conduction), hard magnetic materials (magnetic flux enhancement), and electrically conductive materials (generation of magnetic flux), are related to the magnetic circuit of the machine. For AM materials to reach mainstream for EM construction, the printed materials must exhibit at least equivalent or superior properties compared to their commercial counterparts. In the study, the main criteria for evaluation of each material type are material-specific:

- Soft magnetic - core losses (W/kg) and polarization (T) at specific field strength.
- Hard magnetic - coercivity (kA/m) and remanence (T) magnetization.
- Electrically conductive - relative electrical conductivity (% IACS).

A total of 62 academic research articles were identified from the literature, which included all the relevant data necessary for compiling a comparative analysis. Some research was excluded – research with either incomplete data for the survey or with more exotic alloys or a few research items that were overlooked by accident.

The most widely encountered AM method in this study by far (47%) was laser powder bed fusion (L-PBF). This is unsurprising due to its commercial maturity and capacity for fusing high-density, low porosity parts. Excessive porosities in electromagnetic materials have been linked to magnetic domain restriction (especially intragranular porosities [30]) and reduced electron mobility [24]. Nevertheless, a full 25% of the studies included different extrusion-based methods, which are well-known for challenges related to low printed part density. Extrusion methods were utilized most extensively for printing hard magnetic materials. That is, for materials that benefit from nonhomogeneous material structure (increasing material coercivity by the introduction of abundant domain restraining defects). Other common metal printing methods were less represented in the study: with electron beam melting (EBM) constituting for 6% of the total literature analyzed, directed energy deposition (DED) for 10%, and binder jetting (BJ) for 12%. The common AM methods encountered in this study are summarized in Fig. 1.3.

Each of the three investigated material types exhibited one specific alloy, which has received significantly more scientific interest. For soft magnetic materials, this alloy was silicon steel, with 58% of all relevant literature focused on its optimization (with either ~3% or ~6.5% silicon content). In fact, when conducting the survey, we could not find a single article describing AC core losses reduction in non-silicon steel samples, such as Fe-Co, Fe-Ni, or amorphous materials. This is likely due to the recognition of Fe-Si as the material of choice for electrical power devices (almost 80% of the market is occupied by Fe-Si [31]). For Fe-Co



Fig. 1.4. Reference source analysis based on the studied alloy type and publication date.

– the costs involved are significantly higher; for Fe-Ni and amorphous materials – the magnetic saturation is too low, and loss reduction is not relevant at low frequency.

For AM conductive materials, the preferred studied material was high purity copper, with roughly 50% of all literature describing its AM process optimization. This is hardly surprising as copper conductors are the gold standard we can encounter in virtually every industry. Additionally, some instances of aluminum (mainly AlSi10Mg) and copper alloys (CuCrZr, CuNiSi, Cu10Zn, CuCr, CuSn0.3) have been investigated, which generally exhibited improved printability/machinability or mechanical strength at the cost of somewhat lower electrical conductivity.

Lastly, neodymium-based alloys were the most investigated printed hard magnetic materials, constituting 72% of all of the relevant literature reviewed. NdFeB-based permanent magnet alloys (PMs) are in the spotlight, likely due to their high magneto-crystalline anisotropy and the exceptionally high magnetic moments of lanthanide element atoms (e.g., Sm, Nd). This means higher power densities are achievable, even with relatively low fill factors of hard magnetic phase within the magnet. Extruded permanent magnets can be loaded up to ~40–60% of nonmagnetic binding material [23]. Other common hard magnetic materials were also encountered within the literature, with some instances of printed ferrite, AlNiCo, and SmCo studies.

The distributions of both the publication date and studied alloy within the reviewed articles are summarized in Fig. 1.4. Unique compounds with only a single reference are compacted to larger nominators, such as polymer-bound, amorphous, or Cu alloys. The publication time is divided into three larger periods: 2021–2020, 2019–2019 and older articles. Research into AM electromagnetic material properties is a novel topic, as 75% of the articles reviewed have been published within the last four years (2018–2021). The oldest article of the survey was published eight years ago in 2014. Based on the survey, it would appear that the research interest in hard magnetic materials has lowered steadily over the recent years, whereas the interest in electrically conductive and soft magnetic materials has increased substantially.

1.4. Review goals

This review has three major objectives:

- Conduct a comparative analysis of printed electromagnetic material properties: to illustrate the gap, if any remaining, between the conventional and printed materials. Based on the results, the maturity of

each material type for integration in electrical machine construction is evaluated.

- Present the electromagnetic material characteristics available in the academic literature within the same framework – due to the lack of standardization in the field.
- Provide information on the trends and recent advances in the prototyping of additively manufactured components for EMs.

2. Metal additive manufacturing

The idea of incrementally adding material during the manufacturing process to create functional tools and components is perhaps as old as civilization itself: as exemplified by traditional crafting techniques. Additive manufacturing differentiates from these time-worn techniques mainly by the increment scale and spatial accuracy of the added material, which for modern systems are usually in the range of 25–500 μm. Repeatable accuracy on this scale cannot be achieved without fully digitalized production systems, which is why the history of additive manufacturing is relatively short. The earliest description of a modern metal printing system was described in a 1972 patent by A. Ciraud, introducing the concept of metal layer fabrication by selectively melting powders using electron, laser, or plasma beams [32]. In 1979, a powder laser sintering process was presented by Housholder in a patent [33]: discussing sequentially depositing planar layers and solidifying a portion of each layer selectively. Back then, the technology was still not mature enough to complete printing system prototyping. The groundwork for the inception of AM systems was laid through massive leaps in digital computing and robotics in the 1980 s and 90 s. In 1998, Optomec commercialized the very first metal additive manufacturing system – a DED-based printer, followed by a year later with an L-PBF based printing system by SLM Solutions [34]. The following time period saw rapid advances in both the availability and versatility of metal 3D printing systems. In roughly the mid-2010 s, metal additive manufacturing systems were finally starting to reach the mainstream. Previously, they were simply too unreliable and unaffordable for niche commercial applications or scientific work. Consequently, in 2010–2020, the AM industry recorded a remarkable annual growth of 27%, as reported by Wohlers Associates in their annual report on AM trends, outlook, and forecasts [35].

For the AM of electromagnetic materials, four types of printing systems have been utilized the most heavily, as presented in Fig. 1.3. These include powder bed fusion systems (both with electron beam – EB-PBF

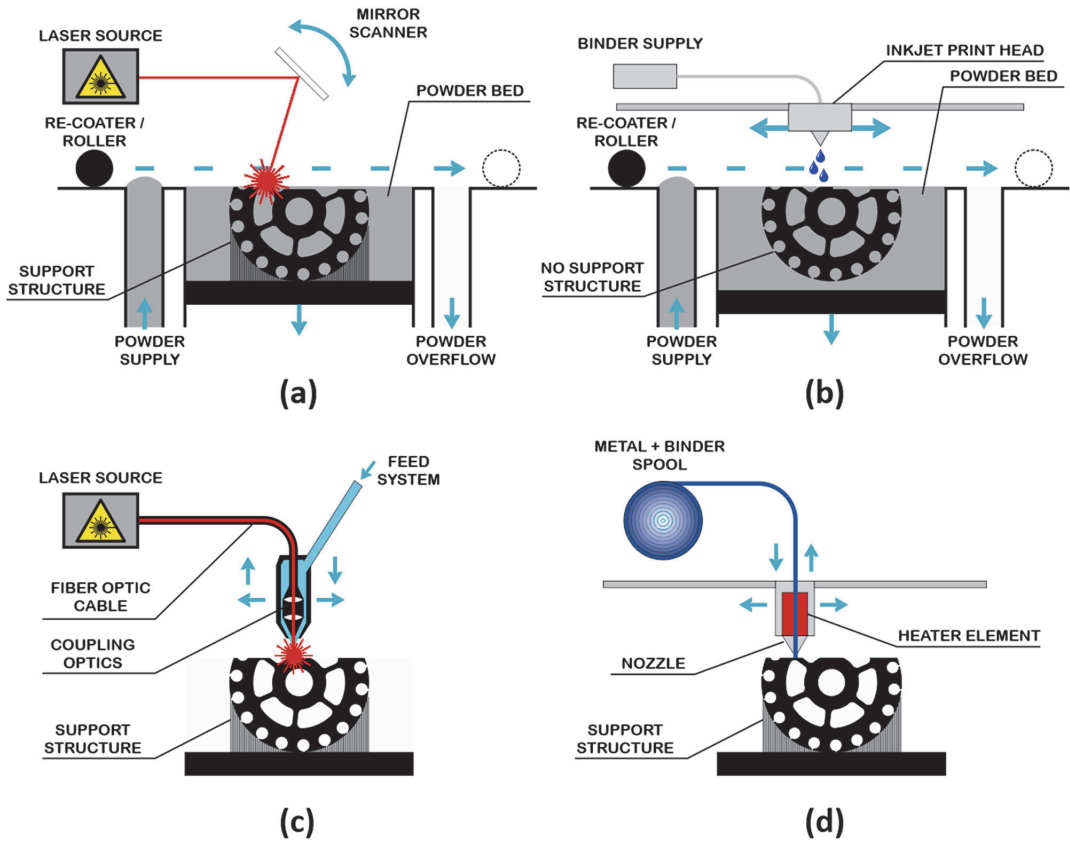


Fig. 2.1. Common metal AM methods: (a) laser powder bed fusion (L - PBF), (b) binder jetting (BJ), (c) directed energy deposition (DED), (d) fuse deposition modelling (FDM).

and laser – L-PBF fusion), binder jetting (BJ), directed energy deposition (DED), and various similar extrusion-based methods (most commonly known as fuse deposition modeling – FDM). The working principles of the methods are described in Fig. 2.1. Both BJ and L/EB-PBF are powder bed-based technologies – where the printed parts are submerged into the powder bed during the printing process one layer at a time. In L/EB-PBF, the raw powder is fused together with an energy beam, in BJ – with a binding agent. In both DED and extrusion-based methods, the printed part can remain fully stationary, while the print head is in three-dimensional motion. In these methods, the raw material is supplied directly by the print head itself: for DED via a pressurized powder / inert gas mixture or a wire feeder, for FDM via a filament of mixed metal particles within a thermoplastic binder agent. Importantly, methods involving binding agents for raw material fusion, like FDM and BJ, require additional post-printing processes. These include debinding and furnace sintering of the green part to remove the binding agents from within the part and to promote metallic phase densification. For a more in-depth comparison, a summary of the advantages and disadvantages of each method is presented in Table 2.1.

3. Additive manufacturing of soft magnetic materials

Soft magnetic materials are used in EM construction for magnetic field conduction. The materials exhibit both high permeability ($> 10^3$ x higher than vacuum) and a narrow hysteresis loop (low coercive field): involving minimal energy for the cyclic magnetization of the material.

For electrical power devices, the three most important characteristics for these materials are low power loss (high efficiency) and high saturation polarization (high power density) at a low material price point. The family of soft magnetic materials is extensive, with a large variation in both cost and performance, as shown in Fig. 3.1. For low switching frequency applications (50–60 Hz), the best balance between these characteristics can be found in crystalline silicon steel alloys. At higher (kHz/MHz) operation frequencies, amorphous and nanocrystalline materials are far superior in terms of losses, justifying their higher cost. Where higher power densities are critical (i.e., aerospace), cobalt-based alloys are often used.

Whether produced through subtractive or additive means, the realization of high-performance soft magnetic materials for EM applications is technically challenging. First, the alloys are primarily composed of ferromagnetic transitional metals (Fe, Co, and Ni) exhibiting high melting points and hardness, which complicates their casting, machining, or printing. Secondly, their magnetic characteristics heavily depend on the material structure: e.g., crystallographic structure, elemental composition, and any residual stresses or impurities present within the materials. The comparison of the soft magnetic material properties obtained by the various research groups is also complicated due to significant variations in the test sample design and measurement methods. The authors have organized the material comparison onto two figures: Fig. 3.2 and Fig. 3.3, summarizing the two material characteristics we consider the most significant: core losses and polarization at specific field strength. Both data sets are compared to the typical values

Table 2.1
Comparison of common metal printing methods.

AM Method	Advantages	Disadvantages
L-PBF	<ul style="list-style-type: none"> • High printed material density – typically >99% for iron alloys [36] • High spatial accuracy – printing resolution up to 15 μm (dependent on the powder and laser spot size) [37]. • Promising future multi-material printing possibilities [29]. 	<ul style="list-style-type: none"> • Low build rate: L-PBF processes are well known for their low build rate. The reported rates are anywhere between 5 (single laser 200 W) [38] to $\sim 90 \text{ cm}^3/\text{h}$ (manufacturer declaration – dual 1 kW lasers [39]). Most of the reported rates in the literature fall somewhere in between. • Printing systems are typically more expensive. • Requires extensive supporting during printing; support removal can be time-consuming and complicated.
DED	<ul style="list-style-type: none"> • Excellent for repair or feature addition – can print directly on parts. [40] • Fast build rate: depending on the feed mechanism: 70 (powder) – 700 (wire) cm^3/h [32]. • High printed material density – typically >99% for iron alloys. [41] • Simple integration with subtractive manufacturing 	<ul style="list-style-type: none"> • Low accuracy and surface finish – limited complexity of printed parts. [40] • Very limited maximum overhang angle. [42] • Increased waste material – parts are typically printed larger and machined to net-shape.
BJ	<ul style="list-style-type: none"> • No printing supports – less post-processing, more design options [43] • Fast build rate – some authors claim practical speeds up to 200 cm^3/min [44] are achievable. • Best for indirect production – preparation of sand-casting cores and molds. 	<ul style="list-style-type: none"> • Shrinkage – typically 15 – 20% [44], [45] depending on the density of the green part, alloy type, and sintering temperature. Unpredictable shrinkage can result in non-desired part dimensions. • Low density – obtaining 50 - 90% relative density is common for BJ sintered iron alloy samples [45], [46] in the literature; some studies describe obtaining densities above 99% [47] – but with unspecified ratio of metallic to binder phase • Shrinkage – similar to BJ process, FDM metal parts undergo debinding and sintering post-printing. FDM parts have shown similar shrinkage: in the range of 15 – 20% [51], [52], [53]. • Low relative density – results range from 93 - 95% dense steel samples [54], [55] to insignificant metallic phase content samples [56], [57].
FDM	<ul style="list-style-type: none"> • Most simplistic and least expensive approach to metal 3D printing [40]. • Largest extrusion-based printers (BAAM) are well known for their impressive size (in multiple meters) and build rate (50 kg/h) [48]. • Currently the most capable multi-metal printing options [49]. • Machinery can be considered the easiest and safest to operate [50]. 	

of commercial top-grade soft magnetic materials to investigate the gap yet to be filled between the additive and traditional materials. Fig. 3.2 illustrates the magnetic polarization achieved for printed materials, segregated in terms of alloy and printing method based on the data available in [58]–[76]. The typical working points and saturation limit for commercial non-oriented (NO) and grain-oriented (GO) electrical steels are included for comparison.

[79,59,60,61,64,63,62,80]

The figure shows two distinct groups of measurements: magnetic measurements at low (10^3 – 10^4 A/m) and high field strengths ($\sim 10^6$ A/m). The magnetic polarization obtained at low field strength signifies the material magnetization we can expect for practical applications: such as printed electrical power devices. High field strength measurements reveal the theoretical maximum magnetization of the material (material polarization is at $\mu_r = 1$). For commercial EM materials, magnetic polarization is typically specified at 800 or 2500 A/m on material datasheets.

For the compilation of the comparative figure, two considerations were made:

- Both B_{max} (at low field strength) and J_{max} (at high field strength) are considered equivalent for comparison purposes. This presentation is accurate since at low field strengths $\mu_0 H$ is orders of magnitude smaller than J and can be disregarded. The flux density and polarization are described by Eq. (1) [77]:

$$B = J + \mu_0 H, \quad \mu_0 = 4\pi \cdot 10^{-7} \frac{\text{N}}{\text{A}^2} \quad (1)$$

- Magnetic polarization and field strength were converted from Gaussian units into SI where needed: through (2) and (3) [77], where ρ is the approximate absolute density in g/cm^3 of the material in question.

$$1 \text{ [Oe]} = 1 \cdot \frac{10^3}{4\pi} \left[\frac{\text{A}}{\text{m}} \right] \quad (2)$$

$$1 \left[\frac{\text{emu}}{\text{g}} \right] = 1 \cdot \frac{\rho}{4\pi \cdot 10^4} \text{ [T]} \quad (3)$$

L-PBF processed silicon steels showed similar magnetic polarization compared to commercial NO $\sim 6.5\%$ and $\sim 3\%$ silicon steel sheets [75]. Presently, the performance equivalent to GO steels has been out of reach, as strong preferred granular orientation in AM processed soft steels has not been achieved. The utilization of other printing methods and alloys has been less common in the literature: including some studies of DED, FDM, BJ methods and FeCo, amorphous and magnetic polymer composite materials. The lowest total saturation polarizations were exhibited for bonded FDM printed samples (polymer binder) and the highest – printed FeCo (Both SLM and DED). All printed crystalline samples were annealed at high temperatures (1100–1200 °C) for grain growth and stress relief.

The comparison of obtained total core losses of the printed samples and commercial materials is presented in Fig. 3.3. The figure presents the most extensive dataset that could be compiled from the literature: core losses measured at 50–60 Hz, at magnetic polarization of 1 T. For commercial non-oriented 3% silicon steels, the losses are typically presented at $W_{15,50}$ (this is 15 kGauss or 1.5 T polarization, at 50 Hz excitation switching). The lower 1 T common characterization point for the printed materials is likely due to the lower overall polarization obtainable from the printed samples due to high silicon content in some samples or suboptimal processing parameters in others. For each dataset, the physical dimensions of the samples are included – as the total core losses are geometry dependent (i.e., include classical eddy current loss). Most measurements have been conducted on ring samples, with the outer dimension ranging from 28 to 60 mm. For solid printed samples, core losses are significant, up to approximately 10 W/kg ($W_{10,50}$). Significantly lower losses were obtained with refined sample topologies: with the results ranging between 1.2 and 1.7 W/kg (depending on the individual sample topology and its chemical composition). All of the refinements to the studied printed cores were realized through air-gapped designs (both parallel and perpendicular to the build direction). In comparison, for typical commercial materials, the total core losses are significantly lower. For NO JNEX super core laminations 0.5 W/kg, for NO 3% Fe-Si Laminations 0.8 W/kg, and for SMC ~ 5 W/kg [75].

Comparison of the total core losses would indicate the apparent superiority of 3D printed soft magnetic cores to SMC cores and approximately double the losses compared to commercial stampings. However, if the losses were investigated per volume of the sample, this conclusion would not stand. This is because the air gaps introduced into the printed parts for eddy current suppression also significantly reduce the fill factor of the magnetic material: requiring larger material volume for

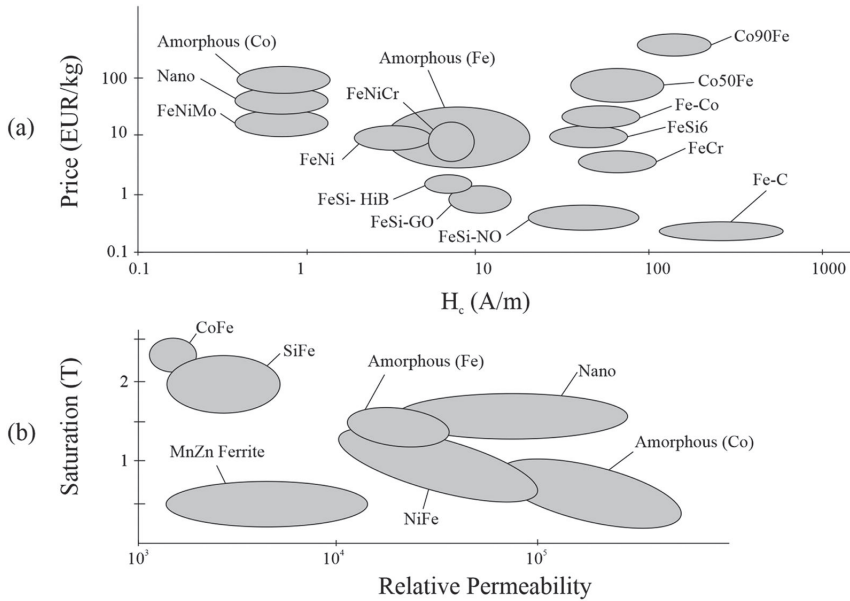


Fig. 3.1. Diversity of soft magnetic materials: common materials compared in terms of cost (a) and magnetic properties (b) (adopted from [31]).

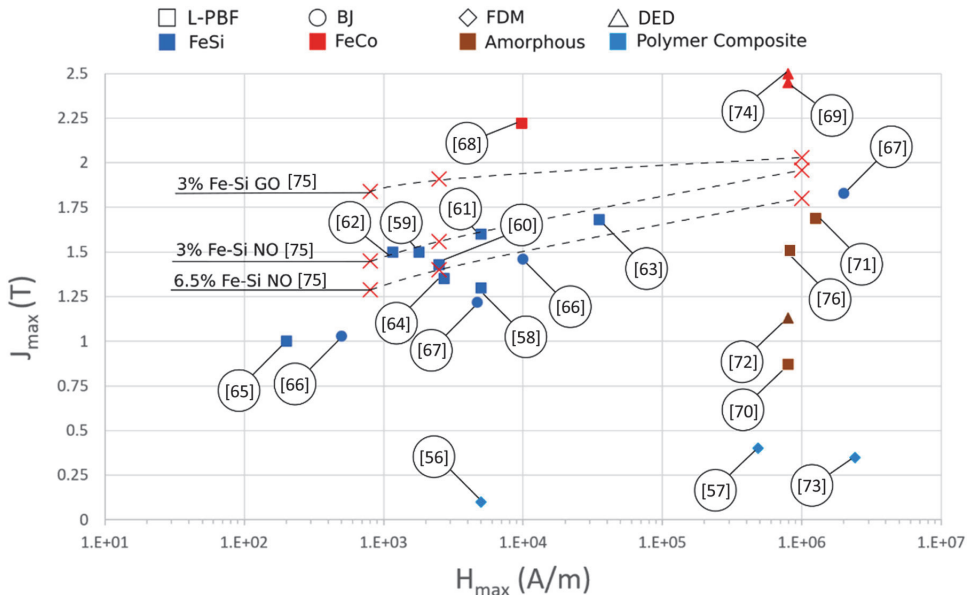


Fig. 3.2. Material polarization comparison of printed soft magnets at varying field strengths with common commercial electrical steels. [65,66,68-74].

conducting the same total magnetic flux. The fill factor for laminations is typically near 96% [31] compared to the fill of approximately 60% [62], [59], [64] for state-of-the-art air-gapped printed cores. To the authors' knowledge, the highest fill factor for a 3D printed soft magnetic core exhibiting segregated topology is 89% for an SLM additively manufactured E-type transformer core [81]. Different strategies for eddy current suppression from the literature are presented in Fig. 3.4.

In addition to the classical eddy current losses induced in the

magnetic material with time-variant magnetic flux, total core losses also consist of additional hysteresis and excess loss components [82]. The study of the segregated hysteresis component (also DC or quasi-static core loss) has been far less common in the literature than total losses. Based on some results obtained from the literature, the hysteresis losses of the printed heat-treated materials are close to or equivalent to the commercial materials: reaching 0.61–0.7 [59], [60] ($W_{10,50}$), and 1.7 [59] W/kg ($W_{15,50}$). As a comparison, NO 6.5% silicon steel sheets

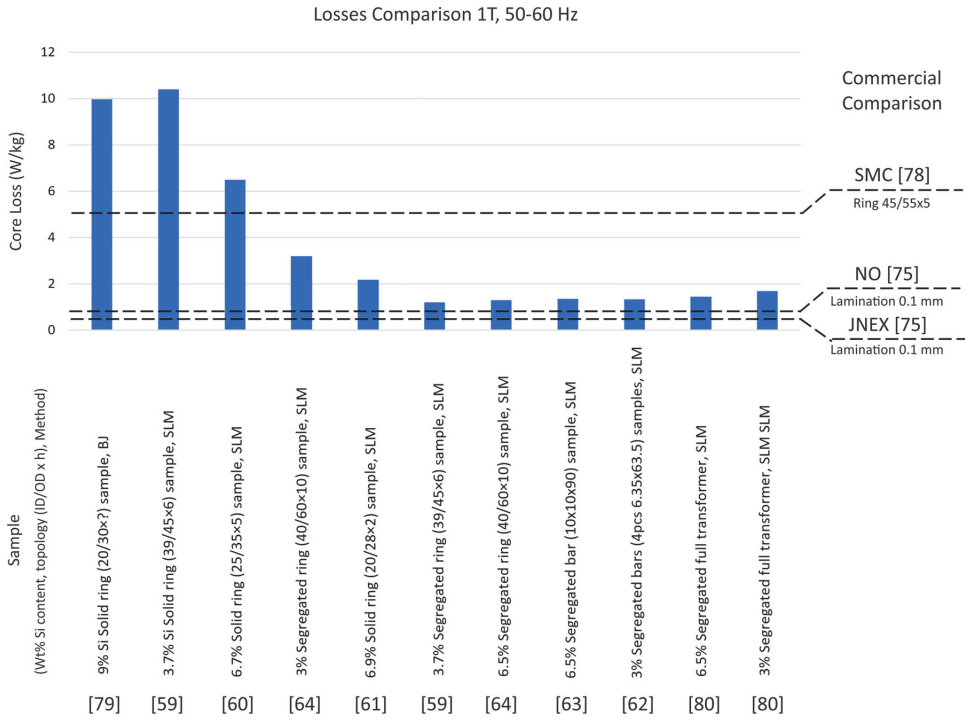


Fig. 3.3. Comparison of total core losses of additively manufactured soft magnetic Fe-Si cores and typical commercial materials from the literature. (ID/OD x h) denotes the topology of the sample – inner diameter/outer diameter x h. [78].

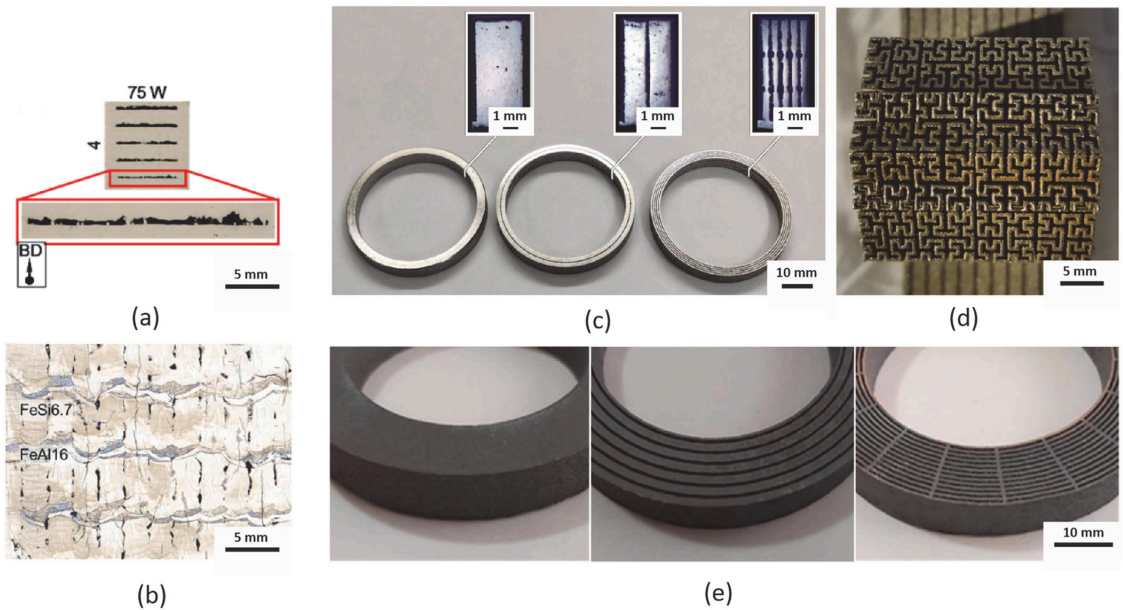


Fig. 3.4. Strategies for eddy current loss reduction in AM soft magnetic materials: (a) Intra-part air-gaps perpendicular to print direction [85], (b) Finite air-gaps parallel to build direction + intermetallic layers [60], (c-e) Broad air-gaps parallel to build direction [59,64,80].

Table 4.1
Common permanent magnet materials for electrical machine applications [86].

Material	$(BH)_{\max}$ (kJm ⁻³)	B_r (T)	H_c (kAm ⁻¹)	Commentary
NdFeB	220–500	0.97–1.45	740–1000	Developed in 1980 s Highest $(BH)_{\max}$ Low corrosion resistance Low temperature resistance
SmCo	120–240	0.85–1.1	620–840	Developed in 1960 s Expensive High temperature resistance
Ferrite	7–42	0.2–0.48	120–360	Highly oxidation resistant Developed in 1930 s Inexpensive
AlNiCo	10–35	0.6–1.16	40–120	Low $(BH)_{\max}$ Developed in 1930 s Easily demagnetized – low H_c Low $(BH)_{\max}$

typically exhibit hysteresis losses between 0.5 and 0.7 W/kg ($W_{10,50}$) [83]. As a rule of thumb, for commercial materials, the hysteresis loss component is not typically specified. As of now, excess core loss magnitude and behavior in 3D printed soft magnetic materials have not been thoroughly investigated.

Mechanical properties of printed steels have been shown to be well above the required/minimum yield strength of 400 MPa of conventional lamination steels with 3.5% silicon content [84], [67]. Of course, this applies only to printed near fully dense material – for air-gapped or otherwise refined/manipulated topologies, considerably lower mechanical properties can be expected.

SLM-prepared silicon steels were by far the most thoroughly investigated AM soft magnetic steels in the literature. Suitable material characteristics for electrical machine construction were obtained when prepared through an optimized process: i.e., from near fully dense samples prepared from high purity powder, which were annealed at

high temperature. The utilization of the AM soft magnetic steels in EM constructions is further expanded in the paper's discussion section.

4. Additive manufacturing of hard magnetic materials

In electrical machines, hard magnetic materials (permanent magnets) are used for flux generation without the application of an electrical current. As these materials are used for storing magnetic energy, a wide hysteresis loop area is essential. The central figure of merit used to characterize a particular grade of permanent magnet material is the maximum energy product: larger $(BH)_{\max}$ translates to higher material power density. Over the 20th century, the material limits for storing magnetic energy have increased steadily: culminating with alloys of rare earth elements with ferromagnetic cobalt (Co) or iron (Fe). Typical properties of the common permanent materials (PM) used in electrical machines are provided in Table 4.1, with NdFeB PMs providing the highest power density.

It is challenging for traditional manufacturing methods (sintering and bonding) to produce complex net-shaped permanent magnets. Feasible magnet topologies are limited, as the techniques involve dies and pressing tools, with the green-shaped parts also undergoing significant shrinkage upon sintering (up to 25% vol) [87]. Similar to soft magnetic materials, additive means have been suggested for producing topology-optimized permanent magnets. In the literature, the printing systems used for the additive manufacturing of PMs are notably more diverse when compared to soft magnetic materials: including significantly more extrusion-based methods. This can be explained by the inherently dissimilar nature and requirements for PM materials and, by extension, for AM systems. In PMs, microstructure impurities are advantageous. With smaller grain size and other interdomain impurities, more pinning sites can be obtained for the magnetic domains, and a larger coercive field H_c is obtained [88]. The optimal size for the NdFeB magnetic grains has been shown to be in the same range as the magnetic domain sizes (in the range of 250 nm [89]). In comparison, the optimal grain size in soft magnetic steel laminations is significantly higher – approximately 150 μm at $W_{15,50}$ magnetization [89].

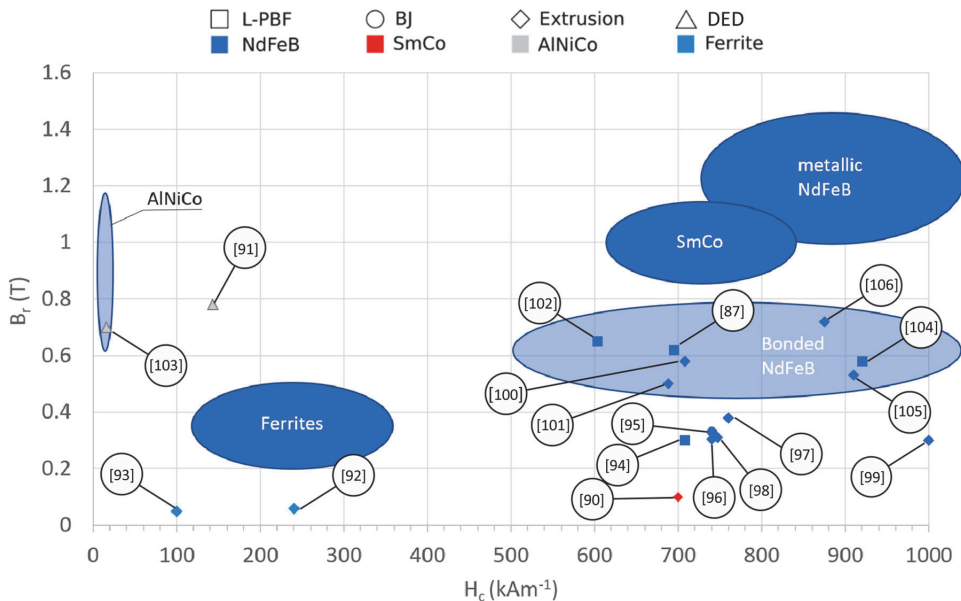


Fig. 4.1. Comparison of printed hard magnetic materials with common commercial materials [107], [108], [86] from the literature in terms of material coercivity and remanence.

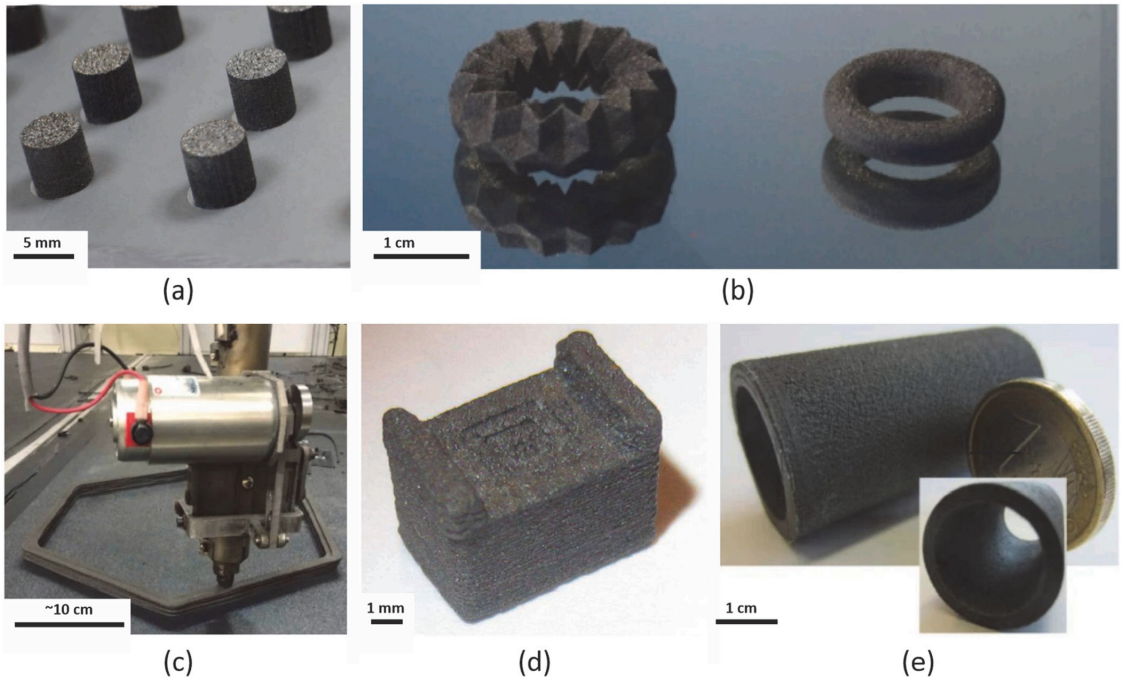


Fig. 4.2. Additively manufactured hard magnetic materials: (a), (b) L-PBF printed near net shaped PM samples (no post-printing sintering required) [87], [111], (c) Big area additive manufacturing (BAAM) of Neodymium PM composite with an approximate scale bar, (d) FDM extruded PM with field shape optimization [96]. (e) FDM extruded PM cylinder with a variable magnetic compound fraction distribution to generate a predefined stray field inside the cylinder [98].

Magnetic coercivity and remanence of AM permanent magnets are compared with typical commercial materials in Fig. 4.1 based on the data available in [86,87], [90–108]. Similar to the comparison of soft magnetic materials in Fig. 3.2, conversions from Gaussian units into SI were conducted through (2) and (3), where necessary. The most extensively investigated additively manufactured PM materials have been the NdFeB rare earth magnets, which have achieved roughly equivalent magnetic properties to their commercial bonded counterparts. The maximum energy products of the printed PM-s are currently under 58 kJm^{-3} , slightly below 63 kJm^{-3} – the typical value for commercial isotropic neodymium bonded magnets [23]. In comparison, standard commercial sintered neodymium magnets exhibit maximum energy product up to 400 kJm^{-3} (grade N52 with 52 MGOe maximum energy product in Gaussian units). In the case of AM hard magnetic materials, the main obstacle in storing more magnetic energy remains in the relatively low hard magnetic phase density. The printed magnets typically exhibit large porosity and/or binder content and consequently low saturation magnetization (maximum energy density is proportional to J_s^2).

In parallel, additively manufactured PM samples exhibit relatively high coercivities: reaching $700\text{--}800 \text{ kJm}^{-1}$ in the majority of the investigated literature. This can be attributed to AM materials' inherently finite granular structure and high structural impurities content. In addition to NdFeB, 3D printing of other hard magnetic compounds has been less common, including some instances of ALNiCo [91], SmCo [90], and Ferrite magnets [92], [93]. Regarding other characteristics, such as thermal resistance: Li et al. [100] obtained a maximum operating temperature of 110°C for extruded PM samples (samples exhibiting less than 5% flux loss after aging at 110°C for 1000 h). This is similar to commercial M or H temperature class NdFeB counterparts, but still relatively low for electrical machine applications, where the operating temperatures can climb substantially higher (even above 150°C)

[109]. In the same work, the printed magnets were also tested in a practical permanent magnet DC electrical machine setup. Roughly equivalent machine performance with the substituted commercial sintered ferrite PMs was obtained. Some instances of the printed hard magnetic components are presented in Fig. 4.2, illustrating the limitations and possibilities of current AM systems.

AM of hard magnetic materials have not evolved past early-stage attempts in maturity and seems currently unsuitable for prototyping topology optimized EMs. The limitations are predominantly due to the low power density of the printed PMs and their relatively simplistic topology – commercial PMs are currently simply superior in every way.

The simplistic shape of printed PMs can be attributed to major three factors:

- The widely employed extrusion-based AM methods present less opportunity for implementing complex part geometries. This is due to the significant shrinkage and mechanical instability involved in the post-printing sintering process [87].
- In parallel to the printing of complex-shaped PM magnet topologies, a magnetization process must also be devised for imparting the necessary three-dimensional magnetization pattern on the material. Ideally, this process would take place in situ, during printing – involving a myriad of technical challenges due to the strong magnetic fields involved [23]. Early-stage work describing a mathematical framework applicable for predicting the degree of alignment in in-situ aligned AM bonded magnets is presented in [110].
- The prevalence of eddy current losses in permanent magnet materials is far less relevant than in soft magnetic cores, enabling the effective use of printed bulk hard magnetic components.

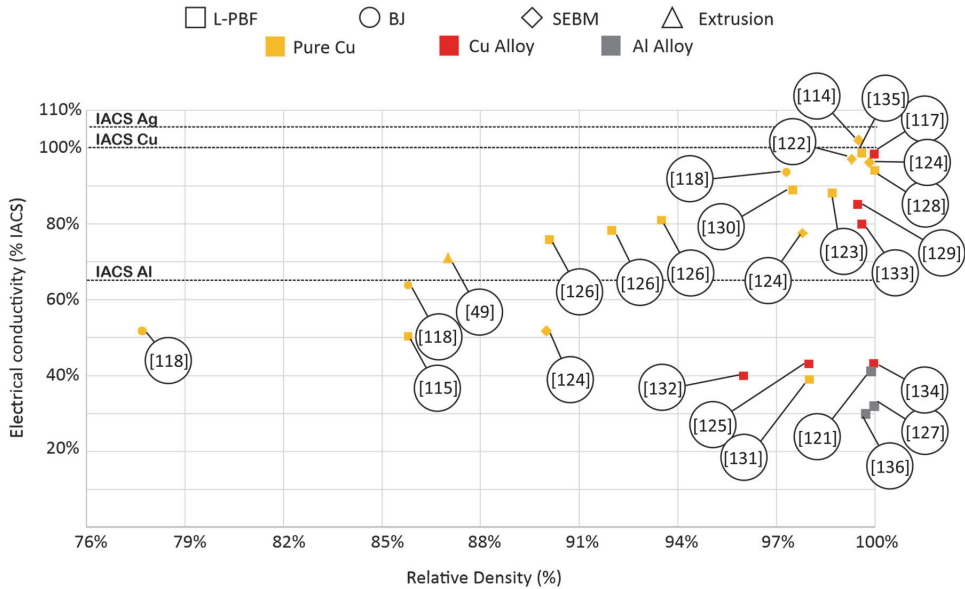


Fig. 5.1. Comparison of printed conductive materials in terms of relative DC conductivity (%IACS) and relative density. For comparison with traditional materials, % IACS limits are given for pure Ag, Cu and Al.

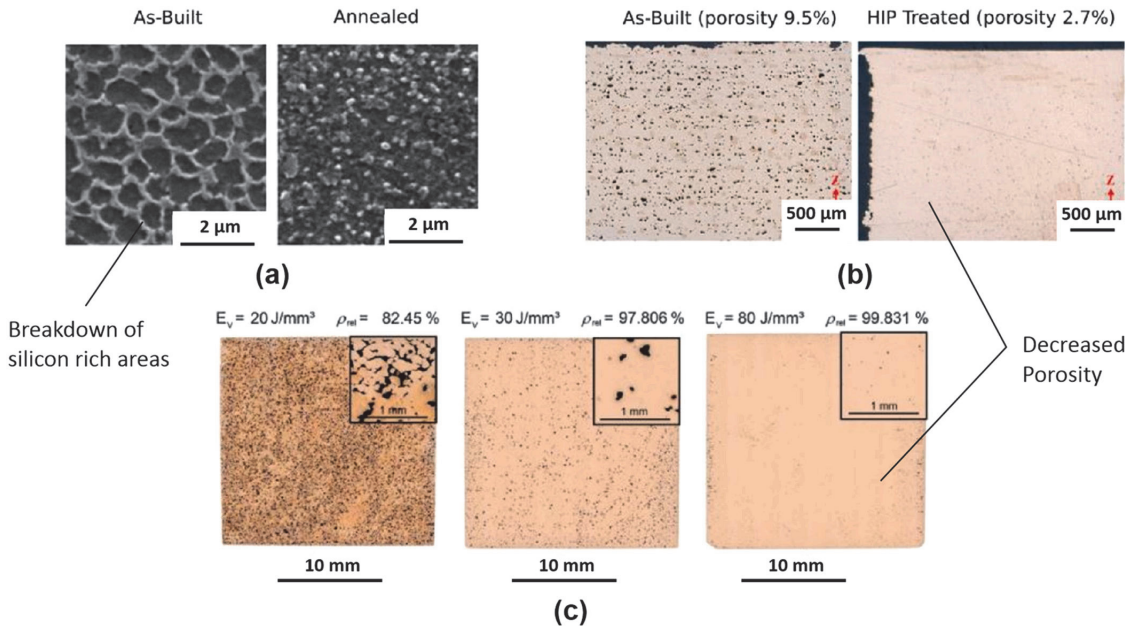


Fig. 5.2. Processing of AM conductive materials: (a) microstructural changes as an effect of annealing in AlSi10Mg alloy [136], (b) Enhancement of BJ printed material density through HIP -treatment [118], (c) Density optimization of SEBM printed pure copper through increased energy input [124].

Table 6.1

Comparison of material properties: state of the art AM electromagnetic and common high-grade commercial materials.

	AM Material Properties	Commercial Material Properties
Soft Magnetic Steel	<ul style="list-style-type: none"> • Polarization • Core Loss • Comments 	<ul style="list-style-type: none"> • $B_{11}^* - 1.5$ T (NO 3% Fe-Si). [62] • $B_{25} - 1.43$ T (NO 6.5% Fe-Si). [60] • $W_{10/50} - 1.2$ W/kg (NO 3.7% Fe-Si, segregated with 59% fill). [59] • $W_{10/60}^* - 1.34$ W/kg (NO 3% Fe-Si, segregated with 56.5% fill). [62] <p>* Similar, not identical comparison conditions with commercial data are available due to non-standardized field.</p>
Permanent Magnet	<ul style="list-style-type: none"> • Maximum Energy Product • Remanence • Intrinsic Coercivity 	<ul style="list-style-type: none"> • $B_{25} - 1.56$ T (NO 3% Fe-Si). [75] • $B_{25} - 1.45$ T (NO 6.5% Fe-Si). [75] • $W_{10/50} - 0.5$ W/kg (NO 6.5% Fe-Si, 0.1 mm). [75] ** • $W_{10/50} - 0.7$ W/kg (NO 3% Fe-Si, 0.35 mm). [75] ** <p>** Fill/stacking of commercial laminations is typically 90-96%, depending on the stamping thickness and quality.</p>
Electrical Conductor	<ul style="list-style-type: none"> • Electrical Conductivity 	<ul style="list-style-type: none"> • $(BH)_{max} \sim 400$ kJm⁻³ (typical N52 sintered anisotropic NdFeB magnet) • $B_r - 1.33$ T (anisotropic sintered 0.99 fill NdFeB) [102] • $H_{ci} - 1480$ kA/m (anisotropic sintered 0.99 fill NdFeB) [102]
	<ul style="list-style-type: none"> • % IACS conductivity - 102% (SEBM melted pure copper) [114] • % IACS conductivity - 98.6% (green laser SLM melted pure copper) [135] 	<ul style="list-style-type: none"> • $(BH)_{max} \sim 400$ kJm⁻³ (typical N52 sintered anisotropic NdFeB magnet) • $B_r - 1.33$ T (anisotropic sintered 0.99 fill NdFeB) [102] • $H_{ci} - 1480$ kA/m (anisotropic sintered 0.99 fill NdFeB) [102] • % IACS conductivity - 102% (Cu-OFB) [113]

5. Additive manufacturing of electrically conductive materials

In electrical machines, electrically conductive materials are used for the sustentation of electrical currents within the machine with minimal Joule heating. These losses occur predominantly within the stator windings for the cyclic energization of the machine electromagnets. The primary intrinsic material property related to Joule losses is the electrical conductivity or its inverse – the material resistivity. The interest in AM methods for EM conductor fabrication is twofold: first, AM facilitates the cost-effective fabrication of novel high-performance winding profiles [112], and secondly, it enables the integration of electro-mechanical components into multi-material printed assemblies [14].

As the most commonly used electrical conductor material is copper, the conductivity of other materials is often quantified as relative to the conductivity of annealed copper. That is the international annealed copper standard (IACS) created at 1913, defining the 100% IACS as the conductivity of pure copper: 5.8×10^7 S/m at 20 °C. The relative conductivity of other common pure conductive metals constitutes to 106% for silver, 72% for gold, and 62% IACS for aluminum. It is also noteworthy that modern alloys can achieve slightly higher conductivities from the IACS standard due to advances in manufacturing methods: such as the oxygen-free high conductivity copper alloy reaching 102% relative conductivity [113].

Unlike magnetic materials, standard L-PBF printing systems are not best suited for the AM forming of highly conductive materials. This is due to the high reflectance of both copper and aluminum at the typical L-PBF laser infrared wavelengths (1000–1100 nm), resulting in low energy absorption (under 2% of energy absorption for Cu) and ineffective melting of powders [114]. More effective melting for PBF processes can be achieved with electron beam melting (80% energy absorption for Cu) or green laser melting (40% energy absorption for Cu [115], [116]). Furthermore, excellent electrical conductors are typically also excellent thermal conductors, causing additional printing challenges. In PBF processes, this results in the rapid conduction of the thermal energy out of the melt pool, resulting in high local thermal gradients, potentially causing delamination, deformations, and part failure [26]. Despite the numerous challenges, additively manufactured copper has reached near equivalency in electrical conductivity with IACS copper, with Selective Electron Beam Melting - SEBM (102% IACS [114]), L-PBF (98.31% IACS [117]), and BJ (93.6% IACS [118]).

3D printing of electrical conductors with non-dedicated metal printing systems has been investigated in less detail. Some authors have shown relative electrical conductivity of FDM fused samples (unsintered) in the range of 0.1% IACS [119], [120] – insufficient for electrical machine purposes. The only reference in the literature investigating the conductivity of sintered extruded copper samples was identified in [49], reaching 87% relative density at 71% IACS conductivity.

The current level of AM conductive materials is illustrated in Fig. 5.1. The figure is focused on comparing printed material electrical conductivities with the IACS standard based on the data available in [49], [114], [115], [117,118], [121–136]. By far, the most studied printed electrically conductive material in the scientific literature was high purity copper, with some instances of copper and aluminum alloys. No references were found for the printing of pure aluminum. Where applicable, multiple data points were included from the studies to better illustrate the relation between printed sample density and conductivity. A roughly linear relationship between the relative density and conductivity was observed – ranging from ~50–60% IACS at ~85% relative density, up to ~96–102% IACS at near full density. The highest conductivities were determined for the highly-dense pure Cu samples printed with SEBM (102% IACS [114]) and green laser L-PBF (98.6% IACS [135]) methods. Alloyed Cu-Cr (98% IACS [117]) samples printed with a high-power 2000 W (1070 nm laser) L-PBF printing system also exhibited near equivalent 98% IACS conductivity [136].

As discussed previously, most of the available L-PBF systems in the market (typically 400 W and below) struggle with the fusing of pure copper. For low-power L-PBF printing, the best results have been obtained with coated particles – for improved optical absorption. In [129] and [137], near fully dense copper alloys samples (approximately 99.5%) were prepared with low-power SLM (350–400 W). These CuCr1Zr samples were shown to reach up to 85% IACS conductivity after post-processing [129]. In [133], CuSn0.3 samples were prepared with a 500 W laser, reaching 99.6% relative density and 80% electrical conductivity.

Heat treatment processes were identified as critical for achieving the full conductivity of Cu and Al alloys. For high purity material, the process was largely omitted, with the exception of hot isostatic pressing (HIP) treatments. In [117], printed Cu alloy conductivity was shown to increase 160% post-heat-treatment at 480 °C (4 h), as the supersaturated Cu-Cr alloy decomposed and the Cr particles were precipitated from the Cu matrix. A similar effect was identified in [136] and [127] in Al alloys. In [118], HIP treatment was used to enhance printed low-density parts, achieving 97.3% final relative density with 93.6% IACS relative conductivity. In [115], the conductivity of low-density pure Cu samples was increased (up to 50.3% IACS) through furnace annealing. This was obtained through the sintering of unmelted copper powder particles encased within the printed samples. Significant processes for obtaining desirable AM-formed conductive material properties are illustrated in Fig. 5.2.

Additively manufactured high purity copper shows properties suitable for commercial applications. Based on the literature, the most effective additive methods for processing the material are beam powder bed-based methods: EBM and green laser PBF. The utilization of AM copper in EM constructions is further expanded in the paper's discussion section.

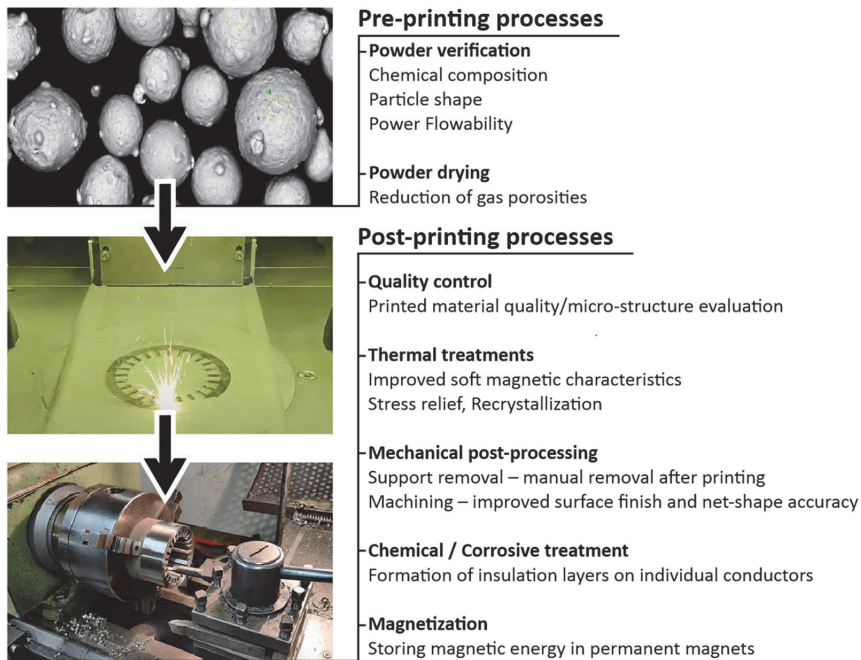


Fig. 6.1. Pre- and post-printing processes for L-PBF electromagnetic components.

6. Discussion

With optimized processing of both the magnetically and electrically conductive materials, quasi-static (DC) properties on par with conventional materials have been achieved. Significant drawbacks were confirmed for printed soft magnetic flux guides for alternating field applications related to unsuppressed induced eddy currents. Further process optimization is still required for printing hard magnetic materials, as the current power densities of the highest performing PMs are relatively low. The summary of the state-of-the-art AM electromagnetic material properties is outlined in Table 6.1. The summary includes the most significant results from the literature and typical values for high-grade commercial materials. It is important to note that for the comparison of printed and commercial soft magnetic materials, similar but not identical comparison conditions are used – this is due to the non-standardized characterization of magnetic materials (tests are often application/electric grid specific).

Clearly, additively prepared magnetically and electrically conductive materials show great promise performance-wise. Mapping the material characteristics allows for the first steps in topology optimization calculation protocols, as the rough outlines of what to expect from printed materials have been determined. However, obtaining useful intrinsic material properties is just one part of the overall process optimization in the development of 3D printed electrical machines. For the determination of the maturity of 3D printed materials to be utilized in commercial electrical machines, the features of AM systems involved must also be considered.

For the AM electromagnetic materials investigated in this study, powder bed fusion type printers were by far the most widely used and mostly rendered the best results. This is unsurprising as these printing systems have been commercially available for nearly 20 years and have evolved into high maturity. PBF systems are well known for their capacity for manufacturing high-purity, near-fully dense parts of almost any metallic material with high spatial accuracy (resolution up to

15 μm). This is perfect for preparing soft magnetic steel or copper for EM applications – where both high material purity and spatial resolution are critical. In parallel, however, the printing process has several drawbacks, which drastically limit the emergence of additively manufactured electrical machines readily available to the end consumer. To evaluate the maturity or the readiness of PBF systems for electrical machine production – we must consider the application or the scale of production in question. For commercial electrical machines? – clearly an impossibility with the build rates of current PBF systems. For particular topology optimized high-performance components? – Yes, AM can surpass conventional manufacturing methods for specific applications in terms of both design complexity and performance. For rapid prototyping? – Undoubtedly. With AM, the academic community's prototyping and verification of topology optimized components are streamlined significantly. Based on the literature reviewed, the overall perspective of the EM research community on integrating AM methods in the EM production cycle is twofold. First, to currently work on prototyping novel components and developing new optimization methods. And secondly, with future breakthroughs in AM fabrication speed and multi-material capacity, build upon the previous work to establish AM electrical machines on a larger scale. That being said, setting up even a small-scale in-house production for prototyping electromagnetic components is a challenging endeavor for individual research groups. It requires expert printing knowledge, a PBF printer purchase, and several supporting facilities for pre-and post-printing processing steps. These steps range from thermal, mechanical, or chemical treatments of the printed parts to in-house process quality control facilities. Based on our experience and relevant literature, the most critical of these additional processes for L-PBF printing electromagnetic components are outlined in Fig. 6.1.

The printed prototype EM components described in the scientific literature can mainly be divided into three larger directions or groupings: topology optimized windings, synchronous rotors, and heat exchangers. In all cases, the main advantages of the prototypes were related to more complex part topologies, resulting in reduced part

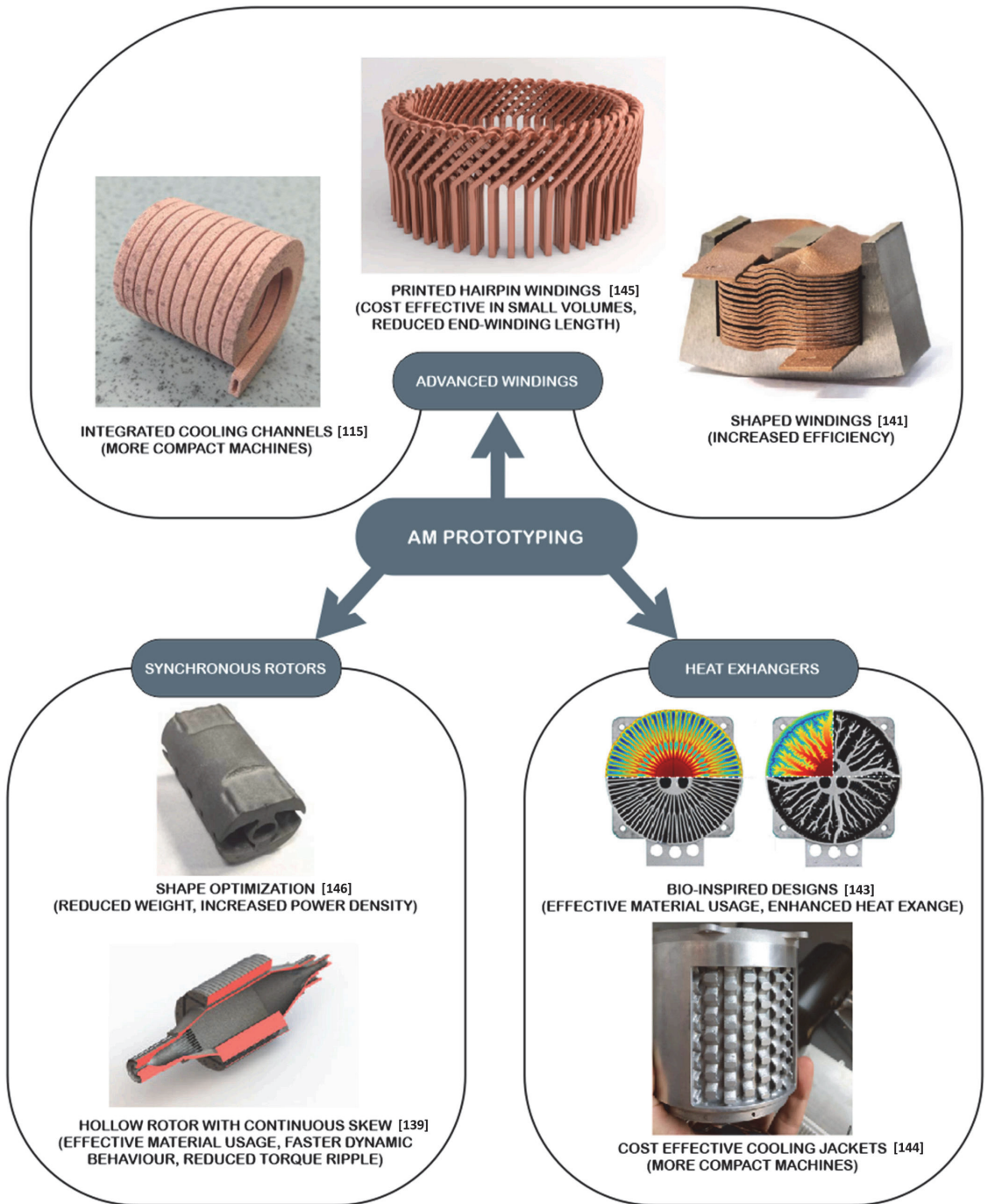


Fig. 6.2. Main directions of prototyping electromagnetic components for EM purposes. [143–146].

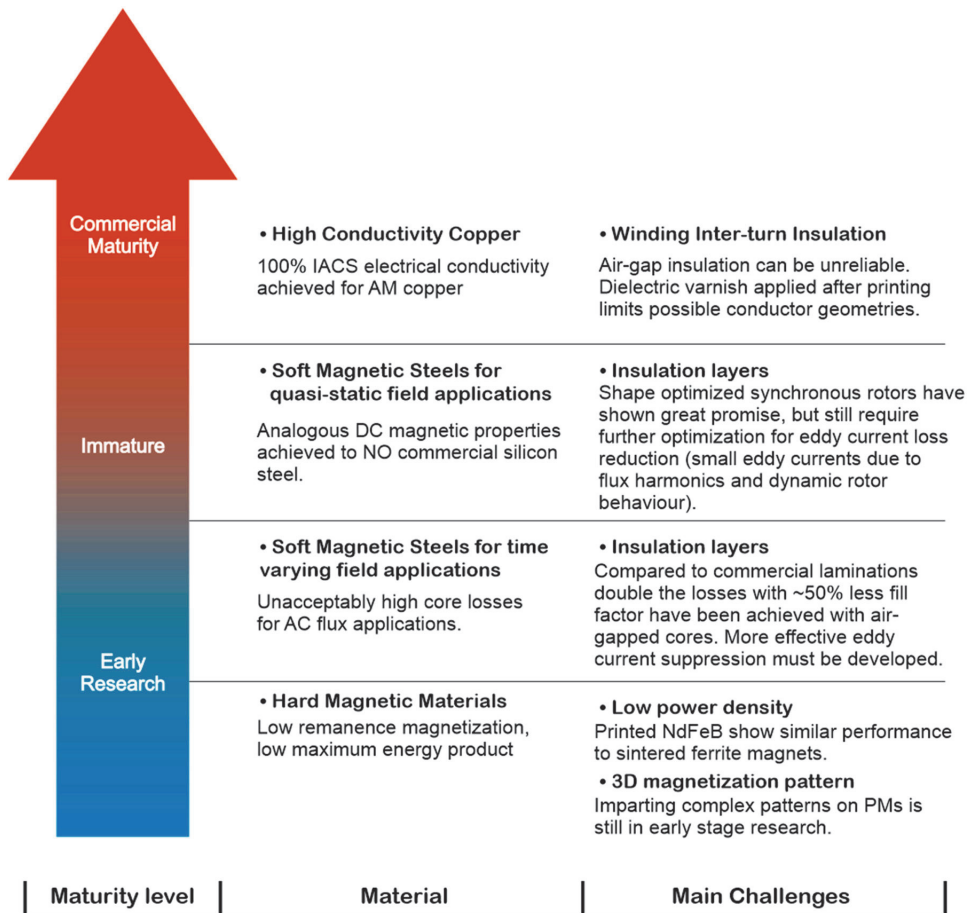


Fig. 6.3. Maturity of AM materials for prototyping electrical machine components.

weight, increased efficiency, or increased power density. The main directions of the prototyped components are presented in Fig. 6.2. For 3D printed permanent magnet prototypes, the only mention for practical use was mentioned in [100], where a printed NdFeB PM was used to substitute a ferrite PM in a DC electrical machine – achieving roughly equivalent performance.

Prototypes of soft magnetic cores for time-varying magnetic fields are almost nonexistent in the literature. No doubt due to difficulties in suppressing Foucault’s currents in the printed single-material constructions. In [81], a prototype transformer core was printed, assembled, and compared in terms of performance with a commercial unit: showing functional though notably reduced performance. This was due to the superior magnetic properties and more segregated topology of the Goss sheet commercial transformer core. The study identified 10% reduced efficiency (from 80.5% to 70.1%) and 34% lower power density (from 59 VA/kg to 39 VA/kg) of the printed transformer. For printed soft magnetic synchronous rotors, obtaining useful prototype performance is considerably less complicated. In ideal conditions, synchronous rotors would conduct a quasi-static magnetic field – suffering no energy lost from the remagnetization. In reality, some eddy current losses are always induced in synchronous rotors due to harmonics of the non-sinusoidal flux distribution over the machine air-gap and dynamic behavior of the machine. These parasitic spatial and temporal harmonics

are responsible for undesirable vibration, noise, extra losses, and control accuracy (lower machine speed and position accuracy [138]). AM methods are ideal for the reduction of these harmonics through more complex core topologies, enabling a smoother spatial transition between the flux switching elements in the machines. The idea is illustrated in [139], where a continuous rotor skewing is introduced to the machine rotor with a significant reduction in cogging torque: achieving approximately 90% reduction of both first and second torque harmonic. The continuous rotor skewing option is a unique advantage for AM-produced PM synchronous rotors. Conventionally, they are introduced stepwise [140], as regulated by the assembly costs involving overabundant stamping geometries. Another unique attribute of the characterized printed rotor was the conical transition region introduced between the machine rotor’s active part and its bearings. The optimized transition allowed for the more effective absorption of bending and torsional loads, translating to reduced shaft weight. 52.7% weight reduction was achieved, which resulted in a 9.4% faster acceleration from standstill to 1000 m-1 revolution and reduced material utilization.

The maturity of 3D printed copper components is high, even suitable for commercial applications. Most notably, AM production freedom and consequent simplified assembly would translate to cost-effective fabrication of nonconventional windings – especially when dealing with small production volumes. This is due to the high complexity and

production costs involved in the individual conductors' insertion, bending, and welding when assembling nonconventional winding types, such as the hairpin winding configuration. There are still, however, some challenges remaining. Like AM core constructions, the development of multi-material metal printers is a prerequisite for unlocking the full potential of printed EM windings. With multi-material AM, higher winding reliability and power density could be achieved by realizing the inter-turn insulation layers as part of the printing process. Even so, for low-voltage applications, including electrical machines, beneficial enhancements have already been shown for single-material copper prototype coils, where the inter-turn insulation is solved via air-gaps. In [141] and [142], monolithic coils were printed with individual conductor profiles, shaped according to their magnetic environment: thus avoiding the high leakage flux areas within the slot and suffering lower AC losses. Another potential innovation from AM windings comes from the Roebel principle [112] – by introducing braided conductor elements within the machine stator, the currents can be distributed more evenly within the conductor groove: i.e., displacement currents suppressed more effectively. This winding type is typically reserved for MW scale machines due to the significant costs involved in the bending and welding of the individual conductors [112]. As with AM, this complex design can be produced without significant extra effort or cost involved over the printing of solid homogenous conductor bars; these coil designs might be integrable to smaller printed machine designs as well.

Lastly, the authors recognize significant advantages for AM copper parts for producing more effective EM winding heat exchangers: including both active and passive methods. This would translate to increased machine power density, as excessive thermal energy can more effectively be removed from the system: through integrated cooling pipes, cooling jackets, or just topology optimized passive heat exchangers. The maturity evaluation of the AM electromagnetic materials for prototyping EM components is summarized in Fig. 6.3.

7. Conclusions

A review on additive manufacturing of electromagnetic materials for the adoption in electrical machine construction has been conducted. The key findings of this study are:

- When processed through optimized methods, printed electrically and magnetically conductive materials show equivalent DC material properties to high-grade commercial materials.
- For electrically conductive materials, equivalent properties to commercial high-conductivity copper have been obtained for high purity copper powders processed with SEBM and green laser L-PBF methods.
- Best results for low-power infrared L-PBF printers can be obtained with coated powder particles (e.g., CuCr1Zr or CuSn0.3) for enhanced optical absorption, reaching roughly 80% IACS conductivity.
- For additively processed silicon steel, infrared L-PBF processing method was the most widely utilized in the literature, with the printed samples showing similar DC magnetic properties compared to commercial non-oriented silicon steel sheets.
- Both printed electrically, and magnetically conductive components suffer from limited multi-material printing capacity. Most prominently, this results in increased eddy current losses in printed soft magnetic flux guides and challenges in forming reliable winding inter-turn insulations.
- Printed hard magnetic materials are still at early-stage research. Further process optimization is still required, as the highest quality printed PM is roughly equivalent to bonded NdFeB magnets – with the printed PM energy product not exceeding $\sim 60 \text{ kJm}^{-3}$. Furthermore, an effective in situ magnetization process is yet to be developed to impart a complex three-dimensional magnetization pattern on a printed PM.

- The maturity of the prototyping or small volume production of electromagnetic components is currently highest with PBF printing systems, where high spatial accuracy, high purity, near fully dense parts can be prepared.
- Current PBF printing systems show great promise for small volume production or prototyping of optimized electrical machine windings, heat exchangers, and synchronous rotors.

CRedit authorship contribution statement

Vaimann Toomas: Project administration, Supervision. **Kallaste Ants:** Supervision, Resources, Funding acquisition. **Tiismus Hans:** Writing – original draft, Writing – review & editing. **Rassõlkin Anton:** Supervision.

Declaration of Competing Interest

The authors declare that they have no known competing financial interests or personal relationships that could have appeared to influence the work reported in this paper.

Acknowledgements

This research work has been supported by Estonian Ministry of Education and Research (Project PSG-137).

References

- [1] "Electricity generation statistics – first results - Statistics Explained." https://ec.europa.eu/eurostat/statistics-explained/index.php/Electricity_generation_statistics_-_first_results (accessed Apr. 14, 2021).
- [2] G. Bramerdorfer, J.A. Tapia, J.J. Pyrhonen, A. Cavagnino, "Modern electrical machine design optimization: Techniques, trends, and best practices", *IEEE Trans. Ind. Electron.* vol. 65 (10) (2018) 7672–7684, <https://doi.org/10.1109/TIE.2018.2801805>.
- [3] "Premium Efficiency Motor Selection and Application Guide." Accessed: Jul. 15, 2021. [Online]. Available: (https://www.energy.gov/sites/default/files/2014/04/f15/amo_motors_handbook_web.pdf).
- [4] "Porsche Present 40% Lighter 3D Printed Electric Drive Housing." (<https://additiv-tech.ru/en/news/porsche-present-40-lighter-3d-printed-electric-drive-housing.html>) (accessed Apr. 20, 2021).
- [5] "Additive Manufacturing in the Space Industry to Reach \$4.7 Billion - Via Satellite -." (<https://www.satellitetoday.com/innovation/2017/08/18/additive-manufacturing-space-industry-reach-4-7-billion/>) (accessed Apr. 21, 2021).
- [6] "GE Aviation 3D Prints 30,000th Metal 3D Printed Fuel Nozzle at Auburn, Alabama Plant." (<https://3dprint.com/226703/ge-aviation-fuel-nozzle-3d-printed-30000/?fbclid=IwAR38NO-0dAF2BwKXhVtC18gAimKnQUSy5KRv-u08InfruK5Zl7Q1PIH1>) (accessed Nov. 26, 2020).
- [7] "Additive Manufacturing Report Summary - Ampower Metal AM Market Report." (https://additive-manufacturing-report.com/additive-manufacturing-report-summary/?gclid=Cj0KCQjwyZmEhCpARIsALzmnJT568PzUw4vqdaWFD6j64aowu3GBprLj1BlchmQbrj78pmgmtgaArr4EALw_wcB) (accessed Apr. 26, 2021).
- [8] R. Poprawe, C. Hinke, W. Meiners, J. Schrage, S. Bremen, S. Merkt, SLM production systems: Recent developments in process development, machine concepts and component design. *Advances in Production Technology*, Springer Nature, Switzerland AG, 2015, pp. 49–65, https://doi.org/10.1007/978-3-319-12304-2_5.
- [9] E. Aguilera, J. Ramos, D. Espalin, F. Cedillos, D. Muse, R. Wicker, E. Macdonald, "3D printing of electro mechanical systems", *Int. Solid Free. Fabr. Symp.* (2013) 950–961.
- [10] M. Garibaldi, C. Gerada, I. Ashcroft, R. Hague, H. Morvan, M. Garibaldi, C. Gerada, I. Ashcroft, R. Hague, H. Morvan, "The impact of additive manufacturing on the development of electrical machines for MEA applications: A feasibility study" no. 1 (2015) 2–5.
- [11] S. Metsä-Kortelainen, T. Lindroos, M. Savolainen, A. Jokinen, A. Revuelta, A. Pasanen, K. Ruusuvaara, J. Pippuri, "Manufacturing of topology optimized soft magnetic core through 3D printing", *NAFEMS Nord. Semin.* (2016).
- [12] S. Lammers, G. Adam, H.J. Schmid, R. Mrozek, R. Oberacker, M.J. Hoffmann, F. Quattrone, and B. Ponick, "Additive Manufacturing of a lightweight rotor for a permanent magnet synchronous machine," in 2016 6th International Electric Drives Production Conference, EDPCC 2016 - Proceedings, 2016, vol. 13, pp. 41–45. doi: 10.1109/EDPC.2016.7851312.
- [13] R.H. Michele Garibali , Ian Ashcroft , Chris Gerada , "Laser Additive Manufacturing of Soft Magnetic Cores for Rotating Electrical Machinery: Materials Development and Part Design," 2018.

- [14] H. Tiismus, A. Kallaste, A. Belahcen, A. Rassolkin, and T. Vaimann, "Challenges of Additive Manufacturing of Electrical Machines," in Proceedings of the 2019 IEEE 12th International Symposium on Diagnostics for Electrical Machines, Power Electronics and Drives, SDEMPED 2019, 2019, pp. 44–48. doi: 10.1109/SDEMPED.2019.8864850.
- [15] R. Wrobel, B. Mecrow, "A Comprehensive Review of Additive Manufacturing in Construction of Electrical Machines," in Proceedings of the IEEE Workshop on Electrical Machines Design Control Diagn., WEMDCD 2019 2019 15 22 doi: 10.1109/WEMDCD.2019.8887765.
- [16] R. Wrobel, B. Mecrow, "A comprehensive review of additive manufacturing in construction of electrical machines", IEEE Trans. Energy Convers. vol. 35 (2) (2020) 1054–1064, <https://doi.org/10.1109/TEC.2020.2964942>.
- [17] M.U. Naseer, A. Kallaste, B. Asad, T. Vaimann, A. Rassolkin, "A review on additive manufacturing possibilities for electrical machines", Energies vol. 14 (7) (2021) <https://doi.org/10.3390/en14071940>, 1940, Mar.
- [18] P.S. Ghahfarokhi, A. Podgornovs, A. Kallaste, A.J.M. Cardoso, A. Belahcen, T. Vaimann, H. Tiismus, B. Asad, "Opportunities and challenges of utilizing additive manufacturing approaches in thermal management of electrical machines", IEEE Access vol. 9 (2021) 36368–36381, <https://doi.org/10.1109/ACCESS.2021.3062618>.
- [19] L. Advancements, Metal additive manufacturing for electrical machines: Technology review and latest advancements, Energies 15 (1076) (2022) 1–18.
- [20] T. Pham, P. Kwon, S. Foster, "Additive manufacturing and topology optimization of magnetic materials for electrical machines—A review", Energies vol. 14 (2) (2021) 283, <https://doi.org/10.3390/en14020283>.
- [21] V. Chaudhary, S.A. Mantri, R.V. Ramanujan, R. Banerjee, "Additive manufacturing of magnetic materials", Prog. Mater. Sci. vol. 114 (2020), 100688 <https://doi.org/10.1016/j.pmatsci.2020.100688> no. February 2019.
- [22] V. Popov, A. Koptuyg, I. Radulov, F. Maccari, G. Muller, "Prospects of additive manufacturing of rare-earth and non-rare-earth permanent magnets", Procedia Manuf. vol. 21 (2017) (2018) 100–108, <https://doi.org/10.1016/j.promfg.2018.02.199>.
- [23] J.M.D. Coey, "Perspective and prospects for rare earth permanent magnets", Engineering vol. 6 (2) (2020) 119–131, <https://doi.org/10.1016/j.eng.2018.11.034>.
- [24] Q. Jiang, P. Zhang, Z. Yu, H. Shi, D. Wu, H. Yan, X. Ye, Q. Lu, Y. Tian, "A review on additive manufacturing of pure copper", Coatings vol. 11 (6) (2021) <https://doi.org/10.3390/coatings11060740>.
- [25] T.Q. Tran, A. Chinnappan, J.K.Y. Lee, N.H. Loc, L.T. Tran, G. Wang, V.V. Kumar, W.A.D.M. Jayathilaka, D. Ji, M. Doddamani, S. Ramakrishna, "3D printing of highly pure copper", Met. (Basel) vol. 9 (7) (2019) 12–20, <https://doi.org/10.3390/met9070756>.
- [26] T. El-Wardany, Y. She, V. Jagdale, J.K. Garofano, J. Liou, and W. Schmidt, "Challenges in 3D printing of high conductivity copper," in ASME 2017 International Technical Conference and Exhibition on Packaging and Integration of Electronic and Photonic Microsystems, InterPACK 2017, collocated with the ASME 2017 Conference on Information Storage and Processing Systems, 2017, pp. 1–10. doi: 10.1115/IPACK2017-74306.
- [27] "Four complete process chains for powder bed and powder nozzle technology." (<http://additivemanufacturing.global/index.php/en/print-en/commercial/3743-four-complete-process-chains-for-powder-bed-and-powder-nozzle-technology>) (accessed Sep. 22, 2021).
- [28] F. Lorenz, J. Rudolph, R. Werner "High Temperature Operation and Increased Cooling Capabilities of Switched Reluctance Machines using 3D Printed Ceramic Insulated Coils" 2018 IEEE Transp. Electr. Conf. Expo., ITEC 2018 2018 146 151 doi: 10.1109/ITEC.2018.8450089.
- [29] "Dual Metal LPBF - Aerosint." <https://aerosint.com/dual-metal-lpbf/> (accessed Nov. 27, 2020).
- [30] A. Globus, "I.-Magnetization mechanisms some physical considerations about the domain wall size theory of magnetization mechanisms", J. Phys. Colloq. vol. 38 (C1) (1977) <https://doi.org/10.1051/jphyscol:19771011>.
- [31] S. Tumanski, Handbook of magnetic measurements. 2016. doi: 10.1201/b10979.
- [32] L.E. Murr, W.L. Johnson, "3D metal droplet printing development and advanced materials additive manufacturing", J. Mater. Res. Technol. vol. 6 (1) (2017) 77–89, <https://doi.org/10.1016/j.jmrt.2016.11.002>.
- [33] D. Bourell, J. Beaman, M. Leu, D. Rosen "A Brief History of Additive Manufacturing and the 2009 Roadmap for Additive Manufacturing: Looking Back and Looking Ahead" 2009 doi: 10.1016/S0190-9622(08)80898-5.
- [34] T. Gornet, W. Wohlers "History Addit. Manuf.," 2016 doi: 10.4018/978-1-5225-2289-8.ch001.
- [35] N.M. Terry Wohlers, Robert Ian Campbell, Olaf Diegel, Joseph Kowen, Ray Huff, "Wohlers Report 2021," p. 375, 2021, Accessed: Jan. 11, 2022. [Online]. Available: <https://wohlersassociates.com/2021report.htm>.
- [36] M. Yakout, M.A. Elbestawi, S.C. Velhuis, "Density and mechanical properties in selective laser melting of Invar 36 and stainless steel 316L", J. Mater. Process. Technol. vol. 266 (2018) 397–420, <https://doi.org/10.1016/j.jmatprotec.2018.11.006> (no. November).
- [37] X. Song, W. Zhai, R. Huang, J. Fu, M. Fu, F. Li, "Metal-Based 3D-Printed micro parts & structures". Reference Module in Materials Science and Materials Engineering, Elsevier, 2020 <https://doi.org/10.1016/b978-0-12-819726-4.00009-0>.
- [38] H. Wong, K. Dawson, G.A. Ravi, L. Howlett, R.O. Jones, C.J. Sutcliffe, "Multi-laser powder bed fusion benchmarking—Initial trials with Inconel 625", Int. J. Adv. Manuf. Technol. vol. 105 (7–8) (2019) 2891–2906, <https://doi.org/10.1007/s00170-019-04417-3>.
- [39] "LASERTEC 30 DUAL SLM - ADDITIVE MANUFACTURING Machines by DMG MORI." <https://en.dmgmori.com/products/machines/additive-manufacturing/powder-bed/lasertec-30-slm> (accessed Jan. 12, 2022).
- [40] T.D. Ngo, A. Kashani, G. Imbalzano, K.T.Q. Nguyen, D. Hui, "Additive manufacturing (3D printing): A review of materials, methods, applications and challenges", Compos. Part B Eng. vol. 143 (2018) 172–196, <https://doi.org/10.1016/j.compositesb.2018.02.012>, no. December 2017.
- [41] M.S.I. Kamariah, W.S. Harun, F. Ahmad, F. Tarlochan, "Mechanical behaviours of selective laser melting 316L stainless steel", J. Addit. Manuf. Adv. Mater. vol. 1 (1) (2020) 1–18.
- [42] E. Nassar, A. Reutzel, "Beyond layer-by-layer Additive Manufacturing – Voxel-wise Directed Energy Deposition A. R. Nassar* and E. W. Reutzel* * Applied Research Laboratory at the Pennsylvania State University, University Park, PA 16802", Appl. Res. Lab. Penn State Univ. (2015) 273–283 [Online]. Available: (<https://pdfs.semanticscholar.org/26a2/2157665982512188b87e8575e5481d873233.pdf>).
- [43] S.A.M. Tofail, E.P. Koumoulos, A. Bandyopadhyay, S. Bose, L. O'Donoghue, C. Charitidis, "Additive manufacturing: Scientific and technological challenges, market uptake and opportunities", Mater. Today vol. 21 (1) (2018) 22–37, <https://doi.org/10.1016/j.matod.2017.07.001>.
- [44] M. Ziaee, N.B. Crane, "Binder jetting: A review of process, materials, and methods", Addit. Manuf. vol. 28 (December 2018) (2019) 781–801, <https://doi.org/10.1016/j.addma.2019.05.031>.
- [45] I. Rishmawi, M. Salarian, M. Vlasea, "Tailoring green and sintered density of pure iron parts using binder jetting additive manufacturing", Addit. Manuf. vol. 24 (October) (2018) 508–520, <https://doi.org/10.1016/j.addma.2018.10.015>.
- [46] G.K. Meenashisundaram, Z. Xu, M.L.S. Nai, S. Lu, J.S. Ten, J. Wei, "Binder jetting additive manufacturing of high porosity 316L stainless steel metal foams", Mater. (Basel) vol. 13 (17) (2020) 1–23, <https://doi.org/10.3390/MA13173744>.
- [47] T. Do, T.J. Bauder, H. Suen, K. Rego, J. Yeom, and P. Kwon, "Additively manufactured full-density stainless steel 316 L with binder jet printing," ASME 2018 13th Int. Manuf. Sci. Eng. Conf. MSEC 2018, vol. 1, no. October, 2018, doi: 10.1115/MSEC2018-6681.
- [48] C.E. Duty, V. Kunc, B. Compton, B. Post, D. Erdman, R. Smith, R. Lind, P. Lloyd, L. Love, "Structure and mechanical behavior of Big Area Additive Manufacturing (BAAM) materials", Rapid Prototyp. J. vol. 23 (1) (2017) 181–189, <https://doi.org/10.1108/RPJ-12-2015-0183>.
- [49] F. Lorenz, J. Rudolph, and R. Werner, "Design of 3D Printed High Performance Windings for Switched Reluctance Machines," 2018 XIII Int. Conf. Electr. Mach., pp. 2451–2457, 2018, doi: 10.1109/ICELMACH.2018.8506845.
- [50] T.N. Lamichhane, L. Sethuraman, A. Dalagan, H. Wang, J. Keller, M. P. Paranthaman, "Additive manufacturing of soft magnets for electrical machines—A review", Mater. Today Phys. vol. 15 (2020), 100255 <https://doi.org/10.1016/j.mtphys.2020.100255>.
- [51] M. Quarto, M. Carminati, G. D'Urso, "Density and shrinkage evaluation of AISI 316L parts printed via FDM process", Mater. Manuf. Process. vol. 36 (13) (2021) 1535–1543, <https://doi.org/10.1080/10426914.2021.1905830>.
- [52] D. Svirlybayev, B. Zharylkassyn, A. Seisekulova, M. Akhmetov, A. Perveen, D. Talamona, "Optimisation of strength properties of FDM printed parts—A critical review", Polym. (Basel) vol. 13 (2021) <https://doi.org/10.3390/polym13101587>.
- [53] M. Quarto, M. Carminati, G. D'Urso, C. Giardini, and G. Maccarini, "Processability of metal-filament through polymer FDM machine," ESAFORM 2021 - 24th Int. Conf. Mater. Form., vol. 13, pp. 1–11, 2021, doi: 10.25518/esaform21.2114.
- [54] Y. Thompson, J. Gonzalez-Gutierrez, C. Kukla, P. Felfel, "Fused filament fabrication, debinding and sintering as a low cost additive manufacturing method of 316L stainless steel", Addit. Manuf. vol. 30 (May) (2019), 100861 <https://doi.org/10.1016/j.addma.2019.100861>.
- [55] C. Tosto, J. Tirillò, F. Sarasini, G. Cicala, "Hybrid metal/polymer filaments for fused filament fabrication (FFF) to print metal parts", Appl. Sci. vol. 11 (4) (2021) 1, <https://doi.org/10.3390/app11041444>.
- [56] M. Ralchev, V. Mateev, I. Marinova, "3D printing of magnetic materials by FFF technology", 2020 12th Electr. Eng. Fac. Conf. BulEF 2020 (2020) 4–7, <https://doi.org/10.1109/BulEF51036.2020.9326060>.
- [57] B. Khatri, K. Lappe, D. Noetzel, K. Pirsche, T. Hanemann, "A 3D-printable polymer-metal soft-magnetic functional composite-development and characterization", Mater. (Basel) vol. 11 (2) (2018) <https://doi.org/10.3390/ma11020189>.
- [58] H. Tiismus, A. Kallaste, A. Belahcen, T. Vaimann, A. Rassolkin, D. Lukichev, "Hysteresis measurements and numerical losses segregation of additively manufactured silicon steel for 3D printing electrical machines", Appl. Sci. vol. 10 (18) (2020) 6515, <https://doi.org/10.3390/app10186515>.
- [59] H. Tiismus, A. Kallaste, A. Belahcen, M. Tarraste, T. Vaimann, A. Rassolkin, B. Asad, P. Shams Ghahfarokhi, "AC magnetic loss reduction of SLM processed Fe-Si for additive manufacturing of electrical machines", Energies vol. 14 (5) (2021) 1241, <https://doi.org/10.3390/en14051241>.
- [60] D. Goll, D. Schuller, G. Martinek, T. Kuerst, J. Schurr, C. Sinz, T. Schubert, T. Bernthaler, H. Riegel, G. Schneider, "Additive manufacturing of soft magnetic materials and components", Addit. Manuf. vol. 27 (December 2018) (2019) 428–439, <https://doi.org/10.1016/j.addma.2019.02.021>.
- [61] M. Garibaldi, I. Ashcroft, J.N. Lemke, M. Simonelli, R. Hague, "Effect of annealing on the microstructure and magnetic properties of soft magnetic Fe-Si produced via laser additive manufacturing", Scr. Mater. vol. 142 (2018) 121–125, <https://doi.org/10.1016/j.scriptamat.2017.08.042>.

- [62] A. Plotkowski, A. Pries, F. List, P. Nandwana, B. Stump, K. Carver, R.R. Dehoff, "Influence of scan pattern and geometry on the microstructure and soft-magnetic performance of additively manufactured Fe-Si", *Addit. Manuf.* vol. 29 (April) (2019) <https://doi.org/10.1016/j.addma.2019.100781>.
- [63] B. Koo, M.S. Jang, Y.G. Nam, S. Yang, J. Yu, Y.H. Park, J.W. Jeong, "Structurally-layered soft magnetic Fe-Si components with surface insulation prepared by shell-shaping selective laser melting", *Appl. Surf. Sci.* vol. 553 (February) (2021) 1–5, <https://doi.org/10.1016/j.apsusc.2021.149510>.
- [64] G. Stornelli, A. Faba, A. Di Schino, P. Folgarait, M.R. Ridolfi, E. Cardelli, R. Montanari, "Properties of additively manufactured electric steel powder cores with increased Si content", *Mater. (Basel)* vol. 14 (6) (2021) <https://doi.org/10.3390/ma14061489>.
- [65] H. Tiismus, A. Kallaste, A. Belachen, S. Member (no. c) "Hysteresis Loss Eval. Addit. Manuf. Soft Magn. Core." 2020 1657 1661.
- [66] T.Q. Pham, S. Member H. Suen, P. Kwon, S.N. Foster, S. Member "Reduction Hysteresis Loss Bind. Jet. Print. Iron Silicon." 2020 1669 1675.
- [67] C.L. Cramer, P. Nandwana, J. Yan, S.F. Evans, A.M. Elliott, C. Chinnasamy, M. P. Paranthaman, "Binder jet additive manufacturing method to fabricate near net shape crack-free highly dense Fe-6.5 wt% Si soft magnets", *Heliyon* vol. 5 (11) (2019), e02804 <https://doi.org/10.1016/j.heliyon.2019.e02804>.
- [68] T. Riipinen, S. Metsä-Kortelainen, T. Lindroos, J.S. Keränen, A. Manninen, J. Pippuri-Mäkeläinen, "Properties of soft magnetic Fe-Co-V alloy produced by laser powder bed fusion", *Rapid Prototyp. J.* (2019) <https://doi.org/10.1108/RPJ-06-2018-0136>.
- [69] V. Chaudhary, N.M. Sai Kiran Kumar Yadav, S.A. Mantri, S. Dasari, A. Jagetia, R. V. Ramanujan, R. Banerjee, "Additive manufacturing of functionally graded Co-Fe and Ni-Fe magnetic materials", *J. Alloy. Compd.* vol. 823 (2020), 153817 <https://doi.org/10.1016/j.jallcom.2020.153817>.
- [70] H.Y. Jung, S.J. Choi, K.G. Prashanth, M. Stoica, S. Scudino, S. Yi, U. Kühn, D. H. Kim, K.B. Kim, J. Eckert, "Fabrication of Fe-based bulk metallic glass by selective laser melting: A parameter study", *Mater. Des.* vol. 86 (2015) 703–708, <https://doi.org/10.1016/j.matdes.2015.07.145>.
- [71] S. Alleg, R. Drablia, N. Fenineche, "Effect of the laser scan rate on the microstructure, magnetic properties, and microhardness of selective laser-melted FeSiB", *J. Supercond. Nov. Magn.* vol. 31 (11) (2018) 3565–3577, <https://doi.org/10.1007/s10948-018-4621-z>.
- [72] T. Borkar, R. Conteri, X. Chen, R.V. Ramanujan, R. Banerjee, "Laser additive processing of functionally-graded Fe-Si-B-Cu-Nb soft magnetic materials", *Mater. Manuf. Process.* vol. 32 (14) (2017) 1581–1587, <https://doi.org/10.1080/10426914.2016.1244849>.
- [73] E. Peng, X. Wei, T.S. Herg, U. Garbe, D. Yu, J. Ding, "Ferrite-based soft and hard magnetic structures by extrusion free-forming", *RSC Adv.* vol. 7 (43) (2017) 27128–27138, <https://doi.org/10.1039/c7ra03251j>.
- [74] M.S.K.K.Y. Nartu, S. Dasari, A. Sharma, V. Chaudhary, S.M. Varahabhatla, S. A. Mantri, E. Ivanov, R.V. Ramanujan, N.B. Dahotre, R. Banerjee, "Reducing coercivity by chemical ordering in additively manufactured soft magnetic Fe-Co (Hiperco) alloys", *J. Alloy. Compd.* vol. 861 (2021), 157998 <https://doi.org/10.1016/j.jallcom.2020.157998>.
- [75] "Super Core TM Electrical steel sheets for high-frequency application." <https://www.jfe-steel.co.jp/en/products/electrical/catalog/11e-002.pdf> (accessed May 13, 2021).
- [76] S. Gao, X. Yan, C. Chang, E. Aubry, P. He, M. Liu, H. Liao, N. Fenineche, "Microstructure and magnetic properties of FeSiBCrC soft magnetic alloy manufactured by selective laser melting", *Mater. Lett.* vol. 290 (2021), 129469 <https://doi.org/10.1016/j.matlet.2021.129469>.
- [77] R.B. Goldfarb and F.R. Fickett, "Units for magnetic properties," 1985. doi: 10.6028/NBS.SP.696.
- [78] "Sintex® Soft Magnetic Composites." (<https://www.sintex.com/en/powder-metal/technical-data/category/smc>) (accessed May 14, 2021).
- [79] T.Q. Pham, T.T. Do, P. Kwon, S.N. Foster, "Additive manufacturing of high performance ferromagnetic materials", 2018 IEEE Energy Convers. Congr. Expo. ECCE 2018 (2018) 4303–4308, <https://doi.org/10.1109/ECCE.2018.8558245>.
- [80] A. Plotkowski, K. Carver, F. List, J. Pries, Z. Li, A.M. Rossy, D. Leonard, "Design and performance of an additively manufactured high-Si transformer core", *Mater. Des.* vol. 194 (2020) <https://doi.org/10.1016/j.matdes.2020.108894>.
- [81] H. Tiismus, A. Kallaste, A. Belachen, A. Rassolkina, T. Vaimann, P. Shams Ghahfarokhi, "Additive manufacturing and performance of E-Type transformer core", *Energies* vol. 14 (11) (. 2021) 3278, <https://doi.org/10.3390/en14113278>.
- [82] A. Krings, J. Souldard, "Overview and comparison of iron loss models for electrical machines", *J. Electr. Eng. vol.* 10 (3) (2010) 162–169.
- [83] G. Ouyang, X. Chen, Y. Liang, C. Macziewski, J. Cui, "Review of Fe-6.5 wt%Si high silicon steel—A promising soft magnetic material for sub-kHz application", *J. Magn. Magn. Mater.* vol. 481 (January) (2019) 234–250, <https://doi.org/10.1016/j.jmmm.2019.02.089>.
- [84] L. Gargalis, V. Madonna, P. Giangrande, S. Member, R. Rocca, M. Hardy, I.A. Ashcroft, M. Galea, S. Member, R. Hague, "Additive manufacturing and testing of a soft magnetic rotor for a switched reluctance motor" vol. 8 (2020), <https://doi.org/10.1109/ACCESS.2020.3037190>.
- [85] J. Gierse, D. Zimmer, T. Tr., "Soft-magnetic behavior of laser beam melted FeSi3 alloy with graded cross-section" vol. 296 (no) (2021), <https://doi.org/10.1016/j.jmatprotec.2021.117183>.
- [86] A. Kallaste, T. Vaimann, A. Belachen, "Influence of magnet material selection on the design of slow-speed permanent magnet synchronous generators for wind applications", *Elektron. Ir. Elektrov. vol.* 23 (1) (2017) 31–38, <https://doi.org/10.5755/j01.eie.23.1.17581>.
- [87] J. Jaćimović, F. Binda, L.G. Herrmann, F. Greuter, J. Genta, M. Calvo, T. Tomšič, R.A. Simon, "Net shape 3D printed NdFeB permanent magnet", *Adv. Eng. Mater.* vol. 19 (8) (2017) 1–7, <https://doi.org/10.1002/adem.201700098>.
- [88] R. Ramesh, G. Thomas, B.M. Ma, "Magnetization reversal in nucleation controlled magnets. II. Effect of grain size and size distribution on intrinsic coercivity of Fe-Nd-B magnets", *Am. Inst. Phys.* (1988) <https://doi.org/10.1063/1.342055>.
- [89] "magnetization reversal in nucleation controlled magnets. I. Theory; and II. Effect of grain size and size distribution on intrinsic coercivity of Fe-Nd-B magnets", *J. Appl. Phys.*, vol. 69, no. 6, p. 3778, 1991, doi: 10.1063/1.348477.
- [90] H.A. Khazdoian, J.S. Manzano, K. Gandha, I.I. Slowing, I.C. Nlebedim, "Recycled Sm-Co bonded magnet filaments for 3D printing of magnets", *AIP Adv.* vol. 8 (5) (2018) <https://doi.org/10.1063/1.5007669>.
- [91] E.M.H. White, A.G. Kassen, E. Simsek, W. Tang, R.T. Ott, I.E. Anderson, "Net shape processing of alnico magnets by additive manufacturing", *IEEE Trans. Magn.* vol. 53 (11) (2017) <https://doi.org/10.1109/TMAG.2017.2711965>.
- [92] E.M. Palmero, D. Casaleiz, N.A. Jimenez, J. Rial, J. De Vicente, A. Nieto, R. Altimira, A. Bollero, "Magnetic-polymer composites for bonding and 3d printing of permanent magnets", *IEEE Trans. Magn.* vol. 55 (2) (2019) <https://doi.org/10.1109/TMAG.2018.2863560>.
- [93] T. Hanemann, D. Syperek, D. Nötzel, "3D printing of ABS barium ferrite composites", *Mater. (Basel)* vol. 13 (6) (2020) 1481, <https://doi.org/10.3390/ma13061481>.
- [94] A.B. Baldissera, P. Pavez, P.A.P. Wendhausen, C.H. Ahrens, J.M. Mascheroni, "Additive manufacturing of bonded Nd-Fe-B - Effect of process parameters on magnetic properties", *IEEE Trans. Magn.* vol. 53 (11) (. 2017) <https://doi.org/10.1109/TMAG.2017.2715722>.
- [95] M.P. Paranthaman, C.S. Shafer, A.M. Elliott, D.H. Siddel, M.A. McGuire, R. M. Springfield, J. Martin, R. Fredette, J. Ormerod, "Binder Jetting: A novel NdFeB bonded magnet fabrication process", *JOM* vol. 68 (7) (2016) 1978–1982, <https://doi.org/10.1007/s11837-016-1883-4>.
- [96] C. Huber, C. Abert, F. Bruckner, M. Groenefeld, O. Muthsam, S. Schuschnigg, K. Sirak, R. Thanhoffer, I. Teliban, C. Vogler, R. Windl, D. Suess, "3D print of polymer bonded rare-earth magnets, and 3D magnetic field scanning with an end-user 3D printer", *Appl. Phys. Lett.* vol. 109 (16) (2016) <https://doi.org/10.1063/1.4964856>.
- [97] A. Shen, C.P. Bailey, A.W.K. Ma, S. Dardona, "UV-assisted direct write of polymer-bonded magnets", *J. Magn. Magn. Mater.* vol. 462 (2018) 220–225, <https://doi.org/10.1016/j.jmmm.2018.03.073>.
- [98] C. Huber, C. Abert, F. Bruckner, M. Groenefeld, S. Schuschnigg, I. Teliban, C. Vogler, G. Wautischer, R. Windl, Di Sues, "3D printing of polymer-bonded rare-earth magnets with a variable magnetic compound fraction for a predefined stray field", *Sci. Rep.* vol. 7 (1) (2017) 1–8, <https://doi.org/10.1038/s41598-017-09864-0>.
- [99] B.G. Compton, J.W. Kemp, T.V. Novikov, R.C. Pack, C.I. Nlebedim, C.E. Dute, O. Rios, M.P. Paranthaman, "Direct-write 3D printing of NdFeB bonded magnets", *Mater. Manuf. Process.* vol. 33 (1) (2018) 109–113, <https://doi.org/10.1080/10426914.2016.1221097>.
- [100] L. Li, K. Jones, B. Sales, J.L. Pries, I.C. Nlebedim, K. Jin, H. Bei, B.K. Post, M. S. Kesler, O. Rios, V. Kunc, R. Fredette, J. Ormerod, A. Williams, T.A. Logrosso, M. P. Paranthaman, "Fabrication of highly dense isotropic Nd-Fe-B nylon bonded magnets via extrusion-based additive manufacturing", *Addit. Manuf.* vol. 21 (no) (2017) 495–500, <https://doi.org/10.1016/j.addma.2018.04.001>, 2018.
- [101] L. Li, A. Tirado, I.C. Nlebedim, O. Rios, B. Post, V. Kunc, R.R. Lowden, E. Laracuzio, R. Fredette, J. Ormerod, T.A. Logrosso, M.P. Paranthaman, "Big area additive manufacturing of high performance bonded NdFeB magnets", *Sci. Rep.* vol. 6 (October) (2016) 1–7, <https://doi.org/10.1038/srep36212>.
- [102] J. Wu, N.T. Aboulkhair, M. Degano, I. Asheroff, R.J.M. Hague, "Process-structure-property relationships in laser powder bed fusion of permanent magnetic Nd-Fe-B", *Mater. Des.* vol. 209 (July) (2021), 109992 <https://doi.org/10.1016/j.matdes.2021.109992>.
- [103] E. White, E. Rinko, T. Prost, T. Horn, C. Ledford, C. Rock, I. Anderson, "Processing of Alnico Magnets by additive manufacturing", *Appl. Sci.* vol. 9 (22) (2019) <https://doi.org/10.3390/app9224843>.
- [104] D. Goll, F. Trauter, T. Bernthaler, J. Schanz, H. Riegel, G. Schneider, "Additive manufacturing of bulk nanocrystalline fendb based permanent magnets", *Micromachines* vol. 12 (5) (2021) <https://doi.org/10.3390/mi12050538>.
- [105] J. Slapnik, I. Pulko, R. Rudolf, I. Anzel, M. Bruncko, "Fused filament fabrication of Nd-Fe-B bonded magnets: Comparison of PA12 and TPU matrices", *Addit. Manuf.* vol. 38 (2021) <https://doi.org/10.1016/j.addma.2020.101745>.
- [106] K. Gandha, L. Li, I.C. Nlebedim, B.K. Post, V. Kunc, B.C. Sales, J. Bell, M. P. Paranthaman, "Additive manufacturing of anisotropic hybrid NdFeB-SmFeN nylon composite bonded magnets", *J. Magn. Magn. Mater.* vol. 467 (June) (2018) 8–13, <https://doi.org/10.1016/j.jmmm.2018.07.021>.
- [107] O. Gutfleisch, M.A. Willard, E. Brück, C.H. Chen, S.G. Sankar, J.P. Liu, "Magnetic materials and devices for the 21st century: Stronger, lighter, and more energy efficient", *Adv. Mater.* vol. 23 (7) (2011) 821–842, <https://doi.org/10.1002/adma.201002180>.
- [108] B.M. Ma, J.W. Herchenroeder, B. Smith, M. Suda, D. Brown, Z. Chen, "Recent development in bonded NdFeB magnets", *J. Magn. Magn. Mater.* vol. 239 (1–3) (2002) 418–423, [https://doi.org/10.1016/S0304-8853\(01\)00609-6](https://doi.org/10.1016/S0304-8853(01)00609-6).
- [109] M.S. Kang, K.M. Kim, H.W. Kwon, D.H. Kim, J.G. Lee, K.H. Shin, "Electrical resistivity and magnetic performance of ceramic-bonded nd-fe-b-type magnet consolidated using dielectric oxide binder", *IEEE Trans. Magn.* vol. 55 (7) (. 2019) <https://doi.org/10.1109/TMAG.2019.2896889>.

- [110] A. Sarkar, M.P. Paranthaman, I.C. Nlebedim, "In-situ magnetic alignment model for additive manufacturing of anisotropic bonded magnets", *Addit. Manuf.* vol. 46 (February) (2021), 102096 <https://doi.org/10.1016/j.addma.2021.102096>.
- [111] F. Bittner, J. Thielsch, W.G. Drossel, "Laser powder bed fusion of Nd-Fe-B permanent magnets", *Prog. Addit. Manuf.* vol. 5 (1) (2020) 3–9, <https://doi.org/10.1007/s40964-020-00117-7>.
- [112] J. Jung, A. Helm, J. Liebold, "Improved efficiency of electric drives with additively manufactured roebel bar windings", *MTZ World* vol. 82 (4) (2021) 54–58, <https://doi.org/10.1007/s38313-021-0634-2>.
- [113] "Copper Conductivity Materials Database: selection criteria and properties." <https://copperalliance.org.uk/about-copper/conductivity-materials/> (accessed Jun. 03, 2021).
- [114] R. Guschlbauer, S. Momeni, F. Osmanlic, C. Körner, "Process development of 99.95% pure copper processed via selective electron beam melting and its mechanical and physical properties", *Mater. Charact.* vol. 143 (March) (2018) 163–170, <https://doi.org/10.1016/j.matchar.2018.04.009>.
- [115] C. Silbernagel, L. Gargalis, I. Ashcroft, R. Hague, M. Galea, P. Dickens, "Electrical resistivity of pure copper processed by medium-powered laser powder bed fusion additive manufacturing for use in electromagnetic applications", *Addit. Manuf.* vol. 29 (July) (2019), 100831 <https://doi.org/10.1016/j.addma.2019.100831>.
- [116] S. Engler, R. Ramsayer, R. Poprawe, "Process studies on laser welding of copper with brilliant green and infrared lasers", *Phys. Procedia* vol. 12 (PART 2) (. 2011) 339–346, <https://doi.org/10.1016/j.phpro.2011.03.142>.
- [117] S. Zhang, H. Zhu, L. Zhang, W. Zhang, H. Yang, X. Zeng, "Microstructure and properties of high strength and high conductivity Cu-Cr alloy components fabricated by high power selective laser melting", *Mater. Lett.* vol. 237 (2019) 306–309, <https://doi.org/10.1016/j.matlet.2018.11.118>.
- [118] A. Yegyan Kumar, J. Wang, Y. Bai, S.T. Huxtable, and C.B. Williams, "Impacts of process-induced porosity on material properties of copper made by binder jetting additive manufacturing," *Mater. Des.*, vol. 182, p. 108001, 2019, doi: 10.1016/j.matdes.2019.108001.
- [119] J.C. Tan, H.Y. Low, "Embedded electrical tracks in 3D printed objects by fused filament fabrication of highly conductive composites", *Addit. Manuf.* vol. 23 (April) (2018) 294–302, <https://doi.org/10.1016/j.addma.2018.06.009>.
- [120] T.B. Palmić, J. Slavić, M. Boltezar, "Process parameters for fff 3d-printed conductors for applications in sensors", *Sens. (Switz.)* vol. 20 (16) (2020) 1–21, <https://doi.org/10.3390/s20164542>.
- [121] T. Rautio, A. Hamada, J. Kumpulaa, A. Järvenpää, T. Allam, "Enhancement of electrical conductivity and corrosion resistance by silver shell-copper core coating of additively manufactured AlSi10Mg alloy", *Surf. Coat. Technol.* vol. 403 (September) (2020), 126426 <https://doi.org/10.1016/j.surfcoat.2020.126426>.
- [122] P. Frigola, O. Harrysson, T. Horn, H. West, R. Aman, J. Rigsbee, D. Ramirez, F. Medina, R. Wicker, E. Rodriguez, "Fabricating copper components with electron beam melting", *Adv. Mater. Process.* (2014) 20.
- [123] S.D. Jadhav, S. Dadbakhsh, L. Goossens, J.P. Kruth, J. Van Humbeeck, K. Vanmeensel, "Influence of selective laser melting process parameters on texture evolution in pure copper", *J. Mater. Process. Technol.* vol. 270 (February) (2019) 47–58, <https://doi.org/10.1016/j.jmatprotec.2019.02.022>.
- [124] S.J. Raab, R. Guschlbauer, M.A. Lodes, C. Körner, "Thermal and electrical conductivity of 99.9% pure copper processed via selective electron beam melting", *Adv. Eng. Mater.* vol. 18 (9) (. 2016) 1661–1666, <https://doi.org/10.1002/adem.201600078>.
- [125] A.P. Ventura, C.J. Marvel, G. Pawlikowski, M. Bayes, M. Watanabe, R.P. Vinci, W. Z. Misiolok, "The effect of aging on the microstructure of selective laser melted Cu-Ni-Si", *Metall. Mater. Trans. A Phys. Metall. Mater. Sci.* vol. 48 (12) (2017) 6070–6082, <https://doi.org/10.1007/s11661-017-4363-8>.
- [126] M. Abdelhafiz, K.S. Al-Rubaie, A. Emadi, M.A. Elbestawi, "Process-structure-property relationships of copper parts manufactured by laser powder bed fusion", *Mater. (Basel)* vol. 14 (11) (2021) 2945, <https://doi.org/10.3390/ma14112945>.
- [127] Y. Shi, P. Rometsch, K. Yang, F. Palm, X. Wu, "Characterisation of a novel Sc and Zr modified Al-Mg alloy fabricated by selective laser melting", *Mater. Lett.* vol. 196 (2017) 347–350, <https://doi.org/10.1016/j.matlet.2017.03.089>.
- [128] S.D. Jadhav, L.R. Goossens, Y. Kinds, B. Van Hooreweder, K. Vanmeensel, "Laser-based powder bed fusion additive manufacturing of pure copper", *Addit. Manuf.* vol. 42 (February) (2021) <https://doi.org/10.1016/j.addma.2021.101990>.
- [129] T. Wegener, J. Koopmann, J. Richter, P. Krooß, T. Niendorf, "CuCrZr processed by laser powder bed fusion—Processability and influence of heat treatment on electrical conductivity, microstructure and mechanical properties", *Fatigue Fract. Eng. Mater. Struct.* vol. 44 (9) (2021) 2570–2590, <https://doi.org/10.1111/ffe.13527>.
- [130] S.D. Jadhav, J. Vleugels, J.P. Kruth, J. Van Humbeeck, K. Vanmeensel, "Mechanical and electrical properties of selective laser-melted parts produced from surface-oxidized copper powder", *Mater. Des. Process. Commun.* vol. 2 (2) (2020) 1–8, <https://doi.org/10.1002/mdp2.94>.
- [131] S.D. Jadhav, S. Dadbakhsh, J. Vleugels, J. Hofkens, P. Van Puyvelde, S. Yang, J. P. Kruth, J. Van Humbeeck, K. Vanmeensel, Influence of carbon nanoparticle addition (and impurities) on selective laser melting of pure copper, *Mater. (Basel)* 12 (15) (2019), 2469, <https://doi.org/10.3390/ma12152469>.
- [132] D. Tiberto, U.E. Klotz, F. Held, G. Wolf, "Additive manufacturing of copper alloys: influence of process parameters and adding elements", *Mater. Sci. Technol. (U. Kingd.)* vol. 35 (8) (2019) 969–977, <https://doi.org/10.1080/02670836.2019.1600840>.
- [133] S.D. Jadhav, D. Fu, M. Deprez, K. Ramharther, D. Willems, B. Van Hooreweder, K. Vanmeensel, "Highly conductive and strong CuSn0.3 alloy processed via laser powder bed fusion starting from a tin-coated copper powder", *Addit. Manuf.* vol. 36 (August) (2020), 101607 <https://doi.org/10.1016/j.addma.2020.101607>.
- [134] S. Zhang, H. Zhu, Z. Hu, X. Zeng, F. Zhong, "Selective Laser Melting of Cu-10Zn alloy powder using high laser power", *Powder Technol.* vol. 342 (2019) 613–620, <https://doi.org/10.1016/j.powtec.2018.10.002>.
- [135] S. Gruber, L. Stepien, E. López, F. Brueckner, C. Leyens, "Physical and geometrical properties of additively manufactured pure copper samples using a green laser source", *Mater. (Basel)* vol. 14 (13) (2021) <https://doi.org/10.3390/ma14133642>.
- [136] C. Silbernagel, I. Ashcroft, P. Dickens, M. Galea, "Electrical resistivity of additively manufactured AlSi10Mg for use in electric motors", *Addit. Manuf.* vol. 21 (2018) 395–403, <https://doi.org/10.1016/j.addma.2018.03.027>.
- [137] E. Uhlmann, A.E. Tekkaya, V. Kasjevko, S. Gies, R. Reimann, and P. John, "Qualification of CuCr1 for the SLM Process," 7th Int. Conf. High Speed Form., no. April, pp. 173–182, 2016, [Online]. Available: <https://eldorado.tu-dortmund.de/handle/2003/34936>.
- [138] J. Kwack, S. Min, J.P. Hong, "Optimal stator design of interior permanent magnet motor to reduce torque ripple using the level set method", *IEEE Trans. Magn.* vol. 46 (6) (2010) 2108–2111, <https://doi.org/10.1109/TMAG.2010.2044871>.
- [139] S. Urbanek, P. Frey, S. Magerkohl, D. Zimmer, L. Tasche, M. Schaper, and B. Ponick, "Design and Experimental Investigation of an Additively Manufactured PMSM Rotor," in 2021 IEEE International Electric Machines & Drives Conference (IEMDC), May 2021, pp. 1–6. doi: 10.1109/IEMDC47953.2021.9449566.
- [140] J. Blum, J. Merwerth, and H.G. Herzog, "Investigation of the segment order in step-skewed synchronous machines on noise and vibration," 2014 4th Int. Electr. Drives Prod. Conf. EDPC 2014 - Proc., Dec. 2014, doi: 10.1109/EDPC.2014.6984413.
- [141] N. Simpson, D.J. North, S.M. Collins, P.H. Mellor, "Additive manufacturing of shaped profile windings for minimal AC loss in electrical machines", *IEEE Trans. Ind. Appl.* vol. 56 (3) (2020) 2510–2519, <https://doi.org/10.1109/TIA.2020.2975763>.
- [142] N. Simpson and P.H. Mellor, "Additive manufacturing of shaped profile windings for minimal AC loss in gapped inductors," 2017 IEEE Int. Electr. Mach. Drives Conf. IEMDC 2017, no. 1, pp. 1–7, 2017, doi: 10.1109/IEMDC.2017.8002337.
- [143] F. Lange, C. Hein, G. Li, and C. Emmelmann, "Numerical optimization of active heat sinks considering restrictions of selective laser melting," *COMSOL Conf. 2018 Lausanne*, no. October, pp. 0–7, 2018.
- [144] "Integrated cooling in electric motor housing developed using metal Additive Manufacturing." (<https://www.metal-am.com/integrated-cooling-in-electric-motor-housing-developed-using-metal-additive-manufacturing/>) (accessed Sep. 28, 2021).
- [145] "Applications - Additive Drives." <https://www.additive-drives.de/en/applications/> (accessed Sep. 02, 2021).
- [146] H. Zhang, S. Wang, "Topology optimization of rotor pole in switched reluctance motor for minimum torque ripple," *Electr. Power Compon. Syst.* vol. 45 (8) (2017) 905–911, <https://doi.org/10.1080/15325008.2017.1310769>.

Publication II

H. Tiismus, A. Kallaste, T. Vaimann, L. Lind, I. Virro, A. Rassõlkin, and T. Dedova, "Laser Additively Manufactured Magnetic Core Design and Process for Electrical Machine Applications," *Energies*, vol. 15, no. 10, 2022, doi: <https://doi.org/10.3390/en15103665>.

Article

Laser Additively Manufactured Magnetic Core Design and Process for Electrical Machine Applications

Hans Tiismus ^{1,*}, Ants Kallaste ¹, Toomas Vaimann ¹, Liina Lind ², Indrek Virro ³, Anton Rassõlkin ¹ and Tatjana Dedova ⁴

¹ Department of Electrical Power Engineering and Mechatronics, Tallinn University of Technology, Ehitajate tee 5, 19086 Tallinn, Estonia; ants.kallaste@taltech.ee (A.K.); toomas.vaimann@taltech.ee (T.V.); anton.rassolkin@taltech.ee (A.R.)

² Department of Mechanical and Industrial Engineering, Tallinn University of Technology, Ehitajate tee 5, 19086 Tallinn, Estonia; liina.lind@taltech.ee

³ Institute of Forestry and Engineering, Estonian University of Life Sciences, Fr. R. Kreutzwaldi 1, 51006 Tartu, Estonia; indrek.virro@emu.ee

⁴ Department of Materials Science, Tallinn University of Technology, Ehitajate tee 5, 19086 Tallinn, Estonia; tatjana.dedova@taltech.ee

* Correspondence: hans.tiismus@taltech.ee

Abstract: Additive manufacturing (AM) is considered the enabling technology for topology optimized components, with its unparalleled, almost free-form design freedom. Over the past decade, AM of electromagnetic materials has evolved into a promising new area of research. Considerable efforts have also been invested by the electrical machine (EM) research community to develop and integrate novel additive components. Several challenges remain, however, in printing soft magnetic flux guides—most prominently, reducing the induced eddy currents to achieve competitive AM core efficiency. This paper demonstrates the workflow of laser additive manufacturing magnetic cores with superior magnetic properties to soft magnetic composites (at 50 Hz excitation): describing the workflow, parameter tuning for both printing and annealing, and shape optimization. Process optimization yielded the optimal energy density of 77 J/mm³ and annealing temperature of 1200 °C, applied to prepare the samples with the highest relative density (99.86%), lowest surface roughness R_z (0.041 mm), minimal hysteresis losses (0.8 W/kg at 1.0 T, 50 Hz), and ultimate yield strength of 420 MPa. For Eddy current suppression, the sample (5 × 5 × 60 mm toroid) with bi-directional grading reached specific core losses as low as 1.8 W/kg (W_{10,50}). Based on the findings, the advantages and disadvantages of AM graded cores are discussed in detail.

Keywords: additive manufacturing; electrical machines; soft magnetic materials; hysteresis loss; eddy current loss; annealing; selective laser melting



Citation: Tiismus, H.; Kallaste, A.; Vaimann, T.; Lind, L.; Virro, I.; Rassõlkin, A.; Dedova, T. Laser Additively Manufactured Magnetic Core Design and Process for Electrical Machine Applications. *Energies* **2022**, *15*, 3665. <https://doi.org/10.3390/en15103665>

Academic Editors: João Filipe Pereira Fernandes and Silvio Vaschetto

Received: 25 April 2022

Accepted: 13 May 2022

Published: 17 May 2022

Publisher's Note: MDPI stays neutral with regard to jurisdictional claims in published maps and institutional affiliations.



Copyright: © 2022 by the authors. Licensee MDPI, Basel, Switzerland. This article is an open access article distributed under the terms and conditions of the Creative Commons Attribution (CC BY) license (<https://creativecommons.org/licenses/by/4.0/>).

1. Introduction

1.1. Additive Manufacturing of Electrical Machines

Metal additive manufacturing (AM) of electromagnetic materials is a developing research field. AM of electrical machines (EMs) has its roots in the beginning of the last decade, in 2013–2015, with the first experimentations and discussions in AM electro-mechanical systems [1,2]. A few years later, in 2018–2019, the first overviews on the feasibility of additively manufactured electrical machines started appearing [3–5]. The reviews proposed two main advantages of 3D-printed EMs. Firstly, it was suggested that the three-dimensional fabrication freedom of AM coupled with the topological optimization capacity of digital systems would open a new epoch in the design of electrical machines. The relatively inert EM industry could benefit from fully three-dimensional complex machine shapes, facilitated by the AMs near free-form production capacity. Some novel EM design features, such as optimized magnetic circuits, weight reduction, coil shaping, or enhanced

heat extraction, have been outlined in [6–9]. Secondly, AM is considered an integral part of the next industrial revolution. Undoubtedly, for printed end-use products to be profoundly meaningful, additional features to just complex structural shaping parts, such as embedded electric, magnetic, or electro-mechanical components are vital. This would translate to streamlined printing of mass-customized goods with integrated moving parts (motors, gearboxes, and actuators) and electrical circuits in industry 4.0 smart factories, without extensive manual post-processing and assembling.

In the current state-of-the-art, additive manufacturing of a complete electrical machine has not yet been completed. Three-dimensional printing of an EM is a technically demanding procedure due to the tight tolerances involved in its moving parts (the smaller the air gap, the larger the power density) and their construction from several vastly different materials. In electrical motors, electrically insulated conductors of magnetic flux and electric current are used. The materials involved, however, exhibit incompatible thermal, chemical, and optical (absorptivity) behaviors, and require the development of advanced hybrid multi-material printing methods for parallel printing. Because of this, prototyping of AM electrical machines has focused on printing individual optimized single-material parts (e.g., copper coils, soft-magnetic rotors, alumina heat-guides etc.) and investigating their impact if inserted within a motorette assembly or a conventional electrical machine.

From the perspective of AM soft magnetic iron cores, considerable steps have been accomplished [10–12]. High core saturation magnetization and permeability values have been achieved. Nevertheless, the process of obtaining structurally optimal AM cores with the lowest core losses is largely uncharted. This paper aims to provide the reader with the optimal process flow (before, after, and during printing) for preparing high-performance soft magnetic cores with laser additive manufacturing. Optimal energy density and parameters are determined for preparing the samples with maximum relative density and minimal surface roughness. Annealing parameters are investigated to obtain the highest sample permeability and lowest quasi-static (also DC or hysteresis) losses. Topological refinement effects (introduction of insulating voids or air gaps) are investigated for eddy current loss purposes. Finally, the obtained material properties are compared with conventional soft magnetic materials in terms of magnetic polarization and total core losses to evaluate the maturity of soft magnetic materials for commercial applications.

1.2. Soft Magnetic Material Properties

AM components can achieve superior characteristics over their commercial counterparts through optimized topologies. If the AM material properties are subpar to conventional materials, however, there is little room to optimize. Therefore, to justify the commercial adaptation of AM components, the intrinsic material properties involved must exhibit at least roughly equivalent characteristics to their commercial counterparts. The industrial standard for electrical motor core construction material is crystalline silicon steel. It offers both low energy losses from cyclic material magnetization (high efficiency) and high flux densities within the core (high power density) at a competitive price point. Whether produced through subtractive or additive means, the realization of high-performance silicon steels is technically challenging. This is because they are iron-based metallic alloys—complicating their casting/machining/printing due to their high melting point and hardness. Secondly, their properties heavily depend on crystallographic texture. Drawing on previous work, it is well established that the five most impactful material characteristics determining the properties of electrical steel alloys are impurity content, granular size, internal residual stress, alloying silicon content, and lamination sheet thickness. The effect of these characteristics on the properties of crystalline steels is summarized in Figure 1. Within the figure, core losses P_c are further subdivided into hysteresis losses P_{hyst} , classical eddy current losses P_{ce} , and anomalous eddy current losses P_{an} with regards to the different physical phenomena involved. Additionally, M_s denotes the maximum magnetic saturation (material polarization at $\mu_r = 1$), H_c —coercivity, σ_y —ultimate tensile strength, σ —material electrical conductivity, and λ —thermal conductivity. The table is

color-coded to correlate better the most impactful physical phenomena associated with each material property. As a rule of thumb, eliminating impurities and internal stresses in crystalline [13–24] soft magnetic materials leads to more useful magnetic properties. This is why annealing is critical in the magnetic steel preparation process, enabling decarburization (in a specific process environment), stress relaxation/grain structure recovery (at low temperature), and recrystallization/grain growth (at high temperature). While indispensable in lowering the material’s hysteresis losses and increasing its magnetic responsiveness, annealing is ineffective in decreasing Joule heating losses—the classical and excess eddy current losses. These losses can most effectively be suppressed through silicon additives, optimized material grain size, and segregated/laminated internal structure to limit the flow of electrical charge through the magnetically exciting material. Before the emergence of AM, EM material-focused research groups were focused mainly on investigating the post-processing effects of commercially available mass-produced lamination sheets produced through thoroughly optimized methods. For example, this included the investigation of cutting [25] or coating [26] effects on the individual stampings to optimize the process even further. With the advent of additive manufacturing of electromagnetic materials and components, significantly more diverse challenges are encountered, as with AM: the full production cycle of an electromagnetic component is completable in-house. Based on the academic literature and our experience with laser AM, we outlined the most impactful steps in Figure 2 for obtaining desirable soft magnetic material physical characteristics with laser powder bed fusion (L-PBF). The considerations are subdivided based on their timing window: i.e., considerations or actions that are applicable before, during, or after printing.

Physical Characteristics	M_s	H_c	μ	P_{hyst}	P_{ce}	P_{an}	σ	λ	σ_y
↑ Impurities	↓	↑	↓	↑	↓	↓	↓	↓	↓
↑ Grain Size	-	↓	↑	↓	-	↑	-	-	↓
↑ Internal Stress	-	↑	↓	↑	-	-	-	-	↑
↑ Silicon Content	↓	↓	↑	↓	↓	↓	↓	↓	↓
↑ Sheet Thickness	↑	↓	↑	↓	↑	↑	↑	↑	↑

							
(a)	(b)	(c)	(d)	(e)	(f)	(g)	(h)

Figure 1. Effect of physical characteristics on soft magnetic material properties: (a) Maximum magnetic saturation (at $\mu_r = 1$) is independent of grain size and proportional to the density of soft magnetic phase in material [13]. With lower sheet thickness and higher silicon content more nonmagnetic material is introduced to the core (varnish and silicon). (b) Imperfections within the crystallographic structure (including lattice dislocations, grain deformation (internal stress), foreign substituting and interstitial atoms, grain boundaries, pores, cracks) act as pinning sites for the magnetic domains [14,15]—requiring more energy for orientation. Thinner lamination layers generally result in higher hysteresis losses due to restricted grain size [16]. (c) High silicon steel content (optimal 6.5%) reduces material magnetostriction (increased permeability) [17], requiring less energy for domain orientation within a magnetic field. (d) Chemical impurities and macroscopic material defects (cracks, pores, delaminations) reduce the overall electron mobility in the metals—reducing both the thermal and electrical conductivity, and by association Joule heating losses [18]. (e) Internal electrical resistance of electrical steel components is best increased through laminated structure—effectively suppressing induced eddy current losses [16]. (f) Anomalous losses account for

the microscopic eddy currents arising from the domain wall motion—with smaller grains; reduced microscopic eddy currents are generated [19]. (g) With silicon content above 3%, the brittleness of steels is increased substantially [20]. Ultimate yield strength of steel has been shown to be relatively insensitive to significant porosity content [21], but highly sensitive to any cracking/delamination [22]. (h) Material yield strength has been shown to be inversely proportional to the square root of its grain diameter [23]. The residual stresses from production processes or cold working (plastic deformation) increase a materials mechanical strength through dislocation accumulation [24].

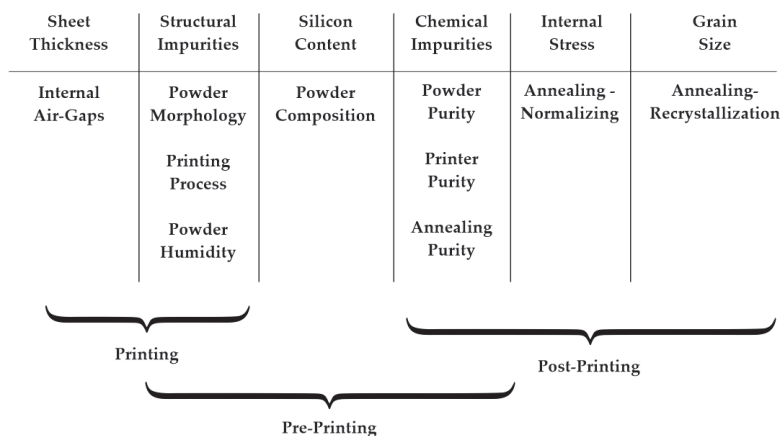


Figure 2. Main considerations before, during, and after printing for improving L-PBF Fe-Si core characteristics.

We propose a five-step workflow for optimizing and mapping AM-prepared soft magnetic materials, as outlined in Figure 3. The utilization of the workflow is demonstrated in the experimental section of the paper. Starting with the pre-printing process, the most critical pre-L-PBF printing step is undoubtedly raw powder preparation. First, only high purity powders should be used, as compositional enhancements of complex parts are most likely unattainable post-printing. Based on our experience, it is imperative to verify the properties of the supplied powder in-house before printing, as it can deviate significantly from the manufacturer’s declaration. Secondly, it is recommended to dry the raw powder before the process [27], as humid powders have been linked to both lower powder flowability and increased hydrogen porosity formation. Thirdly, PBF processes require specific particle shape and size distribution to ensure as uniform and dense powder bed packing as possible [28,29] in order to fuse homogeneous layers. In L-PBF, these powder layers are fused with a laser source in a fashion similar to micro-welding, with a risk of cracking or voids remaining within the substrate. Excessive laser energy input during this process is related to deformed printed parts (warping, uneven growth due to balling, delaminations, and thermal cracking), whereas too low energy input—with insufficient inter-layers/track fusion and subsequent high porosity content. With the powder and printing process optimized to the degree to prepare near fully dense parts, the next critical step is the annealing of the material. Annealing is indispensable in preparing L-PBF soft magnetic components, as rapid cooling rates associated with the micro-welding process result in the formation of a refined granular structure (printed grains are typically in the range of 1 μm or less), well known for its suboptimal soft magnetic characteristics.

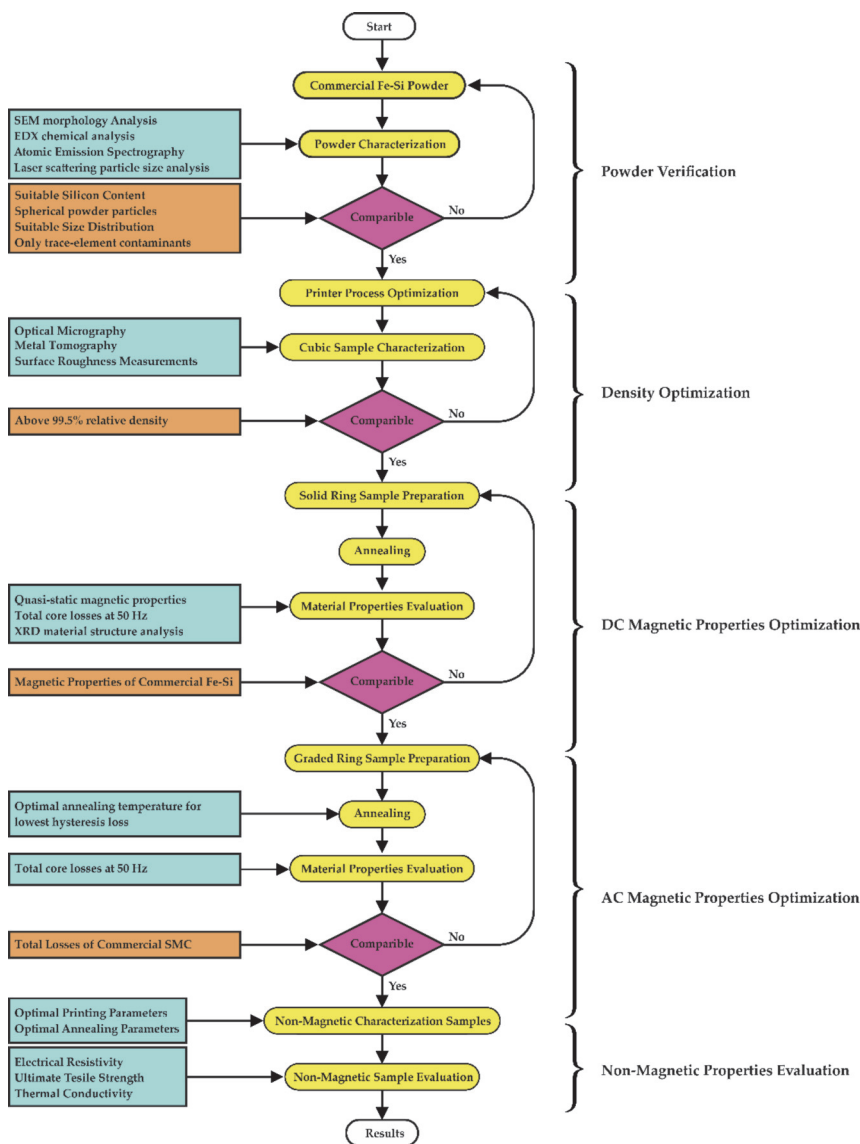


Figure 3. Five step flowchart for L-PBF Fe-Si magnetic core properties optimization process.

The focus of this paper is on obtaining magnetic cores that exhibit useful DC and AC magnetic properties. With the exception of ultimate tensile strength, non-magnetic material properties are not investigated in this paper; they are planned for future work. With the confirmation of desirable powder composition, morphology, and size distribution, the process can advance towards the optimization of printing melting parameters. In this paper, this process aims to obtain a near-fully dense material structure that is above 99.5% relative density. In parallel, the surface roughness of the printed samples is evaluated, as fully dense parts can also be achieved with excessive energy input, which can result in reduced spatial accuracy of the printed parts. This is due to the more intense spattering of droplets at higher input, which can be embedded into the part surface and deteriorate its surface finish [30]. The goals for the magnetic characterization steps are to obtain comparable

results to commercial materials. For the DC study—similar magnetization behavior to crystalline silicon steel; for the AC study—superior core losses to soft magnetic composite (SMC) cores. Obtaining equivalent AC losses to high-grade silicon steel laminations is considered unfeasible due to challenges in segregating the core topology in L-PBF systems (forming laminations). Total core losses at 50 Hz comparable to SMC magnetic cores should be within reach with printed air gaps into the material.

2. Experimental Methods

2.1. Printing Materials and Equipment

The material used in this investigation was commercially available Fe-Si pre-alloyed powder provided by Sandvik Osprey LTD. The powders were manufactured via the gas (nitrogen) atomization process, with a target chemical composition of Bal Fe, 2.0–4.0% Si, 0.05% max C, 0.2% max Mn, 0.2% max Cr, and 0.2% max Ni. Spherical powder particle morphology was targeted in 2% of the powder particles over 45 μm and 5% of those below 10 μm in size. These powder characteristics were ascertained in-house prior to printing.

The chemical composition of powders was determined with two methods: AES (atomic emissions spectrography) using Spectrolab M system and EDX (energy dispersive X-ray analysis) using a HR-SEM (high resolution scanning electron microscope) with an integrated Bruker Esprit 1.8 EDX detector. The SEM facility utilized for imaging was HR-SEM ZEISS FEG-SEM ULTRA-55. For powder particle size analysis, Horiba LA-950V2 laser scattering analyzer was employed. The measurements were conducted in a water dispersive environment. Flowability of the powder was determined with Hall Flowmeter measurements according to the EVS-EN ISO 4490:2018 standard. It comprised flow time measurements of 50 g of raw powder through a Ø2.5 mm hole in the Hall funnel. The powder chemical composition was in a good agreement with the manufacturer’s declaration, with the main constituting elements outlined in Table 1. The powder constituted of roughly spherical particles with the size of 29–58 μm, with a median diameter of 38 μm (d50) as shown in Figure 4a,b. The majority of the particles exhibited smaller attached satellites alongside some elongated elliptical particles. Despite the powder artifacts, the flow rate of the powder was acceptable; it was measured as 19.7 ± 0.24 s/50 g in the Hall funnel.

Table 1. Summary of powder chemical composition.

Elements	Fe	Si	Mn	Cr	Ni	C
Wt%	Balance	3.7	0.2	0.16	0.020	0.01

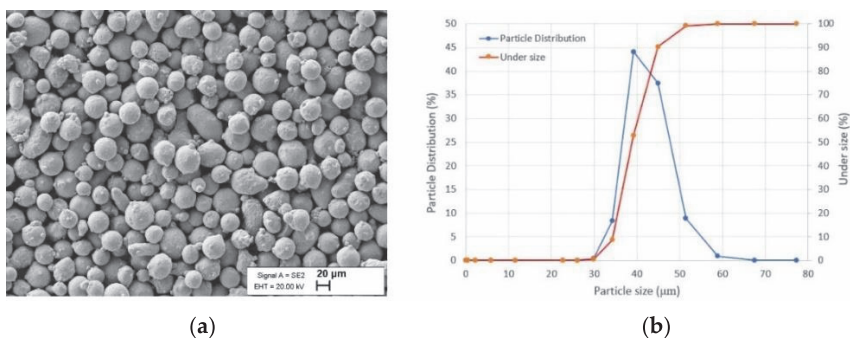


Figure 4. 3.7% silicon content steel powder morphology: (a) SEM micrograph of the powder shape; (b) powder particle size analysis.

All the samples were prepared with an SLM Solutions GmbH Realizer SLM-280 laser powder bed fusion system. The system exhibited a $280 \times 280 \times 350$ maximum build envelope and a single scanning 1070 nm yttrium scanning laser (1×400 W). To streamline research projects, a custom smaller build platform (D100 mm), re-coater, and feeder system were added to the printer. These additions reduced both the overall powder quantity required for printing (the full-sized platform requires 220 kg of 316 L powder to fill the full build envelope) and faster powder swapping between different research projects. The powder reservoir was 3D printed with the same printer on the full-size platform from stainless steel 316 L (wall thickness 1 mm). Initial testing of the re-coater prototype suggested the need to separate the powder reservoir from the substrate through a feeder tube, as the weight of the powder column above the substrate affected powder flowability and its deposition quality. Without the feeder tube, uneven accumulation of powder was observed on printed parts, which quickly evolved into balling-related print failure. The printing system and its custom addons are shown in Figure 5.

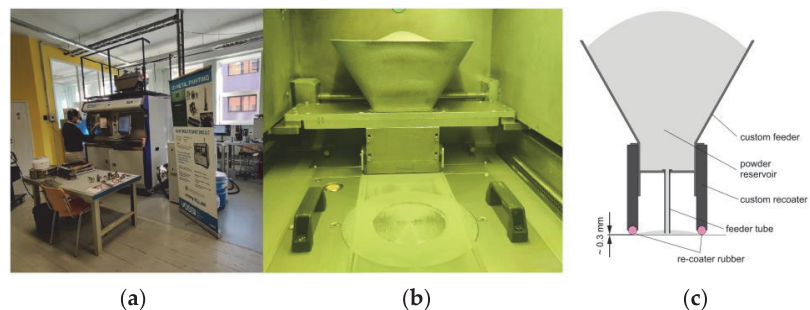


Figure 5. (a) SLM Solutions SLM 280 printing system in Taltech, (b) printer build chamber with custom re-coater, powder reservoir and reduced platform, and (c) cross-section of the custom re-coater system.

2.2. Thermal Treatments

Post-printing thermal treatment processes were performed in a graphite chamber Webb-107 vacuum furnace, which enabled the annealing of parts with dimensions not exceeding $D100 \times 60$ mm. The annealing setup is shown in Figure 6. The investigated temperature range for printed solid toroids was 1200–1350 °C, with a 50° incremental increase. The samples were heated in a ~ 0.1 mBar vacuum environment, with a heating rate of 300°/h up to the target temperature, held for one hour, followed by slow furnace cooling. The duration of each annealing process was roughly 24 h. The optimal annealing temperature in the investigated range was determined from the DC magnetic measurements and was used for the treatment of three segregated cores in the next study step.



Figure 6. (a) Printed soft magnetic core in the annealing furnace; (b) full annealing setup of Webb-107 vacuum furnace.

2.3. Density and Surface Roughness Optimization Study

A study of the printing parameters was conducted to determine the optimal parameters for preparing samples with the highest relative density and lowest surface roughness. A total of 36 pcs $5 \times 5 \times 5$ mm cubical samples were printed, each with a different set of parameters. The finished printed cubes on the substrate and their respective melting parameters are outlined in Figure 7. The initial values for the parametric sweep were adopted from the manufacturer's recommendation for 316 L stainless steel for SLM 280 L-PBF system. The sweep was performed for both laser power (250–400 W) and scanning velocity (0.25–2 m/s), with a constant hatch distance (120 μm) and layer thickness (50 μm). The volumetric energy input of each layer was calculated using Equation (1), where E denotes the energy density (J/mm^3), h —the hatch spacing (mm), t —layer thickness, and v —scan speed (mm/s).

$$E = \frac{P}{v \cdot h \cdot t} \quad (1)$$

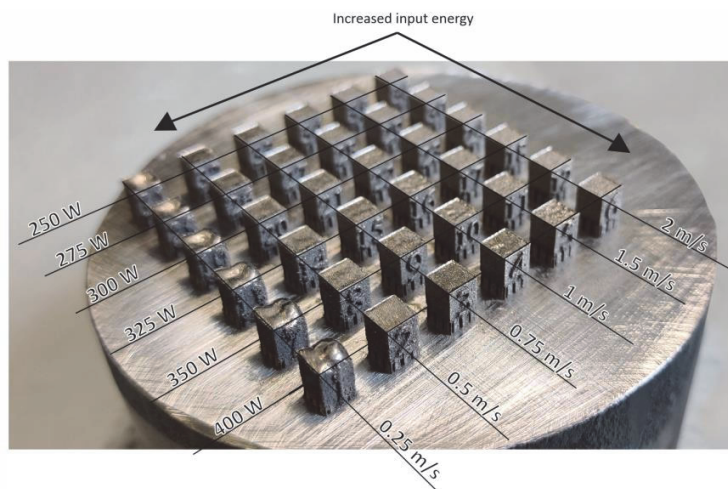


Figure 7. Printed sample cubes on the substrate and the parametric plan of the individual cubes for density optimization.

The printing was performed in a nitrogen environment, with oxygen purged from the chamber below 0.1% content. A stripe scan pattern with 15° rotation between the layers was used for core hatching. The borders of each cube were printed with identical parameters: contour scanning with 100 W laser power at 0.5 m/s. Two-way recoating was considered unsuitable due to the construction of the custom re-coater; the rubber wiper blades could not be aligned perfectly to ensure even layer thickness on both recoating ways. This is why the hatch melting of the cubes was conducted every two layers (every 50 μm) with only the re-coater moving from front to back, whereas the border melting was conducted every layer (every 25 μm) with both recoating directions.

The sample density analysis was conducted on a YXLON FF35 CT computed metal tomography system with a 195 kV transmission tube (Y.FXT 225.48) configuration using a continuous cone beam scan method. The analysis was performed on VGSTUDIO MAX 3.2.2.152742 commercial software using the VGEasyPore algorithm with a low cutoff filter limit of 8 voxels for porosity size. This translated to an axial resolution of approximately 12 μm —with the scan detecting internal defects as small as $1.75 \times 10^{-6} \text{ mm}^{-3}$ in volume. This resolution was deemed appropriate as the irregular lack-of-fusion pores are typically above 100 μm in diameter [31]. Each cube was scanned thrice: once from each of the orthogonal directions for the construction of the CT image. The defect content was calculated from the cube internal core volume; skin volumes 0.5 mm around the lateral faces and 1

mm from the cube base were excluded. This volume was chosen to minimize the effect of any core-skin fusion defects on the core density parameter optimization results. The measurement and assessment of average defect shape, density, and total volume within the cube tomography results enabled the identification of the defect formation phenomena and average relative density.

A Mahr Perthometer Concept Stylus Profilometer was used for surface roughness measurements. The samples were evaluated across all three non-numbered side faces. On each face, both diagonals were measured using a profilometer over a distance of 4 mm and cut-off values of 0.8 mm. The values for arithmetical mean roughness (R_a , μm) and mean roughness depth (R_z , μm) of the profile were calculated as a mean of the three sides of the cubes. The results are presented in the form of R_z , to better evaluate surface roughness-related potential for short circuits within air-gap segregated cores. In contrast, arithmetical mean roughness R_a characterizes the mean value of the whole profile and is less informative regarding the individual peaks or valleys within the profile. Evaluated areas for both porosity and surface roughness of the sample cubes are outlined in Figure 8.

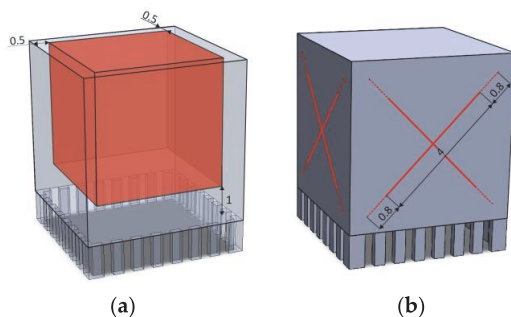


Figure 8. Cubic characterization: (a) volume of each sample accounted for in metal tomography; (b) sample diagonals accounted for surface roughness evaluation.

2.4. Magnetic Properties Study

Ring method measurements were used for the mapping of AM material magnetic properties. Two types of samples were prepared: fully dense toroids and toroids with graded (air-gapped) cross-sections. In both cases, the overall shape and outer dimensions of the samples were identical—with a 60 mm outer diameter (OD), a 50 mm inner diameter (ID), and a rectangular 5×5 mm cross-section. With an outer to inner diameter ratio of 1 to 2, the samples exhibit mostly homogeneous flux distribution [32]. In graded sample designs, horizontal, vertical, and combined air-gaps were printed into the material for eddy current suppression. A detailed description of the aimed core cross-section designs is outlined in Figure 9.

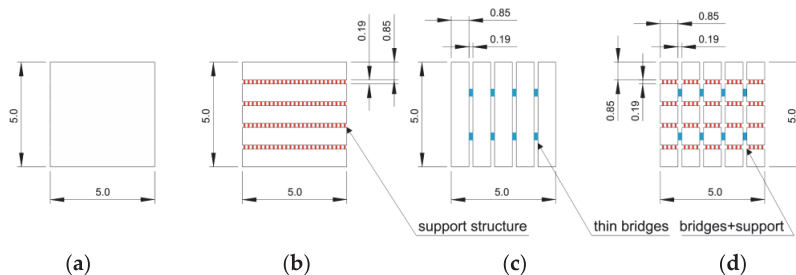


Figure 9. Investigated core topologies: (a) solid, (b) horizontal air gaps, (c) vertical air gaps, and (d) both horizontal and vertical air gaps introduced into the material.

Horizontally air-gapped cores required dense support structures to prevent part deformation during printing. These support structures consisted of thick border elements to prevent part warpage and delamination and thin lattice structures supporting the inner part to promote powder fusion between the layers. In the vertically air-gapped design, scattered bridge-like structures were used between the laminations to consolidate the printed laminations into a single part. The connecting bridges were displaced over the sample volume in an attempt to increase core inter-lamination resistance. The bridges were printed every 18 degrees, with the cycle of two alternating bridge designs repeating every 36 degrees. The discussed design enhancements are outlined in Figure 10a,b.

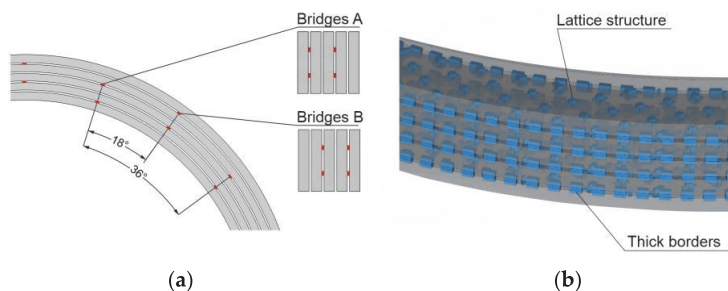


Figure 10. Segregated core design: (a) joining of printed vertical laminations with thin bridges; (b) support structures including border and lattice structures for printed horizontal laminations.

The magnetic properties of the printed cores were measured on an in-house ring measurement setup in accordance with the European standards EN 60404-6 [32] and EN 60404-4 [33]. The measurements were conducted at a near quasi-static frequency of 25 mHz and at 1 and 50 Hz for the investigation of the AC loss component. The magnetic measurements setup schematic is shown in Figure 11a, alongside a wound sample under investigation in Figure 11b. The core excitation was performed by supplying a sinusoidal signal from a waveform generator through a signal amplifier to the primary winding. For that purpose, a Rigol DG1022Z arbitrary function generator and an Omicron CMS 356 voltage and current amplifier were used. Up to 20 A RMS current was applied on the windings. Additionally, the amplification system ensured the uniform sinusoidal waveform shape of the excitation current throughout the experiments. Once exiting the core, a Dewetron DEWE2-M data acquisition system with equipped TRION-2402-HV and TRION-2402-dACC measurement modules was employed for recording the toroidal transformer input and output. These included the current in the primary coil (measured through a voltage drop over a 15 A/75 mV high precision shunt resistor) and the induced flux linked voltage on the secondary coil. The sampling frequency of the acquired data was 10 kHz, with the maximum accuracy of $\pm 0.02\%$ and range $\pm 200 \mu\text{V}$. The recorded empirical data was further processed in a Matlab environment, where the magnetic field strength H on the core was calculated by (2) and the obtained average flux density B within the core by (3):

$$H = \frac{N_1 i}{l_t} \quad (2)$$

$$B = \frac{1}{N_2 \cdot S \cdot F} \int_t e(t) dt \quad (3)$$

where N_1 is the number of turns of the primary winding, N_2 —the number of turns of the secondary winding, i —the instantaneous current on the primary winding, e —the instantaneous induced emf on the secondary winding, l_t —the mean magnetic path length, S —core cross-section area, and F its fill factor. The fill factor of the cores was included to provide an accurate comparison per weight of the samples. If the full cross-sections were used for material characterization, the flux densities of the material would be lower

by a margin of non-magnetic volumes introduced to it. Prior to calculations, the physical toroid measurements were taken with a digital scale and a caliper. Density of the samples was calculated from the weight and volume of the investigated toroids. The constructed hysteresis loops were divided into two datasets, each corresponding to the magnetizing direction. Both of the loop halves were then fitted with cubic splines, which enabled them to reduce noise and data points to simplify the numerical integration of the curves. By subtracting the calculated areas below both curves, the loss density of the investigated material was obtained in J/mm^3 . The specific core losses (P_s) were then calculated by taking into account the average density of the material (ρ) and time period (T) of each hysteresis cycle, as expressed in (4).

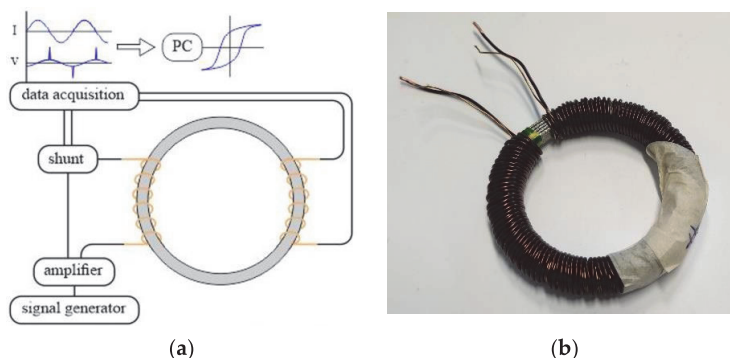


Figure 11. Setup of the magnetic measurements: (a) schematic; (b) wound toroidal core.

Material permeability was evaluated from the magnetization curves constructed from the measured hysteresis curves at increasing excitation levels. The process is illustrated in Figure 12. Permeability of each loop is calculated through its definition: by dividing the corresponding peak B_{max} with the H_{max} of each loop and μ_0 . At low magnetic field strength values, the corresponding permeabilities are low; the field is insufficient to induce significant magnetic domain alignment within the material.

$$P_s = \frac{1}{T \cdot \rho} \left(\int_0^T H_1 dB_1 - \int_0^T H_2 dB_2 \right) \tag{4}$$

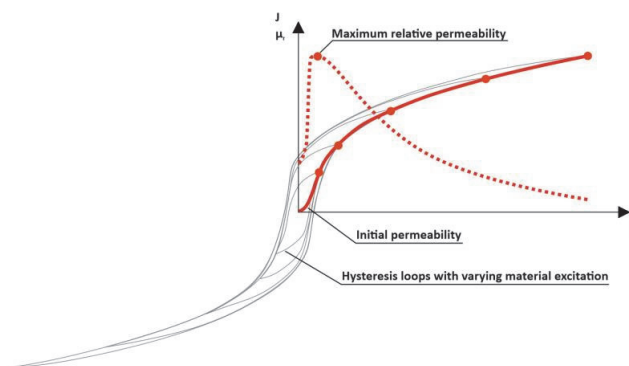


Figure 12. Normal magnetization curve constructed from the individual hysteresis curves measured at different field strengths and the corresponding relative permeability.

2.5. XRD Microstructural Analysis

X-ray diffraction patterns were recorded with a Rigaku Ultima IV diffractometer. A silicon strip detector D/teX Ultra with CuK α radiation ($\lambda = 1.5406 \text{ \AA}$, 40 kV at 40 mA) was used. XRD reference files from the International Centre for Diffraction Data (ICDD, Delaware County, PA, USA) for crystalline phase identification.

2.6. Mechanical Properties

The tensile strength of the materials was measured on an Instron 8516 servo-hydraulic controlled fatigue system with a 100 kN load cell and a 25 mm extensometer, according to the EVS-EN ISO 6892-1 standard. Six test samples were printed with their design based on the E8/E8M—16a ASTM standard [34]: small size specimens proportional to standard (specimen 4). The type-I (conventional round) specimens exhibited a gauge length of 20 mm, a diameter of 4 mm, a radius of fillet of 4 mm, and a length of the reduced parallel section of 24 mm.

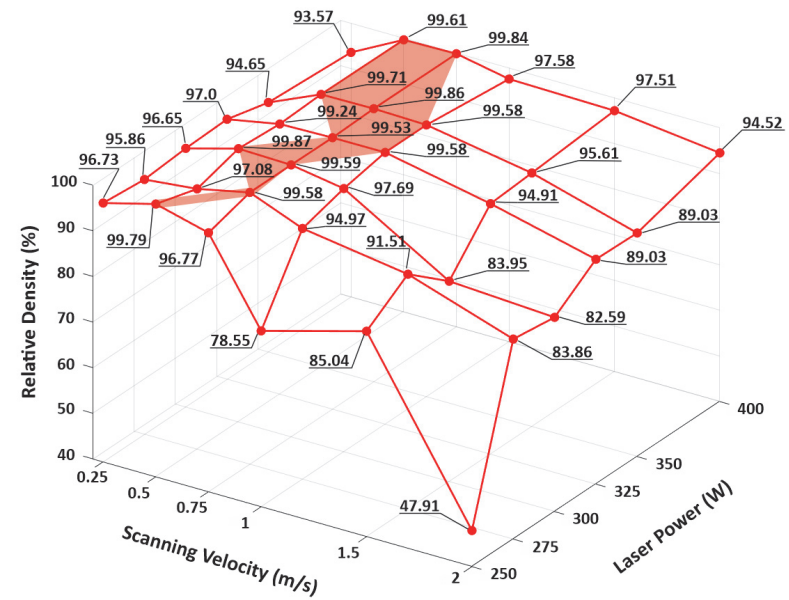
3. Results

3.1. Density and Surface Roughness

The summary of the investigated effect of laser energy input on the relative density and surface roughness of the printed 35 samples is outlined in Figure 13a,b. One sample (nr. 26, 275 W, 0.5 m/s) was excluded from the results due to internal delamination caused by unknown, possibly re-coating-related reasons. Three clear areas of interest can be identified from the figure. First, in the range of 20–50 J/mm³, energy input was insufficient for homogeneous melting of the powder—as irregular lack-of-fusion porosities are abundant in the material. The lowest relative density identified in this study was only 47.91% dense, printed at the lowest settings of this study—20.8 J/mm³ (250 W, 2 m/s).

Secondly, in the region with a volumetric energy density of 66–130 J/mm³, the optimal melting region was identified, with near fully dense net-shaped parts fused, peaking at 100 J/mm³ with a 99.87% dense sample (300 W, 0.5 m/s). Thirdly, with higher input energy, at 166–233 J/mm³, over-melting of the samples was observed, resulting in the monotonous decrease of sample density.

Fully dense parts could be prepared over the entire investigated laser power range (250–400 W), but only within the scanning velocity rate of 0.5–1 m/s. The optimal laser power setting in this study is considered 350 W, 0.75 m/s (77 J/mm³). It offers the highest likelihood of obtaining near fully-dense parts, evaluated through the setting robustness; small deviations in both power and velocity would still result in over 99.5% relative density. The setting also correlated to near-lowest sample surface roughness—a critical requirement for obtaining useful printed structurally graded (air-gapped) magnetic cores. The values for surface roughness ranged from 6.8–18.2 μm for R_a and 36.1–85.2 μm for R_z . The average surface roughness of the printed parts did not increase monotonously with an increase in input energy density. Below 88 J/mm³ input power, all of the characterized sides of the samples were alike. Above it, the three different sides started exhibiting different melting patterns, resulting in an increased measurement dispersion. The samples melted at the highest power settings showed smoother surfaces overall than those melted at 91–133 J/mm³. The four most distinctive samples for illustrating the effect of melting parameters on printed part quality are presented in Figure 14.



■ Above 99.5% average relative Density
● Measured Datapoint

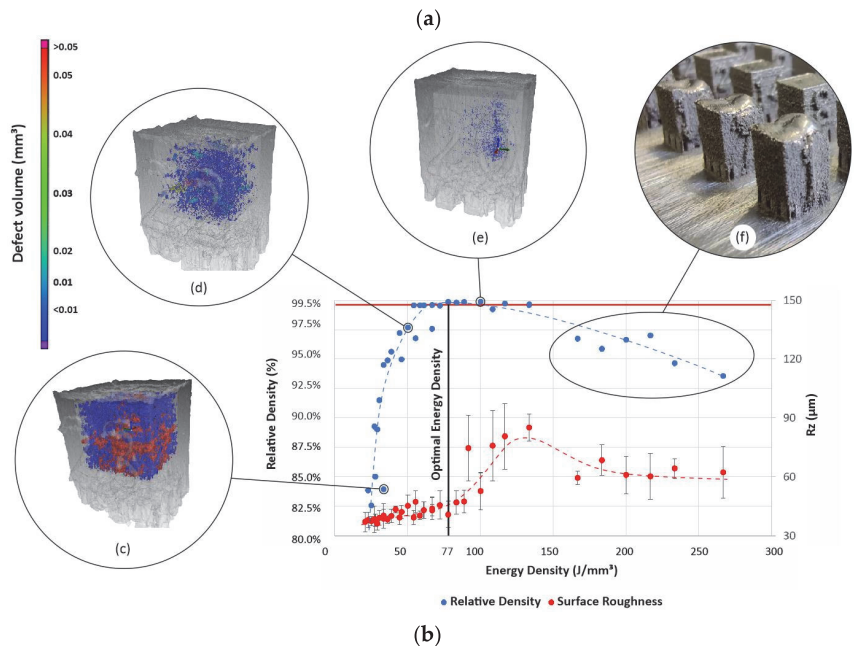


Figure 13. Parameter optimization results: (a) relationship between scanning parameters and relative density of the L-PBF specimens, (b) sample relative density and surface roughness as function of laser input energy density, (c) sample nr 23–300 W, 1.5 m/s, (d) sample nr 22–300 W, 1 m/s, (e) sample nr 20–300 W, 0.5 m/s, and (f) samples deformed from excessive laser input at 250–400 W, 0.25 m/s.

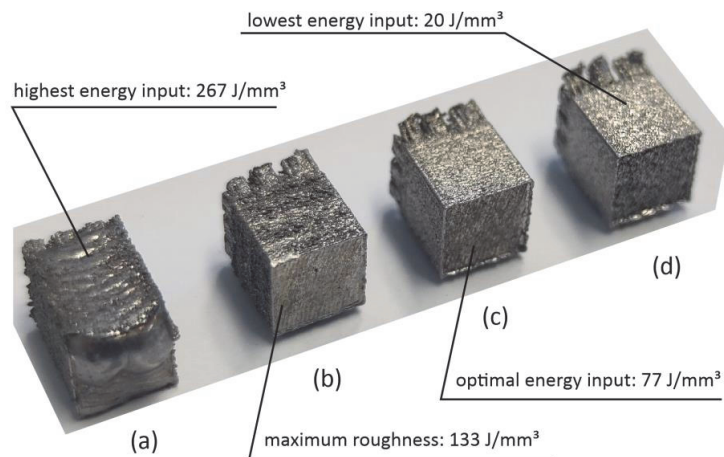


Figure 14. Distinctive surface roughness samples: (a) highest energy input ($R_z = 62 \mu\text{m}$, $R_a = 12 \mu\text{m}$), (b) maximum surface roughness ($R_z = 85 \mu\text{m}$, $R_a = 18 \mu\text{m}$), (c) optimal energy density ($R_z = 41 \mu\text{m}$, $R_a = 8 \mu\text{m}$), and (d) lowest energy input ($R_z = 37 \mu\text{m}$, $R_a = 7 \mu\text{m}$).

3.2. DC Magnetic Properties

The obtained magnetization curves of the characterized toroids, printed with the previously determined optimal parameters and subjected to varying heat treatments, are presented in Figure 15a. Post heat treatment, the magnetization of 1.5 T was achieved at approximately 1500 A/m on average. The as-built sample reached the same level of magnetization at 4000 A/m. The coercivity of the samples varied from 52 A/m (1200 °C) up to 203 A/m (as-built). Hysteresis curves of the material annealed beyond 1200 °C showed a slight deterioration of magnetic properties. This is apparent from the decreasing slope magnetization curves: annealing the samples over 1200 °C resulted in reduced permeability. The measurement noise of the method did not allow for the characterization of the annealed samples below ~0.5 T. Calculated maximum permeabilities decreased from 8900 (1200 °C) to 3700 (1350 °C) and reached as low as 1400 for the as-built sample. Full hysteresis curves for as-built and annealed material at 1200° and 1350 °C at 1.5 T magnetization are illustrated in Figure 15b.

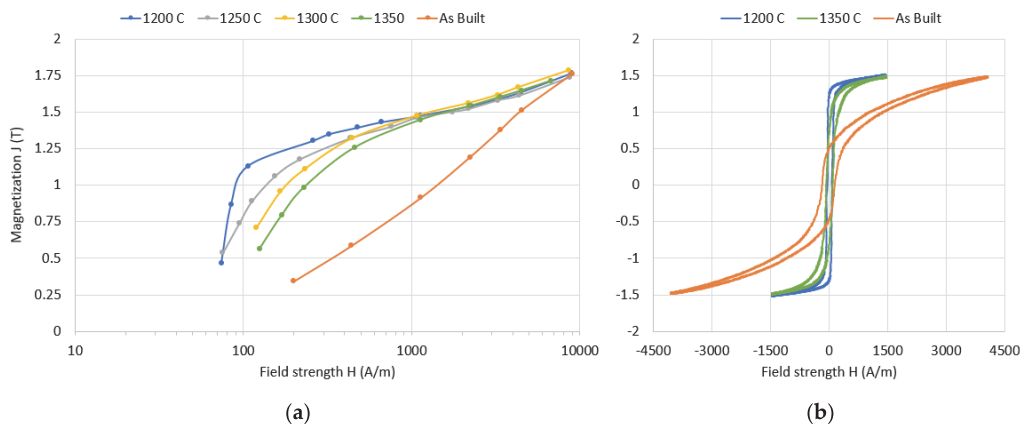


Figure 15. DC (25 mHz) magnetic material properties of the printed cores with varying thermal treatments: (a) magnetization curves; (b) hysteresis loops at 1.5 T.

Hysteresis losses of the samples were obtained from the integrated areas of the quasi-static hysteresis loops. The results are outlined in Figure 16. The non-annealed sample exhibited the highest losses, reaching 0.075 J/kg and 0.14 J/kg at 1 T and 1.5 T, respectively. The annealed samples again exhibited a slight deterioration in magnetic characteristics with an increase in annealing temperature. The lowest hysteresis losses were measured for the 1200 °C annealed sample, with losses as low as 0.016 J/kg (at 1 T) and 0.043 J/kg (at 1.5 T). At a 50 Hz excitation frequency, this translates to a 0.8 W/kg hysteresis loss at 1 T and 2.15 W/kg loss at 1.5 T material magnetization. A slight increase in core losses was observed for samples annealed at higher temperatures, increasing up to 30% at the highest temperature. The comparison of the prepared material with typical commercial materials is presented in Figure 17.

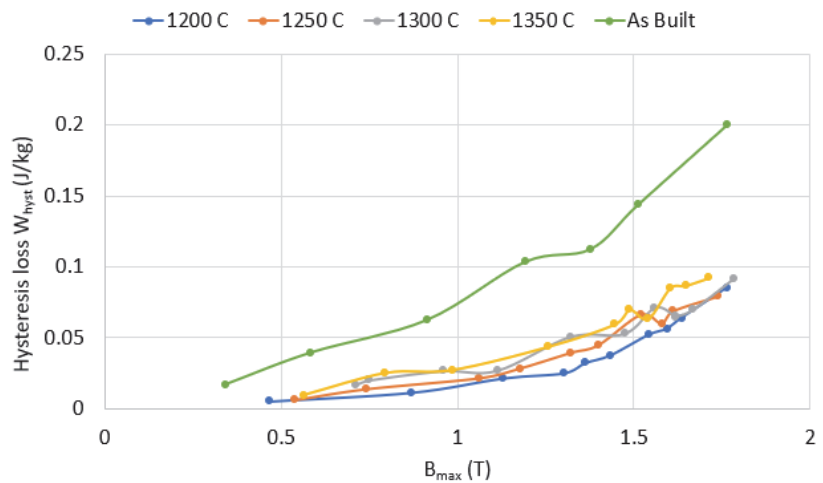


Figure 16. Hysteresis losses (quasi-static) of the solid specimens with varying thermal treatments in the magnetization range ~0.5–1.8 T.

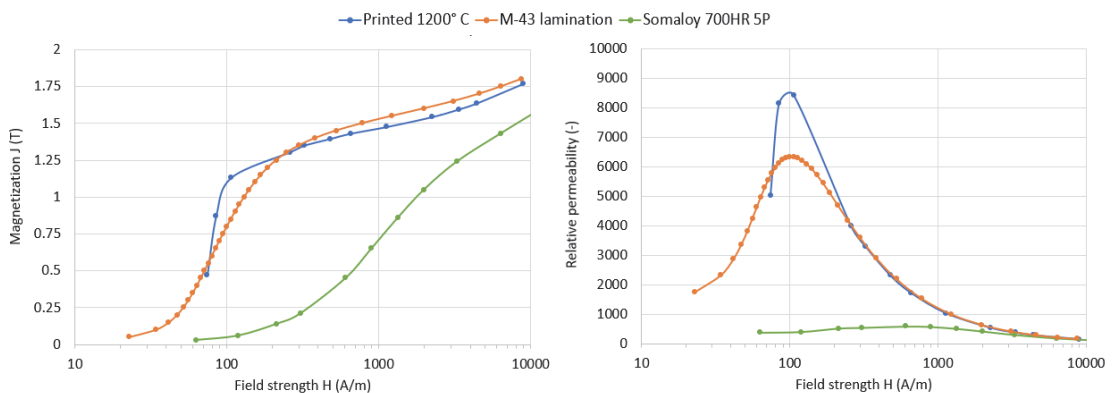


Figure 17. Comparison of the magnetization and permeability curves of commercial M-43 (equivalent to M400-50A) non-oriented silicon steel [35], Somaloy soft magnetic composite [36], and the characterized printed material annealed at 1200 °C.

3.3. Eddy Current Losses

Next, the same toroidal samples were investigated at higher frequencies, increasing from 0.025 Hz to 1 and 50 Hz. Considerably higher iron losses were observed as expected, as eddy current losses are known to be proportional to the square of field switching frequency. This effect is illustrated in Figure 18, showing the widening of the hysteresis loops at elevated frequencies. The previously obtained hysteresis loss of 0.043 J/kg (at 1.5 T) equates to a 2.15 W/kg loss at 50 Hz. This is only 5% of the total core loss measured at 50 Hz, with 95% of the loss constituting classical and excess eddy current loss. At 1 Hz, compared to the DC hysteresis loss, the loss increased threefold. When comparing the iron losses over a wider range, ~0.5–1.9 T, as presented in Figure 19, two observations can be made. First, a sharp increase in loss was observed when magnetizing the samples beyond the knee. This increase was observed to be proportional to the maximum permeability of the material, i.e., materials with “hard saturation” behavior exhibited a sharper increase in core losses beyond the knee point than materials characterized by soft magnetic behavior. Similar behavior was observed in [37]. Secondly, the distinction between unannealed and annealed core loss was more prominent at 1 Hz. This is likely due to the low magnitude of eddy currents at 1 Hz and the significant hysteresis loss of the untreated material: at both 1.5 T and 1 T, 1 Hz, the hysteresis loss constituted 75% of the total measured core loss. Nevertheless, similar to the behavior at 50 Hz, in deeper saturation, despite the substantially lower DC losses, the losses of the annealed samples exceeded those of the untreated sample. All four of the annealed samples exhibited similar loss behavior: roughly 170 W/kg at 1.9 T, 45 W/kg at 1.5 T, 11 W/kg at 1 T, and 2 W/kg at 0.5 T.

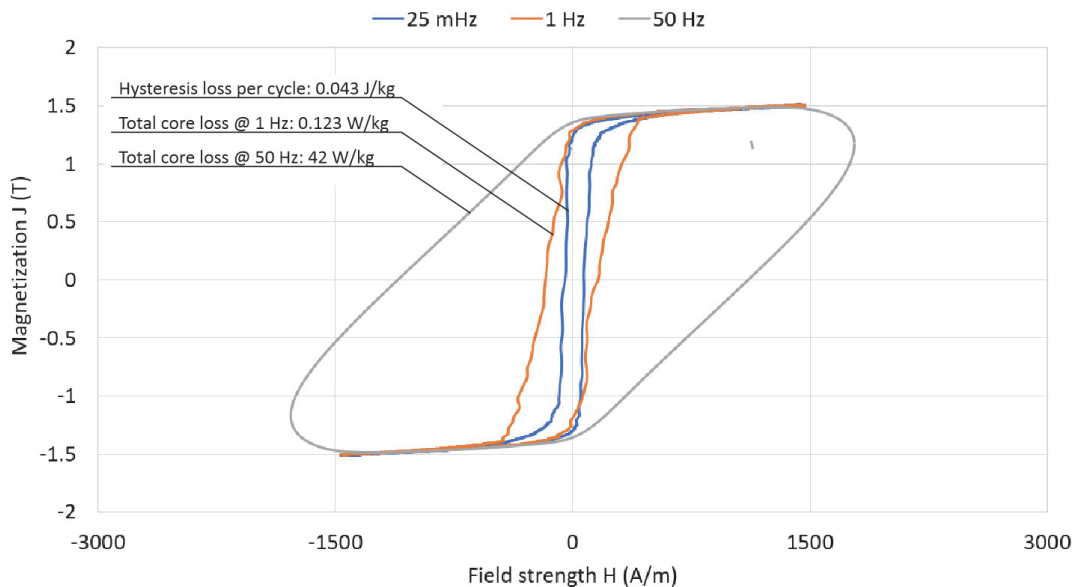


Figure 18. Eddy current loss-related curve shearing: measured loops at 1.5 T magnetization (~1500 A/m field strength), at 0.025, 1, and 50 Hz excitation.

Three additional cores with graded cross-sections were prepared to investigate eddy current suppression possibilities in printed cores. These samples were prepared with the previously determined optimal parameters for printing (350 W, 0.75 m/s, and 77 J/mm³) and thermal treatment (1200 °C 1 h). The initial design of the graded samples is described in Figures 9 and 10. The structure of the finalized prototype cores is presented in Figure 20, illustrating both the voids within the core (obtained through metal tomography) and the joining support structure. The structural study verified the sample fill factors: for the

horizontally graded sample—94.05%, for the vertically graded—78.07%, and for the hybrid core—72.98%. Secondly, the structural study revealed slight dimensional deviations from the initial models, exhibiting 0.32 mm vertical air gaps separating 0.75 mm thick magnetic guides (instead of 0.19/0.85 mm). These gaps were sufficient for removing all the unmelted powder from within the core. Realization of the horizontal air gaps was less successful, however, with the resultant air gap relatively uneven.

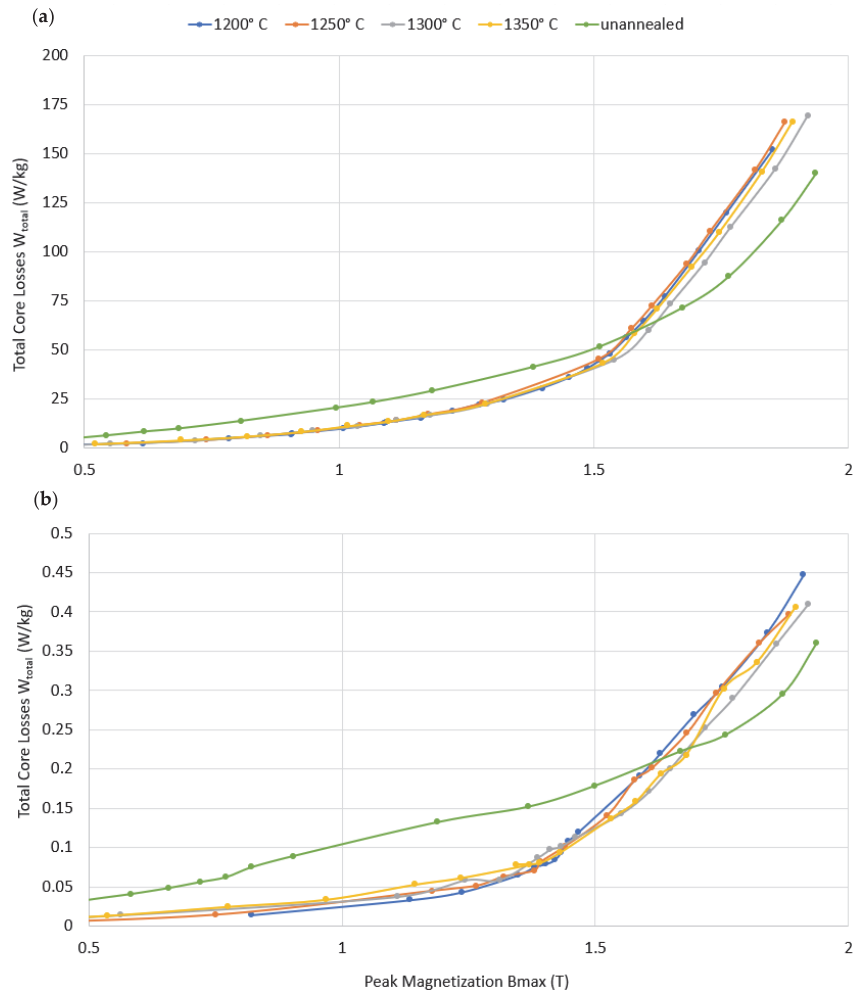


Figure 19. Total core losses of the printed solid toroidal specimens with varying thermal treatments in magnetization range of ~0.5–1.9 T at 50 Hz (a) and 1 Hz (b).

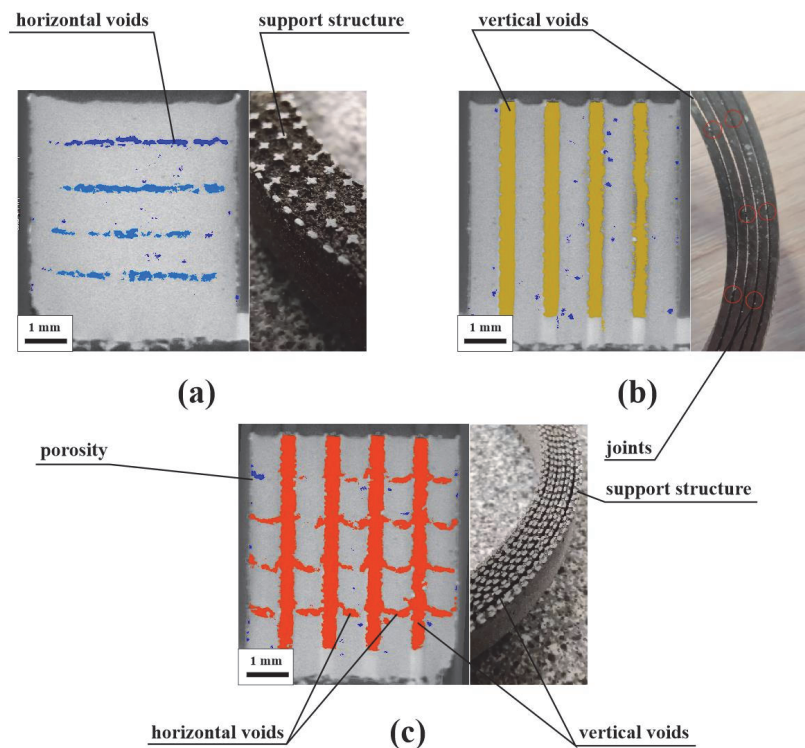


Figure 20. Topology of the segregated AM cores (metal tomography images + photographs): (a) horizontally graded, (b) vertically graded, and (c) horizontally and vertically graded (hybrid).

For the construction of hysteresis curves, the core fill factor was included in the calculations to provide an accurate comparison per weight of the samples (Equation (4)). Without it, flux densities within the material would be lower by a margin of non-magnetic air introduced to it. An amount of 1.5 T magnetization in the iron volume of the samples would translate to 1.1 T in the total volume of the 72.98% dense samples, 1.17 T in the 78.07%, etc. This would, however, give a false perception of the core behavior due to its nonlinearity, especially when considering losses per kilogram of the material (which, unlike W/m^3 , is invariant of air content within the core).

Magnetic measurements confirmed the higher efficiency of vertical to horizontal air gaps for eddy current suppression. Magnetic losses at 50 Hz, in the range of 0.5–1.8 T, are outlined in Figure 21a. At 1.5 T magnetization, total iron losses decreased from 42 W/kg (solid) to 35 W/kg with horizontal grading, 15.5 W/kg with vertical grading, to as low as 11.7 W/kg with hybrid grading. At 1 T, the topological enhancements led to the decrease of total core losses by 81%: from 9.6 W/kg (solid) to 1.8 W/kg (hybrid). The other two graded samples exhibited losses in between: 2.1 W/kg (vertical) and 7.3 W/kg (horizontal). These results are further expanded upon in the Section 4 of the paper.

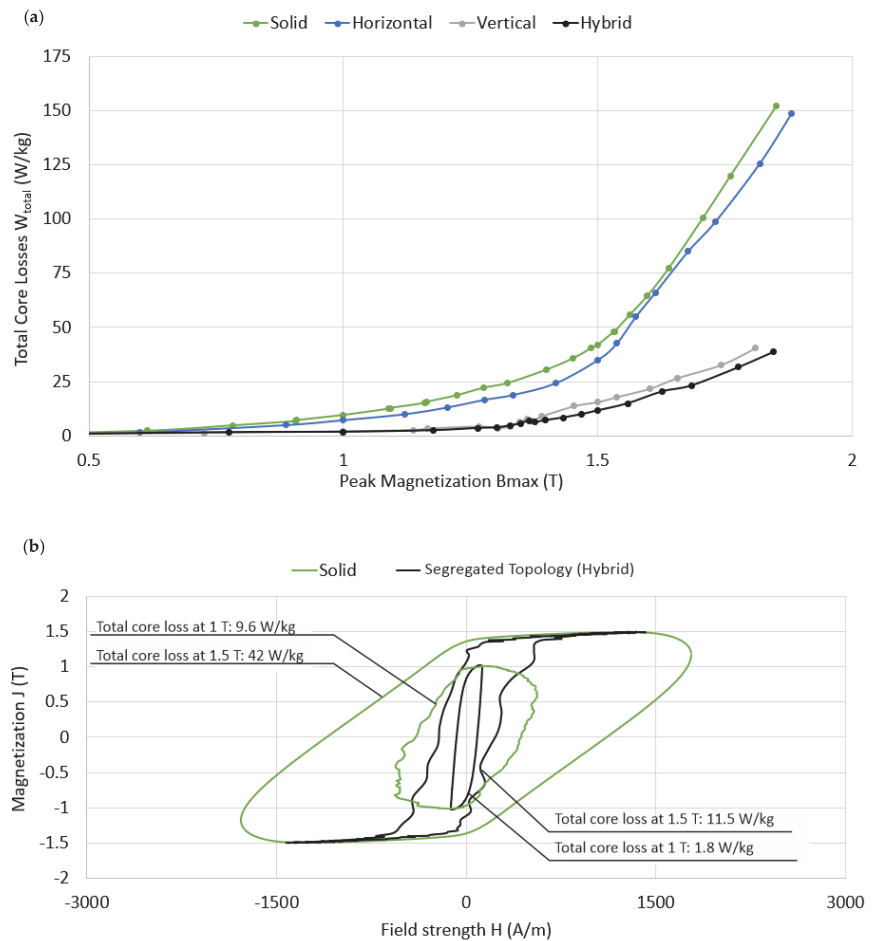


Figure 21. Total iron loss reduction with segregated printed core topology: (a) core losses with solid and investigated topologies over the magnetization range of 0.5–1.9 T; (b) comparison of the hysteresis loops of the solid and segregated topology results at 1 and 1.5 T magnetization.

3.4. XRD Microstructural Study Results

XRD measurements confirmed the formation of a single α -ferrite BCC (body-centered cubic) phase within the samples. High silicon content (3.7%) suppressed the γ -phase formation [38] during solidification. Five peaks from the ferrite phase were obtained between 44 and 116° , without any impurity-related peaks (nitridation, carburization, and oxidation from printing annealing), as presented in Figure 22a for the normalized diffraction patterns. Significant differences between the patterns of samples annealed at different temperatures were not observed. Similar to the work in [39], no superstructural lines were observed, which also suggested that coarse areas of ordered B2 and DO₃ phases were not present in the microstructure. Lattice parameters calculated from the d-spacing of each peak increased slightly with elevated annealing temperatures: from 2.864 to 2.868 Å, but remained roughly within the range of typical data for the alloy [40]. In every sample, the largest crystallite size corresponded to the α Fe-Si (1,1,0) peak: ranging between 236 – 361 nm, with the 1200 °C heat treatment sample exhibiting the largest values.

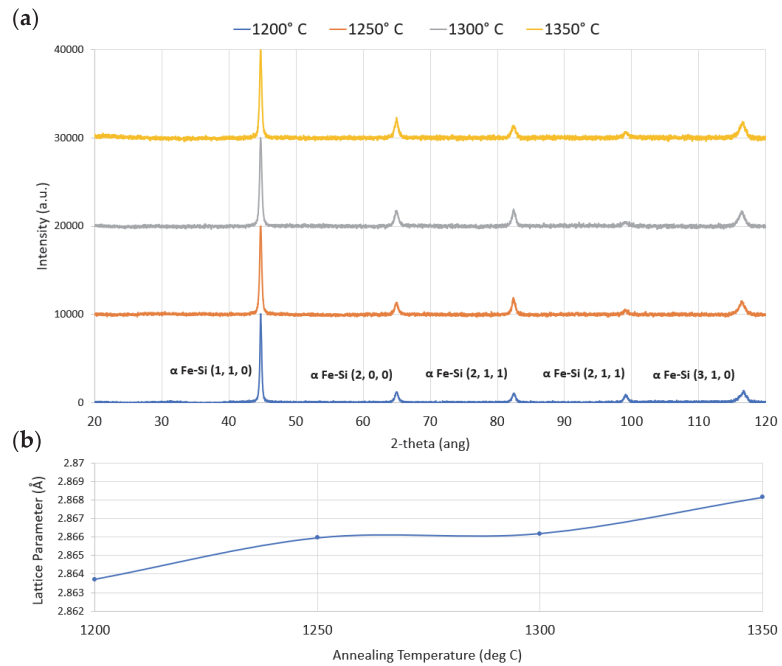


Figure 22. XRD Analysis results of the printed, annealed material: (a) XRD spectra of the samples annealed at 1200–1350 °C; (b) measured lattice parameters at the same temperatures.

3.5. Material Tensile Strength

The material's tensile strength was verified with vertically printed round tension test samples for both 1200 °C annealed and non-annealed (as-built) conditions. The measured stress-strain curves of the six prepared samples (three annealed + three untreated) are outlined in Figure 23. A drop in material yield strength was observed post-annealing: from ~570 Mpa to ~420 Mpa. The elongations at break of the samples were similar for both the untreated and treated material, reaching approximately 25% strain (elongation). These results are further expanded upon in the Section 4 of the paper.

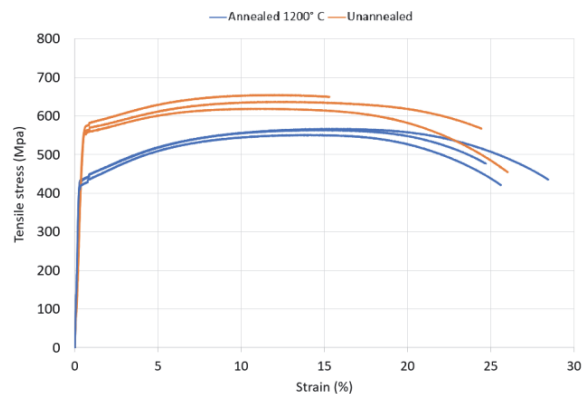


Figure 23. Tensile test results of the as-built and heat-treated material.

4. Discussion

Relatively large variations in the laser processing parameters of silicon steel are available in the literature. The energy density verified as optimal in this study— 77 J/mm^3 (laser power: 350 W; scan speed: 750 mm/s; hatch spacing: $120 \text{ }\mu\text{m}$; layer thickness: $50 \text{ }\mu\text{m}$)—is somewhere between the maximum and minimum values applied in the literature. In [41], 59 J/mm^3 (200 W; 680 mm/s; $100 \text{ }\mu\text{m}$; $50 \text{ }\mu\text{m}$) was used to fuse parts with unknown density (the samples were hot isostatic pressed to remove residual porosity before measurements). In [42], Stornelli et. al. determined the optimal energy density to be 138 J/mm^3 (250 W; 1000 mm/s; $60 \text{ }\mu\text{m}$; $30 \text{ }\mu\text{m}$) for 3% silicon steel samples, with likely overestimated values of relative density. Garibaldi et. al. applied 93 J/mm^3 (70 W; 500 mm/s; $60 \text{ }\mu\text{m}$; $25 \text{ }\mu\text{m}$) to fuse 98.5% dense parts from 6.9% silicon steel. In [43], a considerably higher energy density of 225 J/mm^3 (90 W; 200 mm/s; $80 \text{ }\mu\text{m}$; $25 \text{ }\mu\text{m}$) was applied to fuse 6.5% silicon content parts with above 98% relative density. Similarly, Goll et. al. obtained the lowest hysteresis losses in near fully-dense samples when melting the powder with a 200 J/mm^3 energy density (300 W; 500 mm/s; $60 \text{ }\mu\text{m}$; $50 \text{ }\mu\text{m}$) [44].

Similarly, regarding the maximum relative permeabilities of the characterized AM silicon steel cores in the literature, large variations can be found. For high silicon steel, printed and treated with similar parameters, they have been shown to range from 8000 [43]–31,000 [44]. In this paper, the maximum relative permeability of 8400 was obtained, showing superior values to typical silicon steels (M-43 with 6500 [35]), but considerably lower values when compared to high silicon steel due to larger magnetostriction. These values are relatively low compared to grain-oriented silicon steels, which can reach relative permeabilities of $\sim 100,000$, but are only suitable for applications with a unidirectional magnetization (such as transformers) [45]. Even higher values could be obtained with soft magnetic amorphous glasses, which can reach relative permeabilities in the range of $\sim 500,000$ [46], but require additional research for implementation with additive technologies. In this study, the elevated annealing temperatures resulted in a slight reduction of DC magnetic properties, decreasing both the relative permeability and increasing the material hysteresis losses. As generally larger grain sizes have been linked to improved magnetic properties, this phenomenon is challenging to explain. On one side, it is possible that at elevated temperatures, the sample surface was contaminated more intensely in the annealing furnace with evaporated carbon within the chamber. This might have resulted in the whole carbonized surface of the sample pinning the large recrystallized grains. On the other hand, the recrystallized grains annealed at $1350 \text{ }^\circ\text{C}$ are uncommonly large. Judging by a fracture surface of a test sample (Figure 24), the macroscopic grains are as large as $\sim 2500 \text{ }\mu\text{m}$. Effects of this grain size on the magnetic properties are largely unexplored, with the majority of the studies focusing more on the range $50\text{--}210 \text{ }\mu\text{m}$ [47]. In comparison, in [48], a coarse-grained microstructure with $D_{50} = 720 \text{ }\mu\text{m}$ was obtained at an $1150 \text{ }^\circ\text{C}$ annealing temperature.

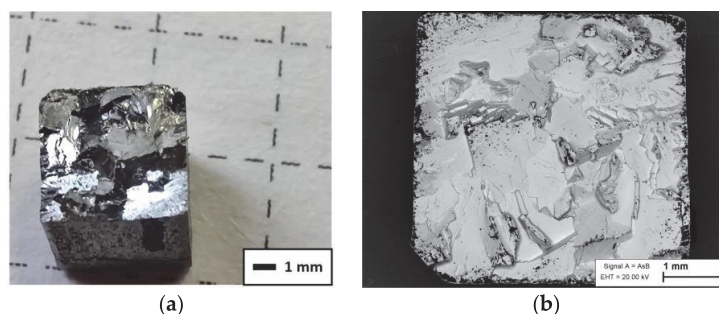


Figure 24. Shattered sample annealed at $1350 \text{ }^\circ\text{C}$, exhibiting a large—up to $\sim 2500 \text{ }\mu\text{m}$ —grain structure on the fracture surface: (a) photograph, (b) SEM image.

The obtained total core losses were lower than initially supposed; the goal of obtaining superior loss behavior to soft magnetic composites (SMCs) was fulfilled successfully. At $W_{10,50}$, total core losses for the segregated topology sample were 1.8 W/kg: this is 2–3 times lower than typical SMCs under the same conditions [36] (of course SMCs are superior for high frequency applications). Moreover, the permeability of the printed material is far superior, exhibiting maximum μ_r values in the range of 8000 in contrast to 500–600 [37] of SMCs. The low losses suggest the capacity of L-PBF to fabricate useful novel electrical machine prototypes; as compared to SMCs, it can be used to fabricate cores with superior energy efficiency and even wider design freedom. Undoubtedly, the comparison only stands per mass of the sample; if compared per volume, similar core losses would be obtained. This is because of the relatively wide voids introduced into the material, reducing the effective cross-section and magnetic material content by 27% (with hybrid core topology). Nevertheless, this means that AM core components would be at a disadvantage only if the size of the component was a critical factor. For applications with weight as the main criterion, AM cores can be used effectively, and perhaps even with improved machine cooling capacity, with the insulating gaps doubling as cooling channels.

In comparison with the gold standard of electrical machine core materials, non-oriented silicon steel laminations, three major conclusions can be drawn. First, the permeabilities and material magnetic polarization obtainable at low field strengths are near equivalent (as presented in Figure 17). The printed material exhibited slightly higher permeability (at low polarization) and lower overall saturation polarization than M-43 commercial steel [36], which can be explained through the likely higher silicon content (exact silicon content in commercial laminations is not usually disclosed) alongside a larger grain size (lamination grain size is typically in the range of 100–200 μm [16]). It is important to note that larger grain size has been shown to be more advantageous at low field strengths, but disadvantageous at higher ones. Shiozaki et. al. showed that in laminations under weak magnetic fields of $W_{14,50}$ or less, large grain diameter (220 to 230 μm) was optimal, offering minimum core loss and maximum permeability, whereas in strong magnetic fields of $W_{15,50}$ or higher, better results were obtained with smaller grain diameters (190 to 110 μm) [47]. A parallel can be drawn between the observations in this paper: annealed samples exhibited lower core losses below the magnetization knee-point and higher losses above it (Figure 19) compared to the as-built sample. The effect seemed to be more profound with higher sample permeability and is likely related to either classical or excess eddy current loss—as it was not observed in DC hysteresis loss. Alternatively, Honma et al. [48] demonstrated the effect of precipitates such as oxides and nitrides on the annealed steel surface layer, which increased hysteresis loss at higher values of core magnetic induction because of difficulties in domain wall motion. This suggests that excessively coarsened grain structure can be suboptimal, due to the longer annealing times required and, consequently, the thicker oxide layers formed on the core surface.

Secondly, the obtained iron loss of 1.8 W/kg at 1 T, 50 Hz of the hybrid AM core are almost competitive with regular non-oriented low-silicon steels. M400-50A (M-43), depending on the manufacturer, exhibits equivalent losses in the range of ~1.4–1.7 W/kg. The EVS-EN 10106 international standard requires M400-50A laminations to exhibit the maximum loss of 1.7 W/kg [49]. Low-grade steels, such as M600-50A or 1000-65A, exhibit higher losses with 2.6 W/kg and 4.11 W/kg, respectively (data obtained from different datasheets [50–52]). At higher flux densities, the same comparison does not stand, however. The 11.7 W/kg loss measured for the hybrid sample exceeds the loss of low-grade 1000-65A steel (8.90 W/kg) [51]. This can again be explained through the sub-optimal grain size associated with high flux density magnetization (excessive grain size) [47].

Thirdly, the tensile strength of the material was well within the requirements for electrical steels. On average, the yield strength of the material was 580 MPa before annealing and 420 MPa after it. These values are in good agreement with the literature. In [53], the typical yield strength of electrical steels was shown to range from 53,000 Psi (365 Mpa) for 3% silicon steel, 60,000 Psi (413 Mpa) for 3.7% silicon content, and 13,000 Psi (90 Mpa)

for 6.5% silicon steel. In a commercial catalogue [50], the yield strength of 350 MPa was disclosed for Isovac 400-50A silicon steel sheets. Despite the relatively high yield strength of the prepared material, the structural stability of the air-gapped core requires additional optimization and testing due to the introduced air gaps. The determination of the optimal size of the connecting bridges between the individual insulated magnetic guides, which ensures mechanical integrity while not sacrificing excessively the core internal electrical resistivity, is necessary.

In regards to the topologies of the investigated prototype cores, several aspects can be improved. A comparison between the planned topology and the actual printed topology is outlined in Figure 25. The integration of horizontal air gaps into the material was relatively unsuccessful, as their efficiency in reducing core eddy currents was low. Undoubtedly, the density of the connecting lattice structure was too high (Figure 20a,c). This resulted in considerable electrical short-circuiting between the optimally fully insulated core volumes. In parallel, the height of the horizontal insulation layers should be increased to enhance both the insulation reliability and to improve powder removal from within the support structure post-printing. With the prototype cores, the overly dense and thin lattice layers prevented the removal of unmelted powder from the cores after printing. If this powder was sintered during the annealing process, it could have also resulted in further increased eddy current losses. In addition to the core printing parameters, the skin parameters also require further optimization to enhance planar printing accuracy—as the width of the printed laminations was lower than initially designed.

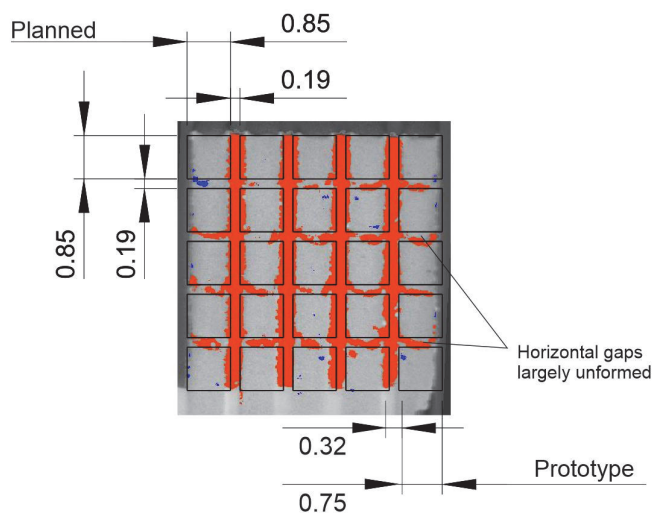


Figure 25. Comparison of the planned 3D model topology with the resultant printed prototype.

5. Conclusions

The paper describes the full optimization process for obtaining laser additively manufactured soft magnetic cores with useful properties. The findings of the paper are the following:

- The optimal energy density for the melting process was 78 J/mm^3 (in the investigated range of $20\text{--}216 \text{ J/mm}^3$), resulting in the fusion of samples with 99.86% relative density and surface roughness values of $41 \text{ }\mu\text{m}$ (R_z) and $8 \text{ }\mu\text{m}$ (R_a). The individual main scanning parameters employed were: laser power—350 W; scanning speed—0.75 m/s; hatch spacing—120 μm ; layer thickness—50 μm ; environment—nitrogen.
- The optimal heat treatment temperature in the range of $1200\text{--}1350 \text{ }^\circ\text{C}$ was 1200° , resulting in the highest relative permeability of the material and lowest quasi-static hysteresis losses.

- DC measurements confirmed equivalent magnetic properties of the printed samples to conventional steels: hysteresis losses of 0.8 W/kg ($W_{10,50}$) and maximum relative permeability of 8400. Magnetization of 1.5 T was reached at 1480 A/m, and 1 T was reached at 90 A/m.
- Shape enhanced printed cores were utilized successfully to limit the eddy current losses within the core to an acceptable level. With a bi-directionally segregated structure (with a fill factor of 72.98%), total iron losses as low as 1.8 W/kg ($W_{10,50}$) were measured. These losses are vastly superior to SMC cores at 50 Hz (5–6 W/kg)—an industrial standard for constructing magnetic cores with unconventional topologies. At 1 T, the obtained total losses of the optimized core are close to the values for typical electrical steel. For M400-50A steel grade, the losses are required not to exceed 1.7 W/kg in the same conditions.

The findings of this paper suggest the applicability of L-PBF fused magnetic cores for the construction of electrical machines. In comparison with SMCs, AM cores are vastly superior for low-frequency applications, as they show superior material properties and a considerably larger geometrical freedom for core design. This would also suggest the usefulness of L-PBF in the preparation of novel transversal flux, multi-axial, and spherical or perhaps completely new machine designs—which can benefit from a wider range of topologies and more refined structures than SMC or lamination-constructed machines.

6. Future Work

Further work on the project will focus first on the extensive AM material microstructural characterization: e.g., granular size, orientation, and effect on material permeability and losses at high and low field strengths; and secondly, on further shape optimization of the segregated cores for enhanced eddy current loss.

Author Contributions: Conceptualization: A.K. and H.T.; methodology: H.T.; validation, A.K.; investigation, H.T., L.L., T.D. and I.V.; resources, A.K.; writing—original draft preparation, H.T.; writing—review and editing, H.T. and A.K.; supervision, A.K. and A.R.; project administration, T.V.; funding acquisition, A.K. All authors have read and agreed to the published version of the manuscript.

Funding: This research work was funded by the Estonian Ministry of Education (Grant PSG-137).

Institutional Review Board Statement: Not applicable.

Informed Consent Statement: Not applicable.

Data Availability Statement: Data is contained within the article.

Acknowledgments: XRD Measurements by the project TK141 (TAR16016EK): “Advanced materials and high-technology devices for energy recuperation systems”; SEM and EDX analyses were supported by the projects IUT-19-28: “New materials and technologies for solar energetics” and TK-141: “Advanced materials and high-technology devices for sustainable energetics, sensorics and nanoelectronics”.

Conflicts of Interest: The authors declare no conflict of interests.

References

1. Aguilera, E.; Ramos, J.; Espalin, D.; Cedillos, F.; Muse, D.; Wicker, R.; MacDonald, E. 3D Printing of Electro Mechanical Systems. In *International Solid Freeform Fabrication Symposium*; University of Texas at Austin: Austin, TX, USA, 2013; pp. 950–961.
2. Garibaldi, M.; Gerada, C.; Ashcroft, I.; Hague, R.; Morvan, H. The Impact of Additive Manufacturing on the Development of Electrical Machines for MEA Applications: A Feasibility Study. In *MEA2015 More Electric Aircraft*; University of Nottingham: Nottingham, UK, 2015; pp. 2–5.
3. Garibaldi, M.; Gerada, C.; Hague, R. Laser Additive Manufacturing of Soft Magnetic Cores for Rotating Electrical Machinery: Materials Development and Part Design. Ph.D. Thesis, University of Nottingham, Nottingham, UK, 2018.

4. Tiismus, H.; Kallaste, A.; Belahcen, A.; Rassolkin, A.; Vaimann, T. Challenges of Additive Manufacturing of Electrical Machines. In Proceedings of the 2019 IEEE 12th International Symposium on Diagnostics for Electrical Machines, Power Electronics and Drives (SDEMPED), Toulouse, France, 27–30 August 2019; Institute of Electrical and Electronics: Manhattan, NY, USA, 2019; pp. 44–48. [[CrossRef](#)]
5. Wrobel, R.; Mecrow, B. A Comprehensive Review of Additive Manufacturing in Construction of Electrical Machines. In Proceedings of the IEEE Workshop on Electrical Machines Design, Control and Diagnosis (WEMDCD), Greece, Balkans, 22–23 April 2019; Institute of Electrical and Electronics: Manhattan, NY, USA, 2019; pp. 15–22. [[CrossRef](#)]
6. Wrobel, R.; Mecrow, B.C. A Comprehensive Review of Additive Manufacturing in Construction of Electrical Machines. *IEEE Trans. Energy Convers.* **2020**, *35*, 1054–1064. [[CrossRef](#)]
7. Naseer, M.; Kallaste, A.; Asad, B.; Vaimann, T.; Rassölkin, A. A Review on Additive Manufacturing Possibilities for Electrical Machines. *Energies* **2021**, *14*, 1940. [[CrossRef](#)]
8. Ghahfarokhi, P.S.; Podgornovs, A.; Kallaste, A.; Cardoso, A.J.M.; Belahcen, A.; Vaimann, T.; Tiismus, H.; Asad, B. Opportunities and Challenges of Utilizing Additive Manufacturing Approaches in Thermal Management of Electrical Machines. *IEEE Access* **2021**, *9*, 36368–36381. [[CrossRef](#)]
9. Selema, A.; Ibrahim, M.N.; Sergeant, P. Metal Additive Manufacturing for Electrical Machines: Technology Review and Latest Advancements. *Energies* **2022**, *15*, 1076. [[CrossRef](#)]
10. Pham, T.; Kwon, P.; Foster, S. Additive Manufacturing and Topology Optimization of Magnetic Materials for Electrical Machines—A Review. *Energies* **2021**, *14*, 283. [[CrossRef](#)]
11. Chaudhary, V.; Mantri, S.A.; Ramanujan, R.V.; Banerjee, R. Additive manufacturing of magnetic materials. *Prog. Mater. Sci.* **2020**, *114*, 100688. [[CrossRef](#)]
12. Tiismus, H.; Kallaste, A.; Vaimann, T.; Rassölkin, A. State of the art of additively manufactured electromagnetic materials for topology optimized electrical machines. *Addit. Manuf.* **2022**, *55*, 102778. [[CrossRef](#)]
13. Igarashi, H.; Okazaki, K. Effects of Porosity and Grain Size on the Magnetic Properties of NiZn Ferrite. *J. Am. Ceram. Soc.* **1977**, *60*, 51–54. [[CrossRef](#)]
14. Goldman, A. *Handbook of Modern Ferromagnetic Materials*; Springer: Berlin/Heidelberg, Germany, 1999.
15. Li, L. Stress Effects on Ferromagnetic Materials: Investigation of Stainless Steel and Nickel. *Retrospect. Theses Diss.* **2004**. [[CrossRef](#)]
16. Krings, A.; Cossale, M.; Tenconi, A.; Soulard, J.; Cavagnino, A.; Boglietti, A. Magnetic Materials Used in Electrical Machines: A Comparison and Selection Guide for Early Machine Design. *IEEE Ind. Appl. Mag.* **2017**, *23*, 21–28. [[CrossRef](#)]
17. Ouyang, G.; Chen, X.; Liang, Y.; Macziewski, C.; Cui, J. Review of Fe-6.5 wt%Si high silicon steel—A promising soft magnetic material for sub-kHz application. *J. Magn. Magn. Mater.* **2019**, *481*, 234–250. [[CrossRef](#)]
18. Galsin, J.S. Physical Effects of Impurities in Metals. In *Impurity Scattering in Metallic Alloys*; Springer: Berlin/Heidelberg, Germany, 2002; pp. 93–123. [[CrossRef](#)]
19. Belahcen, A.; Rasilo, P.; Arkkio, A. Segregation of Iron Losses from Rotational Field Measurements and Application to Electrical Machine. *IEEE Trans. Magn.* **2014**, *50*, 893–896. [[CrossRef](#)]
20. Hawezzy, D. The influence of silicon content on physical properties of non-oriented silicon steel. *Mater. Sci. Technol.* **2017**, *33*, 1560–1569. [[CrossRef](#)]
21. Wilson-Heid, A.E.; Novak, T.C.; Beese, A.M. Characterization of the Effects of Internal Pores on Tensile Properties of Additively Manufactured Austenitic Stainless Steel 316L. *Exp. Mech.* **2018**, *59*, 793–804. [[CrossRef](#)]
22. Sames, W.J.; List, F.A.; Pannala, S.; Dehoff, R.R.; Babu, S.S. The metallurgy and processing science of metal additive manufacturing full critical review. *Int. Mater. Rev.* **2016**, *61*, 315–360. [[CrossRef](#)]
23. Hansen, N. Hall–Petch relation and boundary strengthening. *Scr. Mater.* **2004**, *51*, 801–806. [[CrossRef](#)]
24. Raabe, D. Recovery and Recrystallization: Phenomena, Physics, Models, Simulation. *Phys. Metall.* **2014**, *2014*, 2291–2397. [[CrossRef](#)]
25. Alatawneh, N.; Saleem, A.; Rahman, T.; Lowther, D.A.; Chromik, R. Modelling and analysis of the effects of cutting of core laminations in electric machines. *IET Electr. Power Appl.* **2020**, *14*, 2355–2361. [[CrossRef](#)]
26. Ding, Y.; Gallagher, M.; Brodusch, N.; Gauvin, R.; Chromik, R.R. Coating induced residual stress in nonoriented electrical steel laminations. *J. Mater. Res.* **2014**, *29*, 1737–1746. [[CrossRef](#)]
27. Cordova, L.; Bor, T.; de Smit, M.; Campos, M.; Tinga, T. Measuring the spreadability of pre-treated and moisturized powders for laser powder bed fusion. *Addit. Manuf.* **2020**, *32*, 101082. [[CrossRef](#)]
28. Mussatto, A.; Groarke, R.; O’Neill, A.; Obeidi, M.A.; Delaure, Y.; Brabazon, D. Influences of powder morphology and spreading parameters on the powder bed topography uniformity in powder bed fusion metal additive manufacturing. *Addit. Manuf.* **2021**, *38*, 101807. [[CrossRef](#)]
29. Kotadia, H.; Gibbons, G.; Das, A.; Howes, P. A review of Laser Powder Bed Fusion Additive Manufacturing of aluminium alloys: Microstructure and properties. *Addit. Manuf.* **2021**, *46*, 102155. [[CrossRef](#)]
30. Wang, D.; Wu, S.; Fu, F.; Mai, S.; Yang, Y.; Liu, Y.; Song, C. Mechanisms and characteristics of spatter generation in SLM processing and its effect on the properties. *Mater. Des.* **2017**, *117*, 121–130. [[CrossRef](#)]
31. Aboulkhair, N.T.; Everitt, N.; Ashcroft, I.; Tuck, C. Reducing porosity in AlSi10Mg parts processed by selective laser melting. *Addit. Manuf.* **2014**, *1–4*, 77–86. [[CrossRef](#)]

32. *European Standard EN 60404-6*; Magnetic Materials—Part 6: Methods of Measurement of the Magnetic Properties of Magnetically Soft Metallic and Powder Materials at Frequencies in the Range 20 Hz to 100 kHz by the Use of Ring Specimens. European Comitee for Electrotechnical Standardization: Brussels, Belgium, 2004.
33. *European Standard EN 60404-4*; Magnetic Materials—Part 4: Methods of Measurement of d.c. Magnetic Properties of Iron and Steel. European Comitee for Electrotechnical Standardization: Brussels, Belgium, 2002.
34. American Society for Testing and Materials. *Standard Test Methods for Tension Testing of Metallic Materials*; ASTM International: West Conshohocken, PA, USA, 2010; Volume I, pp. 1–27. [CrossRef]
35. DC Magnetization Curves of Soft Magnetic Materials: Finite Element Method Magnetics. Available online: <https://www.femm.info/wiki/SoftMagneticMaterials> (accessed on 28 March 2022).
36. Hogan. Material Data_Somaloy. Available online: www.hoganas.com/electromagnetic (accessed on 9 June 2020).
37. Tiismus, H.; Kallaste, A.; Belahcen, A.; Vaimann, T.; Rassõlkin, A.; Lukichev, D. Hysteresis Measurements and Numerical Losses Segregation of Additively Manufactured Silicon Steel for 3D Printing Electrical Machines. *Appl. Sci.* **2020**, *10*, 6515. [CrossRef]
38. Sonboli, A.; Toroghinejad, M.R.; Edris, H.; Szpunar, J.A. Effect of deformation route and intermediate annealing on magnetic anisotropy and magnetic properties of a 1 wt% Si non-oriented electrical steel. *J. Magn. Magn. Mater.* **2015**, *385*, 331–338. [CrossRef]
39. Garibaldi, M.; Ashcroft, I.; Simonelli, M.; Hague, R. Metallurgy of high-silicon steel parts produced using Selective Laser Melting. *Acta Mater.* **2016**, *110*, 207–216. [CrossRef]
40. Da Cunha, M.A.; Paolinelli, S.C. Effect of the Annealing Temperature on the Structure and Magnetic Properties of 2% Si Steel. *Mater. Res.* **2002**, *5*, 373–378. [CrossRef]
41. Plotkowski, A.; Pries, J.; List, F.; Nandwana, P.; Stump, B.; Carver, K.; Dehoff, R. Influence of scan pattern and geometry on the microstructure and soft-magnetic performance of additively manufactured Fe-Si. *Addit. Manuf.* **2019**, *29*, 100781. [CrossRef]
42. Stornelli, G.; Faba, A.; Di Schino, A.; Folgarait, P.; Ridolfi, M.; Cardelli, E.; Montanari, R. Properties of Additively Manufactured Electric Steel Powder Cores with Increased Si Content. *Materials* **2021**, *14*, 1489. [CrossRef]
43. Koo, B.; Jang, M.-S.; Nam, Y.G.; Yang, S.; Yu, J.; Park, Y.H.; Jeong, J.W. Structurally-layered soft magnetic Fe-Si components with surface insulation prepared by shell-shaping selective laser melting. *Appl. Surf. Sci.* **2021**, *553*, 149510. [CrossRef]
44. Goll, D.; Schuller, D.; Martinek, G.; Kunert, T.; Schurr, J.; Sinz, C.; Schubert, T.; Bernthaler, T.; Riegel, H.; Schneider, G. Additive manufacturing of soft magnetic materials and components. *Addit. Manuf.* **2019**, *27*, 428–439. [CrossRef]
45. Super Core TM Electrical Steel Sheets for High-Frequency Application. Available online: <https://www.jfe-steel.co.jp/en/products/electrical/catalog/fl-e-002.pdf> (accessed on 13 May 2021).
46. Zhang, M.; Kong, F.; Wang, A.; Chang, C.; Shen, B. Soft magnetic properties of bulk FeCoMoPCBSi glassy core prepared by copper mold casting. *J. Appl. Phys.* **2012**, *111*, 07A312. [CrossRef]
47. Shiozaki, M.; Kurosaki, Y. The effects of grain size on the magnetic properties of nonoriented electrical steel sheets. *J. Mater. Eng.* **1989**, *11*, 37–43. [CrossRef]
48. Honma, K.; Nozawa, T.; Kobayashi, H.; Shimoyama, Y.; Tachino, I.; Miyoshi, K. Development of non-oriented and grain-oriented silicon steel. *IEEE Trans. Magn.* **1985**, *21*, 1903–1908. [CrossRef]
49. EVS-EN 10106:2015—Cold Rolled Non-Oriented Electrical Steel Strip and Sheet Delivered in the fully Processed State. Available online: <https://www.evs.ee/et/evs-en-10106-2015> (accessed on 25 April 2022).
50. Data Sheet of Isovac 400-50A. Available online: https://www.voestalpine.com/stahl/content/download/4542/file/DB_isovac_400-50A_E_280715.pdf?inLanguage=eng-GB (accessed on 14 March 2021).
51. Data Sheet of Isovac 1000-65A. Available online: https://www.voestalpine.com/stahl/content/download/4554/file/DB_isovac_1000-65A_E_280715.pdf?inLanguage=eng-GB (accessed on 14 March 2021).
52. Non Grain Oriented Electrical Steel, Powdercore. Available online: https://www.thyssenkrupp-steel.com/media/content_1/publikationen/lieferprogramme/thyssenkrupp_product-range_no-electrical-steel_powercore_steel_en.pdf (accessed on 16 March 2021).
53. Bozorth, R.M. *Ferromagnetism*; Wiley-IEEE Press: Hoboken, NJ, USA, 1993.

Publication III

H. Tiismus, A. Kallaste, M. U. Naseer, T. Vaimann, and A. Rassolkin, "Design and Performance of Laser Additively Manufactured Core Induction Motor," IEEE Access, pp. 50137–50152, 2022, doi: 10.1109/ACCESS.2022.3173317.

Received April 13, 2022, accepted May 4, 2022, date of publication May 9, 2022, date of current version May 13, 2022.

Digital Object Identifier 10.1109/ACCESS.2022.3173317

Design and Performance of Laser Additively Manufactured Core Induction Motor

HANS TIISMUS^{ID}, (Member, IEEE), **ANTS KALLASTE**^{ID}, (Senior Member, IEEE),
MUHAMMAD USMAN NASEER^{ID}, (Member, IEEE),
TOOMAS VAIMANN^{ID}, (Senior Member, IEEE),
AND ANTON RASSÖLKIN^{ID}, (Senior Member, IEEE)

Department of Electrical Power Engineering and Mechatronics, Tallinn University of Technology, 19086 Tallinn, Estonia

Corresponding author: Hans Tiismus (hans.tiismus@taltech.ee)

This work was supported by the Estonian Ministry of Education and Research under Project PSG-137.

ABSTRACT Over the past decade, additive manufacturing (AM) of functional electromagnetic components has grown into a promising new area of research. Not only does AM allow for unparalleled in-house prototyping speed and flexibility, but it also introduces a completely new set of design rules for obtaining optimized component shapes. Up to date, relatively few functional electromagnetic components or devices have actually been printed, and fewer still actually characterized or compared in terms of performance. This work describes the completion process of a prototype induction motor with fully 3D printed electrical steel cores, from design to printing, post-processing, assembling, and performance evaluation. This work aims to establish a baseline for further optimization and to map the design and production process of a fully functional electrical machine for future reference. The output of the finished motor was measured at 68 W (0.5 Nm) at 34% energy efficiency. This is roughly 2/3 of the efficiency of conventional machines of the same size and type. Further optimization steps for the 3D printed material and core design are proposed to obtain higher motor performance.

INDEX TERMS Electric motor, selective laser melting, soft magnetic material, additive manufacturing.

I. INTRODUCTION

Metal additive manufacturing (AM) technologies have redefined the practical limits of the production industry, enabling a previously unfeasible level of part personalization and topological complexity. With AM, highly intricate parts in small volumes can be produced cost-effectively, as costs involved are largely invariant of both shape complexity (in contrast to subtractive technologies) and lot size (in contrast to mould-based technologies) [1]. This enables innovative next-generation business models and products.

The unprecedented production freedom of AM enables the further development of electrical machines (EMs). Finally, the EM research community has the opportunity to approach the machine design out-of-the-box and introduce previously unfeasible topologies. This means more opportunities for electromagnetic and thermal optimization. Machine flux guides, conductors, and thermal exchangers can be shaped

three-dimensionally according to specific design requirements, likely leading to novel, intricate machines designs. These designs could be more refined versions of existing designs, such as the claw-pole, transversal, or axial flux machine designs, or perhaps more complex multi-axial or spherical motors. The latter would be especially useful for satellite, UAV, or robotics applications.

Discussion on the latest breakthroughs in AM motor design and prototyping can be found in [2]–[6]. Some of the more illustrating examples of the novel design features currently implemented with AM prototypes are presented in Figure 1. For electrical machines, AM has been used to the greatest effect for the realization of single-material metal components, most commonly from silicon steel, cobalt-iron, copper, or aluminum alloys. Most prominently, these components have been either rotors for synchronous machines, enhanced windings, or cooling jackets/fins, taking advantage of the spatial accuracy of 3D printing. These first prototypes have achieved significant weight reduction (improved rotor dynamics) [7], [8], reduced torque ripple [8], reduced

The associate editor coordinating the review of this manuscript and approving it for publication was Francisco Perez-Pinal^{ID}.

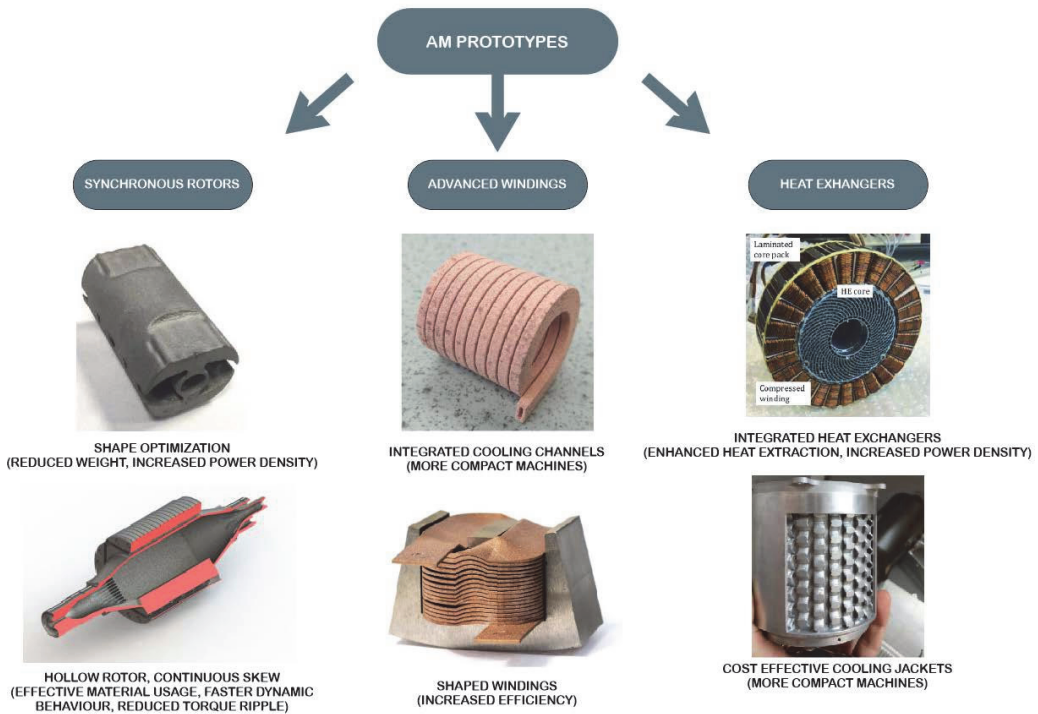


FIGURE 1. Current main directions in AM prototyping electrical machine components: synchronous rotors ([7], [8]), advanced windings ([12], [9]), and heat exchangers ([10], [11]).

AC losses in windings [9], and enhanced machine cooling through more effective cooling jackets [10], heat exchangers [11] and integrated cooling channels within the windings [12]. Nevertheless, AM of full electrical machines is yet to be completed, as the most significant challenge left in the field: limited multi-material capacity of metal printing systems, has yet remained largely unsolved. The technology is still in its infancy but has, alongside *in-situ* alloying, received considerable research focus over the recent years [13]–[16] in both the academic and industrial circles.

Both AM motor windings and soft cores have limited multi-material imposed drawbacks. Most significantly, regarding the formation of insulation layers within the cores for eddy current suppression and for inter-turn separation of the windings. The current state-of-the-art informing insulation layers within printed metal components has been by integrating voids (air-gaps) between the printed solid volumes. In magnetic cores, this approach has had mixed success: in AM air-gapped soft magnetic Fe-Si cores, core losses roughly equivalent to medium grade silicon steels [17] have been obtained (~ 1.5 W/kg at $W_{10,50}$), albeit at a tradeoff in the material fill factor (air-gaps are wider than varnish layers between laminations) [18]. It is also important to note that AM segregated cores have been shown to be superior to SMC cores [17] loss-wise at 50 Hz

(5-6 W/kg at $W_{10,50}$ [19]) – SMCs are the current materials of choice for producing EMs with complex core topologies.

Undoubtedly, with technological advances, AM soft magnetic cores have the potential to surpass conventional laminations in performance. To achieve this, further development of more advanced printing systems (higher accuracy, support-less printing, multi-material options, faster build rate) and the discovery of novel alloys and materials are a requisite. AM is well known for its capacity to form parts from unconventional and capricious materials. The conventionally difficult material to process due to its brittleness: 6.5% silicon steel, has been successfully fused with laser AM, achieving net-shape, crack-free 6.5% samples with useful magnetic properties [20], [21]. Amorphous cores are especially exciting for 3D printed EM applications, as the alloys show exceptionally high values of relative permeability ($\mu_r \sim 100\,000 - 500\,000$), electrical resistivity ($\rho_e = 100 - 130 \mu\Omega \text{ cm}$) [22] and losses in the magnitude of 0.1 W/kg at $W_{10,50}$. They are, however, complex to manufacture, especially into complex shapes. Laser AM has been shown to be suitable in forming bulk cores with high glassy amorphous content [23] as related to the process's fast cooling rates. Perhaps with further research, high-efficiency amorphous cores can be implemented into electrical machine prototypes.

Despite the first successes in AM prototyping and the bright future prospects, presently, relatively few functional electromagnetic components or devices have actually been printed, and fewer still actually characterized in terms of performance (e.g., [24], [25]). This is likely due to the difficulties in setting up an in-house production chain covering all the necessary steps from component design to its printing, post-processing, assembling, and finally, performance measurements. With this work, we hope to provide some insight into the challenges arising in each of the production steps and how to best tackle them.

This work focuses on the in-house design and production process of an electrical motor. For the first time in literature, an electrical machine with fully 3D printed soft magnetic cores (rotor + stator) is produced and evaluated in terms of performance. The design incorporates a novel segregation method for limiting the eddy currents within the core. The objective of this work is to establish a baseline for further optimization and to map the design and production process of an electrical machine for future reference. The contents of the paper are divided into three larger sections. The second to third chapters of the paper describes the prototype design, the fourth its production methods and challenges, and the fifth its performance evaluation.

II. DESIGN PROCEDURE

The main design parameters of the prototype are determined through an analytical procedure. The summary of the finalized parameters is outlined in Table 2, detailing the geometry, and the rated input/output values of the machine. The process in this work follows closely a procedure described by J. Pyrhönen *et al.* in a design handbook titled: “*Design of Rotating Electrical Machines*” [26]. The main constraints on the prototype design were defined by the dimensions of our printing facilities and the properties of the printed material. These two factors dictated that the diameter of the prototype cannot exceed 90 mm and that the efficiency of the motor shall be substantially lower than conventional motors of the same size. Additionally, it was decided to design the machine as a squirrel-cage induction motor (IM). It is relatively robust construction-wise and simple to operate: development of a separate inverter and a drive algorithm is not necessary for verifying the prototype performance empirically. The flowchart of the design process is outlined in Figure 3.

A. INITIAL VALUES

Machine design parameters are divided into fixed and interdependent free variables. Fixed variables remain unchanged as part of the iterative design process and represent either constraints (e.g., frequency of the grid), best practices known from empirical knowledge (e.g., four-pole design for small IM machines), or specific design choices (e.g., single layer non-skewed winding). The free variables are flexible: they are re-evaluated over the iterative design process to find the optimal final parameters satisfying the design criteria. The values for both the fixed and initial free variables of

the design are outlined in Table 1, chosen based on design experience or well-established practices. The output power of IMs of roughly the same size is 0.1 kW, with energy efficiencies in the range of 50-60% [27]. For the prototype, it was estimated that efficiencies 10-20% lower should be achievable at similar core flux densities and output power. This estimation was based on previous material characterization in [28], where equivalent DC properties to high-grade silicon steels were obtained, but with 2-20x higher iron losses depending on the individual part topology. The magnetization curve of the previously characterized printed silicon steel for the prototype preparation compared with typical commercial materials [29], [19] is outlined in Figure 2. The initial

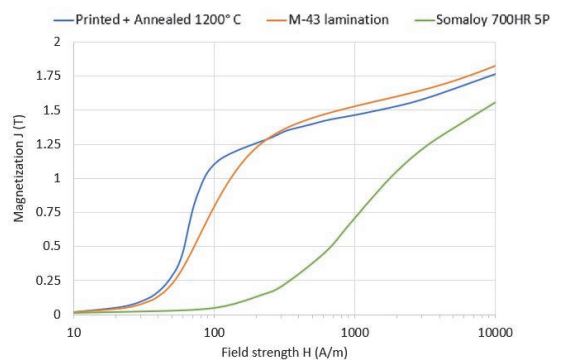


FIGURE 2. Magnetization curve of the pre-characterized printed material, compared to common EM materials.

TABLE 1. Initial design parameters.

Marker	Design Parameter	Value	Unit
FIXED			
η	Efficiency	40	%
J_s	Stator current density	6.5	A/mm ²
p	No. of poles	4	No
f	Frequency	50	Hz
m	No. of phases	3	No
y	Coil Pitch	6	No.
S_{sp}	Slot skewing	0	No.
a	Parallel paths in winding	1	No
FREE			
A	Linear current density	15.95	kA/m
B_s	Peak Air-gap flux density	0.60	T
P_{mec}	Output power	100	W
$\cos\theta$	Power Factor	0.65	-
V	Terminal Voltage	24	V
k_w	Winding Factor	0.95	-
E_m	Induced emf	0.97·V	V
A	Linear Current Density	15	kA/m
α_i	Saturation factor	0.65	-

and high field strength flux densities within the material were extrapolated from the data. The target current densities within the stator were chosen as slightly higher than in standard machines: 6.5 A/mm² to compensate for the high active power drawn by the eddy current losses. This is deemed acceptable, as effective removal of excessive heat has been shown to be a strong advantage of AM electrical machines [4].

Other parameters were chosen based on well-established machine design guidelines. To streamline the prototype assembly, single-layer winding with no rotor and stator slot skewing was chosen. Saturation factor, winding factor and induced EMF were chosen within typical values for IMs. The selected values of terminal voltage, power factor and linear current density are often encountered in small IMs and can be considered a reasonable starting point for the design.

B. MAIN DIMENSIONS

The first step in the design procedure is machine sizing: the calculation of its length and stator inner diameter. First, the machine sizing constant C_{mec} is calculated with (1) from the initial estimated values for terminal voltage V , induced EMF of the stator phase winding E_m , efficiency η , power factor $\cos \theta$, fundamental component winding factor k_{w1} , RMS value of the linear stator current density A and \hat{B}_δ – the peak air-gap flux density.

$$C_{mec} = \frac{V}{\sqrt{2} E_m} \eta \cos \theta \pi^2 k_{w1} A \hat{B}_\delta \quad (1)$$

After calculating the optimal ratio of machine length to diameter X from (2), where l_{eq} is the equivalent machine stack length, D – stator inner diameter and p – the number of poles,

$$X = \frac{l_{eq}}{D} \approx \frac{\pi}{2p} \sqrt[3]{P} \quad (2)$$

the investigated machine dimensions can be obtained from (3), where n_{syn} is the motor synchronous speed, and P_{mec} its output power. The term $D^2 l_{eq}$ is indicative of machine rotor volume V_r as illustrated by (4).

$$P_{mec} = C_{mec} D^2 l_{eq} n_{syn} \quad (3)$$

$$V_r \sim \pi / 4 D^2 l_{eq} \quad (4)$$

C. AIR-GAP

Air-gap width δ can be obtained through (5), where P_{mec} is the mechanical output power of the machine.

$$\delta = 0.18 + 0.006 \cdot \frac{0.4 \cdot P_{mec}}{1000} \quad (5)$$

In this work, if the resultant calculated air-gap is less than 0.35 mm, it will be rounded up to it. This is the approximate accuracy limit of our facilities.

D. WINDING

The winding design process begins by selecting a suitable number of slots per-pole per-phase q_s , which also correlates

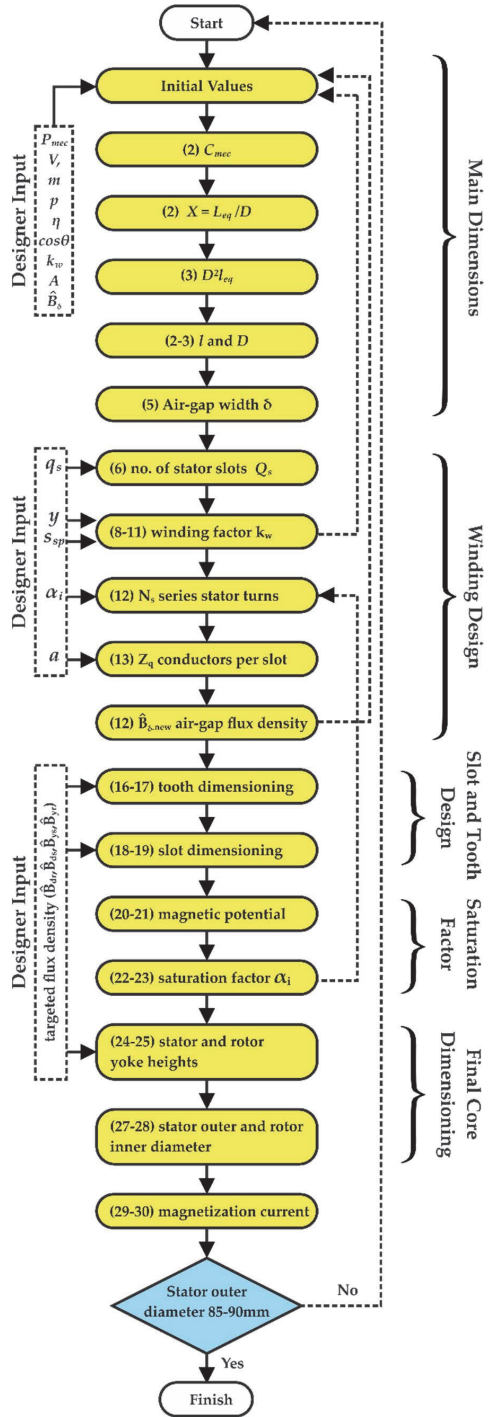


FIGURE 3. Flowchart of the prototype design procedure.

to an optimal number of slot pitch τ_{us} . The slot pitch τ_{us} and the total number of stator slots Q_s are given by

Equations (6) and (7):

$$Q_s = 2pmq_s \quad (6)$$

$$\tau_{us} = \frac{\pi D}{Q_s} \quad (7)$$

where m is the number of stator phases, q_s – the total number of stator slots, and p – the total number of poles. Based on design guidelines, for the obtained 24 stator slots, the optimal number of rotor slots Q_r is 18.

The next step is calculating the fundamental component winding factor k_w to determine the attenuation of the fundamental components of the selected winding design. k_w comprises mainly of the skewing factor k_{sq} , pitch factor k_p , and distribution factor k_d , calculated as follows through equation (8)–(11):

$$k_d = \sin\left(\frac{\pi}{2m}\right) / q \sin\left(\frac{\pi}{2mq_s}\right) \quad (8)$$

$$k_p = \sin(\pi y / 2y_Q) \quad (9)$$

$$k_{sq} = \sin\left(\frac{\pi}{2} \frac{s_{sp}}{mq_s}\right) / \left(\frac{\pi}{2} \frac{s_{sp}}{mq_s}\right) \quad (10)$$

$$k_w = k_d k_p k_{sq} \quad (11)$$

In equations (8)–(11), the k_{sq} denotes the skewing factor, k_p – the pitch factor, k_d – the distribution factor, and k_w – the collective winding factor. The term y/y_Q gives the relative shortening of the coil span, where y_Q is the full pole pitch expressed in the number of slots and y is the actual pitch of the coil (after short pitching) and s_{sp} is the skewing of slots in terms of the number of slot pitches.

The series winding turns per-phase N_s , and the number of conductors in each slot z_Q are calculated as follows:

$$N_s = \sqrt{2} E_m / \omega k_w l_{eq} \tau_p \alpha_i \hat{B}_\delta \quad (12)$$

$$z_Q = 2amN_s / Q_s \quad (13)$$

The obtained number of conductors in the slot z_Q is rounded up to the nearest even integer, resulting in 24 conductors per slot. Finally, with the winding design completed, the new air-gap flux density is recalculated from (12), and the design process is re-evaluated from step one (substituting the initially proposed air-gap flux density value).

The conductor currents in both rotor and stator are obtained with equations (14) and (15).

$$I_s = P_{mec} / mV \eta \cos \theta \quad (14)$$

$$I_r = \frac{z_Q Q_s}{a} I_s \cos \theta \quad (15)$$

where Q_r is the number of rotor slots / bars, and a is the number of parallel paths in the winding.

E. STATOR AND ROTOR TOOTH

For obtaining the stator and rotor tooth designs, approximate flux densities (\hat{B}'_{ds} and \hat{B}'_{dr}) must first be proposed based on well-established magnetization values in IMs.

The stator/rotor tooth width is calculated as follows from equations (16) and (17):

$$b_{ds} = \frac{l_{eq} \tau_{us}}{k_{Fe}(l - n_v b_v)} \hat{B}'_{ds} \quad (16)$$

$$b_{dr} = \frac{l_{eq} \tau_{ur}}{k_{Fe}(l - n_v b_v)} \hat{B}'_{dr} \quad (17)$$

where b_{ds} and b_{dr} are the stator and rotor tooth widths. k_{Fe} is the space factor for the respective core material. τ_{us} and τ_{ur} are the stator and rotor slot pitches. n_v and b_v are the number and width of ventilating ducts, if any, in the respective stator or rotor body.

From the calculated values of z_Q and tooth-widths of stator/rotor, the slots are dimensioned according to respective stator and rotor currents (I_s and I_r), maximum current densities (J_s and J_r), and the resulting values of required cross-sectional areas (S_{cs} and S_{cr}):

$$S_{cs} = \frac{I_s}{aJ_s} \quad (18)$$

$$S_{cr} = \frac{I_r}{J_r} \quad (19)$$

After selecting basic slot dimensions, i.e. slot opening, required insulation thickness, slot type, and average slot width, the slot height and widths at respective heights are calculated according to the required area to house the conductors (S_{cs} and S_{cr}). The slot dimensions and total and wound area are illustrated in Figure 4.

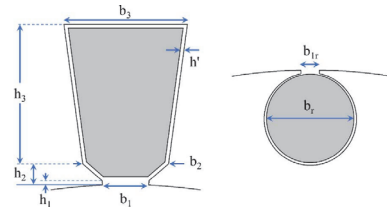


FIGURE 4. Main design dimensions for the rotor and stator slots.

F. SATURATION FACTOR

The initially proposed saturation factor α_i is now calculated from the obtained design for verification. In the four-step process, the first is calculating the flux leakage related to field weakening within core teeth. This corrected flux density \hat{B}_d (initially proposed flux density \hat{B}'_d) is proportional to the ratio of slot area without the iron portion (S_u) to the iron portion of the tooth area (S_d), as described by equation (20).

$$\hat{B}_d = \hat{B}'_d - \frac{S_u}{S_d} \mu_o \hat{H}_{dl} \quad (20)$$

In order to calculate the magnetic potential within the rotor/stator teeth, the field strength H within the teeth is determined. This can be found from (20) and the material magnetization curve by solving either the equation system

or finding the intersection point numerically. The process is illustrated in Figure 5: where the H for the designed machine stator tooth tip is determined. The corresponding intersection points yield corrected flux density \hat{B}_{dl} and magnetic field \hat{H}_{dl} strength values.

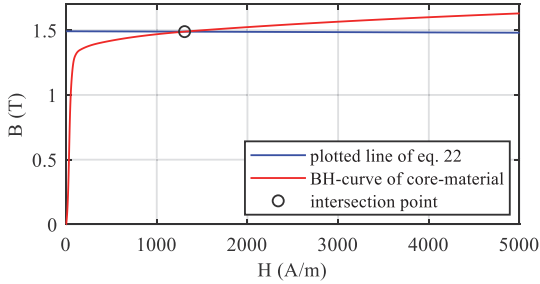


FIGURE 5. Field strength estimation within the stator core tooth tip.

The magnetic potential of the machine air-gap and rotor/stator teeth can now be calculated with the magnetic field strength line integral within the respective geometries with equation (21). The global magnetization within the machine cores can be calculated with equation (22), where $\hat{U}_{m,\delta}$, $\hat{U}_{m,r}$ and $\hat{U}_{m,s}$ are the respective magnetic potentials within machine air-gap, rotor, and the stator core. Finally, the calculated value of saturation factor (k_{sat}) can be utilized to determine the actual value of α_i (with equation 23), which was only assumed initially.

$$U_m = \int H \cdot dl \quad (21)$$

$$k_{sat} = \frac{\hat{U}_{m,s} + \hat{U}_{m,r}}{\hat{U}_{m,\delta}} \quad (22)$$

$$\alpha_i = \frac{1.24k_{sat} + 1}{1.42k_{sat} + 1.57} \quad (23)$$

G. STATOR AND ROTOR YOKE

Calculation of yoke heights for cores begins by first defining the desired flux densities within them. Lower yoke height translates to higher core losses and higher yoke height to a larger machine diameter. In this design, both yoke flux densities (B_{yr} , B_{ys}) were chosen as 1.3 T, 0.2 T lower from tooth tip magnetization. The yoke heights (h_{ys} and h_{yr}) are determined from the estimated peak value of air-gap flux from (24) – (25):

$$h_{ys} = \frac{\hat{\theta}_m}{2k_{Fe}l\hat{B}_{ys}} \quad (24)$$

$$h_{yr} = \frac{\hat{\theta}_m}{2k_{Fe}l\hat{B}_{yr}} \quad (25)$$

The peak air-gap flux density is derived from (25):

$$\hat{\theta}_m = \alpha_i \hat{B}_\delta \tau_p l_{eq} \quad (26)$$

where $\hat{\theta}_m$ is the peak air-gap flux. Finally, the stator outer and rotor inner diameters are calculated as follows:

$$D_{se} = D_s + 2(h_s + h_{ys}) \quad (27)$$

$$D_{ri} = D_r - 2(h_r + h_{yr}) \quad (28)$$

where D_{se} , D_{re} , h_s and h_r are the stator outer-diameter, rotor inner-diameter, stator and rotor slot heights (determined at slot dimensioning step).

H. MAGNETIZING CURRENT/NO-LOAD CURRENT

Rated no-load current of the prototype is determined for inputting to FEM analysis. The fundamental current linkage and hence the magnetization in the machine is produced by the magnetizing current ($I_{s,mag}$) of the rotating stator field and is given by

$$\hat{U}_{m,total} = \hat{\Theta}_{s1} = \frac{mk_w N_s \sqrt{2}}{\pi p} I_{s,mag} \quad (29)$$

$$\hat{U}_{m,total} = \hat{U}_{m,\delta} + \hat{U}_{m,s} + \hat{U}_{m,r} + \hat{U}_{m,ys}/2 + \hat{U}_{m,yr}/2 \quad (30)$$

where $\hat{U}_{m,total}$ is the magnetic voltage for half the magnetic circuit of the machine. $\hat{U}_{m,ys}$ and $\hat{U}_{m,yr}$ are the magnetic potentials of the stator and rotor yokes, respectively, and are calculated with the same procedure described in section-F for other machine parts. With the $\hat{U}_{m,total}$ determined, the no-load magnetizing current of the machine is calculated from (29).

I. DESIGN SUMMARY

The summary of final design parameters is summarized in Table 2. The motor rated speed (subsequently its rated torque) is assumed based on speed values for equivalent machines. These initial values are used as the basis to further develop the machine design into 3D in the next chapter.

III. FINAL DESIGN

For verifying the data obtained from the analytical design, a static finite element analysis was conducted. Modeling of the prototype was completed in an open-source FEM package software: FEMM (Finite Element Method Magnetics). Figure 6 presents the obtained flux distribution within the core alongside its overall dimensions and slot shapes. Similar peak material magnetization values to the analytical model were confirmed: rotor tooth 1.4 T, stator tooth 1.5 T, stator yoke 1.2 T, air-gap 0.7 T. Due to a material reduction introduced after the analytical design within the rotor core around its shaft, the flux densities within the rotor yoke peak at higher value of 1.5 T. The material was reduced to demonstrate the capabilities of additive manufacturing for design weight reduction.

The key challenges in designing the AM machine were obtaining a uniform, narrow 0.35 mm air-gap and minimizing eddy current losses – especially within the stator core. For eddy current loss reduction, a strategy inspired from common EM stampings was devised. It included the introduction of crack-like air-gaps printed within the cores to increase their internal resistance. These air-gaps were introduced in

TABLE 2. Design parameters of the prototype motor.

Machine's Design Parameter	Value	Unit
Machine rated power	80	W
Terminal Voltages (L-N)	20	V
No. of phases	3	No.
No. of poles	4	No.
Frequency	50	Hz
Rated Rotational speed	1400	rpm
Rated torque output	0.55	Nm
Peak Air-gap flux density	0.60	T
Linear current density	15.95	kA/m
Stator outer-diameter	89.00	mm
Stator bore-diameter	57.50	mm
Rotor Diameter	56.80	mm
Machine stack-length	56.00	mm
Air-gap width	0.35	mm
No. of stator slots	24	No.
No. of winding layers	1	No.
No. of parallel paths	1	No.
Pole pitch	45.20	mm
Slot pitch	7.52	mm
Short pitching	0	No.
Stator conductor diameter	1	mm
Stator-slot opening	2.52	mm
Stator-tooth flux density	1.50	T
Stator-tooth width	3.20	mm
Stator-slot height	8.80	mm
Stator-yoke flux density	1.30	T
Stator-yoke height	7.10	mm
Rotor-slot opening	1.00	mm
Rotor-tooth flux density	1.50	T
Rotor-tooth width	3.90	mm
Rotor-bar diameter	5.00	mm
Rotor-yoke flux density	1.30	T
Rotor-yoke height	7.10	mm
No-load magnetizing current	3.65	A

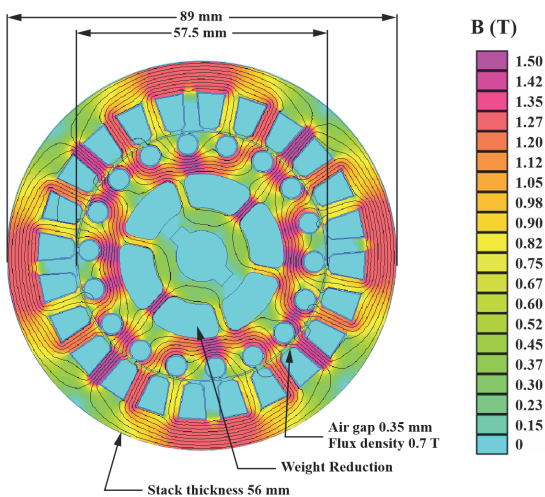


FIGURE 6. Overall dimensions and flux distribution of the designed IM.

perpendicular to the core axes. The opted strategy for eddy current loss reduction is outlined in Figure 7. The final design exhibited 2 mm solid material laminations separated with

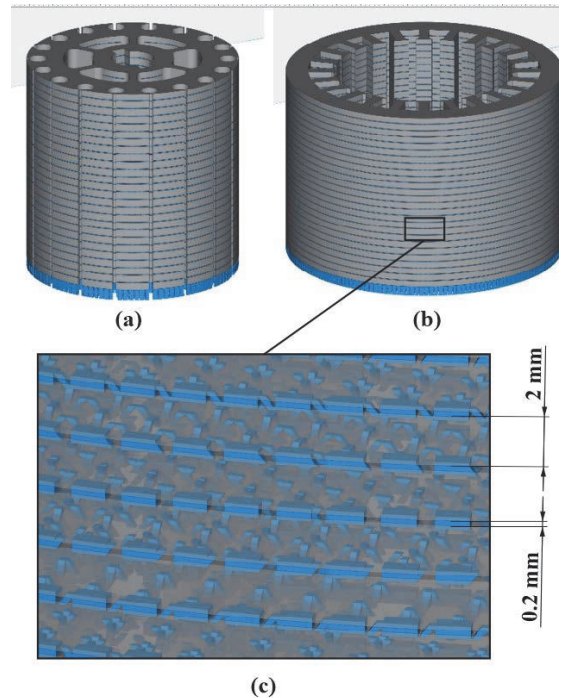


FIGURE 7. Structure for eddy current loss reduction within the printed soft magnetic cores: (a) rotor core, (b) stator core, (c) detailed view of the insulation layers printed within the cores.

0.2 mm air-gaps. Lattice structures were added within the air-gaps to consolidate the printed part into a single core. These support structures consist of thick border elements to prevent part warpage and delamination during printing; and thin lattice structures supporting the part core to enable powder fusion between the layers. To the best knowledge of authors this type of printed core segregation has never been attempted before in the literature. Compared to conventional motor stampings, The opted design has undoubtedly drawbacks in both lower electrical insulation and higher eddy current losses within the 2 mm magnetically active layers. The design will however certainly show superior characteristics to printed solid (higher eddy current losses) or full lattice cores (low fill factor, power density) and will provide a valuable base point for further optimization of AM soft magnetic cores.

The second key challenge was related to achieving a thin and uniform machine air-gap between the printed rotor and stator cores. Even though L-PBF systems are well known for their high spatial accuracy (with resolutions up to 15 μm), when printing larger parts, the volumes are often subjected to some deformations [30]. Therefore, when designing the machine assembly, the individual machine components were designed slightly larger (on the average 0.5 mm on the assembly contact surfaces); with machining allowances and with

design rules of turning machining in mind. After printing, the stator, rotor, and endcaps were all turning machined to ensure part coaxiality and an even motor air-gap.

The exploded view of the full machine assembly is outlined in Figure 8. The full machine assembly included several additional AM and conventional components. These included fully 3D printed machine endcaps from stainless steel 316L (printed on the 280 × 280 mm full sized build plate) and internal fan blades from AlSiMg aluminum alloy for cooling. In addition to the printed components, both the rotor and stator windings, the shaft, fixture rods and bearings were produced through conventional means. This was due to the insufficient accuracy of our current L-PBF system when producing threaded features or bearings and the incapability of fusing pure copper parts (due to low absorption of infrared laser). For the prototype machine, cooling ribs were not included in the design: its thermal optimization is planned as future work with an optimized printed cooling jacket.

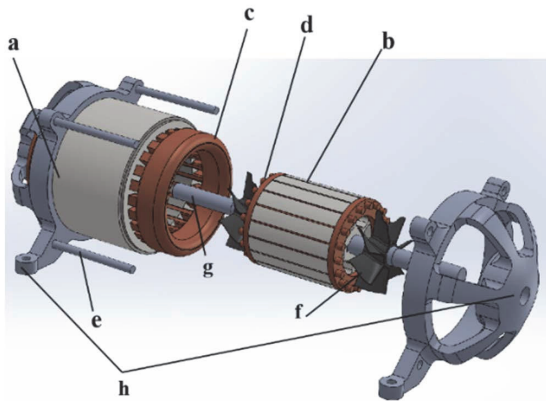


FIGURE 8. Full prototype machine assembly, component information: (a) stator core (printed Fe-Si), (b) rotor core (printed Fe-Si), (c) stator winding (distributed), (d) rotor cage (commercial copper), (e) threaded rods (commercial), (f) cooling fans (printed AlSiMg), (g) shaft (machined stainless steel), (h) endcaps (printed stainless steel), embedded bearings (commercial).

IV. PRINTING PREPARATION

Pre-alloyed, gas-atomized commercially available Fe-Si powder provided by Sandvik group was used to fabricate the machine cores through L-PBF. Beforehand, the chemical composition of the powder was verified through EDX Energy-dispersive X-ray Spectroscopy and Atomic Emission Spectroscopy by Spark AES measurements, with the results summarized in Table 2. The powder constituted roughly spherical particles in size range of 29-58 μm, with a median diameter of 38 μm (d50) as shown in Figure 9 (a-b). The powder size distribution was determined with laser scattering particle size distribution analyzer in water dispersive environment. The shape of powder particles was confirmed through scanning electron microscopy (SEM).

TABLE 3. Powder chemical composition.

	Fe	Si	Mn	Cr	Ni	C
Wt %	Balance	3.7	0.2	0.16	0.020	0.01

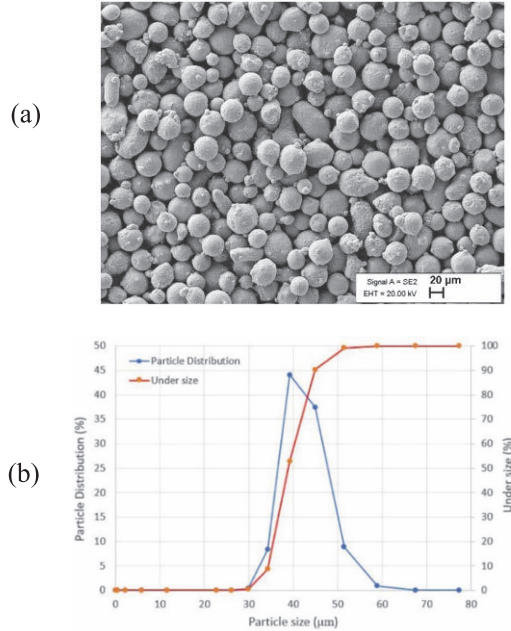


FIGURE 9. (a) SEM magnification of the investigated powder, (b) Powder particle size distribution and percentage of particles below specific particle size.

The core components were prepared on the SLM Solutions GmbH Realizer SLM-280 machine. The printer was equipped with a single 400W 1070 nm infrared yttrium laser and a 100 mm diameter reduced platform. The build process of the machine stator is illustrated in Figure 11(a). Previously determined printing parameters in [28] and [25], with two notable alterations, were employed for part preparation. After initial testing, it was observed that scan strategies ideal for printing small samples were not applicable for printing larger solid volumes: resulting in gradually deteriorating part density, which culminated in billing-related print failure. A possible explanation for this can be found in [31], describing powder denudation during the melting process: fresh powder surrounding the melt-pool is pulled towards the melting plasma plume and ejected towards the fresh powder in the bed. This extra powder and half-melted agglomerates deposited on the fresh bed can then promote poorly wetted melt-pools on the substrate, i.e., powder balling-related irregularities. Based on our experience, this effect is dependent on the length and area of the scan track: by adapting from “stripe” scan pattern to “chessboard” pattern, the survivability of the print job was increased to part completion. These findings are also

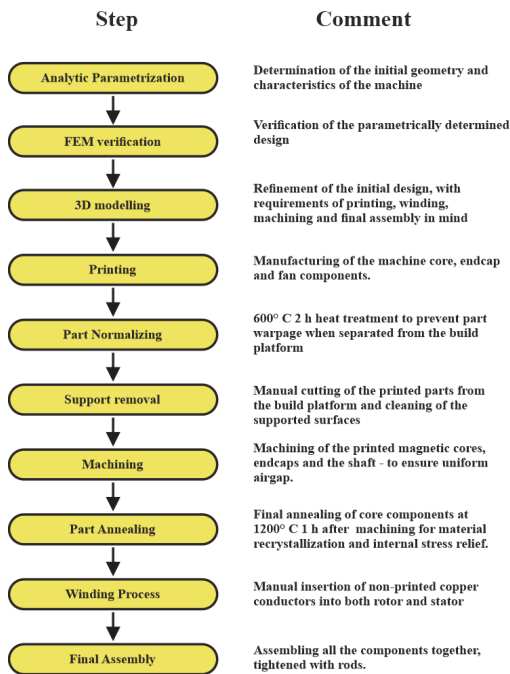


FIGURE 10. Workflow for producing AM core prototype.

in line with those of other authors, who have also reported chessboard strategies leading to parts with higher density, promoting more homogeneous powder fusion [32], [33]. Secondly, re-melting scan strategy was abandoned, as from the initial tests it appeared that the secondary scan sintered the ejected spattered/entrained particles of the primary scan onto the substrate. It seemed to increase the roughness of the top surface, causing uneven powder deposition due to reduced powder flowability [34], which again seemed to promote powder balling related uneven part growth. The main printing processing parameters used for fusing the 3.7% silicon steel powder into electrical machine cores are presented in Table 3.

V. PROTOTYPE PRODUCTION

The main steps in the workflow of the motor are outlined in Figure 10, outlining the necessary pre-printing and post-processing steps taken for obtaining a fully functional AM core electrical machine.

The production process is illustrated in detail in Figure 11. The approximate total production time and cost of the prototype is outlined in Table 4.

The printing of the cores was completed without interruptions, after some adjustments of the printing parameters as described in chapter 2 A. The total build time of the cores was approximately 30 h. The first step in the further processing of the printed cores was post-printing normalization.

TABLE 4. Summary of the printing parameters.

Parameter	Value
Layer thickness	50 μm
Hatch distance	120 μm
Laser Power	250 W
Scanning velocity	0.5 m/s
Volumetric energy density	83 J/mm ³
Scan strategy	Chessboard
Environment	Nitrogen
Oxygen content	~0.1%

The process involved a low-temperature heat treatment for post-printing grain structure recovery to lower the risk of significant part warpage when separating it from the printed support structure. Heating rate of 5° C per hour was used up to the temperature of 600° C, where it was kept 2 h and then slowly oven cooled. The extra allowances of printed cores were then removed through turning machining. Ellipticity of the printed parts was confirmed prior to machining – approximately 0.2 mm, which was removed successfully. The cores were then fitted with motor endcaps and shaft while attempting to keep the motor eccentricity minimal. The final machine air-gap was 0.35 mm, with an eccentricity smaller than we could detect with our workshop facilities. The duration of mechanical machining and assembly fitting was approximately 10 h in total.

With all the necessary machining completed, the printed cores were subjected to high-temperature annealing. The process involved heating the parts near its melting temperature to induce material recrystallization. The process is critical for obtaining useful soft magnetic properties in crystalline materials by lowering the defect content in the material crystallographic structure. For best results, the annealing should be conducted after all the necessary machining steps are concluded. Post-annealing cold working will again introduce lattice defects (increased magnetostriction) within worked surfaces: similar to the effect of punching and cutting on commercial EM laminations [35]. The final annealing process involved slowly heating (5° C/min) the printed cores up to 1200° C, where they were maintained for 1 h, and then slowly oven cooled. In both heat treatment steps, a low vacuum (0.1 mBar) furnace with a graphite lining was used. One annealing cycle lasted roughly 24 hours.

After printing, machining, final fitting, and heat treatments, the printed cores were finally prepared for the winding process. The stator winding was designed as a distributed 24-slot single layer three-phase winding, with its schematic outlined in Figure 12. The winding was completed to the courtesy of Elektrimootorid LLC. Standard winding methods were used: stator slots lined with aramid paper, windings pre-wound (1 mm diameter, 24 turns per slot, insulation class F) and inserted by hand, and the finished stator

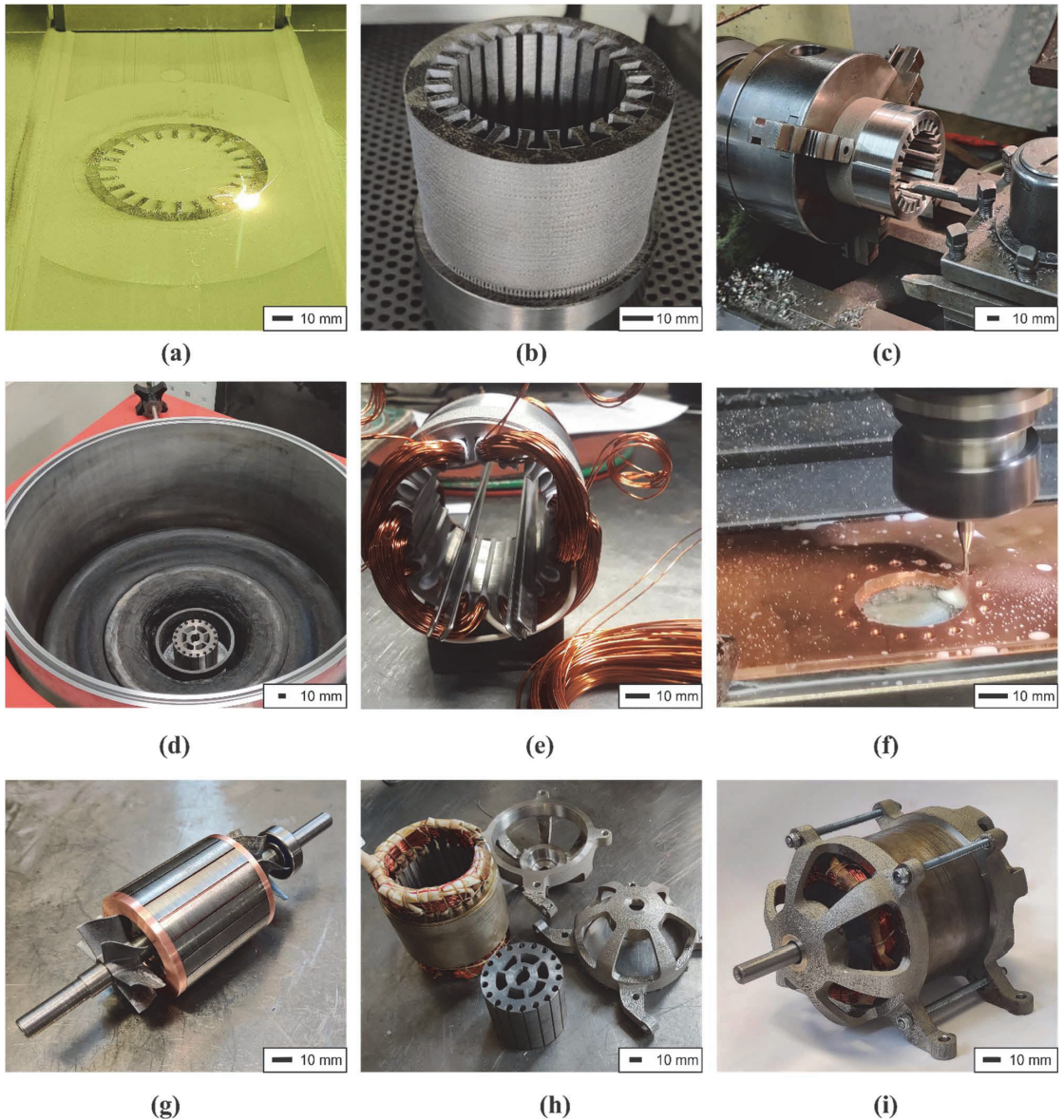


FIGURE 11. Production of the AM core motor: (a) L-PBF process of the motor stator core, (b) finished printed stator core welded to the build platform ready for normalizing, (c) turning machining of the motor stator, (d) machine rotor ready for final anneal treatment, (e) winding process of the machine stator core, (f) milling of the rotor end-rings, (g) assembled rotor with inserted cage, shaft, bearing and cooling fans, (h) motor stator (finish windings), rotor core and endcaps, (i) finished and fully assembled AM core motor.

submerged within a varnish bath for fixing/protection. The finished stator winding exhibited approximately 62% fill factor, with the end-winding height of 26 mm and the winding resistance of 0.7Ω .

The winding time was approximately 4 hours. For traditional EMs, the rotor cage is often cast from molten aluminum. Due to the specific nature of this process, we omitted

to assemble the rotor cage from commercially available copper materials. The Rotor cage was assembled from commercially available high conductivity copper (Cu – ETP) materials: with 4 mm rods (analytically designed 5mm were not available in the market) used as rotor bars and cage endrings milled from 4 mm copper plate. The cage was assembled through mechanical riveting: the rods were

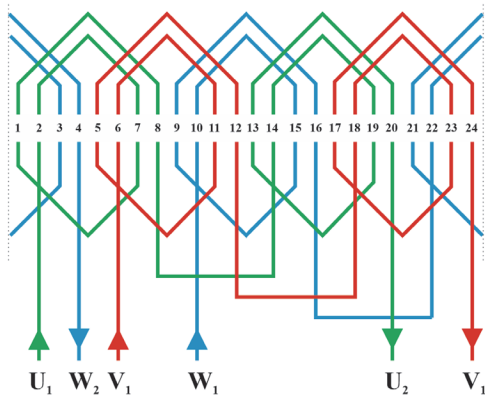


FIGURE 12. Winding layout of the AM core machine.

TABLE 5. Summary of the prototyping costs involved.

Article	Quantity	Costs per unit	Total Costs
Printing Powder	2.5 kg	50 € / kg	125 €
Rotor Copper	1 pc	36 € / pc	36 €
Bearings	2 pcs	8 € / pc	16 €
Printing	50 h	40 € / h	2000 €
Annealing	4 pcs	50 € / pcs	200 €
Machining	24 h	40 € / h	960 €
Stator Winding	1 pc	200 € / pc	200 €
Total:			3537 €

cold-hammered to fill the ending opening chamfers, with any excess protruding material removed through turning machining. Insulating layers between the cage and rotor were not added.

The estimation of the costs involved in manufacturing the prototype is summarized in Table 5.

VI. PROTOTYPE EVALUATION

Three standard tests were performed for the prototype performance evaluation: no-load, blocked rotor, and load test. The first step was initial testing without external load to obtain the first impressions on the machine build quality and the second to gauge the iron losses within the cores. By operating the unloaded motor over a wide voltage range, its iron losses at each voltage level can be calculated by subtracting the copper losses of the magnetizing current from the total active power drawn by the machine. The results of no-load motor testing are summarized in Figure 13.

The results suggest higher iron losses than anticipated, as its full load current value of 5.1 A (6.5 A/mm² current density for the selected conductors) is reached at 19.6 V at no load (20 V was the planned nominal voltage of the machine). This means in further performance evaluation, the motor must be operated at slight undervoltage to compensate for the higher eddy current losses within the core.

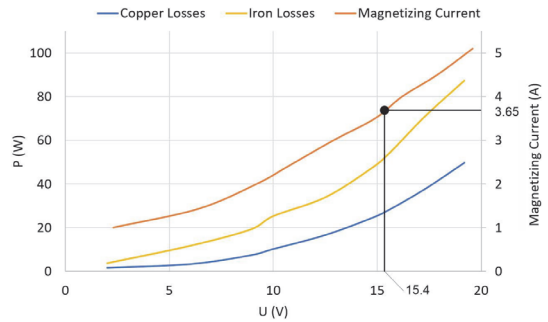


FIGURE 13. No-load test results of the prototype motor.

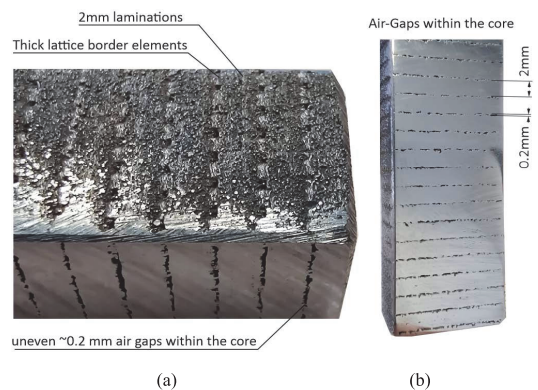


FIGURE 14. Core material structure: (a) printed sample stator element, (b) detailed view of the insulating air-gaps within the core.

The analytically calculated prototype magnetizing current of 3.65 A is reached at 15.4 V excitation. Iron losses at that excitation level were 54 W, almost twice the corresponding copper loss of 28 W. A detailed view of the printed core material structure is outlined in Figure 14 (a-b), with the polished surfaces ground up to 4000 grit sandpaper.

Next, full load tests were performed in order to determine the optimal working point of the prototype and its nominal parameters. The setup is outlined in Figure 15 (b-c). The prototype was joined back-to-back through a torque sensor (NCTE S-4000-50-1) with a commercial machine of a similar size. This allowed to both validate the accuracy of the test setup by comparing the measured commercial motor results to its datasheet and determine the optimal working parameters for the printed core motor.

That is, inputs that provide the optimal balance of output power, efficiency, and rotor speed. Terminal voltage on both the loading and tested machine was controlled through auto-transformers. Measurements were saved on the DEWE2-M Modular Data Acquisition System. The temperature of the printed motor was observed through an embedded PT100 sensor embedded within the stator windings. Measurement results of the star-connected commercial machine correlated

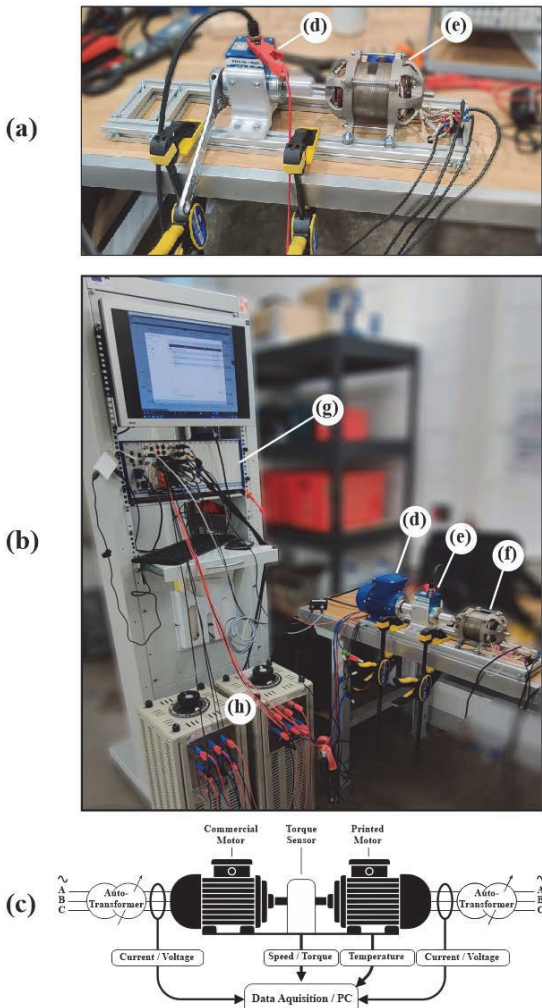


FIGURE 15. Motor evaluation test setup: (a) blocked rotor test setup, (b) load test setup, (c) schematic of the load test, (d) commercial induction motor, (e) torque sensor, (f) AM core motor, (g) DEWETRON data acquisition module/PC, (h) autotransformers.

well with its datasheet [36]: showing 52% efficiency at 230 V terminal voltage, 0.297 A phase current, 1395 rpm rotational speed, 60 W output power. Results of the prototype load-test measurements are outlined in Figure 16. To determine the optimal working point of the prototype machine, it was characterized over a range of terminal voltage of 13 – 24 V and load torque of 0.2-1 Nm. The investigated machine was first energized up to its investigated voltage, to synchronous speed, then loaded incrementally up to desired value. In every measurement step, the input power, current, torque, and speed were recorded. The highest efficiency obtained for the prototype machine was at 36.5%, albeit at a significant slip: at operating speed of 1200-1250 rpm. A closer result (highlighted at Figure 16) to the initially designed machine was obtained

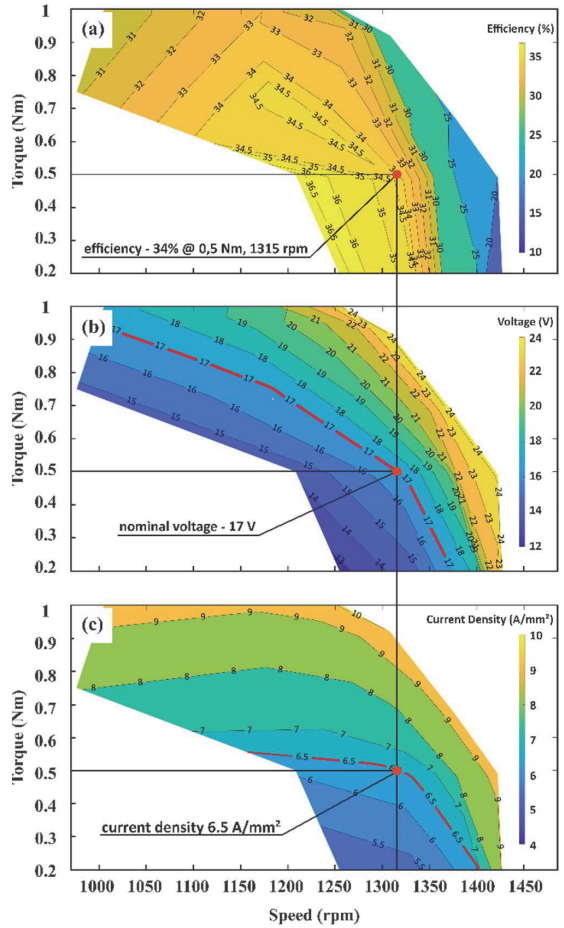


FIGURE 16. Determination of the prototype motor nominal parameters based on the full load test measurement results: (a) efficiency map, (b) speed-torque contour plot of terminal voltage, (c) speed-torque contour plot of winding current density.

at 34% efficiency at 1315 rpm and 0.5 Nm shaft torque. This result was measured at terminal voltage of 17 V while not exceeding the initially established winding current limit of 6.5 A/mm². This set of input and output parameters was chosen as the optimal working point of the prototype machine. In comparison, to achieve the same rated speed (1350 rpm) and torque (0.57 Nm) as the initial design, the motor would need to be supplied with 20 V, reaching an excessive 8 A/mm² current density and a lower 29 % efficiency.

The speed-torque curve of the motor (at 17 V) was measured through load testing for load values above breakdown torque and with a blocked rotor test (Figure 15 a) to obtain the startup torque. The obtained prototype speed-torque characteristic curve is outlined in Figure 17, presented in parallel with the machine power factor at corresponding data points. Both curves accurately illustrate the effect of

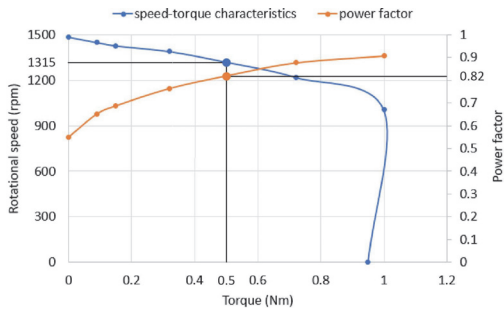


FIGURE 17. Prototype motor speed-torque characteristics and power factor at nominal power.

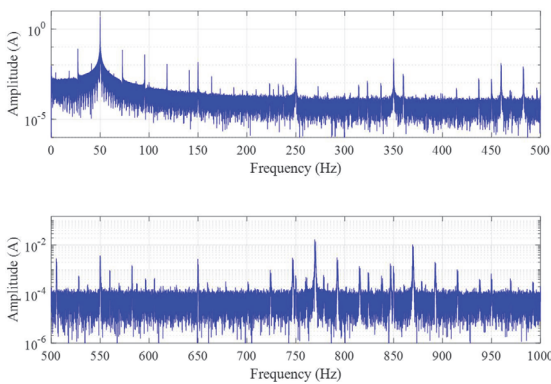


FIGURE 18. Frequency spectrum of the AM prototype stator current.

excessive losses in an EM. High machine power factor is obtained as the increased core losses count as an increased resistive load on the machine: translating to a lower ratio of reactive to active consumed power. The high slip of the machine and the slope of its speed-torque curve demonstrates undervoltage operation of the machine to limit its winding current (to compensate for the high no-load current due to core losses). Additionally, the high slip can be related to the thinner substituted rotor bars (from 5 to 4 mm) and the 0.5 mm air-gaps around them: resulting in higher rotor cage resistance.

As the final step, the frequency spectrum of the stator current was calculated to evaluate the total harmonic distortion of the motor currents. The spectrum is presented in Figure 18. The total harmonic distortion was identified as -42.01 dB, which correlates to the distortion factor of 0.793% - relatively low as it is a grid fed machine. The obtained source current harmonic %THD of the grid fed induction motor is below the 5% THD limit specified by the international standards of IEEE 519 and IEC 61000-3-2 [37], [38].

The comparison between the measured rated parameters of the commercial loading machine and the prototype (with both analytically and experimentally obtained) is presented in Table 6.

TABLE 6. Comparison of the commercial benchmarking machine and the expected / empirical values for the am core prototype.

Rated Values	Design	Experimental	Commercial
Power	80 W	68 W	60 W
Operating Frequency	50 Hz	50 Hz	50 Hz
Rated Voltage	20 V	17 V	230 V
Rated Current	5.1 A	5.1 A	0.3 A
Rated Torque	0.55 Nm	0.5 Nm	0.4 Nm
Speed	1400 rpm	1315 rpm	1395 rpm
Efficiency	40 %	34 %	52 %
Power Factor	0.65	0.82	0.55

VII. DISCUSSION

The AM core prototype machine demonstrated functional characteristics: reaching nominal torque of 0.5 Nm, at 1315 rpm, at 34% efficiency. Measuring the prototype core presents a valuable precedent, as it is the first 3D printed motor with printed metal rotor and stator cores that has been evaluated in terms of performance in scientific literature. Despite the 2 mm thick material layers separated through uneven air-gaps: the 34% obtained efficiency presents an excellent starting point for further optimization of the design, with goals to introduce more intricate core designs for further loss reduction alongside more exotic design options for improved cooling and flux distribution.

A commercial 60 W three-phase induction machine was characterized in parallel as part of this study to provide a reference point for the prototype motor (due to the lack of comparable motors characterized in the scientific literature). The benchmarking machine [36] exhibited 52% efficiency – that is 153% of the printed motor efficiency. The value is typical for small-scale machines of the type. Similarly, from the 2011 ABB catalog for low voltage general performance high-efficiency motors [27], 60 W IE2 (according to IEC 60034-30; 2008) motors are available with 51.1% efficiency at full load. Regarding the performance of printed machines in general, the examples from the literature are sparse. A polymer extrusion-based printed machine with plastic cores reached approximately 10000 rpm at 0.0005 Nm in [39], which translates to output mechanical power of 0.5 W at undisclosed efficiency. Some examples of other polymer printed electric motors can also be found in non-scientific sources [40], which have shown to reach considerably higher performance with 0.6 kW at 80% efficiency. Similar to [39], these are all, however, PM assisted: including a Halbach array of neodymium magnets, which do not allow for much topology optimization. Regarding AM soft iron core prototypes, in [24], a commercial switched reluctance machine rotor was substituted with a fully-dense laser additively manufactured rotor: achieving 18% lower efficiency (decreased from 83% to 65%) at 1500 rpm, ~ 1 kw output power. In [25], the authors produced a laminated (1 mm thickness) 27 VA power transformer, which

exhibited 10% lower efficiency (from 80.5% to 70.1%) and 34% lower power density (from 59 VA/kg to 39 VA/kg) than the commercial transformer it was benchmarked against.

Comparison of the core material printed as part of this work with conventional core materials is complicated, as the average flux density within the material can only be roughly estimated from its FEM model, not accurately measured. By taking into account the average flux path lengths in the stator teeth, rotor teeth, rotor yoke, and stator yoke and average magnetization within them, we obtained a rough estimation for the average flux density of 1.1 T within the core. In the 68 W prototype machine, approximately 71 W of energy was converted to heat in the printed iron cores (obtained from the no-load test). This equates to the iron losses of 29.5 W/kg within the 2.4 kg motor cores at 50 Hz magnetization 1.1 T ($W_{11,50}$). Depending on the grade of the conventional non-oriented electrical steel lamination, its total core losses can most likely be found within the range of 2.3 (M235-35A) – 13 W/kg (M1300-100A) at 1.5T, 50 Hz ($W_{15,50}$) [41]. For comparison at 1.1 T, Isovac 235-35A NO electrical steel exhibits losses of 1.01 W/kg. This translates to approximately 29x higher losses in the printed core than in that conventional high-grade steel, with the 5.7x thicker core layers (2 mm instead of 0.35 mm). These results correlate well with the literature (eddy current proportional to lamination thickness squared [42]), as the 5.7x thicker core layers should exhibit 32.5x higher eddy current losses within the core (electrical conductivities of the materials are similar [28]). The obtained results are

Indeed, to enhance the efficiency of the printed motors, a higher degree of segregation must be achieved within the cores. The demonstrated method did not sacrifice significantly in the mechanical strength nor fill factor of the core, but did exhibit considerably higher losses than the topology optimized cores within the literature (~ 1.5 W/kg at $W_{10,50}$) [18]. As the next optimization step, the lamination thickness needs to be reduced, air-gaps widths increased, and a new set of air-gaps running in parallel to the machine axis should be added (bi-directionally segregated). This process is relatively complex as by adding too few or too thin air-gaps into the material, insufficient internal resistance increase/eddy current loss reduction is achieved; by adding too numerous and wide air gaps, poor fill factor, total flux, and output power are inevitable. A potential solution to this problem lies in next-generation printing technology: dual-metal powder-bed printing systems with selective powder deposition capabilities are just now becoming available [43]. By printing at least two materials in parallel, superior eddy current loss reduction to modern conventional materials should be achievable. By printing at least three materials in parallel, perhaps the entire electrical motor could be printed as a single process. Unfortunately, however, the capabilities of the systems are still relatively unknown and unverified, as the scientific community is yet to explore them.

VIII. CONCLUSION

Even though AM cores are at a significant disadvantage when compared to conventional stamping assembled motors due to the lack of reliable intra-material insulation layers, the results of this first prototype motor are very promising:

- The output of the finished motor was measured at 68 W (0.5 Nm) at 34% energy efficiency. This is roughly 2/3 of the efficiency of conventional machines of the same size and type.
- The evaluation of an electrical machine with printed rotor and stator soft magnetic cores was performed for the first time in scientific literature.
- The prototype includes fully 3D printed stator and rotor cores from 3.7% silicon steel with a novel segregation strategy for limiting eddy currents.
- It is likely that with further refinements in the printed core design, competitive or superior printed core properties are achievable: especially with multi-material metal printing.

ACKNOWLEDGMENT

The authors would like to thank Hans Vallner for his invaluable aid and advice in the prototype machining process and Elektrimotorid LLC for facilitating the machine winding process.

REFERENCES

- [1] R. Poprawe, C. Hinke, W. Meiners, J. Schrage, S. Bremen, and S. Merkt, "SLM production systems: Recent developments in process development, machine concepts and component design," in *Advances in Production Technology*, Nov. 2015, pp. 49–65, doi: 10.1007/978-3-319-12304-2_5.
- [2] R. Wrobel and B. Mecrow, "A comprehensive review of additive manufacturing in construction of electrical machines," *IEEE Trans. Energy Convers.*, vol. 35, no. 2, pp. 1054–1064, Jun. 2020, doi: 10.1109/TEC.2020.2964942.
- [3] M. U. Naseer, A. Kallaste, B. Asad, T. Vaimann, and A. Rassölk, "A review on additive manufacturing possibilities for electrical machines," *Energies*, vol. 14, no. 7, p. 1940, Mar. 2021, doi: 10.3390/en14071940.
- [4] P. S. Ghahfarokhi, A. Podgornovs, A. Kallaste, A. J. M. Cardoso, A. Belahcen, T. Vaimann, H. Tiismus, and B. Asad, "Opportunities and challenges of utilizing additive manufacturing approaches in thermal management of electrical machines," *IEEE Access*, vol. 9, pp. 36368–36381, 2021, doi: 10.1109/ACCESS.2021.3062618.
- [5] A. Selema, M. N. Ibrahim, and P. Sergeant, "Metal additive manufacturing for electrical machines: Technology review and latest advancements," *Energies*, vol. 15, no. 3, pp. 1076–1094, Jan. 2022, doi: 10.3390/en15031076.
- [6] M. Sarap, A. Kallaste, P. S. Ghahfarokhi, and H. Tiismus, "Utilization of additive manufacturing in the thermal design of electrical machines: A review," *Machines*, vol. 10, no. 4, p.251, 2022.
- [7] M. Garibaldi, C. Gerada, I. Ashcroft, and R. Hague, "Free-form design of electrical machine rotor cores for production using additive manufacturing," *J. Mech. Des.*, vol. 141, no. 7, pp. 1–13, Jul. 2019, doi: 10.1115/1.4042621.
- [8] S. Urbanek, P. Frey, S. Magerkohl, D. Zimmer, L. Tasche, M. Schaper, and B. Ponick, "Design and experimental investigation of an additively manufactured PMSM rotor," in *Proc. IEEE Int. Electr. Mach. Drives Conf. (IEMDC)*, May 2021, pp. 1–6, doi: 10.1109/IEMDC47953.2021.9449566.
- [9] N. Simpson, D. J. North, S. M. Collins, and P. H. Mellor, "Additive manufacturing of shaped profile windings for minimal AC loss in electrical machines," *IEEE Trans. Ind. Appl.*, vol. 56, no. 3, pp. 2510–2519, May 2020, doi: 10.1109/TIA.2020.2975763.
- [10] *Integrated Cooling in Electric Motor Housing Developed Using Metal Additive Manufacturing*. Accessed: Sep. 28, 2021. [Online]. Available: <https://www.metal-am.com/integrated-cooling-in-electric-motor-housing-developed-using-metal-additive-manufacturing/>

- [11] R. Wrobel, B. Scholes, A. Hussein, R. Law, A. Mustaffar, and D. Reay, "A metal additively manufactured (MAM) heat exchanger for electric motor thermal control on a high-altitude solar aircraft—Experimental characterisation," *Thermal Sci. Eng. Prog.*, vol. 19, Oct. 2020, Art. no. 100629, doi: [10.1016/j.tsep.2020.100629](https://doi.org/10.1016/j.tsep.2020.100629).
- [12] C. Silbernagel, L. Gargalis, I. Ashcroft, R. Hague, M. Galea, and P. Dickens, "Electrical resistivity of pure copper processed by medium-powered laser powder bed fusion additive manufacturing for use in electromagnetic applications," *Additive Manuf.*, vol. 29, Oct. 2019, Art. no. 100831, doi: [10.1016/j.addma.2019.100831](https://doi.org/10.1016/j.addma.2019.100831).
- [13] S. L. Sing, S. Huang, G. D. Goh, G. L. Goh, C. F. Tey, J. H. K. Tan, and W. Y. Yeong, "Emerging metallic systems for additive manufacturing: *in-situ* alloying and multi-metal processing in laser powder bed fusion," *Prog. Mater. Sci.*, vol. 119, Jun. 2021, Art. no. 100795, doi: [10.1016/j.pmatsci.2021.100795](https://doi.org/10.1016/j.pmatsci.2021.100795).
- [14] G. L. Goh, H. Zhang, T. H. Chong, and W. Y. Yeong, "3D printing of multilayered and multimaterial electronics: A review," *Adv. Electron. Mater.*, vol. 7, no. 10, pp. 1–28, 2021, doi: [10.1002/aeml.202100445](https://doi.org/10.1002/aeml.202100445).
- [15] *Aerosint and Aconity 3D Develop Multi-Material Metal 3D Printer—3D Printing Industry*. Accessed: Apr. 8, 2022. [Online]. Available: <https://3dprintingindustry.com/news/aerosint-and-aconity3d-develop-multi-material-metal-3d-printer-168919/>
- [16] *Defining a New paradigm: Harvard Researchers Invent Multimaterial Multinozzle 3D Printing—3D Printing Industry*. Accessed: Apr. 8, 2022. [Online]. Available: <https://3dprintingindustry.com/news/defining-a-new-paradigm-harvard-researchers-invent-multimaterial-multinozzle-3d-printing-165567/>
- [17] *Powercore A | thyssenkrupp Steel*. Accessed: Apr. 8, 2022. [Online]. Available: <https://www.thyssenkrupp-steel.com/en/products/electrical-steel/electrical-steel-non-grain-oriented/powercore-a/powercore-a.html>
- [18] H. Tiismus, A. Kallaste, T. Vaimann, and A. Rassõlkin, "State of the art of additively manufactured electromagnetic materials for topology optimized electrical machines," *Additive Manuf.*, vol. 55, Jul. 2022, Art. no. 102778, doi: [10.1016/j.addma.2022.102778](https://doi.org/10.1016/j.addma.2022.102778).
- [19] Hogan's. *Material Data_Somaloy*. Accessed: Jun. 9, 2020. [Online]. Available: <https://www.hoganas.com/electromagnetic>
- [20] M. Garibaldi, I. Ashcroft, J. N. Lemke, M. Simonelli, and R. Hague, "Effect of annealing on the microstructure and magnetic properties of soft magnetic Fe-Si produced via laser additive manufacturing," *Scripta Mater.*, vol. 142, pp. 121–125, Jan. 2018, doi: [10.1016/j.scriptamat.2017.08.042](https://doi.org/10.1016/j.scriptamat.2017.08.042).
- [21] D. Goll, D. Schuller, G. Martinek, T. Kunert, J. Schurr, C. Sinz, T. Schubert, T. Bernthaler, H. Riegel, and G. Schneider, "Additive manufacturing of soft magnetic materials and components," *Additive Manuf.*, vol. 27, pp. 428–439, May 2019, doi: [10.1016/j.addma.2019.02.021](https://doi.org/10.1016/j.addma.2019.02.021).
- [22] G. Herzer, "Modern soft magnets: Amorphous and nanocrystalline materials," *Acta Mater.*, vol. 61, no. 3, pp. 718–734, Feb. 2013, doi: [10.1016/j.actamat.2012.10.040](https://doi.org/10.1016/j.actamat.2012.10.040).
- [23] M. G. Ozden and N. A. Morley, "Laser additive manufacturing of Fe-based magnetic amorphous alloys," *Magnetochemistry*, vol. 7, no. 2, pp. 1–24, 2021, doi: [10.3390/magnetochemistry7020020](https://doi.org/10.3390/magnetochemistry7020020).
- [24] L. Gargalis, V. Madonna, P. Giangrande, R. Rocca, M. Hardy, I. Ashcroft, M. Galea, and R. Hague, "Additive manufacturing and testing of a soft magnetic rotor for a switched reluctance motor," *IEEE Access*, vol. 8, pp. 206982–206991, 2020, doi: [10.1109/ACCESS.2020.3037190](https://doi.org/10.1109/ACCESS.2020.3037190).
- [25] H. Tiismus, A. Kallaste, A. Belahcen, A. Rassõlkin, T. Vaimann, and P. S. Ghahfarokhi, "Additive manufacturing and performance of E-type transformer core," *Energies*, vol. 14, no. 11, p. 3278, Jun. 2021, doi: [10.3390/en14113278](https://doi.org/10.3390/en14113278).
- [26] J. Pyrhönen, T. Jokinen, and V. Hrabovcová, *Design of Rotating Electrical Machines*. Hoboken, NJ, USA: Wiley, 2008.
- [27] *Low Voltage General Performance IE2 High Efficiency Motors*. Accessed: Feb. 17, 2022. [Online]. Available: <https://manualzz.com/doc/13816422/abb-all-ie2>
- [28] H. Tiismus, A. Kallaste, A. Belahcen, M. Tarraste, T. Vaimann, A. Rassõlkin, B. Asad, and P. Shams Ghahfarokhi, "AC magnetic loss reduction of SLM processed Fe-Si for additive manufacturing of electrical machines," *Energies*, vol. 14, no. 5, p. 1241, Feb. 2021, doi: [10.3390/en14051241](https://doi.org/10.3390/en14051241).
- [29] *DC Magnetization Curves of Soft Magnetic Materials: Finite Element Method Magnetics*. Accessed: Mar. 28, 2022. [Online]. Available: <https://www.femm.info/wiki/SoftMagneticMaterials>
- [30] Y. P. Yang, M. Jamshidinia, P. Boulware, and S. M. Kelly, "Prediction of microstructure, residual stress, and deformation in laser powder bed fusion process," *Comput. Mech.*, vol. 61, no. 5, pp. 599–615, May 2018, doi: [10.1007/s00466-017-1528-7](https://doi.org/10.1007/s00466-017-1528-7).
- [31] P. Bidare, I. Bitharas, R. M. Ward, M. M. Attallah, and A. J. Moore, "Fluid and particle dynamics in laser powder bed fusion," *Acta Mater.*, vol. 142, pp. 107–120, Jan. 2018, doi: [10.1016/j.actamat.2017.09.051](https://doi.org/10.1016/j.actamat.2017.09.051).
- [32] D. Koutny, D. Palousek, L. Pantelejev, C. Hoeller, R. Pichler, L. Tesicky, and J. Kaiser, "Influence of scanning strategies on processing of aluminum alloy EN AW 2618 using selective laser melting," *Materials*, vol. 11, no. 2, p. 298, Feb. 2018, doi: [10.3390/ma11020298](https://doi.org/10.3390/ma11020298).
- [33] R. M. Gouveia, F. J. G. Silva, E. Atzeni, D. Sormaz, J. L. Alves, and A. B. Pereira, "Effect of scan strategies and use of support structures on surface quality and hardness of L-PBF AlSi10Mg parts," *Materials*, vol. 13, no. 10, p. 2248, May 2020, doi: [10.3390/MA13102248](https://doi.org/10.3390/MA13102248).
- [34] Z. Wang, X. Wang, X. Zhou, G. Ye, X. Cheng, and P. Zhang, "Investigation into spatter particles and their effect on the formation quality during selective laser melting processes," *Comput. Model. Eng. Sci.*, vol. 124, no. 1, pp. 243–263, 2020, doi: [10.32604/cmescs.2020.09934](https://doi.org/10.32604/cmescs.2020.09934).
- [35] C. T. Liu, B. Y. Chang, K. Y. Hung, and S. Y. Lin, "Cutting and punching impacts on laminated electromagnetic steels to the designs and operations of synchronous reluctance motors," *IEEE Trans. Ind. Appl.*, vol. 51, no. 4, pp. 3515–3520, Jul./Aug. 2015, doi: [10.1109/TIA.2015.2399614](https://doi.org/10.1109/TIA.2015.2399614).
- [36] Felandia. *Elektrimootor 0,06kW/1500 p/min MS 561-4 B34: IET: IP55; 230/400V*. Accessed: May 9, 2022. [Online]. Available: https://www.felandia.eu/media/veelandia/product/eu.erply.com/1052-ms-561-4-0-06-tehnilised_andmed_v1.pdf
- [37] *EVS-EN IEC 61000-3-2:2019+A1:2021—Estonian Centre for Standardisation and Accreditation*. Accessed: Apr. 12, 2022. [Online]. Available: <https://www.evs.ee/en/evs-en-iec-61000-3-2-2019%2Ba1-2021>
- [38] *IEEE SA—IEEE 519-2014*. Accessed: Apr. 12, 2022. [Online]. Available: <https://standards.ieee.org/ieee/519/3710/>
- [39] E. Aguilera, J. Ramos, D. Espalin, F. Cedillos, D. Muse, R. Wicker, and E. MacDonald, "3D printing of electro mechanical systems," in *Proc. Int. Solid Freeform Fabr. Symp.*, 2013, pp. 950–961.
- [40] *Building and Testing a 3D Printed Brushless Motor (Until it Explodes!)*. Accessed: Mar. 3, 2022. [Online]. Available: <https://www.rs-online.com/designspark/building-and-testing-a-3d-printed-brushless-motor-until-it-explodes>
- [41] S. Tumanski, *Handbook of Magnetic Measurements*. Boca Raton, FL, USA: CRC Press, 2011.
- [42] A. Goldman, *Handbook of Modern Ferromagnetic Materials*. New York, NY, USA: Springer, 1999.
- [43] *Dual Metal LPBF—Aerosint*. Accessed: Nov. 27, 2020. [Online]. Available: <https://aerosint.com/dual-metal-lpbf/>



HANS TIISMUS (Member, IEEE) was born in Tallinn, Estonia, in 1989. He received the B.Sc. and M.Sc. degrees in engineering physics from the Tallinn University of Technology, Estonia, in 2011 and 2013, respectively, where he is currently pursuing the Ph.D. degree with the Department of Electrical Power Engineering and Mechatronics.



He is also a Junior Researcher with the Department of Electrical Power Engineering and Mechatronics, Tallinn University of Technology. His main research interest includes additive manufacturing of electrical machines.

ANTS KALLASTE (Senior Member, IEEE) was born in Pärnu, Estonia, in 1980. He received the B.Sc., M.Sc., and Ph.D. degrees in electrical engineering from the Tallinn University of Technology, Estonia, in 2004, 2006, and 2013, respectively.

He is currently a Professor of electrical machines with the Department of Electrical Power Engineering and Mechatronics, Tallinn University of Technology. In addition, he is holding the position of the Head of the Chair of Electrical Machines Research Group. He has spent several years in private engineering companies and visited numerous other research institutions. Amongst other research activities, he is involved with expertise and consultations of private companies in the field of electrical machines, drives, and their diagnostics.



MUHAMMAD USMAN NASEER (Member, IEEE) was born in Pakistan, in 1990. He received the B.Sc. degree in electrical engineering from the Islamia University of Bahawalpur, Pakistan, in 2011, and the M.S. degree from the University of Engineering and Technology (UET), Lahore, Pakistan. He is currently pursuing the Ph.D. degree with the Tallinn University of Technology. His research interest includes electrical machines modeling, design, and optimization.



TOOMAS VAIMANN (Senior Member, IEEE) received the B.Sc., M.Sc., and Ph.D. degrees in electrical engineering from the Tallinn University of Technology, Estonia, in 2007, 2009, and 2014, respectively.

He is currently a Senior Researcher with the Department of Electrical Power Engineering and Mechatronics, Tallinn University of Technology. He has been working in several companies as an Electrical Engineer. His main research interest includes diagnostics of electrical machines. He is a member of the Estonian Society of Moritz Hermann Jacobi and the Estonian Society for Electrical Power Engineering.



ANTON RASSÕLKIN (Senior Member, IEEE) was born in Tallinn, Estonia, in 1985. He received the B.Sc. and M.Sc. degrees in electric drives and power electronics from the Tallinn University of Technology (TalTech), Estonia, in 2008 and 2010, respectively, the Dipl.-Ing. degree in automatic from the University of Applied Science Giessen-Friedberg, Germany, in 2010, and the Ph.D. degree in electric drives and power electronics from the TalTech, in 2014.

He has been working in several companies as an Electrical Engineer and universities as a Lecturer. He is currently a Professor of mechatronics at the Department of Electrical Power Engineering and Mechatronics, School of Engineering, TalTech. Moreover, he works as a Visiting Professor at the Faculty of Control Systems and Robotics, ITMO University, St. Petersburg, Russia, and a Visiting Professor at the Department of Power Electronics, Electrical Drives and Robotics, Faculty of Electrical Engineering, Silesian University of Technology, Gliwice, Poland. His main research interests include mechatronics and electrical drives, particularly for electric transportation, as well as autonomous vehicles.

Dr. Rassõlkin is a Senior Member of the Estonian Society of Moritz Hermann Jacobi.

...

Publication IV

H. Tiismus, A. Kallaste, A. Belahcen, A. Rassolkin, T. Vaimann, and P. Shams Ghahfarokhi, "Additive Manufacturing and Performance of E-Type Transformer Core," *Energies*, vol. 14, no. 11, p. 3278, Jun. 2021, doi: 10.3390/en14113278.

Article

Additive Manufacturing and Performance of E-Type Transformer Core

Hans Tiismus ^{1,*}, Ants Kallaste ¹, Anouar Belahcen ², Anton Rassolkin ¹, Toomas Vaimann ¹
and Payam Shams Ghahfarokhi ^{1,3}

- ¹ Institute of Electrical Power Engineering and Mechatronics, Tallinn University of Technology, 19086 Tallinn, Estonia; ants.kallaste@taltech.ee (A.K.); anton.rassolkin@taltech.ee (A.R.); toomas.vaimann@taltech.ee (T.V.); payam.shams@taltech.ee (P.S.G.)
 - ² Department of Electrical Engineering and Automation, Aalto University, 02150 Espoo, Finland; Anouar.Belahcen@aalto.fi
 - ³ Department of Electrical Machines and Apparatus, Riga Technical University, Kaļķu iela 1, LV-1658 Riga, Latvia
- * Correspondence: hans.tiismus@taltech.ee

Abstract: Additive manufacturing of ferromagnetic materials for electrical machine applications is maturing. In this work, a full E-type transformer core is printed, characterized, and compared in terms of performance with a conventional Goss textured core. For facilitating a modular winding and eddy current loss reduction, the 3D printed core is assembled from four novel interlocking components, which structurally imitate the E-type core laminations. Both cores are compared at approximately their respective optimal working conditions, at identical magnetizing currents. Due to the superior magnetic properties of the Goss sheet conventional transformer core, 10% reduced efficiency (from 80.5% to 70.1%) and 34% lower power density (from 59 VA/kg to 39 VA/kg) of the printed transformer are identified at operating temperature. The first prototype transformer core demonstrates the state of the art and initial optimization step for further development of additively manufactured soft ferromagnetic components. Further optimization of both the 3D printed material and core design are proposed for obtaining higher electrical performance for AC applications.

Keywords: additive manufacturing; soft magnetic materials; selective laser melting; iron losses; magnetic properties; transformer



Citation: Tiismus, H.; Kallaste, A.; Belahcen, A.; Rassolkin, A.; Vaimann, T.; Shams Ghahfarokhi, P. Additive Manufacturing and Performance of E-Type Transformer Core. *Energies* **2021**, *14*, 3278. <https://doi.org/10.3390/en14113278>

Academic Editor:
Salvatore Musumeci

Received: 5 May 2021
Accepted: 31 May 2021
Published: 3 June 2021

Publisher's Note: MDPI stays neutral with regard to jurisdictional claims in published maps and institutional affiliations.



Copyright: © 2021 by the authors. Licensee MDPI, Basel, Switzerland. This article is an open access article distributed under the terms and conditions of the Creative Commons Attribution (CC BY) license (<https://creativecommons.org/licenses/by/4.0/>).

1. Introduction

Metal additive manufacturing (AM) is maturing, enabling previously unavailable production possibilities in terms of feasible product complexity and personalization. As currently, the cost per part of AM is still relatively high, it has been most applicable for parts for high tech industries: producing specialized parts benefiting the most from the topology optimization possibilities of AM. For example, 3D printing has been utilized for the production of more efficient and long-lasting inductor coils [1], stronger, cheaper and lighter aircraft fuel nozzles [2], and high performance heat exchangers [3].

In parallel to the printing of structural, thermal, and electrical components, research interest in printed soft magnetic materials and topology optimized electromechanical components has spiked drastically over recent years. It has been proposed that with the easily available computational power and free-form printing capabilities of AM systems, next generation electrical machine designs could be modelled and constructed by the research community. These topology optimized designs (with reduced weight, integrated cooling channels, reduced inertia, increased heat exchange etc.) could be prototyped in-house, significantly reducing the lead time, cost, and machinery involved [4].

State of the art additive manufacturing of electromagnetic devices involves selective laser melting (SLM) printing of conductive and soft magnetic materials with air gaps

partitioning the material structure for separating individual turns in coils and reducing the induced eddy currents in soft magnetic cores [5,6]. The air gaps are printed due to the current lack of multi-material printing capacity of SLM systems, limiting the parallel printing of conductive, core, and insulation materials. The introduction of airgaps considerably reduces the power density of the components, however, as gapped printed component fill factor is typically relatively low (in the range of 60%) [6,7].

Despite extensive material optimization of different soft magnetic alloys, relatively few functional components or devices have actually been printed and characterized. For this reason, in this work, a full small-scale transformer core is printed, characterized, and compared with a commercial transformer. The simplistic design of an E-type transformer makes it ideal for the next step of testing additively manufactured magnetic material capacity and performance for electrical machine applications (succeeding the characterization of small-scale toroidal samples). In this paper, a novel interlocking core design is employed for eddy current reduction, which exhibits a competitive component fill factor. The paper is divided into two larger sections. The first part describes the 3D printed core design and its fabrication process, and the second the characterization and comparison of the printed core with conventional cores.

2. Transformer Core Design

2.1. Commercial Transformer

The 3D printed core design investigated in this paper was based on the commercially available 30 VA single phase isolation transformer provided by MS Balti Transformers Ltd (Tallinn, Estonia). The transformer was chosen based on its suitable size, type, and availability. Its shell-type transformer core is constructed from E-type stampings of grain-oriented M 165-35S silicon steel. The conventional transformer design with its dimensions are detailed on Figure 1.

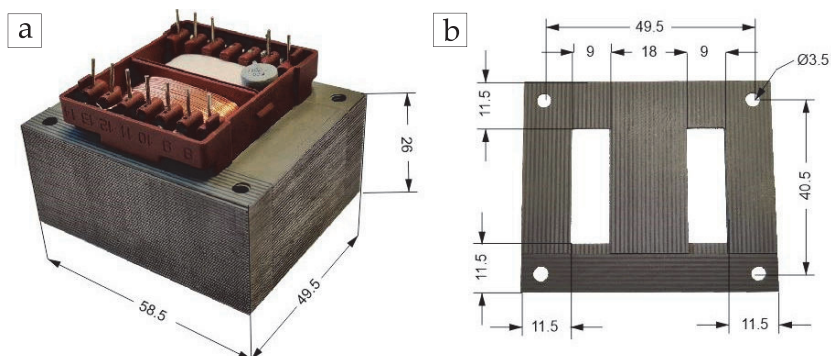


Figure 1. Investigated conventional transformer: (a) Core dimensions, (b) E-type stamping dimensions in detail.

The fully encapsulated modular windings of the transformer are utilized in both the conventional and 3D printed core designs. The modular windings are incorporated in both designs in order to improve the comparability of the transformer core performance and to demonstrate the compatibility of 3D printed and conventional parts. The nominal parameters of the windings are characterized in Table 1.

2.2. 3D Printed Design

Next, an SLM printing system was utilized for the 3D printing of the full transformer core. The 3D printed core design was required to exhibit compatibility with the modular windings, incorporate the segregated structure for classical eddy current loss reduction with high filling factor, and adhere to the printing system requirements. Lamination thickness of

0.95 mm was chosen to obtain high fill factor and mechanical strength of the first prototype. For all segregated designs considered, it was critical to achieve continuous geometries (with minimal air gaps dividing the flux paths) with maximal flux path cross sectional area (high fill factor). Furthermore, since the printed transformer must be comprised of at least two parts (to accommodate the modular winding), optimization of the inter-part air gap must be considered. In conventional transformers, the influence of the inter-stamping airgaps is typically reduced by overlapping stamping layers: which facilitates the flux paths through the adjoining stampings. Similar overlap between the flux-guides can be realized in printed designs.

Table 1. Nominal parameters of the modular transformer coil.

Winding	Turns	Resistance (Ω)	Nominal Voltage (V)	Nominal Current (A)	Insulation Class
Primary	1370	98	230	0.17	H
Secondary 1	151	1.35	25.1	1.3	F
Secondary 2	56	2.7	9.3	0.25	F

For simplicity, in this paper, only conventional stamping inspired designs were considered for 3D printing. In Figure 2, three considered transformer core designs are illustrated: (a) a laterally laminated interlocking design from four parts, (b) an axially laminated gapped design from two parts, and (c) an axially laminated interlocking design from four parts. The axially laminated interlocking design was chosen for printing due to its simplicity and similarity to the conventional design, its high achievable fill factor and its post-processing possibilities: all of the unmelted powder can be removed between the laminations post-printing and, if needed, all of the surfaces can be cleaned and oxidized or varnished for enhanced inter-lamination electrical resistance.

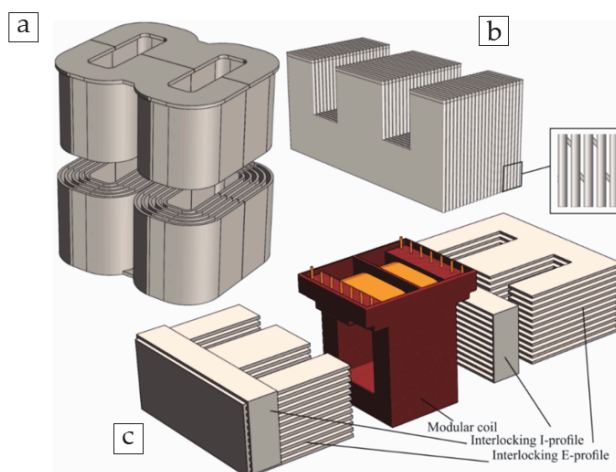


Figure 2. Considered lamination strategies: (a) Laterally laminated interlocking design, (b) Axially laminated design with air-gapped core structure, (c) Exploded view of the 3D printed transformer core design with interlocking axial laminations comprising four individual components.

3. Methods

3.1. Powder Characteristics

Transformer parts were printed with identical powder, processing, and annealing parameters to the previous study characterizing the AC and DC losses of the printed material [6]. Pre-alloyed, gas-atomized Fe-Si provided by Sandvik group was utilized for printing. The powder exhibited roughly spherical particle shape with a median diameter

of 38 μm , and its chemical composition is described in Table 2. The powder size, shape, and chemical composition were verified to verify the manufacturer declaration.

Table 2. Chemical composition of the employed Fe-Si powder.

Elements	Fe	Si	Mn	Cr	Ni	C
Wt%	Balance	3.7	0.2	0.16	0.020	0.01

3.2. SLM Printing of the Transformer Core

Transformer core parts were printed on the SLM Solutions GmbH Realizer SLM-280. The printing system provides a $280 \times 280 \times 350$ maximum build envelope and a single 1070 nm yttrium scanning laser (1×700 W). Custom smaller build platform (D100 mm) and re-coater were used for printing of the transformer core, designed for streamlining the powder substitution between projects for different raw powders.

Laser re-melting strategy was used to prevent the powder balling related uneven growth of the relatively large transformer parts during printing, which can result in rough porous material structure or the termination of the print job due to re-coater jamming. The phenomenon is related to an oxide film on the preceding layer impeding interlayer bonding and leading to balling, due to insufficient wetting of the molten metal on the oxide layer [8]. The balling phenomenon can be reduced in a higher purity environment (oxygen level below 0.1%), applying a combination of high laser powder and low scanning rate or applying re-melting scanning on the part [9].

Stripe (10mm wide) scan pattern was utilized with 30° rotation between layers. All of the printing was conducted in a nitrogen inert gas environment because of its relatively low cost. Platform pre-heating was not utilized as the custom reduced platform is not equipped for it. A summary of the main laser printing parameters is presented in Table 3.

Table 3. Summary of the printing parameters.

Parameter	Value
Layer thickness	50 μm
Hatch distance	120 μm
Laser Power	250 W (primary)/100 W (secondary)
Scanning velocity	0.5 m/s (primary)/0.5 m/s (secondary)
Scan strategy	Stripes
Environment	Nitrogen
Oxygen content	$\sim 0.1\%$

Transformer printing was completed in three parts in a total of 16 h: interlocking E-profiles separately (2×6 h) and the I-profiles in the same build (1×4 h). The printed components are illustrated in Figure 3: showing the surface finish, support structure, and the powder bed post-printing. Some concave warpage of the E-profiles was observed after separation from the build platform due to internal part stress, which obstructed the transformer assembly. Its causality can be traced to the relatively high internal stresses induced in part by the micro-welding process of SLM, and it can be resolved through the annealing of the printed parts at moderate temperature, pre-cutting from the platform for stress relief. Next, the support surfaces were polished and the inter-lamination air-gaps were lightly sanded for improved surface finish and fitting of the components.

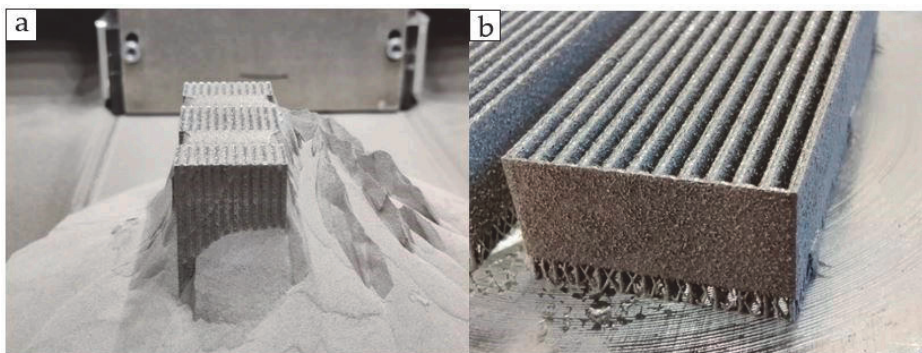


Figure 3. SLM printed transformer components: (a) E-profile component post-printing, (b) I-profile component welded on the baseplate.

3.3. Annealing

After mechanical post-processing, the printed transformer parts were annealed at 1200 °C in a low vacuum environment (~ 0.1 mBar) with a heating rate of 300 K/h, maintained at the target temperature for 1 h and then slowly furnace-cooled to room temperature.

3.4. Material Properties

The additively manufactured 3.7% silicon steel shows comparable magnetic performance to non-oriented conventional silicon steels after thermal treatment. Magnetization of 1.5 T is achieved at 1800 A/m, exhibiting electrical resistivity of $56.9 \mu\Omega\cdot\text{cm}$ and hysteresis losses of 0.61 ($W_{10,50}$) and 1.7 ($W_{15,50}$) W/kg [6]. In comparison, a typical non-oriented steel M235-35A used for electrical machine fabrication exhibits total core losses of 0.92 ($W_{10,50}$) and 2.35 W/kg ($W_{16,50}$), resistivity of $59 \mu\Omega\cdot\text{cm}$, and magnetization of 1.53 T at 2500 A/m. In this paper, we are comparing the additively manufactured core with a conventional Goss textured silicon steel M165-35S (equivalent to M111-35N) core, which shows superior magnetic properties to the non-oriented materials for transformer applications, as presented on Figure 4. The grain-oriented transformer steel shows approximately 0.3 T greater saturation magnetization than both of the non-oriented steels.

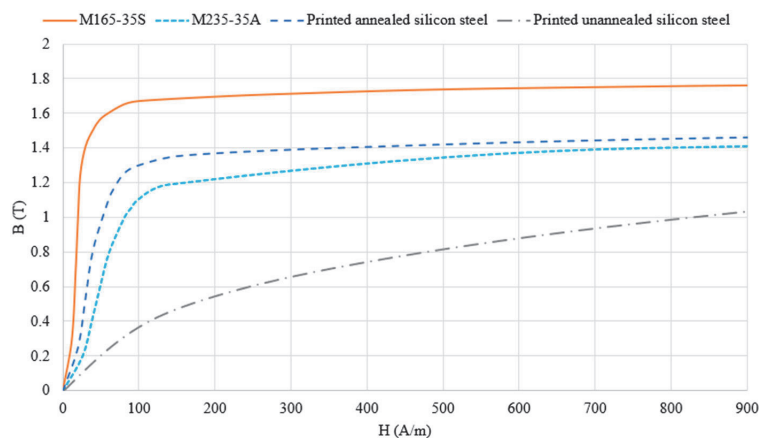


Figure 4. Magnetization curves of the studied materials: grain-oriented silicon steel M165-35S [10,11], non-oriented silicon steel M235-35A [12], printed annealed 3.7% silicon steel, and printed unannealed 3.7% silicon steel [6].

The grade designation of M165-35S of the Goss textured steel specifies 1.65 W/kg losses at 1.7 T ($W_{17,50}$), and a lamination thickness of 0.35 mm. The materials' exact silicon content, resistivity, and other typical properties are unspecified and depend on the manufacturer (manufacturing freedom in the range of grade specifications).

3.5. Transformer Characterization

The nominal performances of both the 3D printed and the conventional magnetic core transformers were characterized through open circuit and full load testing. The nominal parameters of the conventional transformer were obtained from the manufacturer's declaration. A drop in the nominal voltage is expected for the printed transformer due to its reduced fill factor, possible fitting defects (air-gaps between laminations), and lower saturation magnetization of the printed material. Its nominal voltage and iron losses were determined from the open circuit tests of the conventional transformer. To determine the transformer efficiencies, a load test was performed, where the transformer was energized up to nominal power. For thermal performance assessment, steady-state thermal images of the fully loaded transformers were captured with a Fluke Ti10 Thermal Camera.

The open circuit test setup is described in Figure 5, consisting of an autotransformer for variable voltage input and digital multimeters for measuring the voltage, current, and active power consumed in the transformer coil. In the open circuit test, the current drawn by the transformer establishes the magnetic field in the core. The active power consumed by the transformer signifies its total power loss, consisting mainly of magnetizing, and some ohmic, losses. The magnetizing losses summarize the energy lost from each magnetizing cycle, which are classically segregated into the hysteresis, classical, and excess eddy current loss.

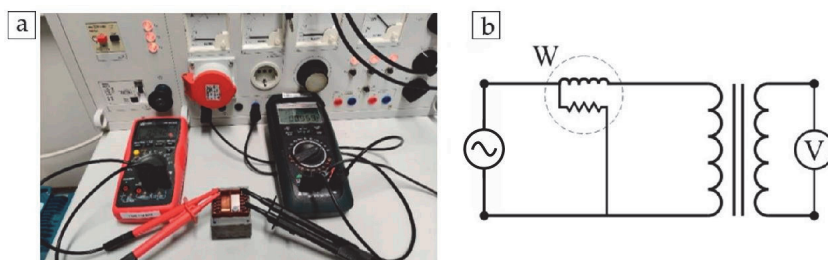


Figure 5. Open circuit transformer: test setup (a) and its schematic (b).

The ohmic losses are induced from joule heating of the coils due to the magnetizing current drawn. The total specific transformer core losses can be calculated from (1), where W is the active power loss measured in the open circuit test, I is the magnetizing current, R is the magnetizing coil resistance, and m is the weight of the core.

$$P = \frac{(W - IR^2)}{m} \quad (1)$$

Traditionally, the magnetic material loss behaviour is discussed in terms of cycle peak polarization (B_{max}) of the core. Unlike in the toroidal cores for magnetic material characterization [6,13], however, the flux density in the investigated transformer core can only be evaluated as an approximation, due to its uneven flux distribution. The analytical expression for calculating the peak polarization in a transformer can be derived from the differential form of Faraday's law (2), where E is the induced electromotive force by the switching magnetic field, N is the number of turns on the primary coil (1370), f is the excitation frequency of the magnetic field (50 Hz), B_{max} is the peak material polarization, S is the core cross sectional area, F is the core filling factor, U is the applied voltage on the primary coil, and U_r is the voltage drop over the primary coil.

$$E = N \frac{d\Phi}{dt} \rightarrow E_{max} = N2\pi fSF B_{max} \rightarrow B_{max} = \frac{E_{max}}{N2\pi fSF} = \frac{U - U_r}{N2\pi fSF} \tag{2}$$

Alternatively, the approximate material polarization can be evaluated from the material B-H curve (as presented on Figure 4) or by the finite element method (FEM) simulation. In both methods, the actual B-H curve of the transformer core can differ from the previously characterized material, most prominently due to air-gap related curve shearing. For B_{max} evaluation, the magnetic field strength in the transformer is calculated from (3), where N is the number of turns on the primary coil, i is the peak magnetizing current and l is the length of the mean magnetic flux path of the core. All FEM simulations are performed in open source finite element analysis software package Finite Element Method Magnetics (FEMM). The model accounts for the transformer cross sectional geometry, magnetized up to the peak magnetizing current measured from the open circuit test, including the material magnetization curve and fill factor, but excluding any gaps in the core internal structure.

$$H = \frac{Ni}{l} \tag{3}$$

4. Results

4.1. Assembled Transformer

The conventional and finished assembled printed transformer cores are presented in Figure 6. The overall transformer core dimensions correlated well, with the printed transformer exhibiting a slightly thinner and lighter core. The fill factor of the 3D printed core was measured from the axial centerline of the interlocking E-cores. For the conventional transformer, the fill factor was adopted from the stamping datasheets. The physical comparison of the transformer cores is presented in Table 4. No additional oxidation, treatment, or varnishing was applied to the surfaces of the 3D printed transformer core for increased eddy current reduction—the insulation is provided by the high natural surface roughness of the printed parts.

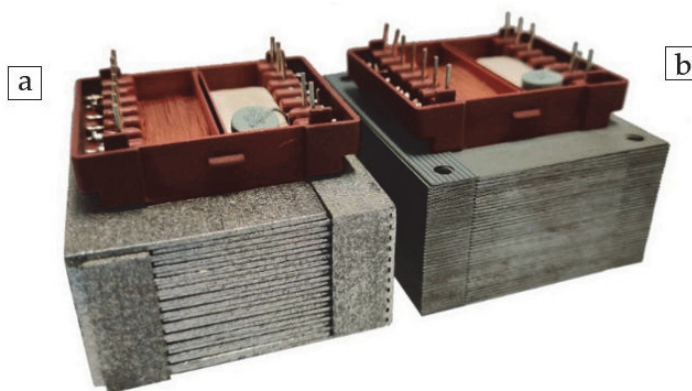


Figure 6. Printed (a) and conventional (b) transformer cores.

Table 4. Physical comparison of the transformer cores.

Core	Lamination Thickness (mm)	Fill Factor	Dimensions (mm)	Weight Core (kg)	Weight Coil (kg)	Varnish
Conventional	0.35	0.96	58.5 × 49.8 × 26.0	0.44	0.095	Yes
Printed	0.95	0.89	58.8 × 49.9 × 25.0	0.41	0.095	No

4.2. Performance

Open circuit tests of the transformers confirmed the flux drop in the core and the reduction of the sustainable operating voltage of the printed transformer. In Figure 7, both

the magnetizing current drawn from the supply for generating the desired voltage and the iron loss behavior calculated from (1) are presented. At 40 mA magnetizing current, the conventional transformer is energized up to 230 V, while the printed transformer is energized to a 30% lower voltage of 160 V. This is due to the lower flux density sustained by the printed material. For energizing the printed transformer up to 230 V, a magnetizing current of 220 mA is required. This is inefficient, however, due to deep core oversaturation, requiring 450% more current than for magnetizing the conventional core and 30% more current than the rated full load current of the winding.

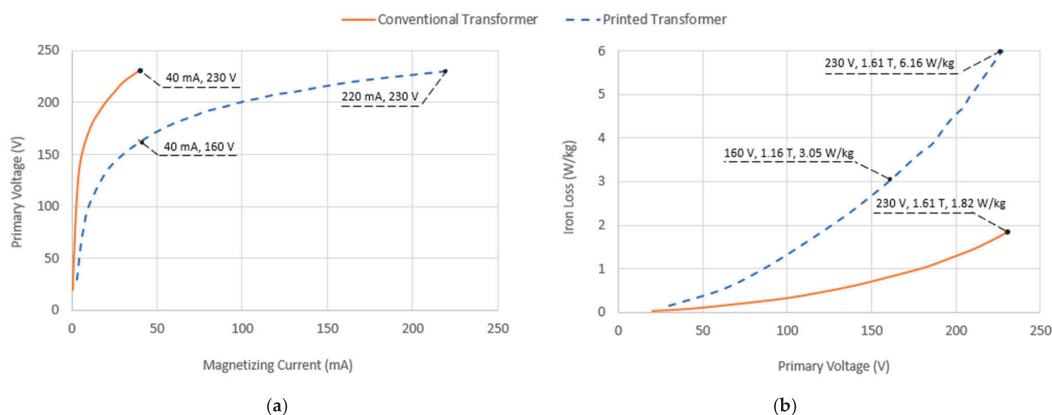


Figure 7. Magnetizing current drawn (a) and the specific core loss (b) of the tested transformers.

At 40 mA RMS excitation current (60 mA peak current), the analytically calculated (3) average H field generated in the magnetic core is 668 A/m, which corresponds to the magnetization of 1.72 T for M165-35S and 1.42 T for the annealed 3D printed material as determined from the magnetization curves in Figure 8. At 40 mA RMS excitation current, analogous excitation of both cores is achieved. Both are magnetized slightly above the approximate material knee-point and exhibit identical copper losses. Excitation of the conventional core to 160 V or the 3D printed core to 230 V would be impractical comparison-wise, as both states exhibit significantly differing magnetic behavior. At 160 V, the conventional core is still at the linear magnetic behavior: drawing only 7.6 mA magnetizing current and exhibiting 0.005 W of copper losses and 0.35 W of iron losses. At 230 V, the printed transformer shows deep saturation behavior, drawing 220 mA of magnetizing current, resulting in a significant voltage drop of 21.6 V, copper losses of 4.7 W, and iron losses of 2.6 W.

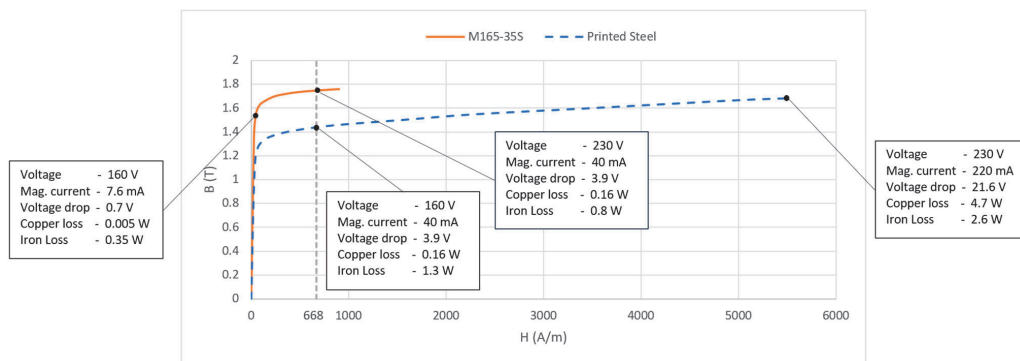


Figure 8. Core material magnetization curves correlated with the no load measurements of the investigated transformers.

FEM simulation of the transformer cores shows similar values of material magnetization: reaching 1.68 T for the conventional and 1.39 for the 3D printed core (Figure 9). Additionally, the simulation illustrates the uneven flux distribution in the core due to variations in transformer limb width. Analytical calculations with (2) show lower core flux density required for inducing a specific voltage in the core. For energizing the transformer up to 230 V, a flux density of 1.65 T is required, while for 160 V, a flux density of 1.26 T is required. The higher magnetization calculated from the experimental current and FEM simulation is most likely the result of intra-lamination air-gaps, which shears the material magnetization curve and requires more current for achieving the same material polarization.

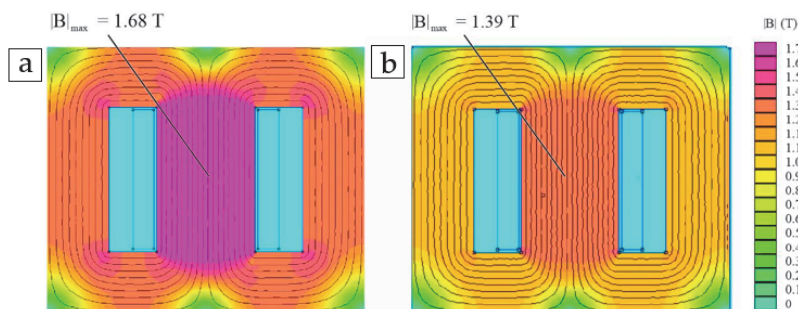


Figure 9. Flux distribution in the (a) conventional and (b) 3D printed transformer core.

Iron losses were identified as 1.82 W/kg for the conventional core at 230 V (at approximately 1.7 T, 50 Hz) and 3.05 W/kg for the 3D printed core at 160 V (in the range of 1.26–1.4 T, 50 Hz). Efficiency of the transformers was calculated from the load test measurements at both the ambient core temperature and the steady state temperature at full load conditions. The transformers reached steady state temperature after four hours of loading. The thermal images of the transformers are shown in Figure 10, with slightly higher heating observed for the 3D printed transformer core. The measured coil hotspot temperature was measured at 91.1 °C for the conventional core and at 95.1 °C for the 3D printed core. The core hotspots were measured with a thermocouple sensor due to the high reflectivity of the printed core, exhibiting temperatures of 71 °C (conventional) and 75 °C (3D printed).

At full load, the measured efficiency of the transformers ranged from 83.8% (21 °C) to 80.4% (71 °C) for the conventional transformer and 74.7% (21 °C) to 70.1% (75 °C) for the 3D printed transformer. The efficiency-load characteristic is presented in Figure 11. The highest efficiencies were measured at 41% load at ambient core temperature, reaching an efficiency of 88.7% for the conventional transformer and 80.5% for the 3D printed core. The efficiency of the 3D printed core was approximately 10% lower over the full measurement range. Due to the material saturation and inter-lamination air-gap related reduction of nominal voltage, the printed transformer core sustained reduced power density when compared to the conventional core. The transformer power density dropped 34% from 59 W/kg to 39 W/kg. The results of the transformer performance characterization are summarized in Table 5.

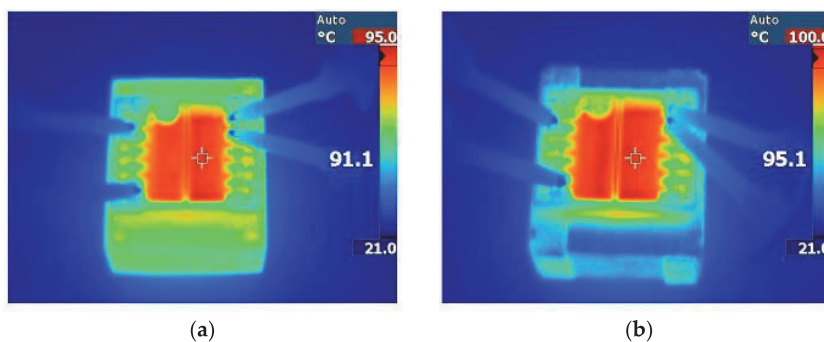


Figure 10. Steady state temperature of the studied transformers in the (a) conventional core and (b) 3D printed transformer core.

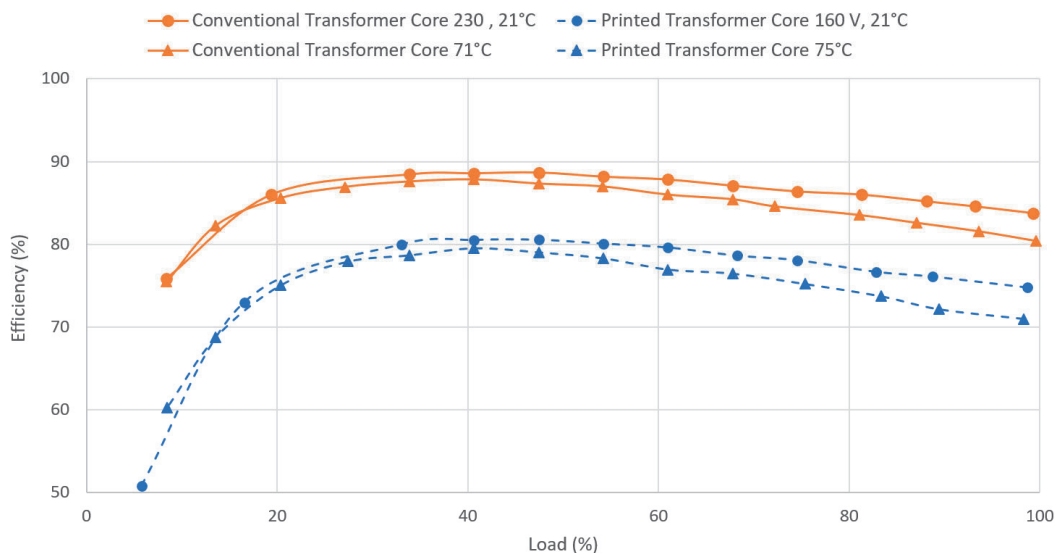


Figure 11. Efficiency-load characteristics of the studied transformers.

Table 5. Comparison of transformer performance.

Parameter (Full Load, 21 °C)	3D Printed Core	Conventional Core
Nominal Voltage	160 V	230 V
Nominal Current	0.17 A	0.17 A
Power Factor	0.97	0.97
Input Power	27.2 VA	39.1 VA
Output power	19.8 VA	31.8 VA
Efficiency (ambient temperature)	74.7%	83.8%
Efficiency (operating temperature)	70.1%	80.5%
Power Density (Core)	47 VA/kg	72 VA/kg
Power Density (Full Transformer)	39 VA/kg	59 VA/kg

5. Discussion

The characterized transformers show typical performance values for small 20–30 VA power rating single-phase transformers. From manufacturer datasheets, the typical efficiency for a 30 VA rated power transformer is in the range of 83 [14]–81% [15], which decreases to 77% [14] at 22 VA and to 65% [14] at 4.5 VA. The rated power densities vary

significantly depending on the design (some designs are fully encased), and are typically in the range of 56 [15]–39 VA/kg [14] for 30 VA rated transformers and slightly lower (50 [16]–39 [14] VA/kg) for 20 VA rated transformers. In this study, we obtained an efficiency of 80.5% for the conventional transformer and 70.1% for the 3D printed transformer core at steady state temperature. The 10% reduced overall transformer efficiency can most prominently be attributed to the eddy currents generated in the 170% thicker laminations of the printed design. The reduced power density of the printed design can be attributed to both a larger degree of assembly defect related air-gaps within the core and the overall lower magnetic saturation of the printed material compared to the Goss textured conventional steel. Both designs are within the range of typical power density values for low power transformers.

The 3D printed core exhibited iron losses of 3.05 W/kg at 160 V transformer energization. Analytical calculations identify an average B_{max} of 1.26 T at this transformer voltage level. Comparing the magnetizing values with previously measured 3D printed material magnetization curves, its shearing is proposed. Due to the air-gaps in the assembled printed design, more magnetizing current is required for the same material polarization and voltage generated by the transformer. Similar iron loss values have been measured by Plotkowski et al. for a 3D printed E-type transformer core [17]. In their work, they achieved a core loss of 3.5 W/kg ($W_{10,60}$) at 1.0 T, 60 Hz magnetization for a printed 3% silicon steel lamination inspired core. They achieved considerably improved losses with more complex geometry, reaching approximately 1.5 W/kg ($W_{10,60}$) to 3.2 W/kg ($W_{15,60}$) with ‘Hilbert pattern’ 6% silicon steel. It is important to note, however, that in their work approximately 56% core fill factor was achieved, resulting in low power density and voltage generation of the transformer.

Further optimization of both the component topology and its material properties are unavoidable for achieving high performance 3D printed transformer cores. To obtain high magnetic polarization (high power density) of the printed material with minimal magnetomotive force, a higher degree of control of the printed material grain structure must be achieved. The effect of the grain structure orientation in relation to the magnetic field is significant as illustrated by Figure 12 [18]. In conventional stampings, the grain-oriented pronounced Goss texture can be achieved with various hot and cold rolling stages of the steel sheets. In printed material, the optimization of the material grain structure is largely immature, with some grain structure evolution observed in [13], in heat treated laser-remelted printed silicon steel samples.

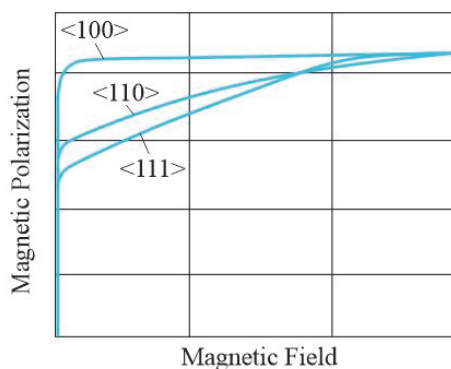


Figure 12. Polarization of the magnetic grains oriented in easy <100>, medium <110>, and hard <111> magnetization axis direction in relation to the magnetic field (in arbitrary units).

Several topological improvements can be applied to the transformer for enhanced performance. The printed transformer topology can be improved by increasing the fill factor of the assembled components, optimizing the lamination thickness for reduced eddy

current loss, and increasing its power density through shape optimization for achieving uniform magnetization. Due to the limited multi-material printing capacity of current SLM systems, two methods are proposed for eddy current reduction: the interlocking and the gapped core designs. With next-generation powder deposition methods [19], multiple metal or intermetallic materials can be utilized in parallel, allowing for more options and more advanced core topologies.

First, for increasing the fill factor, higher accuracy of the printing system must be achieved. With the current settings, the printed parts still suffer from low surface roughness-related reduced fill factor for interlocking designs or inter-lamination short-circuits and sintered unremovable powder for the gapped designs. Secondly, the lamination thickness can be optimized to provide minimal core losses with maximum part fill factor, i.e., to achieve the optimal ratio of air gap to lamination width. Thirdly, the shape of the core can be optimized for achieving uniform magnetization, weight reduction and improved thermal capacity. Several methods for improving ferromagnetic part performance through topology optimization are discussed in further detail in [20,21]. For improved heat exchange of the printed transformer, enhanced convective heat transfer can easily be obtained by increasing its outer surface area with different surface relief structures [22].

6. Conclusions

In this paper, a fully functioning, additively manufactured soft magnetic transformer core was fabricated and tested. For the first time in literature, an electromagnetic device with a fully 3D printed magnetic core was evaluated in terms of efficiency and performance. The prototype core showed uncompetitive performance when compared to modern conventional transformer cores. Although the printed material is not currently suitable for the production of commercial transformer cores, the analysis of the prototype core did allow us to demonstrate the current state of the art, identify the technical challenges involved, and propose next steps for realizing topology optimized 3D printing soft ferromagnetic components.

A novel, interlocking core design was developed and utilized successfully for achieving a relatively high fill factor of 89% (compared to other 3D printed cores) and eddy current reduction of the additively manufactured transformer core. For obtaining higher fill factor with this method, lower surface roughness of the printed parts must be obtained for more precise fitting of the components. Furthermore, the interlocking core design enabled the integration of modular winding to the transformer design, simplifying its assembly process.

The first prototype transformer core showed both lower efficiency (10% reduced) and power density (34% reduced), when compared to the conventional modern transformer at their respective optimal working conditions. These preliminary performance results of the first prototype core are likely to improve with more refined core designs and materials as part of future research. Currently, the main challenge in realizing high-performance 3D printed soft magnetic components is achieving a higher degree of control over the printed material grain texture, since the conventional post-processing methods for Goss textured silicon steel sheets are not suitable for processing geometrically complex 3D printed magnetic components. Even so, for non-grain-oriented applications (such as rotating electrical machines), the current material properties appear suitable, especially with the unprecedented prototyping freedom of 3D printing systems—which could enable the emergence of entirely new types of machines. Although the current 3D printed cores for AC applications suffer either from high eddy current losses or low filling factor, next-generation emerging multi-metal SLM printers can potentially improve the additively manufactured core performance considerably. Future work on this project will include further optimization of both the printed material and component topology for designing and constructing AM topology optimized electrical machines.

Author Contributions: Conceptualization: A.K. and H.T.; methodology: A.R.; validation, A.K.; investigation, H.T. and P.S.G.; resources, P.S.G.; writing—original draft preparation, H.T.; writing—review and editing, H.T. and A.K.; supervision, A.K. and A.B.; project administration, T.V.; funding acquisition, A.K. All authors have read and agreed to the published version of the manuscript.

Funding: This research work has been supported by the Estonian Ministry of Education and Research (Project PSG-137).

Institutional Review Board Statement: Not applicable.

Informed Consent Statement: Not applicable.

Data Availability Statement: Data is contained within the article.

Acknowledgments: The authors would like to thank Balti Transformers Ltd. for cooperation.

Conflicts of Interest: The authors declare no conflict of interests.

References

- How 3D Printing is Redefining Inductor Coil Production | GKN Additive. Available online: <https://www.gknpm.com/en/our-businesses/gkn-additive/how-3d-printing-is-redefining-inductor-coil-production/> (accessed on 26 November 2020).
- GE Aviation 3D Prints 30,000th Metal 3D Printed Fuel Nozzle at Auburn, Alabama Plant. Available online: <https://3dprint.com/226703/ge-aviation-fuel-nozzle-3d-printed-30000/?fbclid=IwAR38NO-0dAf2BwIkXhVtIC18gAimKnQU5y5KRv-u08InfruK5Zl7Ql1P1HI> (accessed on 26 November 2020).
- Conflux Technology is Reinventing Heat Exchangers with 3D Printing » 3D Printing Media Network—The Pulse of the AM Industry. Available online: <https://www.3dprintingmedia.network/conflux-technology-reinventing-heat-exchangers/> (accessed on 26 November 2020).
- Ngo, T.D.; Kashani, A.; Imbalzano, G.; Nguyen, K.T.Q.; Hui, D. Additive manufacturing (3D printing): A review of materials, methods, applications and challenges. *Compos. Part B Eng.* **2018**, *143*, 172–196. [CrossRef]
- Tiismus, H.; Kallaste, A.; Belahcen, A.; Rassolkin, A.; Vaimann, T. Challenges of Additive Manufacturing of Electrical Machines. In Proceedings of the 2019 IEEE 12th International Symposium on Diagnostics for Electrical Machines, Power Electronics and Drives (SDEMPED), Toulouse, France, 27–30 August 2019; pp. 44–48. [CrossRef]
- Tiismus, H.; Kallaste, A.; Belahcen, A.; Tarraste, M.; Vaimann, T.; Rassolkin, A.; Asad, B.; Ghahfarokhi, P.S. AC Magnetic Loss Reduction of SLM Processed Fe-Si for Additive Manufacturing of Electrical Machines. *Energies* **2021**, *14*, 1241. [CrossRef]
- Stornelli, G.; Faba, A.; Di Schino, A.; Folgarait, P.; Ridolfi, M.R.; Cardelli, E.; Montanari, R. Properties of additively manufactured electric steel powder cores with increased si content. *Materials* **2021**, *14*, 1489. [CrossRef] [PubMed]
- Yap, C.Y.; Chua, C.K.; Dong, Z.; Liu, Z.H.; Zhang, D.Q.; Loh, L.E.; Sing, S.L. Review of selective laser melting: Materials and applications. *Appl. Phys. Rev.* **2015**, *2*, 041101. [CrossRef]
- Li, R.; Liu, J.; Shi, Y.; Wang, L.; Jiang, W. Balling behavior of stainless steel and nickel powder during selective laser melting process. *Int. J. Adv. Manuf. Technol.* **2012**, *59*, 1025–1035. [CrossRef]
- Waasner Magnetic and Technological Properties. Available online: http://www.waasner.de/fileadmin/Assets/PDFs/MaterialCharacteristics_201111.pdf (accessed on 1 March 2021).
- Waasner Material Characterization. Available online: http://www.waasner.de/fileadmin/Assets/PDFs/MaterialCharacteristics_201111.pdf (accessed on 1 March 2021).
- Data Sheet Isovac 235-35 A. Available online: https://www.voestalpine.com/division_stahl/content/download/39689/456867/file/DB_isovac_235-35A_E_281015.pdf (accessed on 1 March 2021).
- Tiismus, H.; Kallaste, A.; Belahcen, A.; Vaimann, T.; Rassolkin, A.; Lukichev, D. Hysteresis Measurements and Numerical Losses Segregation of Additively Manufactured Silicon Steel for 3D Printing Electrical Machines. *Appl. Sci.* **2020**, *10*, 6515. [CrossRef]
- Block—PCB Transformers. Available online: <http://www.farnell.com/datasheets/1897307.pdf> (accessed on 1 March 2021).
- Block—FL 30/12 Safety Isolating Transformer. Available online: https://www.block.eu/en_US/productversion/fl-3012/ (accessed on 1 March 2021).
- Brownsburg Electronic Inc. Transformers and Inductors. Available online: <http://www.bei.net/PDF/catalogue2004.pdf> (accessed on 1 March 2021).
- Plotkowski, A.; Carver, K.; List, F.; Pries, J.; Li, Z.; Rossy, A.M.; Leonard, D. Design and performance of an additively manufactured high-Si transformer core. *Mater. Des.* **2020**, *194*, 108894. [CrossRef]
- Suwass, S.; Ray, R.K. *Crystallographic Texture of Materials*; Springer: London, UK, 2014.
- Aconity Additive Manufacturing. Available online: <https://aconity3d.com/> (accessed on 29 March 2021).
- Andriushchenko, E.; Kallaste, A.; Belahcen, A.; Vaimann, T.; Rassolkin, A.; Heidari, H.; Tiismus, H. Optimization of a 3D-Printed Permanent Magnet Coupling Using Genetic Algorithm and Taguchi Method. *Electronics* **2021**, *10*, 494. [CrossRef]

21. Orosz, T.; Rassólkin, A.; Kallaste, A.; Arsénio, P.; Pánek, D.; Kaska, J.; Karban, P. Robust Design Optimization and Emerging Technologies for Electrical Machines: Challenges and Open Problems. *Appl. Sci.* **2020**, *10*, 6653. [[CrossRef](#)]
22. Ghahfarokhi, P.S.; Podgornovs, A.; Kallaste, A.; Cardoso, A.J.M.; Belahcen, A.; Vaimann, T.; Tiismus, H.; Asad, B. Opportunities and Challenges of Utilizing Additive Manufacturing Approaches in Thermal Management of Electrical Machines. *IEEE Access* **2021**, *9*, 36368–36381. [[CrossRef](#)]

Publication V

M. Sarap, S. Member, A. Kallaste, S. Member, P. S. Ghahfarokhi, H. Tiismus, S. Member, T. Vaimann, and S. Member, "The effect of build direction on the thermal conductivity of additively manufactured AlSi 10 Mg and silicon-steel samples," in *Proceedings - 2022 International Conference on Electrical Machines, ICEM 2022, Sept 2022*. (accepted, under publication).

The effect of build direction on the thermal conductivity of additively manufactured AlSi₁₀Mg and silicon-steel samples

M. Sarap, *Student Member, IEEE*, A. Kallaste, *Senior Member, IEEE*, P. Shams Ghahfarokhi, *Member, IEEE*, H. Tiismus, *Student Member, IEEE*, T. Vaimann, *Senior Member, IEEE*

Abstract – Increasing power densities in electrical machines create a demand for more powerful thermal solutions, which additive manufacturing can provide. However, the material properties of additively manufactured objects are unknown. In this paper, the anisotropic thermal conductivities of an aluminum alloy (AlSi10Mg) and high-silicon steel (Fe-3.7%w.t.Si) samples manufactured using selective laser melting (SLM) were analyzed before and after heat-treatment. It was found that the thermal conductivities of the as-built aluminum samples were significantly higher in the SLM build direction, while the annealed samples showed higher thermal conductivities and no anisotropy. The silicon-steel samples showed constant thermal conductivity and no anisotropy before and after heat-treatment. The results of this study will be beneficial for designing future AM thermal solutions for electrical machines.

Index Terms— Electrical machines, three-dimensional printing, thermal conductivity, material anisotropy, annealing.

I. INTRODUCTION

Additive manufacturing (AM) is providing advances in the design of electrical machines by enabling the production of optimized geometries. Otherwise known as 3D printing, it is the process of manufacturing a physical item via the consecutive fabrication of thin layers. This gives it unparalleled flexibility in creating many kinds of complex structures, meaning that virtually any object that can be digitally modelled can also be manufactured. In the field of electrical machines, the versatility of AM is leveraged to produce optimized components with novel designs [1]. Considerable attention is also given to novel thermal management solutions [2], where mathematically optimized designs can be fully utilized. Typical AM solutions incorporate complex internal geometries, lattice structures, coolant flow channels, topology-optimized shapes, and other design elements, which hitherto have been prohibitively expensive to manufacture. The most relevant AM method for

manufacturing functional metal parts, and therefore electrical machine components, is selective laser melting (SLM), which has risen in popularity due to a wide selection of materials with excellent properties. During the SLM process, layers of powder are completely melted, resulting in a nearly fully dense part [3]. However, the significant temperature gradients [4] and rapid cooling rates in the order of 106 K/s [5] create microstructures inside the material, which can lead to anisotropy [6]. Therefore, in addition to laser other printing parameters, the properties of parts produced with SLM are affected by manufacturing orientation.

The mechanical properties of different SLM materials have been thoroughly investigated. Hitzler et al. [7] measured the Young's modulus of SLM AlSi10Mg alloy samples and observed lower values for the samples printed in the Z-direction. Orientation-dependent mechanical properties have also been found by several other researchers [8-10] with the general conclusion being lower strength but higher elasticity in the build direction. In the context of thermal management, the most essential material parameter is thermal conductivity, which defines the temperature gradient across the material with a given heat flow. Thermal anisotropy can be evident from measurements of the material's elastic modulus, as it has been found to be proportional to the lattice thermal conductivity of SLM CM247LC alloy [11]. Anisotropic thermal properties were directly measured by Zhou et al. [12], who used laser flash analysis to measure the thermal conductivity of an SLM Cu-2.4Ni-0.7Si alloy in two perpendicular directions. The obtained values of 187.83 and 62.86 W/m/K for the vertical and horizontal directions, respectively, show a roughly three times higher thermal conductivity in the vertical direction. A higher thermal conductivity in the vertical direction for SLM AlSi10Mg was also observed by Strumza et al. [13], Yang et al. [14] and Kim [15], albeit their results show a difference of only around 10%. Research also shows that the anisotropy can be reduced and the material properties altered by subjecting the material to heat treatment [16].

Two relevant materials regarding thermal solutions for AM electrical machines are AlSi10Mg and silicon-steel. The aluminum alloy is widely used in thermal solutions for its good physical and mechanical properties in addition to good printability [17]. The soft-magnetic cores of AM electrical machines are most commonly manufactured from silicon-steel, which retains its good magnetic properties after the AM process [18]. Due to the design freedom offered by AM, even the geometry of the machine's core can be optimized

This work has been supported by the European Regional Development Fund within the Activity 1.1.1.2 "Postdoctoral Research Aid" of the Specific Aid Objective 1.1.1 "To increase the research and innovative capacity of scientific institutions of Latvia and the ability to attract external financing, investing in human resources and infrastructure" of the Operational Programme "Growth and Employment" (No.1.1.1.2/VIAA/3/19/501) & Estonian Ministry of Education and Research (Grant PSG-137).

M. Sarap, A. Kallaste, H. Tiismus and T. Vaimann are with the Department of Electrical Power Engineering and Mechatronics, Tallinn University of Technology, Estonia (e-mail: martin.sarap1@taltech.ee).

P. S. Ghahfarokhi is with the Department of Electrical Machines and Apparatus, Riga Technical University, Latvia.

for thermal performance, meaning that accurate knowledge of the core material's thermal conductivity in each direction becomes important. For example, in the case of a typical air-cooled electrical motor, the majority of the heat flow is directed radially from the windings towards the machine outer surface, while axial heat flow in the core is insignificant. Due to this, the axial thermal conductivity of the material, while possibly having a higher value in the case of an AM machine, has no impact on the machine's overall thermal performance.

Therefore, when considering AM materials with significant anisotropy, the thermal conductivity may depend on direction, meaning that a scalar value is insufficient and the thermal conductivity tensor is required. In this paper, the thermal conductivities of the as-built and heat-treated aluminum and silicon-steel samples manufactured in different orientations via SLM are measured. This provides information on the effect of build direction on the physical characteristics of two popular materials in the field of AM electric machines, which is valuable for modelling future designs.

II. METHODOLOGY

There are several ways of measuring a material's thermal conductivity. The most widely used method for accurate measurements of solid materials is laser flash analysis (LFA). Although LFA can provide accurate results quickly and at a wide temperature range, it is only applicable for fully dense and homogenous materials [19]. As the AM samples are assumed to have some internal porosity and inhomogeneity, the laser flash analysis method is not suitable. For this reason, the thermal conductivity of the AM samples is measured via the longitudinal heat flow method.

The longitudinal heat flow method includes heating the rod-shaped sample from the 'hot' end, cooling it from the 'cold' end, and measuring the temperature difference over a known length (Fig. 3). If the total heat flow through the sample is known, then its thermal conductivity can be calculated through Fourier's law of conduction. The heat flow through the sample is not directly measured, but is instead approximated using the total energy input and the insulation losses, with the former being accurately measured and the latter being calculated with a thermal model. This model includes the temperature measurements of the heat sink and the surface of the insulation, meaning that these can be given as constant temperature boundary conditions, which greatly simplifies the model. Since the heat flows uniformly through the entire area of the sample and only in one direction, the results are affected by the porosity of the material and any anisotropy can be identified. Therefore, this method is comparable to a practical thermal solution, making the results relevant for designing electrical machines.

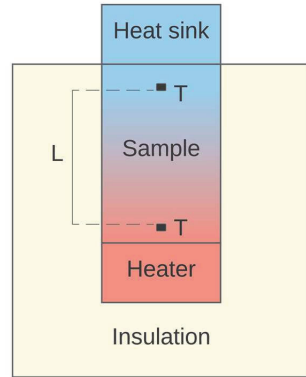


Fig. 3. Longitudinal heat flow technique used for measuring the thermal conductivity of the samples with T – temperature sensor and L – active length of the sample.

A. Test Samples

Five samples from two different materials were manufactured using SLM. With this AM process, consecutive layers of powder are applied with the recoater and the cross sections melted with a high-powered laser to manufacture the three-dimensional object. Each layer is formed on the build platform in the X-Y plane and stacked vertically in the Z-axis. Fig. 2 illustrates the production of an electrical machine stator via SLM.

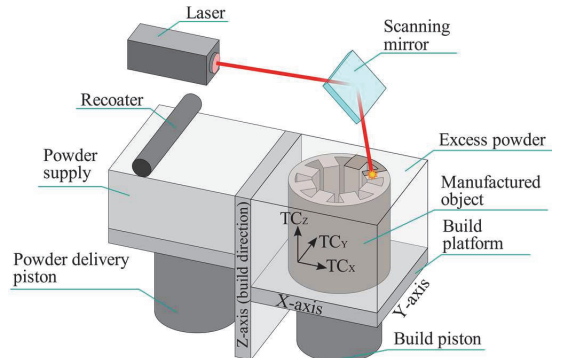


Fig. 2. SLM process with the anisotropic thermal conductivity of the manufactured object denoted as T_z , T_y and T_x .

Three of the samples were manufactured from the aluminum alloy AlSi10Mg at different orientations. The first one (Al_z) vertically to determine the thermal conductivity in the build direction. The second sample (Al_x) was printed lying down, with the axis of the sample being perpendicular to the build direction, to determine the in-plane thermal conductivity. The third specimen (Al_{45°) was printed at a 45° angle to observe any intermediate effects of printing orientation. The thermal conductivity of this material is given by the manufacturer as 130-150 W/m/K at 20°C after heat treatment [20], and at 100-110 W/m/K before heat-treatment by another manufacturer of the same alloy [21]. After the initial measurements, the aluminum samples were heat-treated at 300°C for 2 hours. Fig. 3 illustrates the orientation of the aluminum specimens on the build platform during the SLM process.

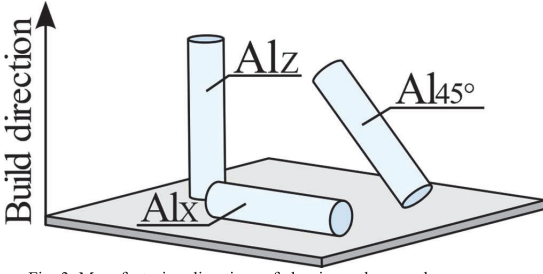


Fig. 3. Manufacturing directions of aluminum the samples.

Two of the samples were manufactured from silicon-steel (Fe-3.7%w.t.Si) which is a typical material used as the soft magnetic core in electrical machines. One sample (Fe_z) was printed vertically and the other one (Fe_x) horizontally. The exact composition and magnetic properties of this material have been previously measured by Tiismus et al. [22], although the thermal conductivity of AM silicon steel is not well known, which is why a commercially available 3.0% Si electrical steel with a thermal conductivity of 28 W/m/K [23] is used as a comparison. The steel samples were heat-treated at 1200 °C for 1 hour with a heating rate of 300 °C/h. The AM samples together with the important dimensions are presented in Fig. 4. All the samples have small radially placed rectangular holes for the PT100 temperature sensors. These are dimensioned such that the exact location of the sensors can be accurately known, as the distance between the sensors is used to calculate the thermal conductivity of the samples.

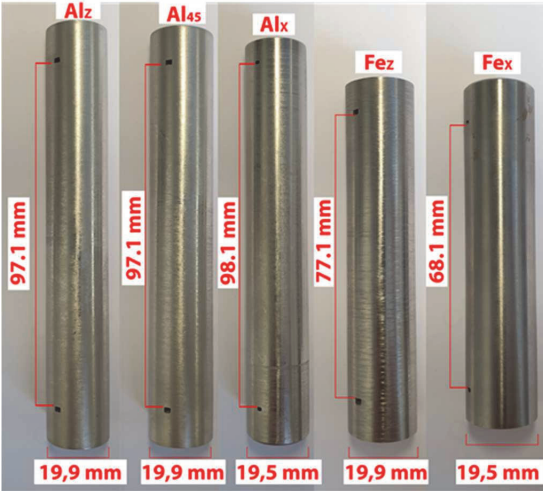


Fig. 4. SLM aluminum alloy and silicon-steel samples.

The physical properties of AM parts are also highly dependent on the printing parameters. For example, the correlation between laser energy density and porosity has been thoroughly researched [24], [25] and it is known that too low or high energies create porosity in the printed part due to partial melting and material evaporation respectively. Another important parameter is hatch spacing, which defines the distance of adjacent scan paths and can affect the relative

density and hardness of the AM part [26]. The scan strategy defines the movement pattern of the laser beam and can affect the crystallographic texture of the part, which could produce anisotropy in the material [27]. The values for the important printing parameters are presented in Table I.

TABLE I
IMPORTANT PRINTING PARAMETERS

Parameter	Value (aluminum)	Value (steel)
Layer thickness	50 μm	50 μm
Hatch distance	170 μm	120 μm
Laser Power	350 W	250 W
Scanning velocity	1.15 m/s	0.5 m/s
Scan strategy	Stripes	Stripes
Environment	Nitrogen	Nitrogen
Oxygen content	~0.1 %	~0.1 %

B. Experimental Setup and Procedure

The measurements were carried out in a thermally stable room with minimal airflow. Measurements were taken at several different heating powers to determine the temperature dependence of the thermal conductivity. For each measurement, the system was given several hours to reach steady state, which eliminates any effect of thermal capacitance. To achieve this, it was important to ensure a stable ambient temperature and input power. The hot side of the sample was heated with a power resistor, so that the total input energy could be accurately measured. The cold side was cooled with a high-performance water-cooling unit to minimize the thermal resistance of the sample stack and therefore heat travel through the insulation. The measurement setup is presented in Fig. 5.

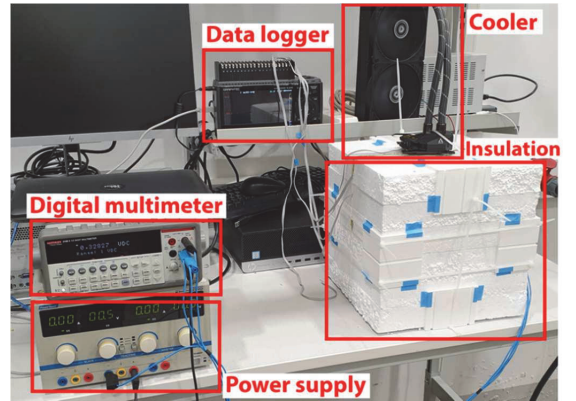


Fig. 5. Measurement setup.

C. Uncertainty Analysis

The uncertainties of the measurement results are determined by using the uncertainty of each measurement to calculate the maximum and minimum values for the thermal conductivities. The majority of the uncertainty is due to the accuracy class of the temperature sensors, which is defined in the IEC 60751 standard as $\pm 0.1 + 0.0017|T|$. Some is caused by the uncertainty of the measurements on the physical dimensions of the samples, most notably the distance between the sensors. These were measured with an

accuracy of 0.01 mm. Another source of uncertainty is the approximation of insulation losses with the use of a mathematical model. As heat flow through the insulation is comparatively very low, the relative uncertainty of effective heat flow could be calculated to be around 0.5-1%, depending on the sample. Very minor sources of uncertainty, like the electrical power measurements, are also considered. Therefore, the relative errors for the thermal conductivity measurements fell into the range of 3-5%. It should be noted, that the uncertainty is mostly relevant for the absolute values, as the method is extremely consistent when comparing different samples.

III. RESULTS AND DISCUSSION

The results of the measurements together with the calculated uncertainties for the as-built aluminum samples are presented in Fig. 6. The measurements of the pre-annealed samples revealed a roughly 10% increased thermal conductivity in the Z-direction (~ 115 compared to ~ 105 W/m/K). For each sample, an approximately linear correlation between thermal conductivity and temperature was noted, which is typical for this alloy at the measured temperature range [14].

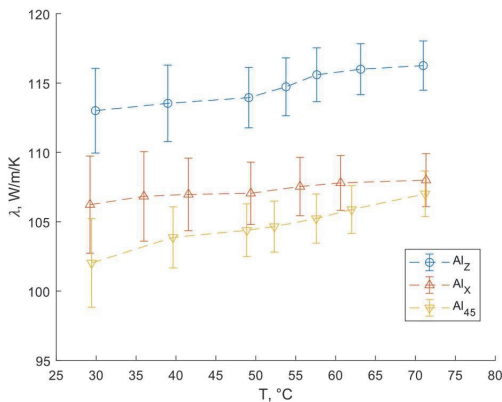


Fig. 6. Measured thermal conductivity values for the as-built aluminum samples.

The higher thermal conductivity in the Z-direction could be explained by a preferred grain orientation, which can form in the crystal structure during the SLM process, leading to more grain boundary scattering in one direction (Fig. 7). In the case of AlSi10Mg, rapid cooling during the SLM process has been shown to result in the growth of long grains oriented towards the heat source [28]. Additionally, with some alloys, the bulk thermal conductivity of the material is often significantly affected by the presence silicon in the crystal structure [29]. If the SLM process caused the Si to form an ordered state instead of the normally occurring random distribution, it could be another source of anisotropy [28]. It is interesting to note that the results for the Al₄₅ sample measured slightly lower than the Al_X sample, suggesting that the thermal conductivity is not linearly correlated to the printing orientation.

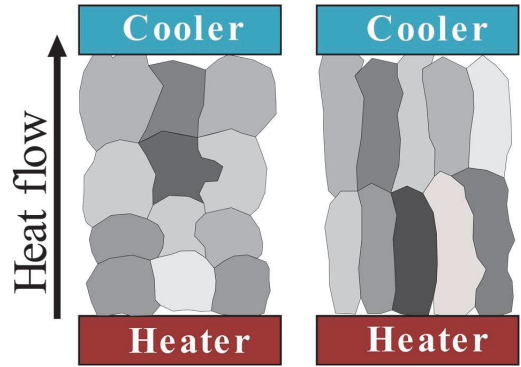


Fig. 7. Example of heat flow in the case of an isotropic (a) and anisotropic (b) grain structures. In the second case, the heat flowing through the material encounters less grain boundaries, resulting in increased thermal conductivity.

Additively manufactured metal parts are often annealed to achieve more favorable properties and reduced anisotropy. This involves heating the part above its recrystallization temperature for a suitable amount of time and then allowing it to cool down. By controlling the heating and cooling rates, the crystal structure can be manipulated in a desirable way. The annealing of SLM produced AlSi10Mg has been shown to result in increased strength [30] and thermal conductivity [31]. The measurement results for the annealed samples are presented in Fig. 8. As expected, the values are significantly higher for all samples at around 148 - 150 W/m/K. The results strongly indicate that the effects of orientation are completely nullified by annealing, as no meaningful anisotropy could be identified, although the correlation between thermal conductivity and temperature remains.

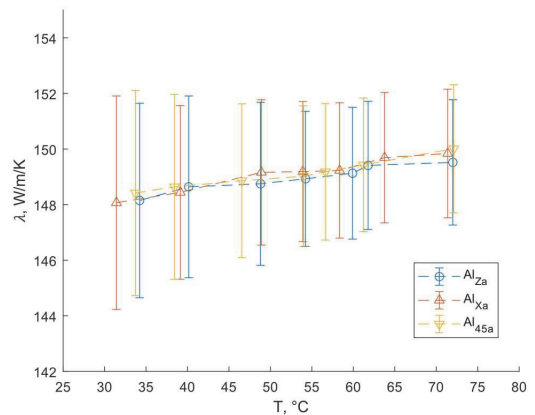


Fig. 8. Measured thermal conductivity values for the annealed aluminum samples.

The results obtained from the silicon-steel samples are presented in Fig. 9. In this case, the measured values fell into the range of 24.43 - 27.47 W/m/K and are very similar for all samples, showing no appreciable effect of print orientation or heat-treatment on the thermal conductivity. This agrees with electrical resistivity measurements performed by Tiismus et al. [32] on a similar material, which did not show any

anisotropy either. The thermal conductivities of the silicon-steel samples increase with higher temperatures, which is also the case with other steels at this temperature range [33]. When compared to the commercially available 3.0% Si electrical steel, the thermal conductivity of the AM material is slightly lower. This is expected, as the low thermal conductivity of silicon is more significant at higher concentrations. Because the difference with the commercial material is small, it can be said that the SLM process does not inhibit the thermal conductivity of silicon-steel.

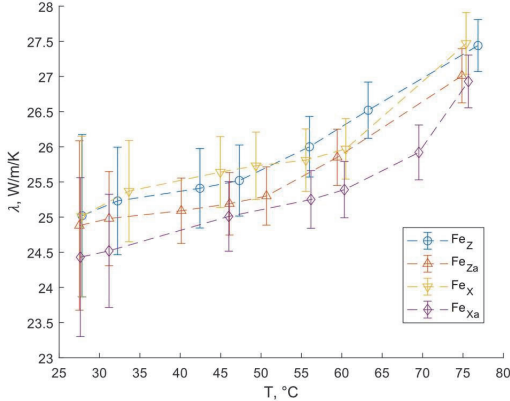


Fig. 9. Measured thermal conductivity values for the as-built and annealed silicon-steel samples.

In addition to a lack of anisotropy, the results show no difference in thermal conductivity between the as-built and annealed samples. This differs from the electromagnetic properties of AM silicon-steel, which have been shown to be anisotropic. For example, Kang et al. [34] found anisotropic magnetic properties in high-silicon steel manufactured via SLM, which they proposed could potentially be attributed to rod-like structures formed in the material by the SLM process. Moreover, the electromagnetic properties of AM silicon-steel have been shown to be affected by heat-treatment, as Garibaldi et al. [35] measured the effects of annealing on the magnetic properties of Fe-6.9%wt.Si samples manufactured with SLM. They observed a roughly 50% drop in power losses by annealing the sample at 1150 °C for 1h, which they attributed to the increased grain size inside the steel. Therefore, while it appears that the SLM process creates some anisotropy in silicon-steels, it has no appreciable effect on the material's thermal conductivity. A summary of the measurement results is presented in Table II. The values for the specific temperatures are interpolated and the uncertainty of a measurement at the nearest lower temperature is used.

TABLE II
MEASURES THERMAL CONDUCTIVITIES OF THE SAMPLES

Sample	λ at 35 °C (W/m/K)	λ at 70 °C (W/m/K)
Alz / annealed	113.3 ± 3.1 / 148.2 ± 3.5	116.2 ± 1.8 / 149.5 ± 2.3
Al45 / annealed	103.0 ± 3.2 / 148.5 ± 3.7	106.9 ± 1.7 / 149.9 ± 2.4
Alx / annealed	106.7 ± 3.5 / 148.2 ± 3.8	108.0 ± 2.0 / 149.8 ± 2.3
Fez / annealed	25.3 ± 0.8 / 25.0 ± 0.7	27.0 ± 0.4 / 26.6 ± 0.4
Fex / annealed	25.4 ± 0.7 / 24.6 ± 0.8	26.9 ± 0.4 / 26.0 ± 0.4

IV. CONCLUSION

The thermal conductivities of SLM AlSi10Mg and Fe-3.7%wt.Si samples manufactured in different orientations were measured using a longitudinal heat flow technique. The results reveal notable anisotropy in the pre-annealed aluminum samples, suggesting that with SLM comparatively higher values of thermal conductivity can be achieved in the Z direction. After annealing, the thermal conductivity of the aluminum samples increases significantly and the anisotropy disappears. These results are in agreement with previous research. The silicon-steel samples showed practically identical thermal conductivity before and after annealing, without any significant anisotropy in either state. This is a desirable result in the context of AM electrical machines, as the soft-magnetic core parts can be freely printed in the orientation that favors electromagnetic properties or printing success. Similarly, the lack of effect of heat-treatment on the thermal conductivity suggests that the specific heat-treatment method used on AM silicon-steel can be freely chosen based on the desirable electromagnetic and mechanical parameters. Further research needs to be done to determine the effects of other printing parameters on the thermal conductivity of AM silicon-steel.

V. REFERENCES

- [1] M. U. Naseer, A. Kallaste, B. Asad, T. Vaimann, and A. Rassökin, "A review on additive manufacturing possibilities for electrical machines," *Energies*, vol. 14, no. 7. MDPI AG, Apr. 01, 2021, doi: 10.3390/en14071940.
- [2] P. S. Ghahfarokhi et al., "Opportunities and Challenges of Utilizing Additive Manufacturing Approaches in Thermal Management of Electrical Machines," *IEEE Access*, vol. 9, pp. 36368–36381, 2021, doi: 10.1109/ACCESS.2021.3062618.
- [3] G. B. Bang et al., "Effect of process parameters for selective laser melting with SUS316L on mechanical and microstructural properties with variation in chemical composition," *Materials & Design*, vol. 197, p. 109221, Jan. 2021, doi: 10.1016/J.MATDES.2020.109221.
- [4] D. Barba, C. Alabort, Y. T. Tang, M. J. Viscasillas, R. C. Reed, and E. Alabort, "On the size and orientation effect in additive manufactured Ti-6Al-4V," *Materials & Design*, vol. 186, p. 108235, Jan. 2020, doi: 10.1016/J.MATDES.2019.108235.
- [5] I. Rosenthal, A. Stern, and N. Frage, "Microstructure and Mechanical Properties of AlSi10Mg Parts Produced by the Laser Beam Additive Manufacturing (AM) Technology," *Metallography, Microstructure, and Analysis*, vol. 3, no. 6, pp. 448–453, Dec. 2014, doi: 10.1007/S13632-014-0168-Y/FIGURES/10.
- [6] L. Hitzler, J. Hirsch, B. Heine, M. Merkel, W. Hall, and A. Öchsner, "On the Anisotropic Mechanical Properties of Selective Laser-Melted Stainless Steel," *Materials* 2017, Vol. 10, Page 1136, vol. 10, no. 10, p. 1136, Sep. 2017, doi: 10.3390/MA10101136.
- [7] L. Hitzler et al., "Direction and location dependency of selective laser melted AlSi10Mg specimens," *Journal of Materials Processing Technology*, vol. 243, pp. 48–61, May 2017, doi: 10.1016/J.JMATPROTEC.2016.11.029.
- [8] E. Chlebus, B. Kuźnicka, T. Kurzynowski, and B. Dybała, "Microstructure and mechanical behaviour of Ti-6Al-7Nb alloy produced by selective laser melting," *Materials Characterization*, vol. 62, no. 5, pp. 488–495, May 2011, doi: 10.1016/J.MATCHAR.2011.03.006.
- [9] P. Hartunian and M. Eshraghi, "Effect of Build Orientation on the Microstructure and Mechanical Properties of Selective Laser-Melted Ti-6Al-4V Alloy," *Journal of Manufacturing and Materials Processing* 2018, Vol. 2, Page 69, vol. 2, no. 4, p. 69, Oct. 2018, doi: 10.3390/JMMP2040069.
- [10] S. Y. Liu, H. Q. Li, C. X. Qin, R. Zong, and X. Y. Fang, "The effect of energy density on texture and mechanical anisotropy in selective laser

- melted Inconel 718,” *Materials & Design*, vol. 191, p. 108642, Jun. 2020, doi: 10.1016/J.MATDES.2020.108642.
- [11] K. Kim, J. Koo, E. Park, N. Kim, and W. Kim, “Anisotropic Thermal Conductivity of Nickel-Based Superalloy CM247LC Fabricated via Selective Laser Melting,” *Applied Sciences* 2021, Vol. 11, Page 4843, vol. 11, no. 11, p. 4843, May 2021, doi: 10.3390/APP11114843.
- [12] Y. Zhou, X. Zeng, Z. Yang, and H. Wu, “Effect of crystallographic textures on thermal anisotropy of selective laser melted Cu-2.4Ni-0.7Si alloy,” *Journal of Alloys and Compounds*, vol. 743, pp. 258–261, Apr. 2018, doi: 10.1016/J.JALLCOM.2018.01.335.
- [13] E. Strumza, O. Yeheskel, and S. Hayun, “The effect of texture on the anisotropy of thermophysical properties of additively manufactured AlSi10Mg,” *Additive Manufacturing*, vol. 29, p. 100762, Oct. 2019, doi: 10.1016/J.ADDMA.2019.06.013.
- [14] P. Yang, L. A. Deibler, D. R. Bradley, D. K. Stefan, and J. D. Carroll, “Microstructure evolution and thermal properties of an additively manufactured, solution treatable AlSi10Mg part,” *Journal of Materials Research*, vol. 33, no. 23, pp. 4040–4052, Dec. 2018, doi: 10.1557/JMR.2018.405.
- [15] M. S. Kim, “Effects of Processing Parameters of Selective Laser Melting Process on Thermal Conductivity of AlSi10Mg Alloy,” *Materials* 2021, Vol. 14, Page 2410, vol. 14, no. 9, p. 2410, May 2021, doi: 10.3390/MA14092410.
- [16] M. Liu, T. Wada, A. Suzuki, N. Takata, M. Kobashi, and M. Kato, “Effect of Annealing on Anisotropic Tensile Properties of Al–12%Si Alloy Fabricated by Laser Powder Bed Fusion,” *Crystals* 2020, Vol. 10, Page 1007, vol. 10, no. 11, p. 1007, Nov. 2020, doi: 10.3390/CRYST10111007.
- [17] N. T. Aboulkhair, M. Simonelli, L. Parry, I. Ashcroft, C. Tuck, and R. Hague, “3D printing of Aluminium alloys: Additive Manufacturing of Aluminium alloys using selective laser melting,” *Progress in Materials Science*, vol. 106, p. 100578, Dec. 2019, doi: 10.1016/J.PMATSCI.2019.100578.
- [18] H. Tiismus, A. Kallaste, A. Belahcen, T. Vaimann, A. Rassõlkin, and D. Lukichev, “Hysteresis measurements and numerical losses segregation of additively manufactured silicon steel for 3D printing electrical machines,” *Applied Sciences (Switzerland)*, vol. 10, no. 18, pp. 1–15, 2020, doi: 10.3390/APP10186515.
- [19] ASTM, “Standard Test Method for Thermal Diffusivity by the Flash Method,” 2013.
- [20] SLM Solutions, “Material Data Sheet Al-Alloy AlSi10Mg/EN AC-4300/EN AC-AlSi10Mg.”
- [21] “EOS Aluminium AlSi10Mg Material Data Sheet Metal Solutions”.
- [22] H. Tiismus et al., “Ac magnetic loss reduction of slm processed fe-si for additive manufacturing of electrical machines,” *Energies*, vol. 14, no. 5, Mar. 2021, doi: 10.3390/en14051241.
- [23] Si 3 and A. 0 4%, “Chemical composition, typical Electrical Steel, Thin Non-Oriented Grades Coating SURALAC ® 7000”.
- [24] W. R. Kim et al., “Fabrication of porous pure titanium via selective laser melting under low-energy-density process conditions,” *Materials & Design*, vol. 195, p. 109035, Oct. 2020, doi: 10.1016/J.MATDES.2020.109035.
- [25] T. Peng and C. Chen, “Influence of energy density on energy demand and porosity of 316L stainless steel fabricated by selective laser melting,” *International Journal of Precision Engineering and Manufacturing-Green Technology* 2018 5:1, vol. 5, no. 1, pp. 55–62, Feb. 2018, doi: 10.1007/S40684-018-0006-9.
- [26] S. Greco, K. Gutzeit, H. Hotz, B. Kirsch, and J. C. Aurich, “Selective laser melting (SLM) of AISI 316L—impact of laser power, layer thickness, and hatch spacing on roughness, density, and microhardness at constant input energy density,” *International Journal of Advanced Manufacturing Technology*, vol. 108, no. 5–6, pp. 1551–1562, May 2020, doi: 10.1007/S00170-020-05510-8/FIGURES/13.
- [27] L. Thijs, K. Kempen, J. P. Kruth, and J. van Humbeeck, “Fine-structured aluminium products with controllable texture by selective laser melting of pre-alloyed AlSi10Mg powder,” *Acta Materialia*, vol. 61, no. 5, pp. 1809–1819, Mar. 2013, doi: 10.1016/J.ACTAMAT.2012.11.052.
- [28] C. Silbernagel, I. Ashcroft, P. Dickens, and M. Galea, “Electrical resistivity of additively manufactured AlSi10Mg for use in electric motors,” *Additive Manufacturing*, vol. 21, pp. 395–403, May 2018, doi: 10.1016/J.ADDMA.2018.03.027.
- [29] T. Kimura, T. Nakamoto, M. Mizuno, and H. Araki, “Effect of silicon content on densification, mechanical and thermal properties of Al-xSi binary alloys fabricated using selective laser melting,” *Materials Science and Engineering: A*, vol. 682, pp. 593–602, Jan. 2017, doi: 10.1016/J.MSEA.2016.11.059.
- [30] J. CHEN, W. HOU, X. WANG, S. CHU, and Z. YANG, “Microstructure, porosity and mechanical properties of selective laser melted AlSi10Mg,” *Chinese Journal of Aeronautics*, vol. 33, no. 7, pp. 2043–2054, Jul. 2020, doi: 10.1016/J.CJJA.2019.08.017.
- [31] R. R. J. Selo, S. Catchpole-Smith, I. Maskery, I. Ashcroft, and C. Tuck, “On the thermal conductivity of AlSi10Mg and lattice structures made by laser powder bed fusion,” *Additive Manufacturing*, vol. 34, p. 101214, Aug. 2020, doi: 10.1016/J.ADDMA.2020.101214.
- [32] H. Tiismus, A. Kallaste, T. Vaimann, A. Rassõlkin, and A. Belahcen, “Electrical resistivity of additively manufactured silicon steel for electrical machine fabrication,” 2019, doi: 10.1109/PQ.2019.8818252.
- [33] Y. Xing, W. Wang, and H. Al-azzani, “Assessment of thermal properties of various types of high-strength steels at elevated temperatures,” *Fire Safety Journal*, vol. 122, p. 103348, Jun. 2021, doi: 10.1016/J.FIRESAF.2021.103348.
- [34] N. Kang et al., “Controllable mesostructure, magnetic properties of soft magnetic Fe-Ni-Si by using selective laser melting from nickel coated high silicon steel powder,” *Applied Surface Science*, vol. 455, pp. 736–741, 2018, doi: 10.1016/j.apsusc.2018.06.045.
- [35] M. Garibaldi, I. Ashcroft, J. N. Lemke, M. Simonelli, and R. Hague, “Effect of annealing on the microstructure and magnetic properties of soft magnetic Fe-Si produced via laser additive manufacturing,” *Scripta Materialia*, vol. 142, pp. 121–125, Jan. 2018, doi: 10.1016/J.SCRIPTAMAT.2017.08.042.

VI. BIOGRAPHIES

Martin Sarap was born in 1996 in Kuressaare, Estonia. He received his BSc and MSc degrees in electrical power engineering from Tallinn University of Technology, Estonia, in 2018, 2021 respectively. He is currently a junior researcher and a PhD student in Tallinn University of Technology, Department of Electrical Power Engineering and Mechatronics. His main research interests are thermal solutions for additively manufactured electrical machines.

Ants Kallaste was born in Pärnu, Estonia in 1980 and received his BSc, MSc and PhD degrees in electrical engineering from Tallinn University of Technology, Estonia, in 2004, 2006 and 2013 respectively. He is currently a Professor of Electrical Machines in Tallinn University of Technology, Department of Electrical Power Engineering and Mechatronics. In addition, he is holding the position of Head of Chair of Electrical Machines Research Group. He has spent several years in private engineering companies and visited numerous other research institutions. Amongst other research activities, Ants Kallaste is involved with expertise and consultations of private companies in the field of electrical machines, drives, and their diagnostics.

Payam Shams Ghahfarokhi was born in Iran, in 1986. He received the B.Sc. degree in electrical power engineering from IAUN, Iran, in 2010, the M.Sc. degree in electrical power engineering from Newcastle University, U.K., in 2011, and the Ph.D. degree in electrical engineering and machines from the Tallinn University of Technology, Estonia, in 2019. He is currently a Senior Researcher and a Postdoctoral Researcher with the Department of Electrical Machines and Apparatus, Riga Technical University, Latvia. His main research interests include electromagnetic design and thermal management of PM, and synchronous reluctance electrical machines.

Hans Tiismus was born in 1989 in Tallinn, Estonia. He received his BSc and MSc degrees in engineering physics from Tallinn University of Technology, Estonia, in 2011, 2013 respectively. He is currently a junior researcher and a PhD student in Tallinn University of Technology, Department of Electrical Power Engineering and Mechatronics. His main research interest is the additive manufacturing of electrical machines, the material properties and optimization of 3D printed soft ferromagnetic materials and components.

Toomas Vaimann received his BSc, MSc and PhD degrees in electrical engineering from Tallinn University of Technology, Estonia, in 2007, 2009 and 2014 respectively. He is currently a senior researcher in Tallinn University of Technology, Department of Electrical Power Engineering and Mechatronics. He has been working in several companies as an electrical engineer. He is the member of IEEE, Estonian Society of Moritz Hermann Jacobi and Estonian Society for Electrical Power Engineering. His main research interest is the diagnostics of electrical machines.

Curriculum vitae

Personal data

Name: Hans Tiismus
Date of birth: 21.01.1989
Place of birth: Tallinn
Citizenship: Estonia

Contact data

E-mail: hans.tiismus@taltech.ee

Education

2018–2022 PhD, Tallinn University of Technology
2011–2013 MSC, Engineering Physics, Tallinn University of Technology
2007–2011 BSC, Engineering Physics, Tallinn University of Technology
2004–2007 High school, Rapla Central Gymnasium

Professional employment

2018–2022 Junior Researcher, Tallinn University of Technology
2014–2018 Mechanical engineer / designer – Adfactory LLC
2011–2014 Draftsman/engineer – PKC Estonia AS

Honors and Awards

2022 Hans Tiismus, Research prize of Republic of Estonia in technical sciences for the Dresearch cycle “Additively manufactured electrical machines”
2022 Hans Tiismus, Competition “3 Minute Science”, Estonian Academy of Science, finalist
2019 Hans Tiismus, Best Presenter Award in the session Electrical Machines II at 18th International Symposium “Topical Problems in the Field of Electrical and Power Engineering”, Toila, Estonia
2019 Hans Tiismus, Best Presenter Award in the session “Robotics, Electronics and Automation” at 19th International Conference “Young Specialists on Micro/Nanotechnologies and Electron Devices (EDM)”, Altai, Russia
2019 Hans Tiismus, Second place in the session “IES student forum” in the conference “IEEE 60th International Scientific Conference on Power and Electrical Engineering of Riga Technical University (RTUCON 2019)”, Riga, Latvia
2019 Hans Tiismus, TUT Arengufond’s Mati Jostov’s scholarship

Elulookirjeldus

Isikuandmed

Nimi: Hans Tiismus
Sünniaeg: 21.01.1989
Sünnikoht: Tallinn
Kodakondsus: Eesti

Kontaktandmed

E-post: hans.tiismus@taltech.ee

Hariduskäik

2018–2022 PhD, Elektroenergeetika ja mehhatroonika,
Tallinna Tehnikaülikool
2011–2013 MSC, Tehniline füüsika, Tallinna Tehnikaülikool
2007–2011 BSC, Tehniline füüsika, Tallinna Tehnikaülikool
2004–2007 Keskaridus, Rapla Ühisgümnaasium

Teenistuskäik

2018–2022 Nooremteadur, Tallinna Tehnikaülikool
2014–2018 Mehaanikainsener / kujundaja – Adfactory OÜ
2011–2014 Projekteerija – PKC Eesti AS

Teaduspreemiad ja tunnustused

2022 Hans Tiismus, Eesti Vabariigi teaduspreemia tehnikateaduste alal tööde tsükli “Kihltisandustehnoloogial põhinevad elektrimasinad” eest
2022 Hans Tiismus, Konkurss “Teadus 3 minutiga”, Eesti Teaduste Akadeemia, finalist
2019 Hans Tiismus, Parim ettekanne sektsioonis “Elektrimasinad II” 18. Rahvusvaheline sümpoosium “Topical Problems in the Field of Electrical and Power Engineering”, Toila, Eesti
2019 Hans Tiismus, Parim ettekanne sektsioonis “Robotika, elektroonika, automatiseerimine”, 18. Rahvusvaheline konverents: “Young Specialists on Micro/Nanotechnologies and Electron Devices (EDM)”, Altai, Venemaa
2019 Hans Tiismus, Teine koht sektsioonis “IES õpilasfoorum” konverentsil “IEEE 60th International Scientific Conference on Power and Electrical Engineering of Riga Technical University (RTUCON 2019)”, Riia, Läti
2019 Hans Tiismus, Tallinna Tehnikaülikooli Arengufondi Mati Jostovi nimeline stipendium

ISSN 2585-6901 (PDF)
ISBN 978-9949-83-880-6 (PDF)